Australian Telecommunications Research Institute

(ATRI)

Frequency Dependent Digital Compensation in DSP Based FM Modulators

John Douglas Tuthill

January 2000

To Sandra and Luke

Acknowledgements

Many people have helped me in one way or another to finish the research work presented in this thesis. In particular I would like to acknowledge :

My Supervisor Professor Tony Cantoni for his encouragement, enthusiasm and expert guidance throughout the course of this research. He has the rare combination in engineering of being a talented theoretician and a gifted practitioner and I consider myself very privileged to have had the opportunity to work with and learn from him. In addition I would like to thank him for his prompt reviews of edits of this document.

My Associate Supervisor Dr Yee-Hong Leung for much help in the early stages of this research and for many useful discussions throughout the course of the research.

Dr Kevin Fynn for many helpful discussions and, in particular, for giving me the opportunity to work on the GIRD (Government Industry Research Development) project "DSP for Radio Base Stations" from which this research sprung.

Mr Russell McWhirter for his generous and cheerfully given help and advice on many aspects of the hardware implementation component of the research project.

My wife Sandra who provided an enormous amount of support and encouragement to me throughout my research and helped me celebrate all the milestones along the way.

My Mother, Father and Brother for their continued support.

The staff and students at ATRI/ATcrc for providing a stimulating, open minded and enjoyable work environment. In particular my room mates Dr Kuo Hsien Chen and Mr Brad Williamson.

Finally, I would also like to gratefully acknowledge the financial assistance from The Australian Telecommunications Research Institute and the Australian Postgraduate Award scheme.

Abstract

This thesis reports original work on digital compensation for frequency dependent transfer characteristics and errors in digital PAM/CPFSK (Pulse Amplitude Modulation/Continuous Phase Frequency Shift Keying) quadrature modulators.

A particularly flexible and cost effective approach to the implementation of the base-band section of a radio transmitter is to synthesise base-band signals digitally using a DSP (Digital Signal Processor). This approach is limited, however, by the transfer characteristics and errors in the implementation of practical analogue sub-systems. These practical limitations result in undesirable in-band frequency-dependent shaping of the transmitted signals. In the case of FM (Frequency Modulation) signals, this leads to the generation of unwanted side-lobes in the transmitted RF signal spectrum that interfere with signals in adjacent frequency channels. This results in the transmitted signal failing to meet transmission standards requirements.

The digital compensation techniques developed and presented in this thesis allow the reduction of undesirable in-band frequency-dependent signal shaping. It is shown that this enables strict requirements on the spectral emissions from the FM transmitter to be met using a flexible and cost effective DSP based modulator system.

The contributions of the thesis are in three primary areas:

(i)   The development of a structure for frequency dependent digital compensation.

(ii)   The formulation and solution of an optimisation problem that allows the free parameters within the structure to be determined such that effective reduction of unwanted in-band frequency-dependent signal shaping is achieved.

(iii)   The development of techniques that allow the digital compensation procedure to be successfully implemented on a practical DSP platform.

The new digital compensation structure that is proposed uses two digital FIR (Finite Impulse Response) filters in the digital base-band section of the quadrature

modulator: one in the in-phase (I) channel and one in the quadrature (Q) channel. The tap-weights of the FIR filters are determined by solving two optimisation problems: one for each channel. The optimisation problems are formulated using a new approach that ensures that the degrees of freedom in the optimisation i.e., the FIR filter tap-weights, are used effectively to meet the objective of reducing in-band frequency-dependent signal shaping in analogue sub-systems further down the transmission path.

A characterisation of the solutions to the optimisation problems enables the identification of techniques that need to be adopted to successfully implement the proposed digital compensation on a practical DSP-based system.

The digital compensation technique is demonstrated by implementing and testing the technique on a DSP platform. The results of experimental studies are presented which clearly demonstrate that the digital compensation technique leads to substantial reductions in adjacent channel interference.

Table of Contents

Authors Publications

1. "Optimum Pre-compensation Filters for IQ Modulation Systems," *IEEE Trans. Comm.'s*, Vol. 47, No. 10, p. 1466 - 1469, October 1999. (with A. Cantoni)

2. "Implementation of Automatic Digital Compensation in IQ Modulator Systems," *Accepted for Publication*, Proceedings of the European Signal Processing Conference (EUSIPCO-2000). (with A. Cantoni)

3. "Automatic Digital Pre-compensation in IQ Modulators," *Proceedings of the IEEE International Conference on Acoustics, Speech and Signal Processing (ICASSP)*, Phoenix, Arizona, USA, March 1999. (with A. Cantoni)

4. "Optimum Pre-compensation Filters for IQ Modulation Systems," *Proceedings of the 6th IEEE International Workshop on Intelligent Signal Processing and Communication Systems (ISPACS'98)*, Melbourne, Australia, vol. 1, pp. 158-162, November 1998. (with Y.-H. Leung and A. Cantoni)

Chapter 1. Introduction

1.1 Background

Wireless communications is currently undergoing enormous growth and change. Mobile telephony applications that have traditionally been limited by the bandwidth available in the analogue wireless access network are moving to systems that are fundamentally based on digital technology. These new digitally-based systems are setting out to deliver the throughput that previously needed wired connections. The promise of *"Anywhere, anytime"* service for voice, images and data in multimedia applications places increasing pressures on capacity and spectrum. The radio spectrum has become a precious commodity and this is driving intense research efforts in developing technology that uses the spectrum more efficiently.

Much of the current development in wireless communications is based on digital communication principles. Digital sub-systems are used extensively to implement radio transceivers [1-10]. Indeed, the current trend in *software radios* is the replacement of as much of the analogue sub-section of a radio transceiver as possible with programmable digital hardware [5].

In [2] several digital transceiver architectures are identified including *superheterodyne, digital IF* and *direct-conversion*. A versatile and widely used [1], [2] technique in transceiver architecture is Inphase/Quadrature (IQ) modulation. IQ modulation is one of a number of techniques that can be used to generate amplitude, phase or frequency modulated signals. Indeed, one of the advantages of the IQ modulator structure is its utility in generating a wide variety of modulation formats.

In this thesis, the superheterodyne transceiver architecture that incorporates IQ base-band modulation/demodulation as shown in Figure 1.1 is considered.
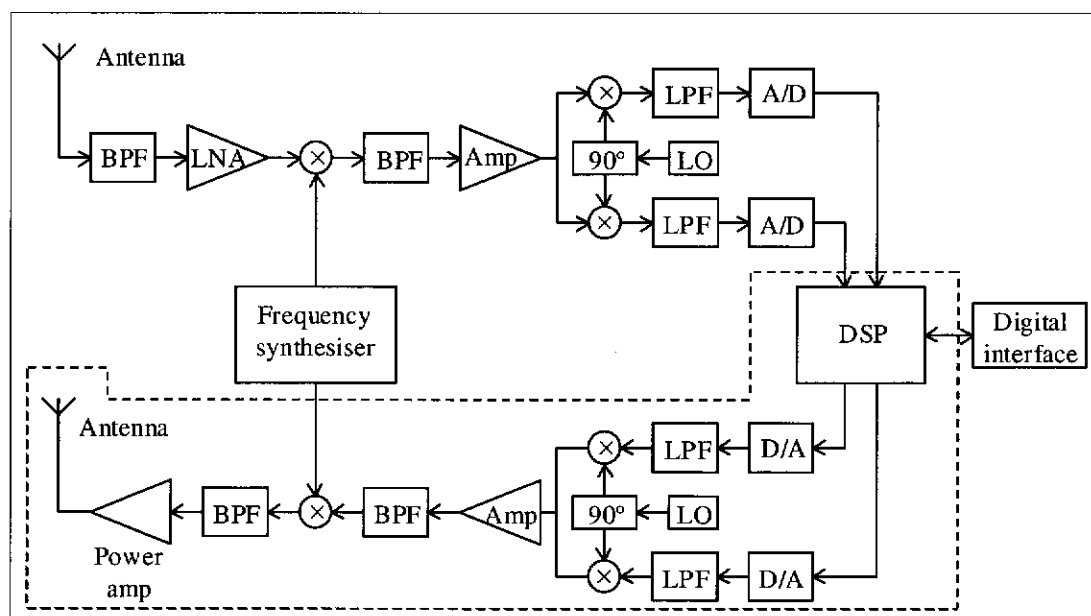
Figure 1.1. DSP based superheterodyne transceiver.

The work presented in this thesis is concerned the base-band and intermediate frequency/radio frequency (IF/RF) transmitter elements of the transceiver bounded by the dashed line in Figure 1.1.

This work forms part of a larger joint university/industry project within the AT-CRC (Australian Telecommunications Cooperative Research Centre) involving the design and implementation of a modulation and transmission system based on DSP (Digital Signal Processor) and FPGA (Field Programmable Gate Array) technology that is capable of generating a range of modulation formats. Two modulation formats that have received particular attention are the ERMES (Enhanced Radio Messaging System) [11] and POCSAG (Post Office Code Standardisation Advisory Group) paging formats. A block diagram of the modulator and transmitter is shown in Figure 1.2.
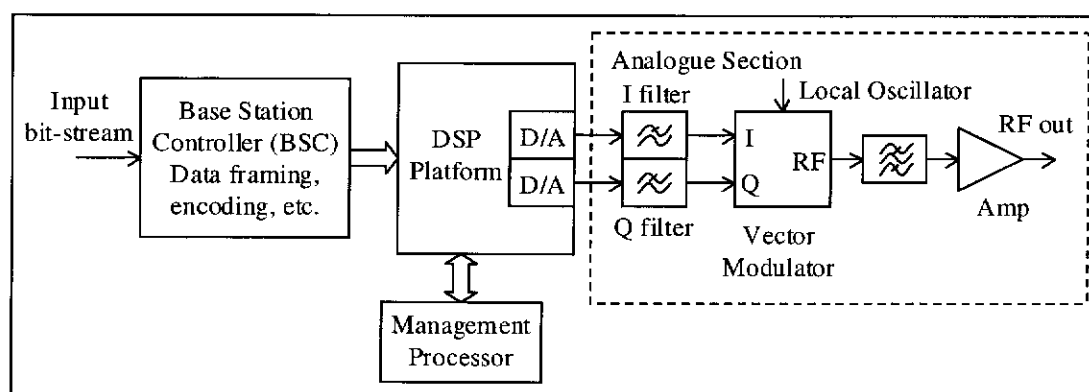
Figure 1.2. DSP-based modulator and transmitter system.

A photograph of the hardware implementation of the DSP platform block is given in Figure 1.3 showing the FPGA chip in the lower left and the DSP chip in upper right.
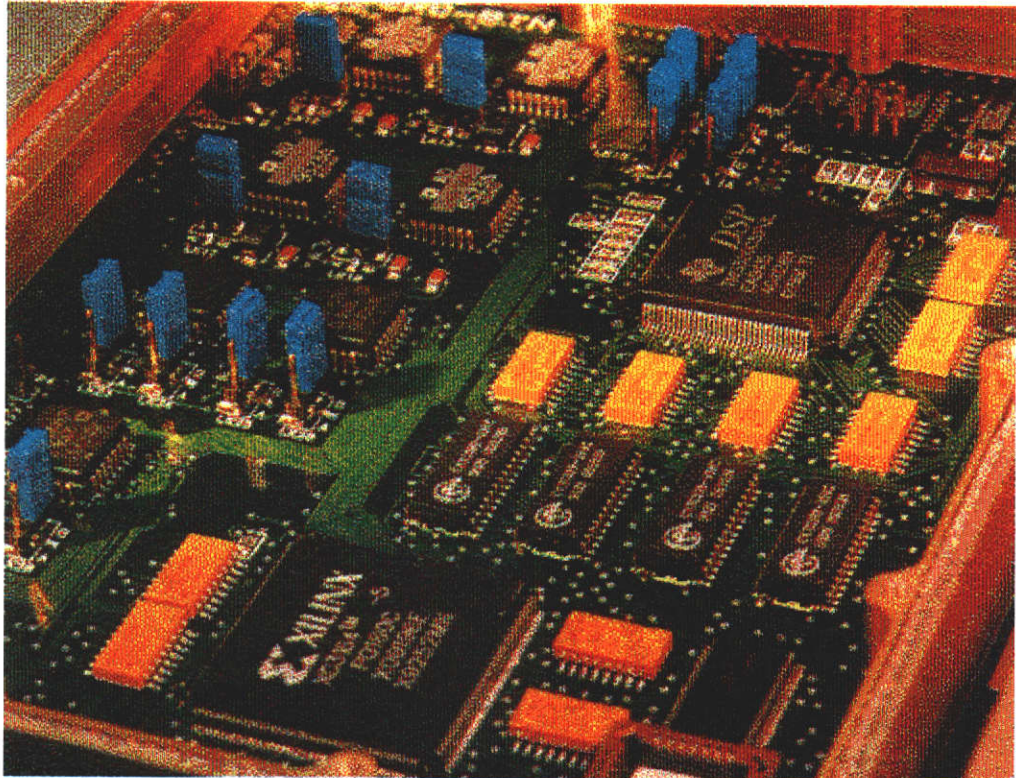
Figure 1.3. DSP platform hardware.

The DSP-based design incorporating a vector modulator to up-convert the base-band signals to IF or RF directly as shown in Figure 1.2 is attractive for several reasons, including:

- Reduced complexity of analogue hardware.

- Ease of configuration via software to generate a range of modulation formats for example FSK, QAM, QPSK, etc.

- Simplicity of interface design to external digital data sources.

- Repeatable and predictable system characteristics of a DSP allowing tight signalling specifications to be met.

- Allows implementation of algorithms to compensate for errors and limitations in the practical analogue components in the base-band, IF or RF stages.

As mentioned at the beginning of this chapter, the electromagnetic spectrum has become a precious commodity and in current transmission standards there are strict regulations on the amount of power transmitted into adjacent channels. The Adjacent

Channel Power (ACP) is a common measure of the degree to which a transmission interferes with signals in adjacent channels [12] and is typically specified between − 50 dBc and −70 dBc (dB relative to the carrier power) [13], [14].

Practical limitations and implementation errors in analogue components in the base-band, IF and RF sections of the transmitter system causes spreading of the transmitted signal spectrum into regions outside the channel's allotted frequency band. This can result in the failure of the system to meet the ACP requirements of the signal specification.

An important practical aspect of the transmitter chain and one that has received much attention in the literature is the impact of non-linear transfer characteristics in the RF power amplifier (PA) on the transmitted signal spectrum [12-34].

Most RF PA's can be adequately described by a pair of AM-to-AM and AM-to-PM conversion characteristics [16] that relate distortion in the amplitude and phase of the output signal to fluctuation in the input RF signal envelope function. Passing an RF signal that has a varying envelope through an RF PA that has a non-linear transfer characteristic generally causes spreading of the transmitted signal spectrum. For signals such as M-QAM or QPSK that have non-constant RF signal envelopes, two approaches to this problem are [12]:

1. Use Class A amplifiers with appropriate amount of *back-off* to ensure a linear operating characteristic. This approach has the disadvantage of low power efficiency.

2. Use power efficient but non-linear Class AB, B or C PA's and linearisation techniques. These techniques are often termed *predistortion*.

Extensive work has been done on digital *predistortion* techniques [12, 13, 17-34] that compensate for non-linearities in the power amplifier shown in Figure 1.1 and Figure 1.2 in an effort to reduce spreading of the transmitted signal spectrum into adjacent frequency channels.

The impact of non-linear power amplifiers on constant envelope signals such as continuous phase frequency shift keying (CPFSK) is manageable. In [35] it is shown

that passing a constant envelope FM signal through a non-linear device results in an amplitude scaled version of the original signal and additional harmonic products that can be removed by band-pass filtering providing a suitable choice of carrier frequency is made. Thus, constant RF envelope is an important property of CPFSK signals as it allows the use of non-linear yet power efficient PA's in the transmitter section.

This thesis is concerned with the generation of CPFSK signals using the DSP-based structure illustrated in Figure 1.2.

Practical limitations and implementation errors in the digital-to-analogue interface and the analogue vector modulator in Figure 1.2 cause a loss of the desired constant envelope property of the RF signal [36]. This, in turn, results in unacceptable spreading of the transmitted signal spectrum after passing through the non-linear power amplifier. In order to fully realise the inherent advantages of highly non-linear but power efficient PA's with this class of modulation signals, expensive, high tolerance analogue components and *adjust-on-test* approaches must be adopted.

Shortcomings in the analogue components can be classified into two categories:

1. Static errors including DC offsets in the I and Q channels, DC gain imbalances between the channels and phase errors in the vector modulator.

2. Frequency dependent transfer characteristics and errors in the I and Q channels that produce departures from constant magnitude, linear phase in each channel and magnitude and phase imbalance between the channels.

The effect of static errors on quadrature modulator/demodulator performance was the subject of earlier work on RADAR [37-39] and has been investigated extensively since in communications applications [12, 36, 40-48]. Effective techniques for compensating for offset errors, gain imbalance and phase errors have been developed and successfully implemented [44] as part of the larger DSP-based modulator project discussed earlier.

The principal sources of frequency dependent transfer characteristics and imbalances in the I and Q channels of the quadrature modulator are the two analogue signal

reconstruction filters. These filters, together with the two D/A converters, form the digital-to-analogue interface in the system and attenuate unwanted digital image components in the base-band signal spectra before modulation and transmission.

While digital techniques have made strong inroads into the compensation for the non-linear characteristics of RF power amplifiers there has been relatively little research into the impact of the signal reconstruction filters on the performance of a DSP-based modulator. Faulkner et al in [12] and [14] have considered the effects of analogue reconstruction filters on certain aspects of modulator and transmitter performance as follows.

In [12] the effects of reconstruction filters on digital base-band predistortion linearisers for PA's is considered in terms of their contribution to undesirable memory effects that limit the performance of linearisation schemes. The authors present design approaches for reconstruction filters and also the digital system sampling rate such that the impact of the reconstruction filters on PA linearisers is minimised.

In [14] the effects of frequency dependent magnitude and phase imbalance between the I and Q channel reconstruction filters are considered in the context of a multi-channel FDM (Frequency Division Multiplexing) environment. It is shown that magnitude and phase imbalance in the analogue reconstruction filters cause unwanted side-bands within the system bandwidth that interfere with other channels in the FDM scheme. An adaptive compensation technique is proposed whereby a number of variable side-band components are introduced into individual base-band channels prior to a wide-band combiner. These variable components cancel unwanted side-bands at a number of frequencies across the total system bandwidth. The technique presented in [14], however, is specific to multi-channel environments and does not address the issue of frequency-dependent compensation within each channel's frequency band. Furthermore, the work assumes linear PA's.

An area that has not been addressed is an effective method of utilising the DSP to mitigate the impact of frequency dependent transfer characteristics of practical reconstruction filters on the output spectrum of a non-linear transmitter PA for (ideally) constant envelope signals such as CPFSK.

The work presented here is motivated by a problem encountered in the development of a DSP-based modulator and transmitter system. With the need to develop a cost-effective DSP-based modulator and transmitter, high tolerance analogue components and adjust-on-test approaches must be avoided.

In this thesis a technique for digitally compensating for the frequency dependent characteristics of the analogue reconstruction filters is presented. The technique is suitable for implementation on practical DSP systems. Experimental results from an implementation of the technique on the modulator system shown in Figure 1.2 and Figure 1.3 verify that the technique is highly effective in reducing ACP in the output RF signal spectrum.

1.2 Summary of Contributions

The key contributions of this thesis are:

I.   The development of a digital compensation structure based on the introduction of two digital FIR filters into the I and Q channels of the DSP-based modulator.

II.   The formulation and solution of an optimisation problem that provides the tap-weights of the two FIR digital filters that allows the objectives on ACP reduction to be met.

III.   An approach for choosing a *desired* I and Q channel frequency response that ensures that the degrees of freedom in the optimisation problem are used effectively in reducing ACP in the output RF signal.

IV.   The development of techniques that allow the digital compensation procedure to be successfully implemented on a finite precision DSP platform.

1.3 Thesis Outline

This thesis consists of seven chapters.

In Chapter 2, a mathematical model for CPFSK signals is introduced and a particular digitally-based modulator structure that can be used to generate CPFSK signals is outlined. Definitions and assumptions that underpin work in subsequent chapters are provided. The chapter introduces the important role that the frequency dependent characteristics of the reconstruction filters play in determining the nature of the RF signal envelope function. This motivates the work presented in Chapter 3 that focuses on the frequency domain characteristics of the two analogue reconstruction filters.

In Chapter 3, the specific requirements of the two analogue reconstruction filters are identified. Investigations detailed in Chapter 3 highlight particular frequency domain characteristics of the two filters that significantly impact on envelope ripple in the RF signal envelope. The identification of the critical frequency domain characteristics is essential to the development of an efficient and effective digital compensation scheme in Chapter 4.

In Chapter 4, a structure for digital compensation is proposed. The free parameters within the digital compensation structure are determined from the solution to an optimisation problem. Information gained from the reconstruction filter investigations in Chapter 3 is used in formulating the optimisation problem to ensure that the resulting compensation is effective in reducing ripple in the envelope of the RF signal. A characterisation of the solution to the optimisation problem identifies techniques that need to be adopted to successfully implement the digital compensation on a practical DSP system. Equivalent formulations of the optimisation problem in terms of frequency domain and time domain parameters provide a framework for automatic digital compensation. This is the subject of Chapter 5.

In Chapter 5, channel parameter identification techniques are developed that can be used to automatically establish and update estimates of the optimum digital compensation filters. Two separate techniques are presented. The first technique is

based on the frequency domain formulation of the optimisation problem given in Chapter 4. The second identification technique is based on a time domain formulation of the optimisation problem. Numerical studies demonstrate the effectiveness of each technique in meeting the objective of reducing ripple in the RF signal envelope. The effects of implementation characteristics such as quantisation and system noise on each technique are characterised.

In Chapter 6, the effectiveness of the automatic digital compensation technique developed in Chapters 4 and 5 is demonstrated. It is shown that effective digital compensation can be successfully implemented on a practical DSP platform. Additional implementation issues not dealt with in Chapter 5 that must be considered are highlighted. The results of experimental studies presented in Chapter 6 clearly demonstrate that the digital compensation technique leads to substantial improvements in ACP.

Chapter 7 draws together the conclusions made in each of the chapters and contains suggestions for further work.

1.4 Glossary

1.4.1 Mathematical Symbols and Notation

$\text{Im}[z]$	Imaginary part of the complex number z
$\text{Re}[z]$	Real part of the complex number z
$a(t) * b(t)$	Convolution of $a(t)$ with $b(t)$
A^T	Transpose of the matrix A
A^*	Conjugate of the matrix A
A^H	Conjugate transpose (hermitian transpose) of the matrix A
A^+	Moore-Penrose pseudo-inverse of the matrix A
$\mathcal{F}\{h(t)\}$	Fourier transform of the function $h(t)$
$\mathcal{F}^{-1}\{H(f)\}$	Inverse Fourier transform of the function $H(f)$
$\text{sinc}(x)$	Sinc function given by $\sin(x)/x$
$Z\{g(nT)\}$	The Z-transform of $g(nT)$
$\mathbb{R}$	The set of real numbers
$\mathbb{C}$	The set of complex numbers
$\mathbb{Z}$	The set of integers
$X \in \mathbb{R}^{N \times M}$	The matrix X is a member of the set of real $N \times M$ matrices
$V \in \mathbb{C}^{K \times L}$	The matrix V is a member of the set of complex $K \times L$ matrices
$\nabla_g J(g)$	The derivative of the function $J(g)$ with respect to the vector g
$\min_g J(g)$	Minimise the function $J(g)$ with respect to the vector g
$[R]_{k,l}$	The $(k,l)^{\text{th}}$ element of the matrix R
$[p]_k$	The kth element of the vector p
$E[\hat{\alpha}]$	The expected value of the estimate $\hat{\alpha}$
$\text{var}\left[\hat{\beta}\right]$	The variance of the estimate $\hat{\beta}$
$\det[V]$	The determinant of the matrix V
$x \bmod(y)$	X modulo y

1.4.2 Abbreviations and Acronyms

ACP	Adjacent Channel Power
A/D	Analogue to Digital converter
AM	Amplitude Modulation
dBc	Decibels relative to the carrier power
CPFSK	Continuous Phase Frequency Shift Keying
D/A	Digital to Analogue converter
DFT	Discrete Fourier Transform
DSA	Dynamic Signal Analyser
DSP	Digital Signal Processor
ERMES	Enhanced Radio Messaging System
FDM	Frequency Division Multiplexing
FIR	Finite Impulse Response
FM	Frequency Modulation
FPGA	Field Programmable Gate Array
FSK	Frequency Shift Keying
IF	Intermediate Frequency
IQ	In-phase and Quadrature
LPF	Low-pass Filter
m-sequence	Maximal-length linear feedback shift register sequence
PA	Power Amplifier
PAM	Pulse Amplitude Modulation (M-PAM is M-level PAM)
PDF	Probability Density Function
PM	Phase Modulation
PRBN	Pseudo-Random Binary Noise
PSD	Power Spectral Density
QAM	Quadrature Amplitude Modulation
QPSK	Quadrature Phase Shift Keying
RF	Radio Frequency
RMS	Root Mean Square value
VSA	Vector Signal Analyser
ZOH	Zero Order Hold

Chapter 2. Background

2.1 Introduction

This chapter serves to introduce a signal model for *Pulse Amplitude Modulation/Continuous Phase Frequency Shift Keying* (PAM/CPFSK) signals and outline the particular IQ modulator structure considered in this thesis. In Chapter 1 the transfer characteristics and implementation errors in practical analogue signal reconstruction filters were introduced as primary contributors to frequency dependent errors in the IQ modulator structure. In this chapter the two analogue signal reconstruction filters are identified within the IQ modulator structure. Furthermore, the place of the two reconstruction filters in the modulator signal model is highlighted.

The aims of this chapter are to:

1. Introduce a mathematical model for *Pulse Amplitude Modulation/Continuous Phase Frequency Shift Keying* (PAM/CPFSK) signals.

2. Provide a background to the technique of IQ modulation and outline a particular modulator structure that can be used to generate these signals.

3. Provide a definition for the signal envelope function that will underpin much of the work presented in subsequent chapters.

This chapter makes three key points in respect to the work to follow in subsequent chapters of this thesis.

The first key point is a mathematical model for CPFSK signals. It will be shown that the model suggests a structure that can be used to generate these signals.

The second key point is the development of a DSP based IQ modulator structure that can be used to generate CPFSK signals. There are a number of techniques for generating CPFSK signals and in the work presented here the method of IQ (In-phase and Quadrature) modulation is considered. In this chapter the structure of an IQ

modulator is introduced that uses a digital sub-system to synthesise the base-band I and Q signal components and an analogue section to convert the digital signals into a continuous time, analogue CPFSK output signal. The conditions under which the output signal of the digitally based modulator approximates, with sufficient accuracy, the output of an ideal, continuous time IQ modulator are highlighted.

The third key point is a definition of the *envelope* function of CPFSK signals. In FM transmitter systems that contain elements having non-linear transfer characteristics (power amplifiers for example), fluctuations in the envelope of the FM signal result in spreading of the transmitted signal spectrum into adjacent channels. An important factor, therefore, in the adjacent channel performance of the transmitter system is the level of ripple present in the envelope function of the FM signal. The definition of the CPFSK signal envelope will be used as a principal measure of the effectiveness of the compensation techniques to be developed and investigated in the later chapters of this thesis.

This chapter is organised into six main sections. In the next section (Section 2.2) a signal model for M-PAM/CPFSK signals is presented. In Section 2.3 the envelope function of a CPFSK signal is defined and the relation between this definition and other definitions of the envelope found in the literature is given.

Section 2.4 is concerned with the *structure* of systems that can be used to generate CPFSK signals and is divided into three parts. In the first part the structure of an M-PAM/CPFSK continuous time modulation system is introduced. In the second part a modulator structure is investigated that uses a digital sub-system to synthesise base-band components of the CPFSK signal. In the third part a specific example of a 4-PAM/CPFSK modulation format signal and modulator are considered.

In Section 2.5 a model of the modulator is proposed that takes account of certain errors resulting from hardware implementation of the system. Section 2.6 contains conclusions from the work presented in the chapter.

2.2 PAM/CPFSK Signals

A Pulse Amplitude Modulation signal corresponding to an M-level data sequence $\{s_n\}$ can be represented as [49]

$$m(t) = \sum_{n=0}^{\infty} s_n b(t - nT_d) \tag{2.1}$$

where T_d is the input data *symbol period* defined by

$$T_d = \frac{1}{f_d} \tag{2.2}$$

and where f_d is the input data *symbol rate*. The function $b(t)$ is a pulse function whose amplitude is weighted by the current data value at each symbol period.

A PAM Frequency Shift Keying (PAM/FSK) signal can be represented in terms of positive and negative frequency deviations from a carrier frequency, f_c, that are proportional to the amplitude of the message signal, $m(t)$. A real-valued PAM/FSK signal can be modelled as [50]

$$y(t) = A\cos\left(\omega_c t + K_0 \int_0^t m(\tau) d\tau + \phi_0\right), \tag{2.3}$$

where $\omega_c = 2\pi f_c$ is the radian carrier frequency. The real, positive constant A is the PAM/FSK signal amplitude and K_0 is a scaling factor that relates the instantaneous frequency displacement to the message signal amplitude. The phase of the signal, $y(t)$, at $t = 0$ is given by the arbitrary random phase parameter, ϕ_0.

If $m(t)$ does not contain impulse functions then $y(t)$ has continuous phase and is called a PAM, *Continuous Phase* FSK (PAM/CPFSK) signal [51].

Defining the phase function $\phi(t)$ as

$$\phi(t) = K_0 \int_0^t m(\tau) d\tau + \phi_0, \tag{2.4}$$

equation (2.3) can be rewritten as

$$y(t) = A\cos\big(\omega_c t + \phi(t)\big). \tag{2.5}$$

Expanding the cosine term in (2.5), the signal $y(t)$ can be written in the form

$$y(t) = i(t)\cos\big(\omega_c t\big) - q(t)\sin\big(\omega_c t\big), \tag{2.6}$$

where the *in-phase* and *quadrature* signals, $i(t)$ and $q(t)$ respectively, are given by

$$i(t) = A\cos\big(\phi(t)\big), \tag{2.7}$$

and $\qquad\qquad q(t) = A\sin\big(\phi(t)\big). \tag{2.8}$

2.3 The Signal Envelope

With the PAM/CPFSK signal expressed in the form given by (2.6) the *envelope* function, $r(t)$, of the signal $y(t)$ is defined in terms of the specified signals $i(t)$ and $q(t)$ as

$$r_y(t) \triangleq \sqrt{i^2(t) + q^2(t)}. \tag{2.9}$$

The envelope function of the CPFSK signal given in (2.9) will be used as a principal measure of the effectiveness of the compensation techniques to be developed and investigated in the later chapters of this thesis.

From (2.7), (2.8) and (2.9), the PAM/CPFSK signal envelope can be rewritten as

$$\begin{aligned} r_y(t) &= A\sqrt{\cos^2\big(\phi(t)\big) + \sin^2\big(\phi(t)\big)} \\ &= A, \end{aligned} \tag{2.10}$$

i.e., the envelope function of the PAM/CPFSK signal is a constant value.

There are a number of definitions for the envelope of a signal, see for example [52], [53] and [54] and in the following the definition in (2.9) is compared with other definitions found in the literature.

The *complex natural envelope* of $y(t)$ is defined in [52] for signals of the form given by (2.6) as

$$r_n(t)e^{j\varphi_n(t)} \triangleq i(t) + jq(t),$$ (2.11)

where

$$r_n(t) = \sqrt{i^2(t) + q^2(t)},$$ (2.12)

and

$$\varphi_n(t) = \arctan\left(\frac{q(t)}{i(t)}\right).$$ (2.13)

It is understood that $r_n(t) \geq 0$ and that $\varphi_n(t)$ lies in the quadrant defined by the signs of the signals $i(t)$ and $q(t)$.

Note that the magnitude of the complex natural envelope, $r_n(t)$, in (2.12) is the same as the envelope function defined in (2.9), i.e.,

$$r_y(t) = r_n(t).$$ (2.14)

Another definition for the envelope of a signal that appears in the literature is the *complex analytic envelope* [52-54]. If the signal $y(t)$ has the Fourier transform $Y(f)$, then the complex analytic envelope of $y(t)$ is defined in [52] as

$$r_a(t)e^{j\varphi_a(t)} \triangleq 2\int_0^\infty e^{j(\omega - \omega_c)t} Y(f)\,df$$ (2.15)

where $\omega = 2\pi f$ and $r_a(t) \geq 0$.

When $y(t)$ has the form given in (2.6), it is shown in [52] that the complex natural envelope and the complex analytic envelope are related by

$$r_a(t)e^{j\varphi_a(t)} = r_n(t)e^{j\varphi_n(t)} + J(t),$$ (2.16)

where

$$J(t) = 2je^{-j\omega_c t}\,\mathrm{Im}\!\left[e^{-j\omega_c t}\int_{f_c}^{\infty} e^{j\omega t}\left(I(f) - jQ(f)\right)df\right],$$ (2.17)

and where $I(f)$ and $Q(f)$ are the Fourier transforms of $i(t)$ and $q(t)$ respectively.

It can be shown [52] that if $i(t)$ and $q(t)$ are band-limited in the sense that

$$\left.\begin{array}{l} I(f) = 0 \\ Q(f) = 0 \end{array}\right\}|f| > f_c$$ (2.18)

then

$$J(t) = 0,$$ (2.19)

and (2.16) can be rewritten as

$$r_a(t)e^{j\varphi_a(t)} = r_n(t)e^{j\varphi_n(t)},$$ (2.20)

i.e., the complex natural envelope is the same as the complex analytic envelope.

2.4 IQ Modulator Structure

2.4.1 Continuous Time Modulator

The PAM/CPFSK signal, $y(t)$, in (2.3) can be generated by the continuous-time (analogue) IQ modulator shown in Figure 2.1.
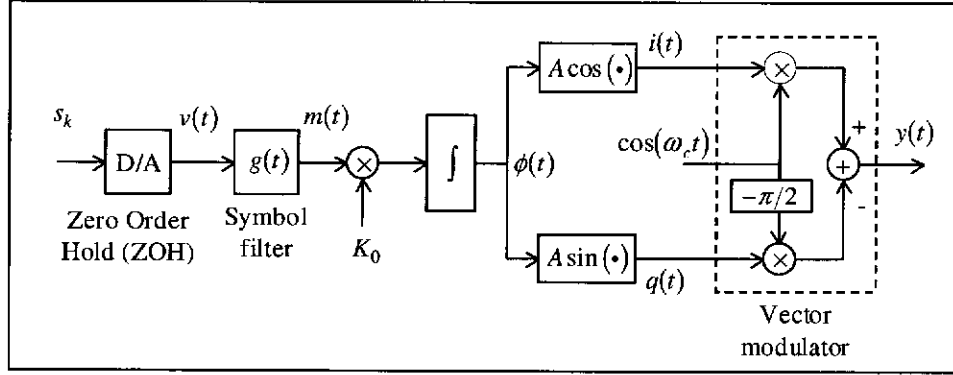
Figure 2.1. Continuous-time PAM/CPFSK IQ modulator system structure derived from (2.3), (2.4), and (2.6)-(2.8).

The source symbol sequence feeding the symbol filter is assumed to be given by

$$v(t) = \sum_{n=0}^{\infty} s_n p(t - nT_d), \tag{2.21}$$

where T_d is defined by (2.2) and where $\{s_k\}, k = 0,1,2,\ldots$ denotes a sequence of numbers representing the message symbols to be transmitted. The function $p(t)$ is the unit pulse function given by

$$p(t) = \begin{cases} 1 & 0 < t < T_d \\ 0 & \text{otherwise} \end{cases}. \tag{2.22}$$

The message signal, $m(t)$, at the output of the symbol filter is thus given by

$$\begin{aligned} m(t) &= v(t) * g(t) \\ &= \sum_{n=0}^{\infty} s_n b(t - nT_d), \end{aligned} \tag{2.23}$$

where $[*]$ denotes convolution. The pulse function, $b(t)$, is defined by

$$b(t) = p(t) * g(t),\qquad(2.24)$$

i.e., the response of the symbol filter to a square pulse of duration T_d seconds.

2.4.2 Digital Modulator

In this section the structure of an IQ modulator based on a digital sub-system is introduced that synthesises samples of the base-band I and Q signal components. An analogue section converts the I and Q channel sample sequences into continuous time analogue signals. In the following, the term *digital modulator* is used to refer to both digital and analogue sections. Conditions are outlined under which the digital modulator output signal approximates, with sufficient accuracy, the output signal of the continuous time modulator in Figure 2.1.

Consider the IQ modulator system shown in Figure 2.2.

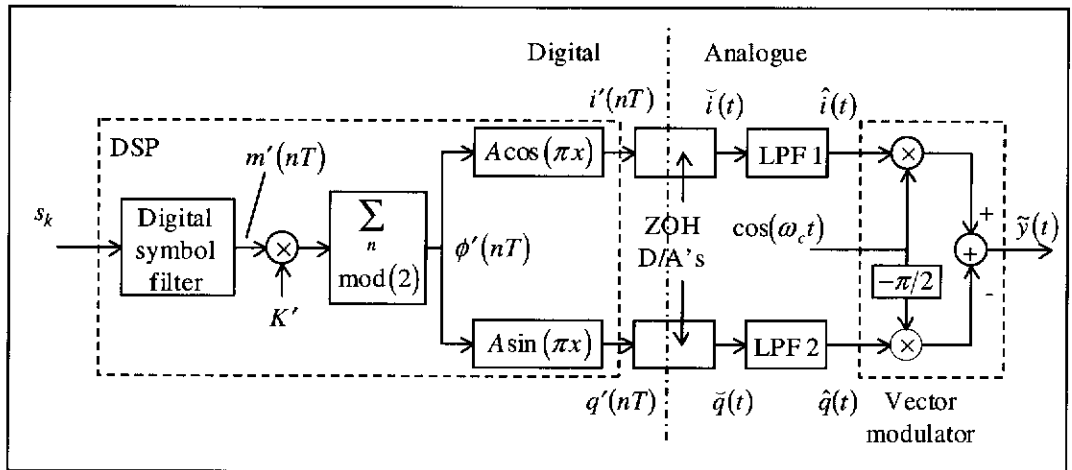**Figure 2.2.** DSP implementation of an IQ modulator incorporating digital
synthesis of the I and Q channel signals and an analogue-to-digital
converter section consisting of Zero-Order-Hold (ZOH) D/A
converters and analogue low-pass filters (LPF1 and LPF2).

The digital section of the modulator in Figure 2.2 synthesises two sample sequences, $i'(nT)$ and $q'(nT)$, given by

$$i'(nT) = A\cos\left(\pi\phi'(nT)\right)$$

$$\text{and} \tag{2.25}$$

$$q'(nT) = A\sin\left(\pi\phi'(nT)\right),$$

where T is the digital system sampling period. The system sampling frequency is defined by

$$f_s = \frac{1}{T}. \tag{2.26}$$

The discrete-time phase function, $\phi'(nT)$, is related to the continuous-time phase function, $\phi(t)$, as follows

$$\phi'(nT) = \left.\frac{\phi(t)}{2\pi}\right|_{t=nT}. \tag{2.27}$$

In Appendix A it is shown that samples $\phi'(nT), n = 0,1,2,\ldots$ can be computed using a simple recursive procedure provided that the following two conditions are satisfied:

1. The message symbol period is an integer multiple of the digital system sampling period, i.e.,

$$T_d = LT; L \in \mathbb{Z}. \tag{2.28}$$

2. The step response of the symbol filter in the continuous time modulator reaches its steady state within a finite number of symbol periods,

$$g_{step}(t) = g_{ss}; t \geq NT_d, N \in \mathbb{Z} \tag{2.29}$$

where $g_{step}(t)$ is the step response of the symbol filter in Figure 2.1 and g_{ss} is the step response steady state value, i.e.,

$$g_{ss} = g_{step}(t)\big|_{t\to\infty}. \tag{2.30}$$

The digital, discrete time sequences, $i'(nT)$ and $q'(nT)$, are converted into analogue signals using D/A converters and analogue signal reconstruction filters (LPF1 and

LPF2) shown in Figure 2.2 before vector modulation. It is assumed that the D/A converters have a *Zero-Order Hold (ZOH)* characteristic as shown in Figure 2.2. The signals $\bar{i}(t)$ and $\bar{q}(t)$ are thus given by

$$\bar{i}(t) = \sum_n i'(nT) p_s (t - nT),$$ (2.31)

and
$$\bar{q}(t) = \sum_n q'(nT) p_s (t - nT),$$ (2.32)

where $p_s(t)$ is a unit pulse function given by

$$p_s(t) = \begin{cases} 1 & 0 < t < T \\ 0 & \text{otherwise} \end{cases}.$$ (2.33)

From (2.9), the definition of the envelope of the vector modulator output signal is

$$r_{\bar{y}} = \sqrt{\bar{i}^2(t) + \bar{q}^2(t)}.$$ (2.34)

It follows from (2.25), (2.31), (2.32) and (2.34) that

$$r_{\bar{y}}^2(t) = A^2 \left[\left(\sum_n \cos\left(\pi\phi'(nT)\right) p_s(t - nT) \right)^2 + \left(\sum_n \sin\left(\pi\phi'(nT)\right) p_s(t - nT) \right)^2 \right],$$ (2.35)

and in Appendix A it is shown that

$$r_{\bar{y}}^2(t) = A^2,$$ (2.36)

i.e., if the signals, $\bar{i}(t)$ and $\bar{q}(t)$, were applied directly to an ideal vector modulator, the output signal would have a constant envelope.

The characteristics of the two analogue low-pass filters, LPF1 and LPF2 in Figure 2.2, are selected to

1. limit the bandwidth of the input signals, $\hat{i}(t)$ and $\hat{q}(t)$, to the vector modulator, and

2. retain constant envelope of the vector modulator output signal.

It is assumed that the digital system sampling rate defined by (2.26) is selected to ensure that the vector modulator output signal, $\bar{y}(t)$, in Figure 2.2 represents, with sufficient accuracy after filtering by the two low-pass filters, the spectrum requirements of the M-PAM/CPFSK signal, $y(t)$, generated by the continuous-time modulator in Figure 2.1.

It should be noted that in practice the requirements on the transmitted M-PAM/CPFSK signal spectrum are generally specified as a mask and this affords some latitude in the selection of the digital system sampling rate.

In the next section a particular example of the digital IQ modulator that generates a specific modulation format is considered.

2.4.3 ERMES Signals

The signal format specified in the ERMES (Enhanced Radio Messaging System) standard [11] is an example of M-PAM/CPFSK which will be considered in detail from time to time to illustrate the application of the work in this thesis.

The ERMES standard defines a 4-level PAM/CPFSK modulation with a symbol rate of 3125 baud, i.e.,

$$T_d = 1/3125 = 320\mu s. \tag{2.37}$$

The symbol sequence is produced by encoding di-bits from an input bit-stream at 6250 bits/s into one of four di-bit symbols using a Gray code. Each symbol is mapped to a pulse amplitude value that in turn results in a proportional frequency deviation from the carrier. The symbol alphabet, PAM levels and corresponding frequency deviations are summarised in Table 2.1.

Di-bit	PAM level	Frequency deviation
10	+3	+4687.5 Hz
11	+1	+1562.5 Hz
01	-1	-1562.5 Hz
00	-3	-4687.5 Hz

Table 2.1. ERMES symbol alphabet and corresponding frequency deviations.

The value of the frequency-deviation scaling constant, K_0, is chosen to yield the PAM symbol level *vs* frequency deviation relationship given in Table 2.1 and is given by

$$K_0 = 2\pi \times 1.5625 \times 10^3.$$ (2.38)

The transmitted ERMES 4-PAM/CPFSK format signal must conform to the RF (Radio Frequency) spectrum mask shown in Figure 2.3.
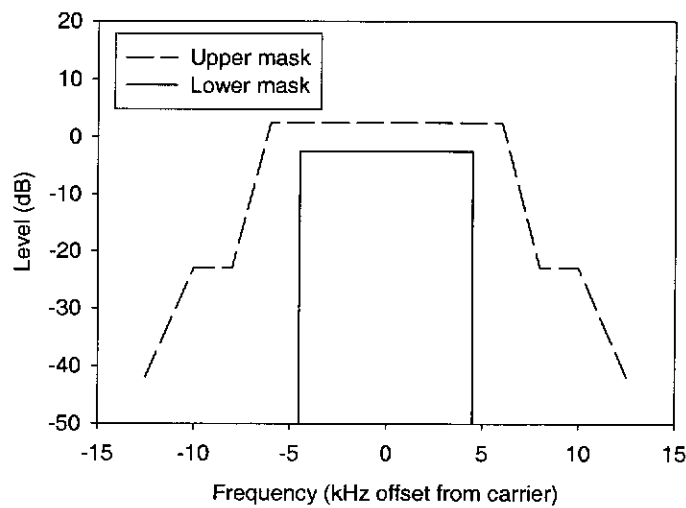

Figure 2.3. ERMES base-station transmitter output RF spectrum mask.

The symbol filter in Figure 2.1 provides pulse shaping of the rectangular PAM signal, $v(t)$, in order to band-limit the modulator output power spectrum. A 10th order low-

pass Bessel filter with a 3 dB bandwidth of 3900 Hz meets the time domain and frequency domain mask requirements on the symbol filter specified by the ERMES standard. The step response of the continuous time (analogue) symbol filter is shown in Figure 2.4.
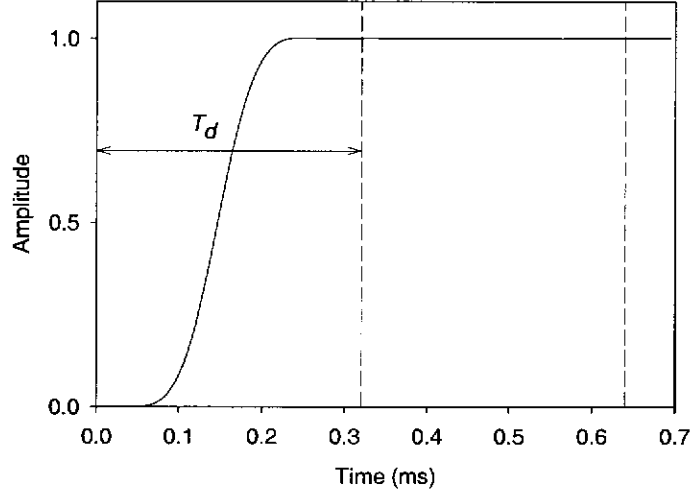
Figure 2.4. Step response of the 10th order Bessel filter that forms the symbol filter shown in Figure 2.2 in the ERMES implementation of the IQ modulator. The parameter T_d is the sampling period for the digital synthesis section of the modulator for the ERMES implementation.

In [10] the digital modulator structure shown in Figure 2.2 is proposed as a means to implement an ERMES modulation format transmitter. It is shown [10] that the strict requirements of the ERMES standard on the modulator output power spectrum (shown in Figure 2.3) and on the demodulator output eye-pattern can be met using a digital system sampling rate of 200 kHz. The digital system sampling period, T, is therefore given by

$$T = 1/\left(200 \times 10^3\right)$$
$$= 5\mu s.$$
(2.39)

From (2.37) and (2.39), the ratio of the input symbol rate to the digital system sampling rate is given by

$$\frac{T_d}{T} = 64,$$
(2.40)

i.e., the symbol period is an integer multiple of the digital system sampling period.

Note from Figure 2.4 that the step response of the continuous time symbol filter reaches its final value, approximately, within one symbol period, i.e.,

$$g_{step}(t) \cong g_{ss}; t \geq T_d.$$ (2.41)

From (2.40) and (2.41) it can be seen that the conditions defined by (2.28) and (2.29) in Section 2.4.2 are indeed met for the ERMES case and hence samples of the discrete time phase function, $\phi'(nT)$, can be computed such that they closely approximate samples of the scaled continuous time phase function, $\left(\phi(t)/2\pi\right)_{t=nT}$

Since the 10th order Bessel symbol filter rolls off at 3900 Hz, a sampling frequency of 200 kHz is approximately 50 times the message signals half-power bandwidth and therefore results in minimal aliasing when sampling the signals $m(t)$ and $\phi(t)$.

2.5 Modulator Error Model

The effect of implementation errors on the modulator system can be modelled as shown in Figure 2.5 where

κ represents gain imbalances in the D/A converters, reconstruction filters and vector modulator inputs,

I_{off}, Q_{off} represent I and Q channel DC offset errors in the D/A converters, reconstruction filters and vector modulator inputs,

φ represents phase error in the vector modulator, and

$h_i(t)$ and $h_q(t)$ represent the individual dynamic responses of the two analogue reconstruction filters which may exhibit departures from constant magnitude and linear phase in the pass-band and frequency-dependent gain and phase imbalances between the two reconstruction filters.
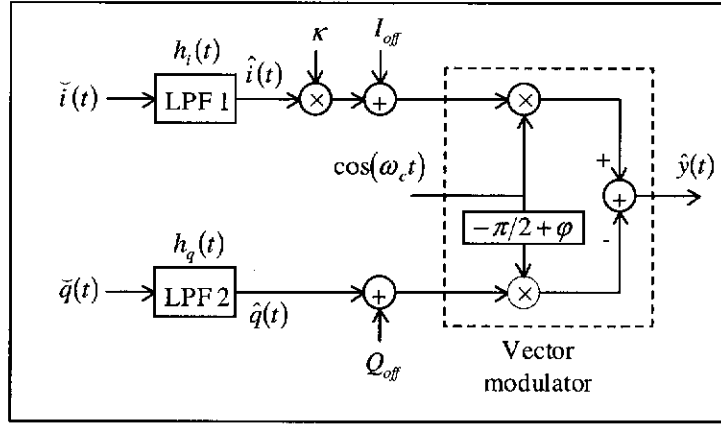
Figure 2.5. Error model of the DSP-based IQ modulator analogue sub-section.

The error model incorporates the static errors κ, φ, I_{off} and Q_{off}

and the dynamic errors contained within the analogue filter responses

$h_i(t)$ and $h_q(t)$.

The output, $\hat{y}(t)$, in Figure 2.5 will deviate from the output, $\breve{y}(t)$, of the digital modulator in Figure 2.2 due to implementation errors listed above and is given by

$$\hat{y}(t) = \left(\kappa\left(\breve{i}(t) * h_i(t)\right) + I_{off}\right)\cos(\omega_c t)$$
$$-\left(\breve{i}(t) * h_i(t) + Q_{off}\right)\sin(\omega_c t + \varphi). \tag{2.42}$$

Rewriting (2.42) gives

$$\hat{y}(t) = \left[\kappa\left(\breve{i}(t) \otimes h_i(t)\right) + I_{off} + \left(\breve{q}(t) \otimes h_q(t) + Q_{off}\right)\sin\varphi\right]\cos(\omega_c t)$$
$$-\left[\left(\breve{q}(t) \otimes h_q(t) + Q_{off}\right)\cos\varphi\right]\sin(\omega_c t). \tag{2.43}$$

A study of (2.9) and (2.43) reveals that in general the vector modulator output signal, $\hat{y}(t)$, will not have a constant envelope.

An effective technique for digitally compensating for the error sources represented by the parameters κ, φ, I_{off} and Q_{off} has been developed and successfully implemented (see [44]). With the digital compensation in place for the static errors, the quantities κ, φ, I_{off} and Q_{off} can be eliminated from (2.43) and the signal model in (2.43) rewritten as

$$\hat{y}(t) = \hat{i}(t)\cos\omega_c t - \hat{q}(t)\sin\omega_c t$$
$$= \left(\breve{i}(t)\otimes h_i(t)\right)\cos\omega_c t - \left(\breve{q}(t)\otimes h_q(t)\right)\sin\omega_c t. \tag{2.44}$$

The signal model given in (2.44) can be represented by the structure shown in Figure 2.6.
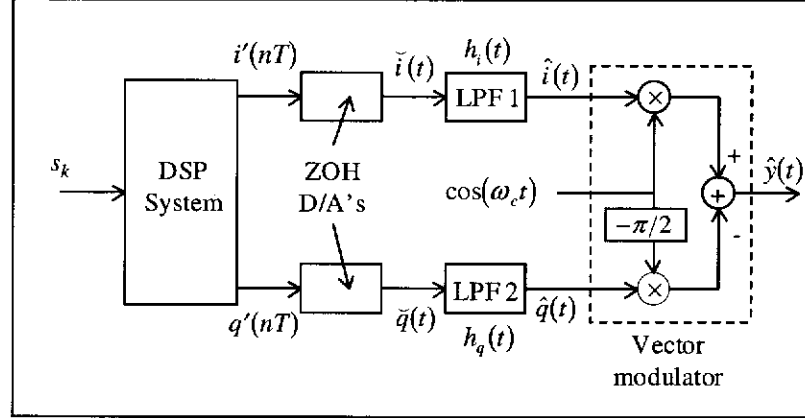
Figure 2.6. IQ modulator system with digital base-band synthesis and

incorporating digital compensation for static errors in the analogue

sub-section.(Note that the reconstruction filter responses, $h_i(t)$ and

$h_q(t)$, are different in general.)

From (2.44) and (2.9) the following expression for vector modulator output signal envelope is obtained

$$r_{\hat{y}}(t) = \sqrt{\hat{i}^2(t) + \hat{q}^2(t)}$$
$$= \sqrt{\left(\breve{i}(t)\otimes h_i(t)\right)^2 + \left(\breve{q}(t)\otimes h_q(t)\right)^2}. \tag{2.45}$$

From (2.45) it can be seen that the two reconstruction filters, identified by their impulse responses $h_i(t)$ and $h_q(t)$, play a fundamental role in determining the nature of the envelope function of the vector modulator output signal.

2.6 Conclusion

Errors in the implementation of the digital IQ modulator system result in a loss of the constant envelope property of the vector modulator output CPFSK signal. Techniques have been developed that effectively compensate for static implementation errors in the modulator. Practical realisation and implementation errors, however, will also result in the dynamic, frequency-dependent characteristics of the two analogue reconstruction filters departing from the desired characteristics. From (2.34), (2.36) and (2.45) it is clear that any in-band frequency-dependent *shaping* of I and Q channel analogue signals, $\bar{i}(t)$ and $\breve{q}(t)$, will directly impact on departures from a constant envelope in the modulator output signal and hence on the modulator performance.

Chapter 3. Reconstruction Filters

3.1 Introduction

In the previous chapter the structure of a digitally based IQ modulator system that can be used to generate PAM/CPFSK signals was introduced. Contained within the modulator structure are two analogue low-pass filters that, together with two D/A converters, serve to reconstruct the base-band I and Q channel analogue signals from their digitally synthesised counterparts. These two filters are termed *reconstruction filters*.

The focus of this chapter is on the two reconstruction filters with the specific aims of:

1. presenting the requirements and specifications of the two filters, and

2. investigating the impact that these two filters have on the envelope function of the vector modulator output signal and on the power spectrum of the transmitted PAM/CPFSK signal.

The key contributions of this chapter are:

• the identification of the particular reconstruction filter characteristics that significantly impact on ripple in the envelope function of the vector modulator output signal, and

• a demonstration that the transfer characteristics and implementation errors in practically realisable reconstruction filters result in ripple in the vector modulator output signal envelope that causes unacceptable spreading of the transmitted PAM/CPFSK signal into adjacent channel regions.

This chapter motivates the work on digital compensation in the following chapters by highlighting the considerable influence that the analogue reconstruction filters have on the critical system parameters of envelope ripple and adjacent channel power. More specifically, by identifying the particular frequency domain reconstruction filter characteristics that impact most on the envelope function, work in this chapter leads

to the development of the frequency-domain digital compensation approach presented in Chapter 4.

This chapter is divided into six sections. Section 3.2 introduces the important specifications of the two analogue reconstruction filters. In Section 3.3 the effects of individual pass-band characteristics of the two reconstruction filters on the envelope function of the vector modulator output are investigated. In Section 3.4 the effects of practically realisable reconstruction filters on the envelope characteristics are considered and in Section 3.5 the connection between ripple in the PAM/CPFSK signal envelope and spreading of the transmitted signals power spectrum into adjacent channels is highlighted. Section 3.6 contains the conclusions of the chapter.

3.2 Filter Specifications

The two key considerations in selecting the characteristics of the I and Q channel analogue signal reconstruction filters shown in Figure 2.6 of Section 2.5 are:

1. The filters must band-limit the I and Q channel signals applied to the vector modulator input ports while still meeting the in-band requirements on the signal.

2. The characteristics of both filters must be selected so as to ensure that any AM in the envelope function of the vector modulator output signal is minimised.

In this section the importance of the first point above is briefly highlighted. The greater part of the work presented in this chapter, however, is devoted to the second point: an investigation into the impact of the reconstruction filters on the PAM/CPFSK signal envelope.

The spectra of the analogue signals, $\breve{i}(t)$ and $\breve{q}(t)$, at the outputs of the two D/A converters shown in Figure 2.6, Section 2.5 contain residual image components that result from the digital synthesis of the I and Q channel base-band signals. The image components in the signal spectra are centred at integer multiples of the system sampling frequency, f_s as shown in Figure 3.1.
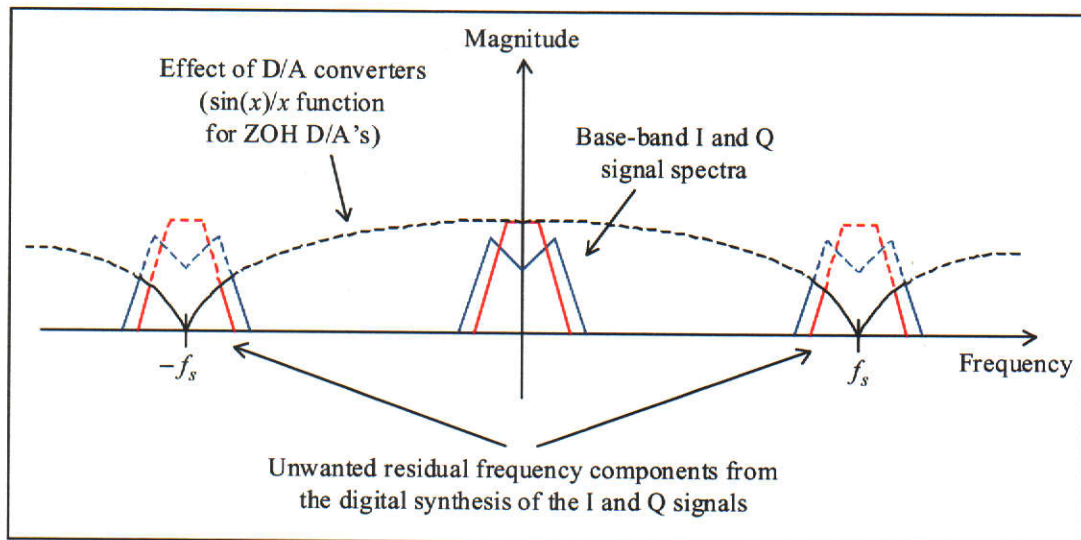
Figure 3.1. Magnitude spectra of the I and Q channel D/A output signals.

The magnitude response stop-band characteristics of the I and Q channel signal reconstruction filters must be selected to ensure that the residual image frequency components shown in Figure 3.1 are sufficiently attenuated that the resulting PAM/CPFSK signal meets the adjacent channel interference specifications of the relevant transmission standard (for example the ERMES standard defined in [11]).

The pass-band magnitude and phase characteristics of the two analogue reconstruction filters are selected to allow the I and Q channel base-band signal components shown in Figure 3.1 to pass through to the vector modulator input ports. In the next section the effects of the pass-band magnitude and phase (or group-delay) characteristics of the reconstruction filters on the envelope of the vector modulator output signal are investigated.

3.3 Effect on the CPFSK Signal Envelope

In this section the effects of each filter parameter in isolation on the resulting envelope function of the vector modulator output signal are investigated. In practice, typically all of the effects studied in this section are manifest to a certain degree in practically realisable filters and in Section 3.4 the effect of practical reconstruction filters on the envelope of the vector modulator output signal is investigated.

The study of the effects of linear filtering on FM signals is by no means new [55], [56] and extensive work on the subject has been reported in the literature over the years. Many of these works are cited in [57-61].

Two approaches to the problem found in the literature are Fourier analysis methods [62-65] and asymptotic methods [66], [67] stemming from the *quasi-stationary approximation* developed in [56].

The inherent complexity of the results obtained using these analytical approaches make it difficult to gain any insight into the effect of underlying filter and signal parameters (eg. group-delay response, filter mismatch in magnitude or phase) on the characteristics of the vector modulator output signal envelope.

Numerical techniques are therefore used to gain insight into the effects of specific filter parameters on the envelope function.

In this section a computer model of the IQ modulator system shown in Figure 2.6, Section 2.5 and with ERMES parameters is used to investigate the effects of specific reconstruction filter parameters on the envelope function of the vector modulator output signal.

In the first part of this section the case where the reconstruction filters have identical, brick-wall magnitude, linear phase frequency responses is considered. This case gives an indication of the levels of ripple in the envelope of the vector modulator output that can be achieved from the digitally based IQ modulator structure. In the remaining four parts the effects of specific filter parameters on the envelope characteristics are considered, namely:

1. *Magnitude Deviation:* deviation from a flat magnitude response through the two filter pass-bands.

2. *Phase Deviation:* deviation from a linear phase characteristic through the two filter pass-bands.

3. *Magnitude Imbalance:* imbalance between the pass-band magnitude responses in the two filters.

4. *Phase Imbalance:* imbalance between constant group-delay of the two filters.

In all cases considered in this section it is assumed that the filter cut-off frequency is selected to meet the in-band specifications on the base-band I and Q signal components while still meeting the requirements on the attenuation of the image frequency components as discussed in Section 3.2.

The I and Q channel reconstruction filters considered in this section are designed to have a cut-off frequency of 20 kHz. (Recall from Section 2.4.3 that the ERMES 4-PAM/CPFSK symbol frequencies are ± 1.5625 kHz for ± 1 input symbols and ± 4.6875 kHz for ± 3 input symbols.)

The envelope function of the vector modulator output signal is characterised by two components:

1. a transient component that occurs at the message symbol transitions, and

2. a steady state component.

By considering the four cases above it will be shown in the following sections that different filter parameters impact on the transient and steady-state components differently. Expressions for the steady-state signal components are derived for magnitude deviation, magnitude imbalance and phase imbalance.

For ease of comparison the modulator input symbol sequence is the same for each case considered. This sequence is shown in Figure 3.2.
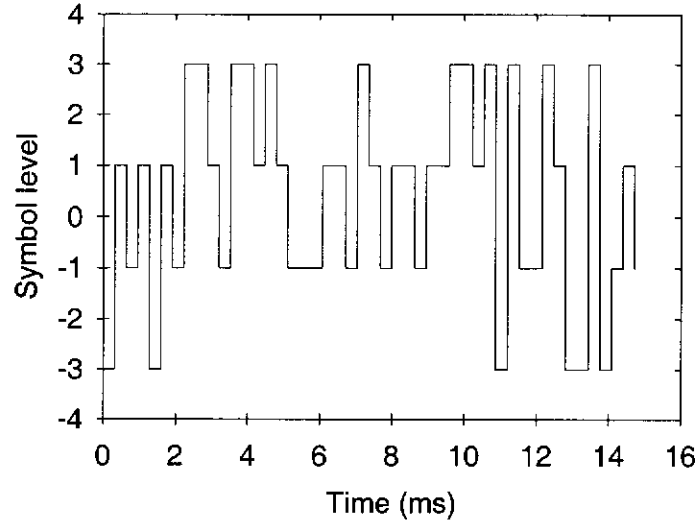
Figure 3.2. Input symbol sequence.

3.3.1 Brick-wall, Linear Phase Reconstruction Filters

In this first computer simulation scenario the two analogue reconstruction filters are chosen to have identical brick-wall magnitude, linear phase frequency responses, i.e., $h_i(t) = h_q(t) = h(t)$ in Figure 2.6, Section 2.5, where $h(t)$ is the impulse response of a filter that has a frequency response defined by

$$H(f) = F\{h(t)\}$$
$$= \begin{cases} e^{-j2\pi f \tau_0} & |f| \le f_c \\ 0 & |f| > f_c \end{cases}, \tag{3.1}$$

where $F\{\cdot\}$ is the Fourier transform. The parameter f_c is the filter cut-off frequency and τ_0 is a constant that defines the group-delay of the filter. The magnitude and linear phase characteristics of the filter response defined by (3.1) are shown in Figure 3.3.

Figure 3.3. Brick-wall, linear phase frequency response.

The impulse response, $h(t)$, of the two filters can be shown to be [68]

$$h(t) = 2f_c \frac{\sin\left(2\pi f_c \left(t - \tau_0\right)\right)}{2\pi f_c \left(t - \tau_0\right)}$$
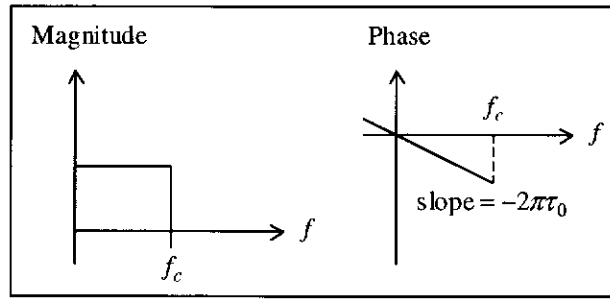
$$= 2f_c \,\text{sinc}\left(2\pi f_c \left(t - \tau_0\right)\right). \tag{3.2}$$

The impulse response defined by (3.2) has infinite duration. To simulate these filters the frequency response is approximated by truncating the impulse response, $h(t)$, to a fixed length such that no measurable difference in the envelope function occurs by increasing the filter length. With the scenario considered here, this results in a FIR filter length of approximately 8000 taps. Oscillations in the pass-band magnitude response of the filters due to Gibbs' phenomenon [69] are reduced by the use of a Hanning window function.

The envelope function of the vector modulator output signal resulting from the modulator input sequence of Figure 3.2 is shown in Figure 3.4, and using an expanded vertical scale, in Figure 3.5. The vertical scale used in Figure 3.4 is also used to plot the envelope functions for the other four cases considered. This makes it easier to visually compare the effects of various reconstruction filter parameters on the envelope characteristics of the vector modulator output signal.
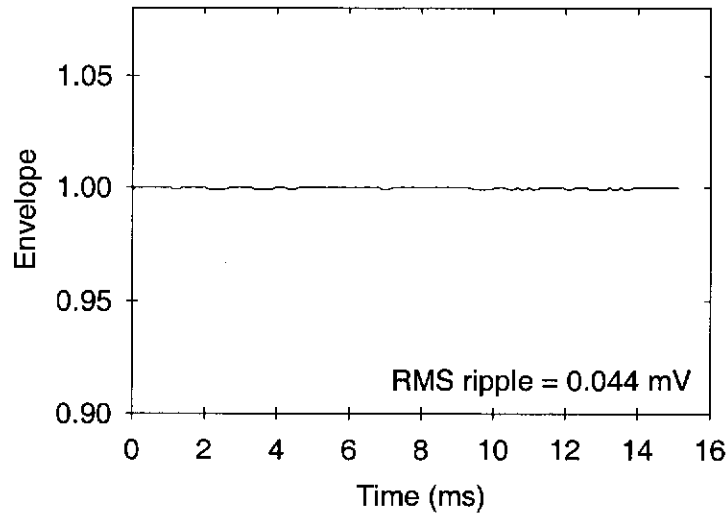
Figure 3.4. Envelope function for identical brick-wall, linear phase reconstruction filters.
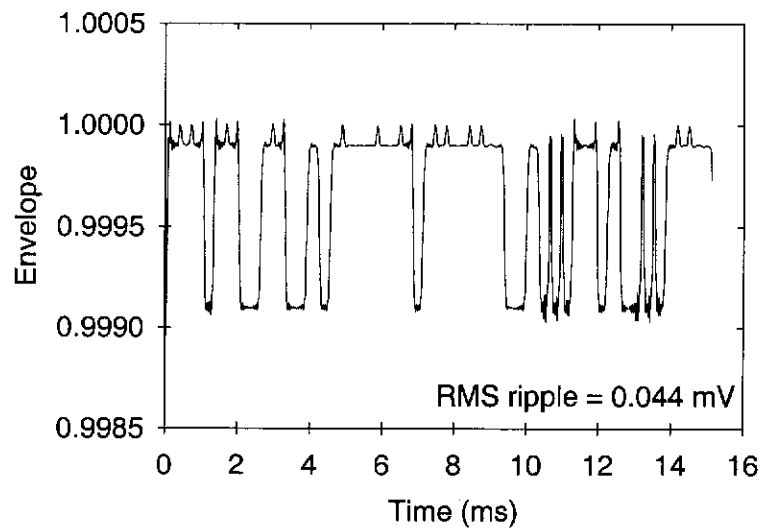
Figure 3.5. Envelope function for identical brick-wall, linear phase reconstruction filters (expanded scale).

As can be seen from Figure 3.5 (with the expanded vertical scale) there is residual AM in the envelope function (approximately $44\mu V$ RMS). This is predominantly caused by the $\sin(x)/x$ magnitude response effect of the zero-order hold D/A converters. (This is considered in more detail in the next section, which deals with magnitude response deviation effects.)

As will be shown in the following cases, the envelope ripple present in Figure 3.4 and Figure 3.5 is small in comparison to that resulting from the effects of filter magnitude and phase imbalances and poor group delay in the reconstruction filter characteristics. The simulation results presented in Figure 3.4 and Figure 3.5, however, provide an indication of the level of ripple in the envelope function that can be achieved.

3.3.2 Deviation from Constant Magnitude

In this section the case where the two reconstruction filters again have identical responses is considered, however the pass-band magnitude characteristic of the filters is chosen to have a small roll-off from DC that is quadratic with frequency. The phase response of the filters is linear.

The I and Q channel reconstruction filter frequency responses are defined as

$$H_i(f) = H_q(f) = H(f) = \begin{cases} A(f)e^{-j2\pi f \tau_0} & 0 \leq f \leq f_c \\ 0 & f > f_c \end{cases}$$

(3.3)

where

$$A(f) = \left(1 - \alpha f^2\right)$$

(3.4)

In the simulation considered here, the value of the quadratic deviation parameter, α, is chosen so that a 5% deviation from a flat magnitude response exists at the filter cut-off frequency, f_c, i.e.,

$$\alpha = \frac{0.05}{f_c}$$

(3.5)

As will be seen in following section on practical reconstruction filters for ERMES signals, magnitude response deviations of this order are typical of the actual analogue reconstruction filter responses used for this modulator.

The impulse response of the filter is found using the frequency sampling method [69], [70].

The effect of deviation from flat magnitude in the frequency response of the reconstruction filters is shown in Figure 3.6 and Figure 3.7. The envelope function plotted in both figures is the same: Figure 3.6 is plotted to allow easy comparison with other results in this chapter and Figure 3.7 is plotted to show the detail in the envelope function more clearly.
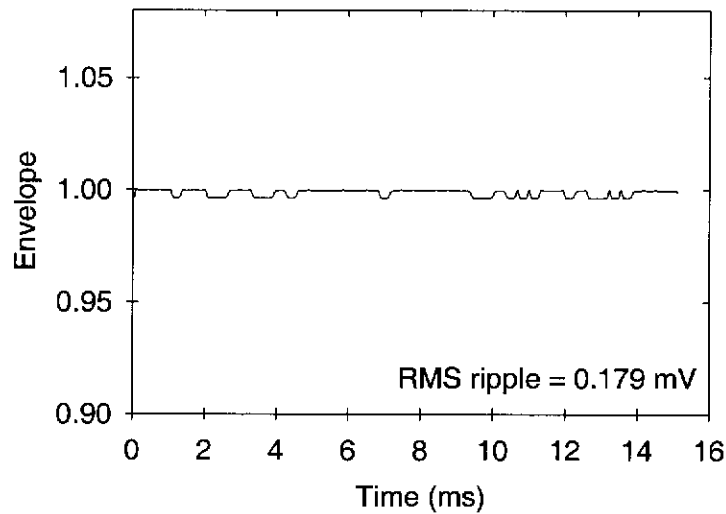

Figure 3.6. Envelope function for identical linear phase filters with magnitude response deviation.
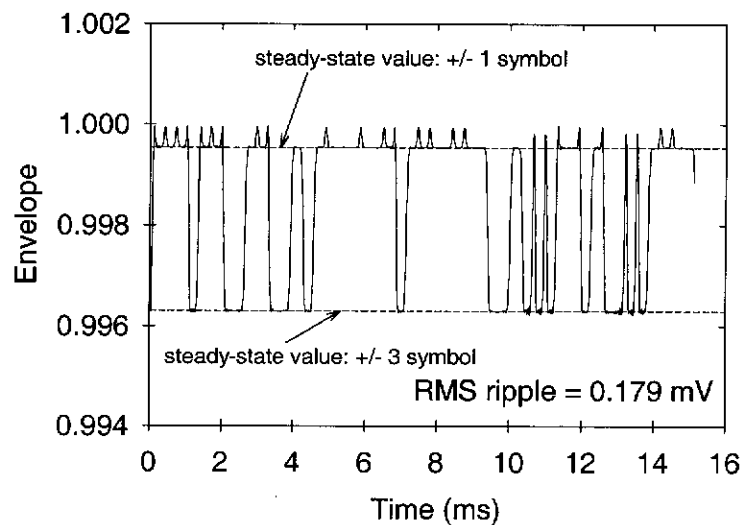

Figure 3.7. Envelope function for identical linear phase filters with magnitude response deviation (expanded vertical scale).

The dotted lines shown in Figure 3.7 are the predicted steady-state values of the envelope function corresponding to the ERMES symbol levels ± 1 and ± 3, and in the case of magnitude response deviation only in the reconstruction filters. These values are derived as follows.

For a constant input symbol to the modulator of level l the corresponding steady-state filter output signals are given by

$$\hat{i}_{l,ss}(t) = G_l \cos(2\pi f_l t + \phi_l)$$
$$\text{and}$$
$$\hat{q}_{l,ss}(t) = G_l \sin(2\pi f_l t + \phi_l)$$

(3.6)

where f_l is the FSK frequency deviation corresponding to the symbol level l. The parameters $G_l = |H(f_l)|$ and ϕ_l are the gain and phase respectively, of the I and Q channel filters at frequency f_l.

From (3.6) and the definition of the envelope function given in (2.8), the steady-state value of the envelope function for a constant input symbol level, l, is given by

$$\hat{r}_{l,ss}(t) = G_l$$

(3.7)

From (3.4), (3.5) and (3.7), the steady-state values of the envelope function for the input symbol levels ± 1 and ± 3 are

$$\hat{r}_{\pm 1,ss}(t) = G_{\pm 1} = 0.99953$$
$$\text{and}$$
$$\hat{r}_{\pm 3,ss}(t) = G_{\pm 3} = 0.9963.$$

(3.8)

(Note that these values include the $\sin(x)/x$ magnitude effect of the ZOH D/A converters.)

As can be seen from Figure 3.7, steps from one steady-state level to the other corresponding to the input symbol sequence dominate the envelope function for the magnitude response deviation scenario investigated in this section.

3.3.3 Deviation from Linear Phase

Here the situation where the phase response of the reconstruction filters departs from a linear characteristic in the pass-band is investigated. Again, both filters have identical responses and in this case both have a brick-wall magnitude characteristic.

The I and Q channel reconstruction filter frequency responses are defined by

$$H_i(f) = H_q(f) = H(f) = \begin{cases} e^{-j2\pi f(\tau_0 - \beta f)} & 0 \leq f \leq f_c \\ 0 & f > f_c \end{cases} \tag{3.9}$$

From (3.9), the filter frequency response has a phase characteristic that departs from a linear function, determined by τ_0, in a quadratic fashion according to the choice of the parameter β. The group-delay characteristic is

$$\tau_g(f) = \tau_0 + 2\beta f, \quad 0 \leq f \leq f_c \tag{3.10}$$

i.e. a linear function of frequency with slope 2β.

In the case considered here, a value of β is chosen such that the group-delay of the filter at the cut-off frequency, f_c, is 5% greater than the DC delay value, τ_0. The value of β is therefore given by

$$\beta = \frac{5\tau_0}{200 f_c}. \tag{3.11}$$

The value chosen for β corresponds to a difference in the I and Q channel filter group-delay characteristics between DC and f_c of $25\mu s$. As will be seen in later sections, this is a conservative choice since differences of the order of $100\mu s$ can exist between the DC and cut-off frequency group-delay values in typical low-pass reconstruction filters used in ERMES.

As in the previous case, the filter impulse response is found using the Frequency-sampling method.

The envelope function corresponding to the input symbol sequence in Figure 3.2, and with these reconstruction filters in place, is shown in Figure 3.8.
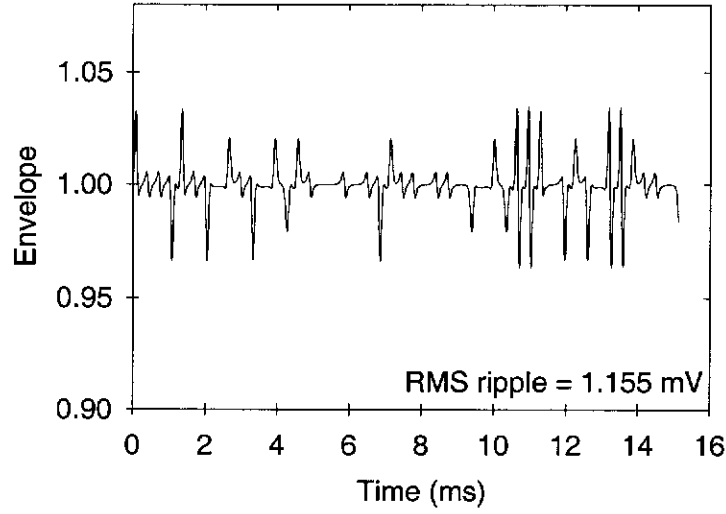
Figure 3.8. Envelope function for identical brick-wall filters with phase functions that deviate from a linear characteristic.

From Figure 3.8 it can be seen that the envelope function for the case considered in this section is dominated by transient components that occur at the symbol transitions.

3.3.4 Magnitude Imbalance

Here, the effect of imbalances between the magnitude responses in the I and Q channel reconstruction filters is investigated. The I and Q channel reconstruction filter frequency responses are chosen as follows

$$H_i(f) = \begin{cases} (1+\Delta_m)e^{-j2\pi f \tau_0} & 0 \le f \le f_c \\ 0 & f > f_c \end{cases}$$

and (3.12)

$$H_q(f) = \begin{cases} (1-\Delta_m)e^{-j2\pi f \tau_0} & 0 \le f \le f_c \\ 0 & f > f_c \end{cases}$$

From (3.12) it can be seen that both filters have a brick-wall magnitude, linear phase response, however the pass-band magnitude responses differ by $2\Delta_m$. The filter impulse responses are found using the same method described in Section 3.3.1.

In the following example the value $\Delta_m = 0.025$ is chosen which corresponds to a gain imbalance of approximately 0.4 dB. The resulting envelope function is shown in Figure 3.9.
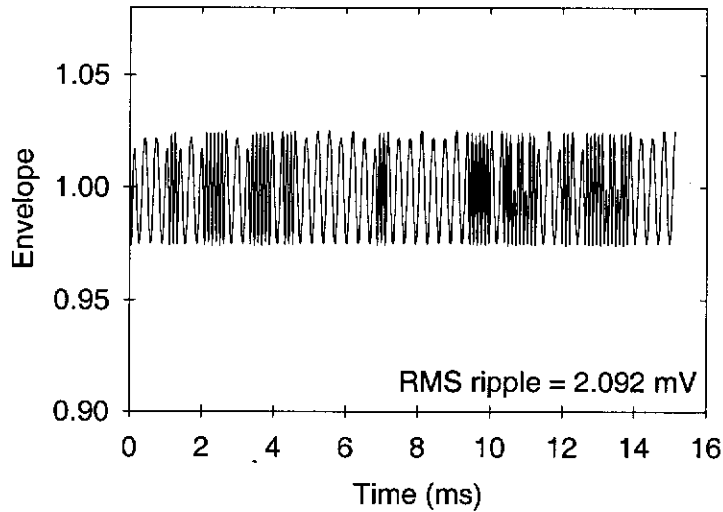
Figure 3.9. Envelope function for magnitude response imbalances in the reconstruction filters.

For a constant input symbol of level l to the modulator, the steady-state envelope function of the vector modulator output signal is derived below.

The steady-state I and Q channel reconstruction filter output signals for a constant input symbol level, l, are given by

$$\hat{i}_{l,ss}(t) = (1 + \Delta_m)\cos(2\pi f_l t + \phi_l)$$

and

$$\hat{q}_{l,ss}(t) = (1 - \Delta_m)\sin(2\pi f_l t + \phi_l). \qquad (3.13)$$

where f_l and ϕ_l are the FSK frequency deviation and reconstruction filter phase response respectively, corresponding to the input symbol level l. (Recall from (3.12) that the gains of the two filters, while different from each other, are constant in the filter pass-bands.)

From the definition of the envelope function

Chapter 3   43

$$\hat{r}_{l,ss}(t) = \sqrt{\hat{i}_{l,ss}^2(t) + \hat{q}_{l,ss}^2(t)}$$
$$= \sqrt{\left(1 + \Delta_m^2\right) + 2\Delta_m \cos\left(2\left(2\pi f_l t + \phi_l\right)\right)} \tag{3.14}$$

From (3.14), the steady-state envelope of the vector modulator output signal, $\hat{r}_{l,ss}(t)$, is the square root of a sinusoidal function that is scaled by $2\Delta_m$ and offset by $\left(1 + \Delta_m^2\right)$ and that has a frequency that is twice the input symbol frequency. The function $\hat{r}_{l,ss}(t)$ in (3.14) is shown plotted in Figure 3.10 for the input symbol sequence in Figure 3.2.
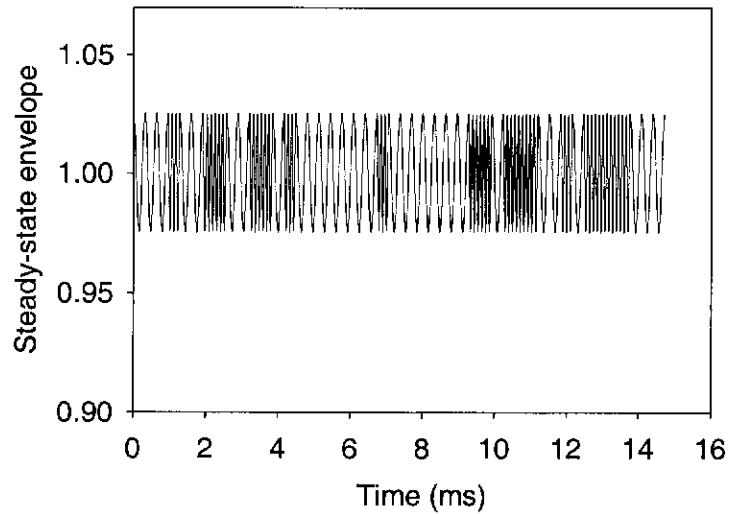
Figure 3.10. Theoretical steady-state component of the vector modulator output signal envelope (filter magnitude imbalance only).

Comparing Figure 3.10 with Figure 3.9 it can be seen that the two functions are very similar. It can be concluded, therefore, that magnitude response imbalance in the two reconstruction filters has a far more significant impact on the steady-state component of the resulting vector modulator envelope function than on transient components of this function.

3.3.5 Phase Imbalance

In this last case the effects of phase imbalance between the I and Q channel reconstruction filters are investigated.

The I and Q channel reconstruction filters are chosen to have identical brick-wall magnitude responses. The phase responses however, while both linear, have slightly different slopes. This corresponds to constant, but slightly different group-delay through the two filters. The filter frequency domain characteristics are defined by

$$H_i(f) = \begin{cases} e^{-j2\pi f \tau_i} & 0 \le f \le f_c \\ 0 & f > 0 \end{cases}$$

and   (3.15)

$$H_q(f) = \begin{cases} e^{-j2\pi f \tau_q} & 0 \le f \le f_c \\ 0 & f > 0 \end{cases}$$

In this example the values of τ_i and τ_q are chosen to be

$$\tau_i = 514.56\,\mu s$$
$$\tau_q = 509.44\,\mu s$$ (3.16)

This corresponds to a group-delay difference of approximately $5\mu s$ between the two filters or a 1% imbalance. As will be seen in later sections in this chapter on practical reconstruction filters, a group-delay (or phase) imbalance of this order is conservative for typical reconstruction filter circuits used in modulators for ERMES signals.

With the modulator input symbol sequence shown in Figure 3.2, the resulting envelope function is shown in Figure 3.11.
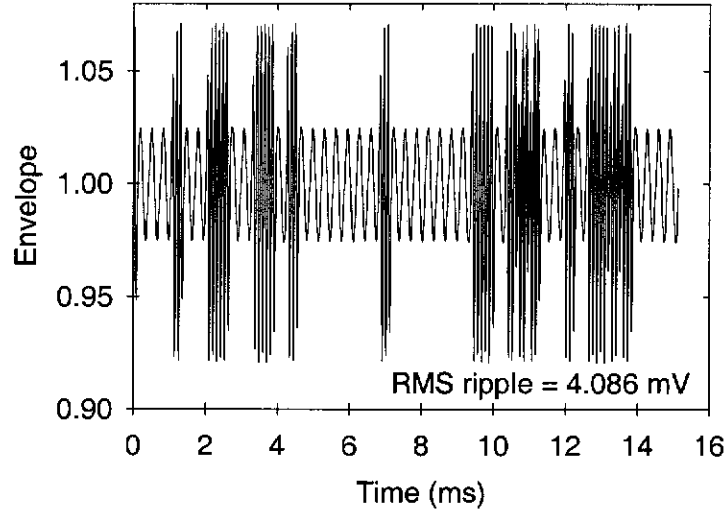
Figure 3.11. Envelope function for phase response imbalances in the reconstruction filters.

Comparing Figure 3.11 with the envelope plots for the previous cases one can see that even relatively small phase imbalances between the two reconstruction filters result in significant ripple in the envelope of the vector modulator output signal.

In the following it is shown that the vector modulator output signal envelope function shown in Figure 3.11 is dominated by steady-state components of the envelope signal.

For a constant input symbol to the modulator of level l the corresponding steady-state output signals from the I and Q channel reconstruction filters defined by (3.15) are given by

$$\hat{i}_{l,ss}(t) = \cos\left(2\pi f_l\left(t - \tau_i\right)\right)$$

$$\text{and}$$

$$\hat{q}_{l,ss}(t) = \sin\left(2\pi f_l\left(t - \tau_q\right)\right).$$

(3.17)

The corresponding envelope of the vector modulator output signal is

$$\hat{r}_{l,ss}(t) = \sqrt{\hat{i}_{l,ss}^2(t) + \hat{q}_{l,ss}^2(t)}$$

$$= \sqrt{\cos^2\left(2\pi f_l\left(t - \tau_i\right)\right) + \sin^2\left(2\pi f_l\left(t - \tau_q\right)\right)}.$$

(3.18)

Expanding the cos and sin terms in (3.18) gives

$$\hat{r}_{l,ss}(t) = \sqrt{1 + \sin\left(2\pi f_l\left(\tau_i - \tau_q\right)\right)\sin\left(4\pi f_l t - 2\pi f_l\left(\tau_i + \tau_q\right)\right)}. \tag{3.19}$$

Letting

$$\gamma_{l,\tau_i,\tau_q} = \sin\left(2\pi f_l\left(\tau_i - \tau_q\right)\right), \tag{3.20}$$

and

$$\varphi_{l,\tau_i,\tau_q} = 2\pi f_l\left(\tau_i + \tau_q\right), \tag{3.21}$$

equation (3.19) can be rewritten as

$$\hat{r}_{l,ss}(t) = \sqrt{1 + \gamma_{l,\tau_i,\tau_q}\sin\left(4\pi f_l t - \varphi_{l,\tau_i,\tau_q}\right)}. \tag{3.22}$$

From (3.22) it can be seen that the steady-state envelope function is the square root of a sinusoid that is offset by 1.0. The frequency of the sinusoid is twice that of the FSK frequency deviation corresponding to the input symbol level and the amplitude, γ_{l,τ_i,τ_q}, is a function of the symbol frequency and the difference between the constant group delay values of the two reconstruction filters.

From (3.20) it can be seen that for small imbalances in the phase responses of the two reconstruction filters ($\left|\tau_i - \tau_q\right| \ll 1/(4 f_l)$), the amplitude, γ_{l,τ_i,τ_q}, of the sinusoid in (3.22) is approximately given by

$$\gamma_{l,\tau_i,\tau_q} \cong 2\pi f_l\left(\tau_i - \tau_q\right), \tag{3.23}$$

i.e., the magnitude of the steady-state envelope ripple is approximately proportional to the symbol frequency and will therefore be greater for higher symbol frequencies.

The steady-state envelope function, $\hat{r}_{l,ss}(t)$, in (3.22) is shown plotted in Figure 3.12 for the group delay values given in (3.16) and the input symbol sequence of Figure 3.2.
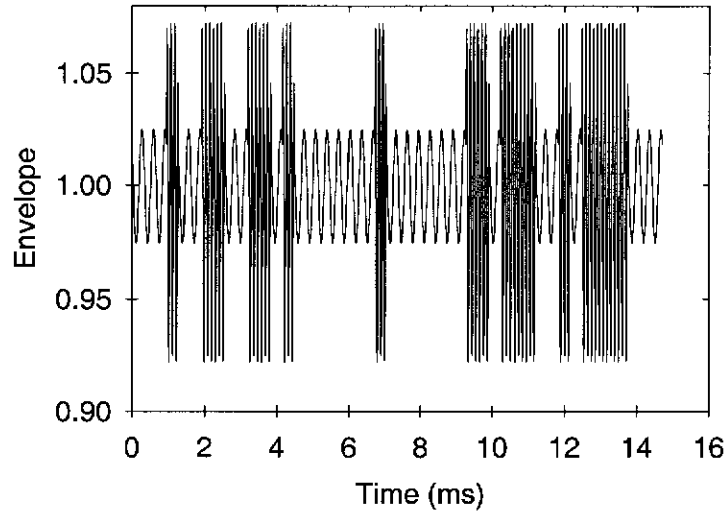
Figure 3.12. Theoretical steady-state component of the vector modulator

output signal envelope. (filter phase imbalance only).

Comparing the theoretical steady-state envelope component in Figure 3.12 with the actual envelope function in Figure 3.11 it can be seen that the two functions are very similar. It can be concluded, therefore, that for phase imbalance between the two reconstruction filters the resulting envelope function of the vector modulator output signal is predominantly composed of the steady-state component given by (3.22).

3.3.6 Section 3.3 Summary

Table 3.1 gives a quantitative comparison of the ripple present in the envelope functions for the cases studied in Section 3.3.

Filter characteristic	RMS Ripple (mV)	Peak-to-peak level (mV)	Factor increase in RMS ripple (relative to Case 1)
Brick-wall, linear phase	0.044	1.0	1
Magnitude deviation	0.179	3.7	4.1
Phase deviation	1.155	71.5	26.3
Magnitude imbalance	2.092	50.8	47.5
Phase imbalance	4.086	150.5	92.9

Table 3.1. RMS envelope ripple for isolated characteristics in the I and Q

channel reconstruction filters.

From the envelope functions plotted in Sections 3.3.1 to 3.3.5 and the quantitative results summarised in Table 3.1 a number of observations can be made concerning

the effects of isolated reconstruction filter parameters on the characteristics of the vector modulator output signal envelope:

- Deviation from a flat magnitude response in the pass-band has relatively minor effects on the ripple in the envelope in comparison to the effects of the other parameters investigated. (This is assuming that the magnitude response is the same for both filters and that the filter band-width is selected to be higher than the I or Q channel base-band signal components.)

- Phase deviation, magnitude imbalance and phase imbalance in the filter pass-band responses all result in high RMS levels of ripple in the vector modulator output envelope function. Of particular concern is phase imbalance where an increase in RMS ripple of almost two orders of magnitude over the brick-wall, linear phase case is observed.

- Deviation from linear phase and magnitude imbalances in the filter pass-bands result in similar values of RMS ripple in the envelope, however, the transient levels are significantly higher for the phase deviation case.

- Magnitude deviation, magnitude imbalance and phase imbalance in the filter pass-bands all result in vector modulator output envelope characteristics that are dominated by steady-state components. Expressions for the steady-state envelope functions are derived for these cases and are shown to closely approximate the actual envelope characteristics.

- Deviation from linear phase in the filter pass-bands results in vector modulator output envelope characteristics that are dominated by transient components.

3.4 Practical Reconstruction Filters

In the Section 3.3 the effects of isolated filter parameters on the envelope function of the vector modulator output signal were considered. In this section the effects of practically realisable reconstruction filters on the characteristics of the envelope function are investigated where some or all of the effects observed in Section 3.3 might be manifest. In the investigations a computer model of the digitally based IQ modulator structure shown in Figure 2.6, Section 2.5 with ERMES signal parameters is used.

The analogue reconstruction filters must meet the two requirements highlighted in Section 3.2. For ERMES signals, it has been found that Butterworth characteristic reconstruction filters of around 5th or 6th order meet the first requirement by adequately attenuating the digital image components in the base-band signal spectra. However, it will be shown that typical filter responses that result from realisations of filter circuits where components very within practical tolerance ranges cause unacceptable ripple in the PAM/CPFSK signal envelope function. Moreover it will be shown that the resulting envelope ripple can cause the modulator output to fail adjacent channel transmission requirements when the PAM/CPFSK signal passes through non-linear elements in the transmission path.

To illustrate the impact of the reconstruction filter implementation on the modulator performance the reconstruction filters in the numerical example that follows have a nominal 6th order Butterworth low-pass frequency response with a cut-off frequency of 20 kHz. The filter circuit component values are perturbed randomly within their tolerance ranges (5% for resistors and 10% for capacitors) to obtain realisations of the I and Q channel filters.

The magnitude and group-delay response characteristics for 100 realisations of the filter circuit are shown in Figure 3.13 and Figure 3.14 respectively.
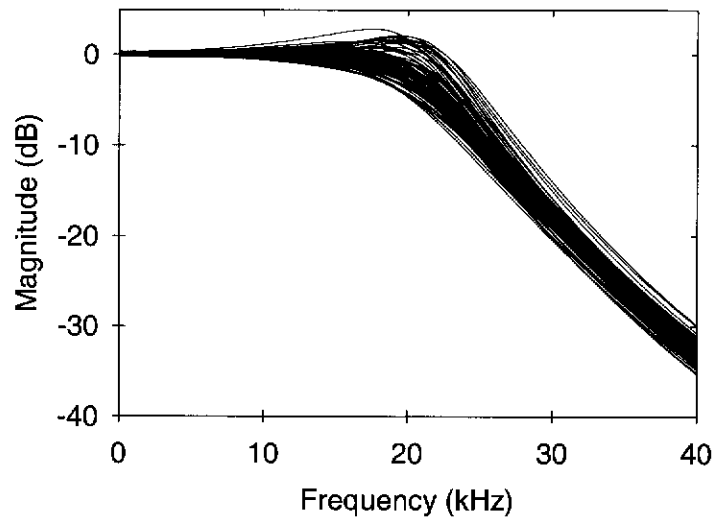
Figure 3.13. Magnitude response curves for 100 realisations of the Sallen-Key filter circuit.
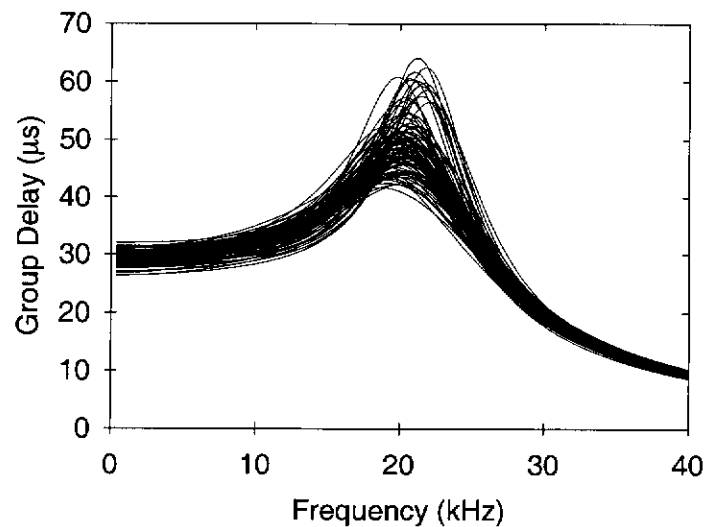
Figure 3.14. Group delay response curves for 100 realisations of the Sallen-Key filter circuit.

For the following example, two separate realisations of the filter circuit are taken for the I and Q channel reconstructions filters. The magnitude and group delay responses of the two filters used are shown in Figure 3.15 and Figure 3.16 respectively. For reference, the nominal or design responses of the 6th order Butterworth characteristic are also shown.
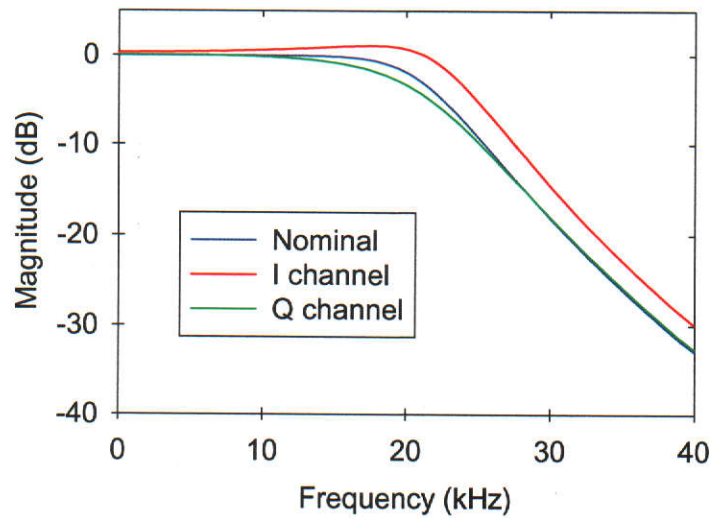
Figure 3.15. I and Q channel reconstruction filter magnitude responses.
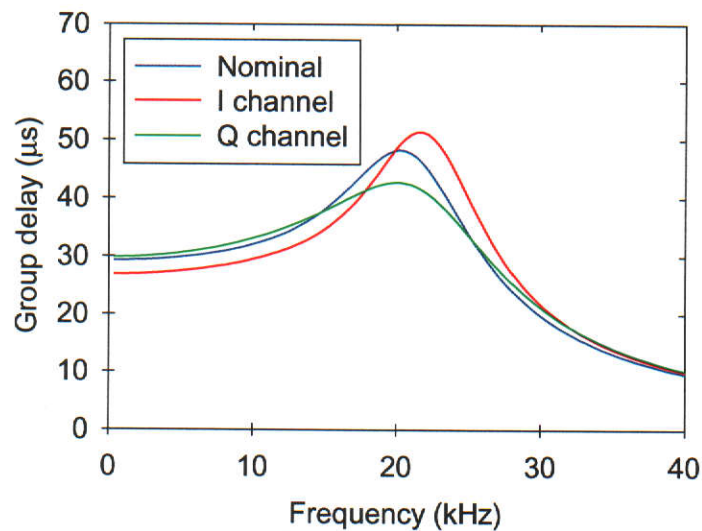
Figure 3.16. I and Q channel reconstruction filter group delay responses.

Comparing Figure 3.15 and Figure 3.16 with Figure 3.13 and Figure 3.14, respectively it can be seen that the I and Q channel reconstruction filters used in this example have magnitude and group delay responses that are typical of practical reconstruction filters implemented with the prescribed circuit tolerances and ERMES design parameters.

With these two filters in place in the IQ modulator, the input symbol sequence given in Figure 3.2 is applied and the envelope of vector modulator output signal calculated. This is shown in Figure 3.17.
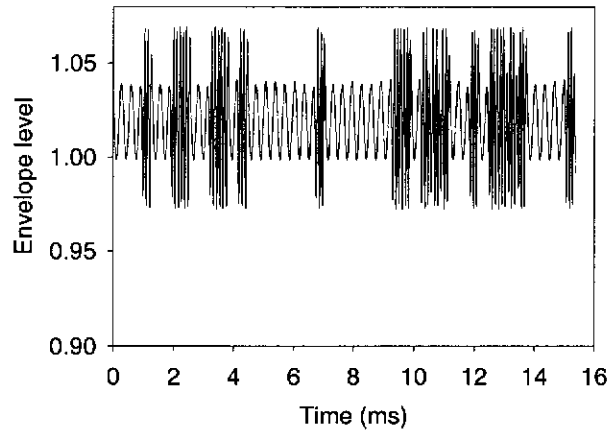
Figure 3.17. Envelope function: practical reconstruction filters.

For ease of comparison, the vertical axis in this figure is the same as that used for the envelope plots in the previous section. Note the similarity between the envelope function in Figure 3.17 and that for the case of pure phase imbalance with constant group delay shown in Figure 3.11.

3.5 Envelope Ripple and the Transmitted Signal Spectrum

The work presented in this thesis is motivated by a need to reduce the effects of the I and Q channel signal reconstruction filters on spreading of the transmitted PAM/CPFSK signal into adjacent channels.

In Chapter 2 it was shown that the ideal PAM/CPFSK signal has constant envelope. In [35] it is shown that passing a constant envelope FM signal through a channel with amplitude non-linearities results in an amplitude scaled version of the original signal and additional harmonic products that can be removed by band-pass filtering providing a suitable choice of carrier frequency is made.

However, as has been shown in Sections 3.3 and 3.4, transfer characteristics and implementation errors in the two analogue reconstruction filters cause ripple in the envelope function of the PAM/CPSFK signal appearing at the output of the vector modulator. If the vector modulator is followed by transmission elements having non-linear amplitude and phase characteristics, ripple in the signal envelope can lead to the generation of unacceptable side-lobes in the transmitted signal spectrum through processes of AM-AM and AM-PM conversion [15], [16], [19], [72]. This can, in turn

lead to the failure of the system in meeting adjacent channel emission requirements of the transmission standard (measured as *Adjacent Channel Power (ACP)*).

Most RF power amplifiers can be adequately described by a pair of AM/AM and AM/PM conversion characteristics [16]. The AM-AM response identifies a non-linear relationship between the instantaneous input and output levels of the device, while the AM-PM response gives the devices output phase as a function of the instantaneous input level.

In the following numerical example, the vector modulator output is assumed to be connected to a power transmitter with a non-linear transfer characteristic modelled using a two-parameter formula proposed in [15] and used in [16].

For an input signal to the amplifier given by

$$x(t) = r(t)\cos(\omega_c t + \phi(t)) \tag{3.24}$$

the output is modelled by

$$y(t) = A[r(t)]\cos(\omega_c t + \phi(t) + \psi[r(t)]), \tag{3.25}$$

where

$$A[r(t)] = \frac{2r(t)}{1 + r^2(t)}, \tag{3.26}$$

and

$$\psi[r(t)] = \frac{\pi}{6} \cdot \frac{2r^2(t)}{1 + r^2(t)}. \tag{3.27}$$

Note that $A[r(t)]$ and $\psi[r(t)]$ represent the AM-AM and AM-PM conversion characteristics respectively of the non-linear power amplifier.

The plots shown in Figure 3.18 were produced by applying a random sequence of 4000 symbols to the input of the modulator system. The power spectral density of the transmitter power amplifier (modelled as above) was computed for the IQ modulator system with:

1. identical brick-wall, linear phase reconstruction filters, and

2. practical reconstruction filters whose responses are shown in Figure 3.15 and Figure 3.16.
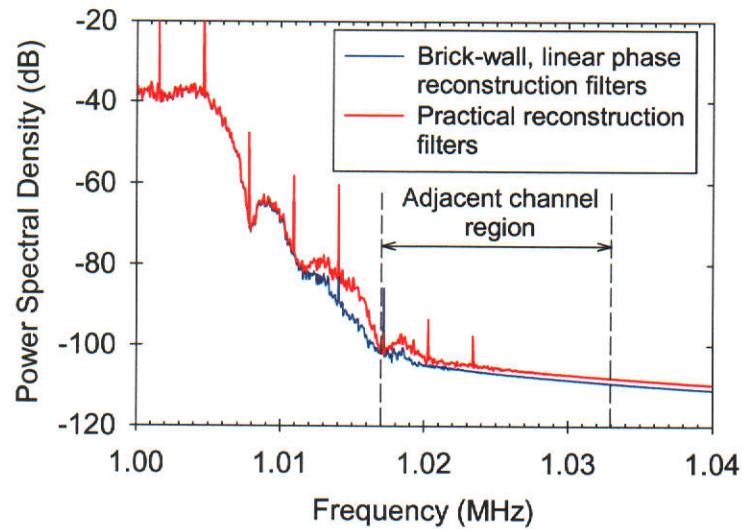
Figure 3.18. Power spectrum for the transmitter amplifier output.

Note the increased side-lobes and out-of-band power in the spectrum for the modulator system that contains the practical signal reconstruction filters.

The adjacent channel power is defined for the ERMES standard as the power in the band from 17 to 33 kHz either side of the carrier frequency (shown by the dashed lines in Figure 3.18) and must be less than −70dBc. The ACP values computed from the power spectrum plots in Figure 3.18 are −72 dBc for the modulator with brick-wall, linear phase reconstruction filters and −66 dBc for the modulator with the real filters in place. Therefore, in this example the ACP requirements on the transmitted signal spectrum have not been met for the system with practically realisable reconstruction filters.

3.6 Conclusion

Analogue low-pass signal reconstruction filters are included in the I and Q channels of the DSP based IQ modulator to remove image components in the base-band signal spectra caused by the digital synthesis process.

From the investigations in Section 3.3 into the effects of reconstruction filter pass-band parameters in isolation on the characteristics of the vector modulator output envelope, the following conclusions can be drawn:

Deviation from constant magnitude:

When the magnitude characteristics of the two reconstruction filters are identical but are non-constant through the pass-band the I and Q channel signals are both simply attenuated by the same amount for a given symbol frequency. When the symbol frequency changes, however, the *common* attenuation factor also changes. Thus, the stepped appearance in the envelope function in Figure 3.6 and Figure 3.7 corresponds to the difference in the filter gain at the two input symbol frequencies.

Deviation from linear phase:

When the phase responses of the two reconstruction filters are identical but have a common non-linear characteristic (non-constant group-delay), the I and Q channel signals are both shifted in phase by the same amount through the reconstruction filters, *provided* there is no relative difference in frequency between the two signals. For a given constant input symbol frequency then, the amount of common phase shift introduced into the I and Q channel signals is determined by the value of the phase characteristic at that frequency. However, when the I and Q channel signals are *swept* from one symbol frequency to the next at an input symbol transition, a relative difference between the instantaneous frequencies of the I and Q channel signals is generated. This is due to the phase of the I and Q signals changing in opposite directions during a symbol transition. Therefore, during this transition period the phases of the I and Q channel reconstruction filter output signals are not balanced resulting in additional terms in the envelope function. These additional terms are manifest as the transients located at the symbol transitions seen in Figure 3.8.

Magnitude imbalance:

In this case the I and Q channel reconstruction filters both have constant but different pass-band amplitude responses. When the I and Q channel signals are passed through these filters they will be attenuated by different, but constant amounts at all in-band frequencies. The result is a net constant-amplitude frequency modulated sinusoidal function impressed on the envelope and given by (3.14) and shown in Figure 3.11. The amplitude of the impressed function is proportional to the difference in the pass-band magnitude responses of the two filters and has a frequency that is double the input symbol frequency.

Phase imbalance:

In this case the I and Q channel filters both have a linear pass-band phase response but different phase slopes. When the I and Q channel signals are passed through these filters, the I channel signal is phase shifted by a different amount to the Q channel signal. This results in an amplitude and frequency modulated function impressed onto the envelope as seen in Figure 3.11. The function is given by (3.22) and has an amplitude given by (3.23) that is proportional to both the symbol frequency and the difference in group delay between the I and Q channels at the symbol frequency. The frequency of the impressed signal is twice the input symbol frequency.

From these considerations and from the investigations in Section 3.3 two key conclusions can be made:

1. Deviation from linear phase in each filter and magnitude and phase imbalances between the filters have a far more significant impact on envelope ripple than deviation from flat magnitude.

2. The envelope ripple resulting from deviation from linear phase pass-band responses is predominantly transient in nature while that resulting from magnitude and phase imbalances is dominated by steady-state components.

These two points provide a clear indication of the critical filter characteristics that need to be addressed in the development of compensation schemes in subsequent chapters of this thesis.

In practically realisable reconstruction filters, transfer characteristics and implementation errors result in the introduction of significant levels of AM in the envelope of the vector modulator output signal. The shortcomings in the frequency-domain characteristics of practical reconstruction filters that contribute to envelope ripple can be grouped into two categories:

1. departures from a constant magnitude, linear phase frequency response in the pass-bands of each of the two filters, and

2. magnitude and phase imbalances between the two filters.

When a transmitter amplifier that has non-linear transfer characteristics follows the vector modulator, the envelope ripple in the PAM/CPFSK signal results in the introduction of unwanted in-band and out-of-band signal components through processes of AM-PM and AM-AM conversion. As demonstrated in Section 3.5 the out-of-band effects of envelope ripple are increased side-lobes and power levels that result in an unacceptable increase in adjacent channel emissions.

Chapter 4. Optimum Digital Compensation Filters

4.1 Introduction

In the previous chapter it was shown that transfer characteristics and implementation errors in the two analogue signal reconstruction filters can result in significant levels of AM in the envelope of the vector modulator output signal. It was shown that this, in turn, can result in unacceptable spreading of the transmitted signal spectrum into adjacent channels when non-linear amplifiers are used in the transmitter.

This chapter contains a major part of the development towards an effective and practically realisable digital compensation scheme. A digital compensation structure is proposed based on the introduction of two digital FIR (Finite Impulse Response) filters into the I and Q channels of the digital modulator. The FIR filter tap-weights are chosen such that the frequency responses of the analogue I and Q channel reconstruction filters, in cascade with their corresponding FIR filters and D/A and A/D converters, closely approximate an overall desired complex channel response. The desired channel response is selected to ensure low levels of AM in the vector modulator output envelope.

Key contributions of this chapter are:

- The outline of a structure for compensation within the digital modulator

- The formulation of an optimisation problem such that optimum digital compensation filters can be determined.

- An approach for choosing the desired channel response that ensures that the degrees of freedom in the optimisation problem are used effectively in reducing the AM present in the envelope of the vector modulator output.

- A characterisation of the solution to the optimisation problem.

- An algorithm for determining the I and Q channel digital compensation filters incorporating a sub-space approach that ensures a stable solution in a finite numerical precision environment.

It is shown that the optimisation problem formulated in terms of I or Q channel frequency-domain parameters can be formulated equivalently in terms of the respective channels time-domain parameters. This motivates the work in Chapter 5 on both frequency-domain and time-domain identification techniques so that the required I and Q channel parameters can be estimated.

The digital compensation structure and algorithm for determining the digital compensation filter tap-weights developed in this chapter form the foundation of an automatic compensation system implemented on the DSP modulator described in Chapter 6.

This chapter is organised into nine sections. In Section 4.2 the digital compensation structure is outlined and in Section 4.3 the optimisation of the parameters of the structure is formulated. A key contribution of Section 4.4 is the formulation of a desired channel response that ensures the degrees of freedom in the optimisation are used effectively in reducing envelope ripple. Section 4.5 contains a number of sub-sections concerning the characterisation of the solution to the posed optimisation problem. In Section 4.5 the optimisation problem is formulated in the time-domain and the eigen-structure of the equations to be solved is investigated. In Section 4.6 some numerical aspects relating to the solution the optimisation problem are considered and an approach for computing a solution that is robust to finite numerical precision effects is developed. This approach forms the basis of the algorithm presented in Section 4.7 which summarises a step-by-step process for calculating the I and Q channel FIR filter tap-weights. The results of computer simulation studies are presented in Section 4.8 that highlight the effectiveness of the digital compensation technique. Section 4.9 contains the conclusions of the chapter.

4.2 Digital Compensation Structure

The IQ modulator incorporating digital synthesis of the base-band I and Q signals as discussed in Chapter 2, together with additional components required for the proposed digital compensation is shown in Figure 4.1.
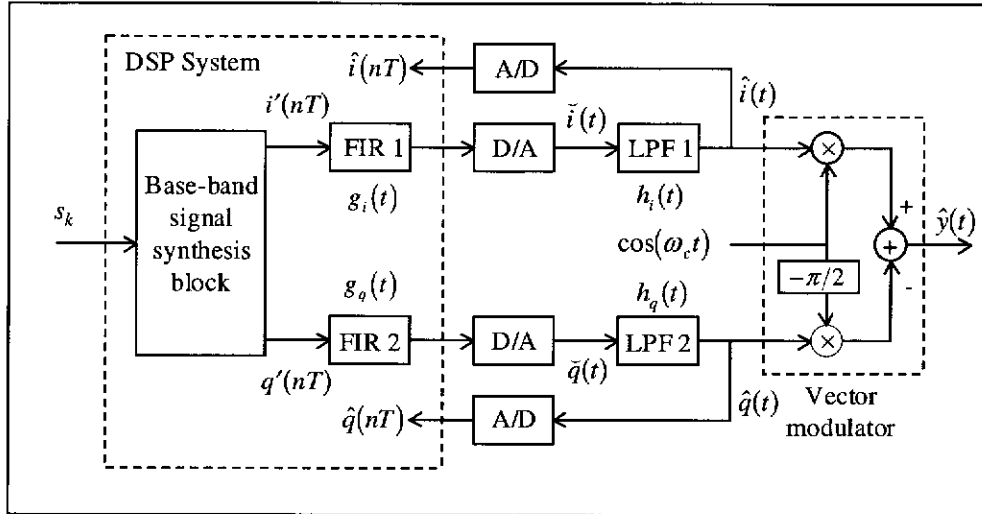

Figure 4.1. Digital compensation structure.

The key additional components of the digital compensation structure are the two digital FIR filters, FIR 1 and FIR 2. These filters are designed to compensate for departures from a desired magnitude and phase response in the pass-bands of each of the signal reconstruction filters, LPF 1 and LPF 2, and to achieve gain and phase balance between these two filters.

Note that since the actual analogue filters, $h_i(t)$ and $h_q(t)$, differ from each other, the optimal impulse responses of FIR 1 and FIR 2 will also be different in general.

The two A/D converters shown in Figure 4.1 allow measurements made on the outputs of the signal reconstruction filters to be used to determine the optimal FIR compensation filters as will be described in Chapter 5.

The "Base-band signal synthesis block" takes the input data symbol sequence, $\{s_k\}$ and generates samples of the I and Q base-band components of the M-PAM/CPFSK signal at the DSP system sampling as described in Chapter 2.

In the next section an optimisation problem is formulated in the FIR filter tap weights such that an optimum set of tap-weights can be found.

4.3 Problem Formulation

The optimisation problem for determining the sets of I and Q channel FIR filter tap-weights is based on the structures shown in Figure 4.2.
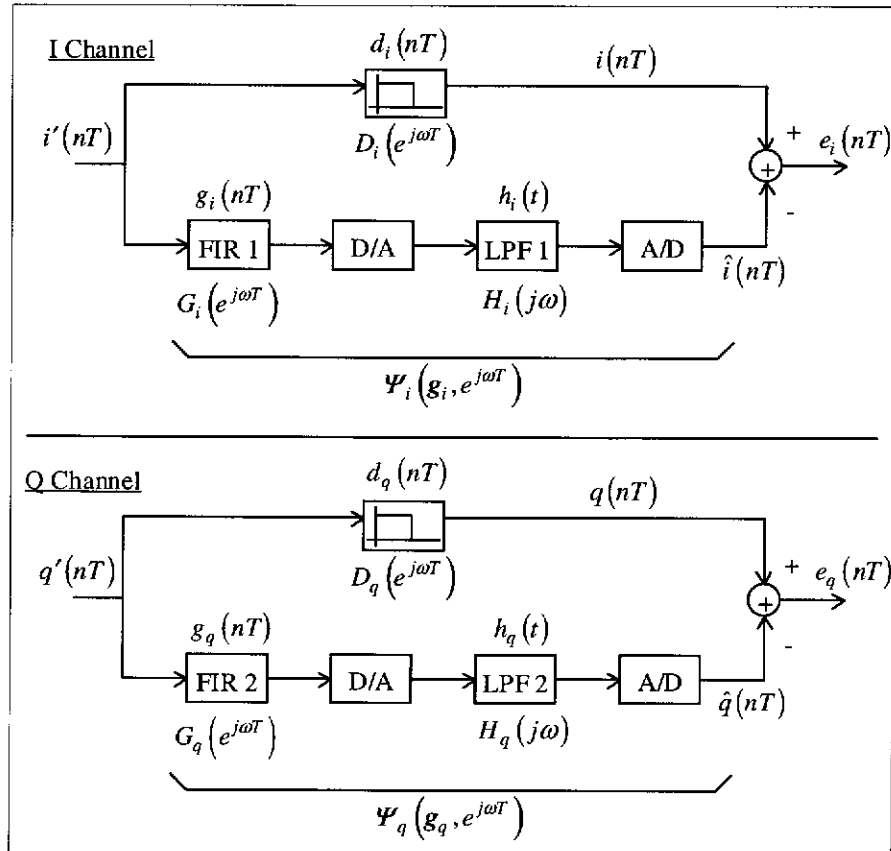
Figure 4.2. I and Q channel optimisation structures.

In each of the structures for the I and Q channels shown in Figure 4.2, the lower branches represent the actual channels (from the FIR filter input to the A/D converter output) of the system shown in Figure 4.1. The upper branches represent the nominal desired systems, i.e., the specific responses that the I and Q channels are required to have.

Since the I and Q channel magnitude and phase responses must be balanced, the following constraint is imposed on the desired I and Q channel responses

$$d_i(nT) = d_q(nT) = d(nT)$$

or equivalently $\qquad\qquad\qquad\qquad\qquad$ (4.1)

$$D_i\left(e^{j\omega T}\right) = D_q\left(e^{j\omega T}\right) = D\left(e^{j\omega T}\right),$$

where $d(nT)$ and $D\left(e^{j\omega T}\right)$ are the desired impulse and frequency responses respectively for both the I and Q channels.

In the following derivations the generic optimisation structure shown in Figure 4.3 is considered since the same optimisation process will apply to both channels. However it is important to keep in mind that since $h_i(t)$ and $h_q(t)$ are different in general, separate optimisations will need to be carried out for each channel. .
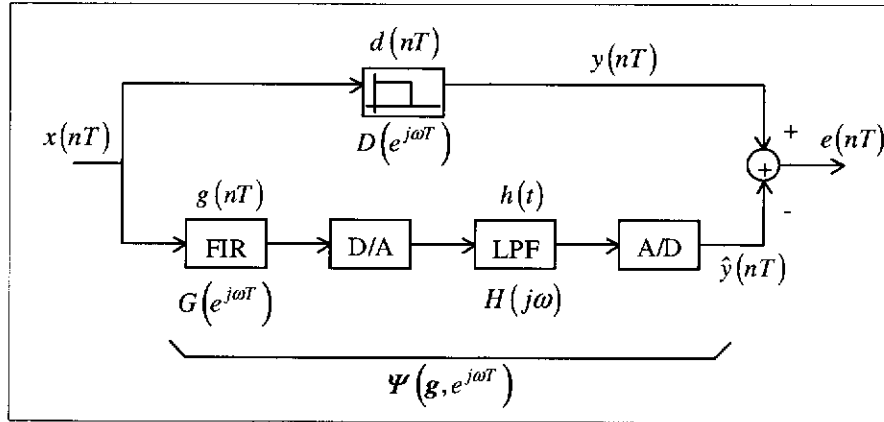

Figure 4.3. Generic optimisation structure.

Using a pulse transfer function [72], the hybrid discrete/continuous-time system in the lower branch of Figure 4.3 can be represented as the discrete-time system shown in Figure 4.4.
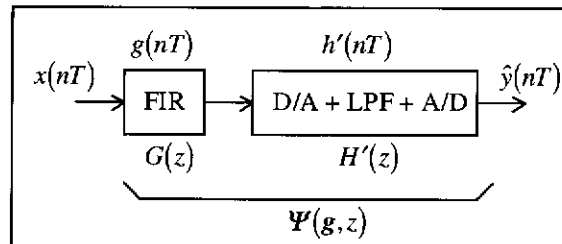

Figure 4.4. Equivalent discrete-time system.

Here $H'(z)$ is the discrete-time transfer function of the zero-order hold D/A converter, analogue low-pass filter and A/D converter in cascade (represented in the z-domain).

In [72, p.108] it is shown that the discrete-time transfer function, $H'(z)$, can be found from the relation

$$H'(z) = (1 - z^{-1}) Z \left\{ \frac{H(s)}{s} \right\}.$$ (4.2)

Note that $Z\{A(s)\}$ represents the z-transform of the sampled impulse response corresponding to $A(s)$, i.e.,

$$Z\{A(s)\} = \sum_{k=-\infty}^{\infty} a(kT) z^{-k},$$ (4.3)

where

$$a(t) = L^{-1} \{A(s)\}$$ (4.4)

and where $L^{-1}\{\bullet\}$ is the inverse Laplace transform.

The transfer function of the total discrete-time system in Figure 4.4 is given by

$$\Psi(g, z) = \frac{\hat{Y}(z)}{X(z)}$$
$$= G(z) H'(z),$$ (4.5)

where $X(z)$ and $\hat{Y}(z)$ are the Z-transforms of the input and output sequences, $x(nT)$ and $\hat{y}(nT)$, respectively. Substituting $z = e^{j\omega T}$ in (4.5) gives the frequency response of the system as

$$\Psi(g, e^{j\omega T}) = G(e^{j\omega T}) H'(e^{j\omega T})$$
$$= g^T s(e^{j\omega T}) H'(e^{j\omega T}),$$ (4.6)

where $g \in \mathbb{R}^{K \times 1}$ is a vector of FIR filter coefficients and $s\left(e^{j\omega T}\right) \in \mathbb{C}^{K \times 1}$ is given by

$$\left[s\left(e^{j\omega T}\right)\right]_l = e^{-j\omega(l-1)T}; l = 1,2,\ldots,K, \tag{4.7}$$

where $[\bullet]_l$ denotes the lth element of the vector.

Define the function $\varepsilon\left(g, e^{j\omega T}\right)$ to be the difference between the desired system complex frequency response, $D\left(e^{j\omega T}\right)$, and the actual complex frequency response, $\Psi\left(g, e^{j\omega T}\right)$, i.e.,

$$\varepsilon(g, \omega) = D\left(e^{j\omega T}\right) - \Psi\left(g, e^{j\omega T}\right), \tag{4.8}$$

where $f_s = \omega_s / 2\pi$ is the digital system sampling frequency. The function $\varepsilon\left(g, e^{j\omega T}\right)$ is defined over the Nyquist interval

$$\Omega = \left[-\frac{\omega_s}{2}, \frac{\omega_s}{2}\right]. \tag{4.9}$$

The set of FIR filter tap-weights, g, are chosen such that $\varepsilon(g, \omega)$ is minimised in the least-squares sense. The cost function for the optimisation problem is defined as

$$\begin{aligned}
J(g) &= \frac{1}{\omega_s} \int_{-\omega_s/2}^{\omega_s/2} \left|\varepsilon(g, \omega)\right|^2 d\omega \\
&= \frac{1}{\omega_s} \int_{-\omega_s/2}^{\omega_s/2} \left|D\left(e^{j\omega T}\right) - g^T s\left(e^{j\omega T}\right) H'\left(e^{j\omega T}\right)\right|^2 d\omega.
\end{aligned} \tag{4.10}$$

An unconstrained least-squares optimisation approach is chosen here over, for example, a Minimax approach or other constrained optimisations as it leads to a analytically tractable problem that has a globally optimum solution. This latter point is critically important when considering practical aspects of the implementation since searching through a number of locally optimum solutions is computationally demanding.

Note that in least-squares problems a weighting function is sometimes included inside the integrals in (4.10). A weighting function has been omitted here and is not considered in the treatment to follow as the choice of a particular weighting function is not motivated by any consideration of the problem.

Expanding (4.10) gives the following quadratic cost function

$$J(g) = d - 2g^T p + g^T R g \tag{4.11}$$

where

$$d = \frac{1}{\omega_s} \int_\Omega \left| D\left(e^{j\omega T}\right) \right|^2 d\omega, \tag{4.12}$$

$$
\begin{aligned}
p = &\frac{1}{\omega_s} \int_\Omega s_R\left(e^{j\omega T}\right)\left(D_R\left(e^{j\omega T}\right)H_R\left(e^{j\omega T}\right) + D_I\left(e^{j\omega T}\right)H_I\left(e^{j\omega T}\right)\right)d\omega \\
&+ \frac{1}{\omega_s} \int_\Omega s_I\left(e^{j\omega T}\right)\left(D_I\left(e^{j\omega T}\right)H_R\left(e^{j\omega T}\right) - D_R\left(e^{j\omega T}\right)H_I\left(e^{j\omega T}\right)\right)d\omega
\end{aligned} \tag{4.13}
$$

$$R = \frac{1}{\omega_s} \int_\Omega \left(s_R\left(e^{j\omega T}\right)s_R^T\left(e^{j\omega T}\right) + s_I\left(e^{j\omega T}\right)s_I^T\left(e^{j\omega T}\right)\right)\left| H'\left(e^{j\omega T}\right)\right|^2 d\omega. \tag{4.14}$$

and where $d \in \mathbb{R}, p \in \mathbb{R}^{K \times 1}, R \in \mathbb{R}^{K \times K}$. The quantities $s_R\left(e^{j\omega T}\right)$, $s_I\left(e^{j\omega T}\right)$, $D_R\left(e^{j\omega T}\right)$, $D_I\left(e^{j\omega T}\right)$, $H_R\left(e^{j\omega T}\right)$ and $H_I\left(e^{j\omega T}\right)$ are given by

$$
\begin{aligned}
s_R\left(e^{j\omega T}\right) &= \mathrm{Re}\left\{s\left(e^{j\omega T}\right)\right\}; s_I\left(e^{j\omega T}\right) = \mathrm{Im}\left\{s\left(e^{j\omega T}\right)\right\} \\
D_R\left(e^{j\omega T}\right) &= \mathrm{Re}\left\{D\left(e^{j\omega T}\right)\right\}; D_I\left(e^{j\omega T}\right) = \mathrm{Im}\left\{D\left(e^{j\omega T}\right)\right\} \\
H_R\left(e^{j\omega T}\right) &= \mathrm{Re}\left\{H'\left(e^{j\omega T}\right)\right\}; H_I\left(e^{j\omega T}\right) = \mathrm{Im}\left\{H'\left(e^{j\omega T}\right)\right\}
\end{aligned} \tag{4.15}
$$

Note from (4.14) that the matrix R is positive semi-definite, i.e.,

$$R \geq 0 \tag{4.16}$$

The optimisation problem can now be formulated as

$$\min_g J(g) = d - 2g^T p + g^T R g. \tag{4.17}$$

A necessary condition for $\breve{g}$ to be a minimum of $J(g)$ in (4.11) is

$$\nabla_g J(g)\big|_{g=\breve{g}} = -2p + 2Rg\big|_{g=\breve{g}} = 0. \tag{4.18}$$

Equation (4.18) can be rewritten as

$$R\breve{g} = p. \tag{4.19}$$

A sufficient condition for the vector $\breve{g}$ to be optimal and a unique solution of (4.19) is that the matrix R be positive definite [73], i.e.,

$$R > 0. \tag{4.20}$$

In this case the optimum vector, $\breve{g}$, that minimises (4.11) can be calculated as

$$\breve{g} = R^{-1}p. \tag{4.21}$$

If the inverse R^{-1} does not exist, a unique solution of minimum Euclidean norm, $(\breve{g}^T\breve{g})$, can be found using [74]

$$\breve{g} = R^+ p \tag{4.22}$$

where R^+ is the pseodoinverse given by

$$R^+ = \left(R^T R\right)^{-1} R^T \tag{4.23}$$

4.4 Desired Response

In Chapter 3 it was shown that departures from a linear-phase characteristic and magnitude and phase imbalances between the two reconstruction filters had a far more detrimental effect on the vector modulator output signal envelope than departures from a flat magnitude response in the pass-bands of the filters.

A desired response is chosen that has the same magnitude characteristic as the nominal response of the analogue filters but has a linear phase characteristic. This allows more degrees of freedom in the optimisation for compensating for the critical

parameters of magnitude and phase imbalances between the reconstruction filters and departures from linear phase in each of the filters.

The desired response can be expressed as

$$D\!\left(e^{j\omega},\tau_0\right)=\left|H(j\omega)\right|e^{-j\omega\tau_0}\,;-\omega_s/2\le\omega\le\omega_s/2,\qquad(4.24)$$

where $H(j\omega)$ is the nominal or design response of the two reconstruction filters.

Note that in selecting the desired response in (4.24) it is assumed that the nominal magnitude characteristic of the reconstruction filters, $\left|H\left(j\omega\right)\right|$, is sufficiently flat through the pass-band to ensure negligible contribution to ripple in the envelope function of the vector modulator output. As will be shown in Section 4.8, this condition is met for realisable filter designs used in the modulator structure.

The desired response in (4.24) is parameterised by a delay τ_0 that determines the slope of the phase function and hence the desired system group delay. Since the optimum value of this parameter is not known *a priori*, the minimisation problem given in (4.17) must be extended to include it. The new optimisation problem can therefore be rewritten as

$$\min_{\tau_0}\min_{g} J\left(g,\tau_0\right)=d\left(\tau_0\right)-2g^T p\left(\tau_0\right)+g^T Rg\qquad(4.25)$$

Note from (4.14) that the matrix R is not a function of the desired response, $D\!\left(e^{j\omega T},\tau_0\right)$, and is therefore independent of the delay parameter τ_0.

4.5 Characterisation of the Solution

In this section the structure of the vector p and the matrix R are investigated and an expression for the asymptotic distribution of the eigenvalues of R is derived.

4.5.1 The structure of the vector p and the matrix R

In Appendix B it is shown that the quantities p and R, expressed in terms of frequency-domain parameters in (4.13) and (4.14), can be equivalently represented in terms of the systems time-domain parameters as

$$[p]_k = \sum_{m=-\infty}^{\infty} h'(mT) d((m-k+1)T);$$
$$k = 1, 2, \ldots, K,$$

(4.26)

and

$$[R]_{k,l} = \sum_{m=-\infty}^{\infty} h'(mT) h'((m-k+l)T);$$
$$k, l = 1, 2, \ldots, K.$$

(4.27)

On inspection of (4.26) one can see that the elements of the vector p are values of the cross-correlation sequence between the desired and actual sampled impulse responses, $d(nT)$ and $h'(nT)$ respectively. From (4.27), the rows and columns of R are shifted segments of the auto-correlation sequence of the discrete-time impulse response $h'(nT)$ shown in Figure 4.4.

4.5.2 Asymptotic Distribution of the Eigenvalues of R

In Appendix B it is shown that the $(k,l)^{th}$ element of the R matrix can be represented as

$$[R]_{k,l} = \frac{1}{2\pi} \int_{-\pi}^{\pi} H_m(e^{j\theta}) e^{-j(k-l)\theta} d\theta$$

(4.28)

where $\theta = \omega T$ and

$$H_m(e^{j\theta}) = \left| H'(e^{j\omega T}) \right|^2 \Big|_{\theta = \omega T}$$

(4.29)

Note from (4.28) that the matrix R is *Toeplitz* since there exist scalars $r_{-(K-1)}, \ldots, r_{-1}, r_0, r_1, \ldots, r_{K-1}$ such that

$$[R]_{k,l} = r_{(k-l)} \tag{4.30}$$

where
$$r_{(k-l)} = \frac{1}{2\pi} \int_{-\pi}^{\pi} H_m\left(e^{j\theta}\right) e^{-j(k-l)\theta} d\theta . \tag{4.31}$$

Let the eigenvalues of R (in arbitrary order) be given by

$$\lambda_1, \lambda_2, \lambda_3, \ldots, \lambda_K . \tag{4.32}$$

Since R is Hermitian, $\lambda_n \in \mathbb{R}$; $n = 1, 2, \ldots, K$.

Define L as the class of all functions $F(\theta) \in \mathbb{C}$ for which the integral

$$\int_{-\pi}^{\pi} |F(\theta)| d\theta \tag{4.33}$$

exists.

In [76] and [77] it is shown, using the theory of equal distributions, that if $H_m\left(e^{j\theta}\right)$ is a real-valued function of the class L and $H_m\left(e^{j\theta}\right)$ is bounded such that

$$b \le H_m\left(e^{j\theta}\right) \le B \quad \text{for all real } \theta \tag{4.34}$$

then the following statements can be made regarding the eigenvalues of the Toeplitz matrix R:

(a)
$$\lim_{K \to \infty} \lambda_{\min} = b \; ; \; \lim_{K \to \infty} \lambda_{\max} = B \tag{4.35}$$

where

$$\lambda_{\min} = \min_n \left[\lambda_n\right]$$
$$\lambda_{\max} = \max_n \left[\lambda_n\right] \tag{4.36}$$

(b) The eigenvalues of the R matrix are asymptotically the following ordinates:

$$\lim_{K \to \infty} \left\{ \begin{array}{l} \lambda_n = \left| H'\left(e^{j\left(-\pi + \frac{2n\pi}{K+1}\right)} \right) \right|^2 \\[2ex] n = 1, 2, \ldots, K \end{array} \right\} \tag{4.37}$$

In the work presented here, $H'\left(e^{j\omega T}\right)$ is the discrete-time transfer function of a D/A converter, analogue low-pass filter and A/D converter in cascade as shown in Figure 4.4. An example of a low-pass characteristic is shown in Figure 4.5.
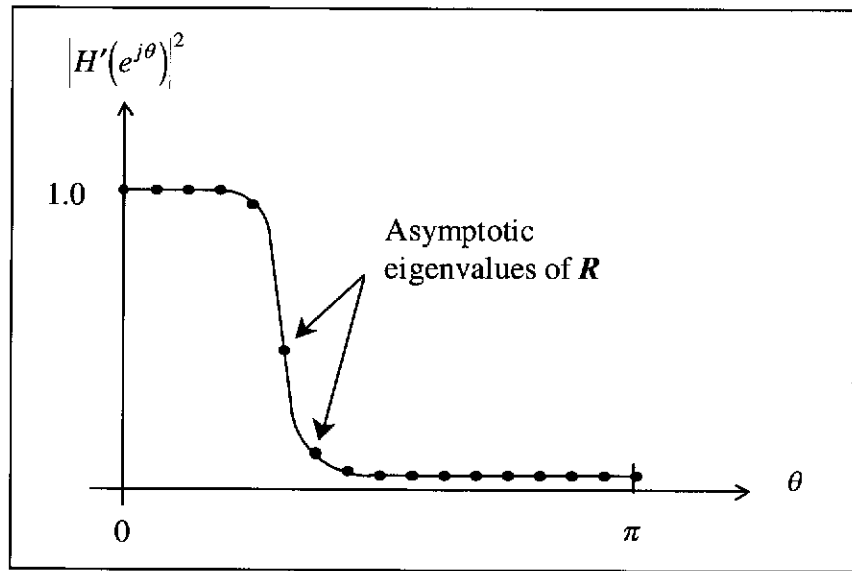

Figure 4.5. Example of a low-pass characteristic with the corresponding eigenvalues of the R matrix (magnitude plotted on a linear scale).

From (4.37) and the example in Figure 4.5 the low-pass function $\left|H'\left(e^{j\theta}\right)\right|^2$ will result in groupings of the eigenvalues of the R matrix: a group close to unity and a group close to zero as is shown in Figure 4.5.

4.6 Numerical Issues

In the previous sections a compensation structure has been proposed and a least-squares problem has been formulated and solved such that optimum sets of FIR filter tap-weights can be found. The derivations were carried out for a *generic* channel, however the computations required to determine the optimum I and Q channel digital

compensation filter tap-weights must be carried out for *each* channel. This point is highlighted by summarising the optimisation for the individual channels.

The optimum I and Q channel FIR filter tap-weight vectors, $\breve{g}_i$ and $\breve{g}_q$, see Figure 4.2, are found by solving the two sets of linear equations

$$
\begin{aligned}
R_i \breve{g}_i &= p_i \\
&\text{and} \\
R_q \breve{g}_q &= p_q
\end{aligned}
\tag{4.38}
$$

where the vectors $p_i, p_q \in \mathbb{R}^{K \times 1}$ and matrices $R_i, R_q \in \mathbb{R}^{K \times K}$ are found by substituting the corresponding channel parameters into (4.13) and (4.14) respectively.

In this section some numerical issues related to the computation of the solutions to the least-squares problems are considered.

For compactness the generic optimisation problem is again used in the following derivations .

The generic optimum FIR filter tap weight vector, $\breve{g}$, is found by solving the set of simultaneous equations given by

$$
R\breve{g} = p
\tag{4.39}
$$

where p and R are given by (4.13) and (4.14) respectively.

4.6.1 Notes on the Condition of the LS Problem

The values of the maximum and minimum eigenvalues of R are given by (4.34)-(4.36). A commonly used measure of the condition of a set of linear equations with respect to their solution is Von Neumann and Goldstine's P-condition number [78] defined by

$$
P(R) = \left| \frac{\lambda_{\max}}{\lambda_{\min}} \right|,
\tag{4.40}
$$

A small value of $P(R)$ (close to unity) indicates that a set of equations is well conditioned and that the solution is relatively insensitive to numerical errors.

From (4.34)-(4.36) and Figure 4.5 it can be seen that for a typical low-pass filter characteristic there is likely to be a large difference between the maximum and minimum eigenvalues of R. From (4.40) this will result in a high condition number and, correspondingly, a solution that is sensitive to errors in the problem coefficients and to finite numerical precision in the calculation process.

In the following section it is shown that by adopting a sub-space approach a FIR filter tap-weight solution vector can be determined that is significantly more robust to coefficient error and finite numerical precision effects. The new tap-weight vector, while sub-optimal, does not appreciably increase the cost, $J(g)$, given by (4.11).

4.6.2 Eigenvalue Decomposition of the R Matrix

From Mercer's theorem [79], the R matrix can be expressed in terms of its eigenvalues and corresponding eigenvectors as

$$R = Q \Lambda Q^T \tag{4.41}$$

where $\Lambda \in \mathbb{R}^{K \times K}$ is a diagonal matrix of the eigenvalues and is given by

$$\Lambda = \text{diag}(\lambda_1, \lambda_2, ..., \lambda_K) \; ; \text{where} \; \lambda_n \geq \lambda_{n+1} \; , n = 1, ..., K-1. \tag{4.42}$$

The columns of the matrix $Q \in \mathbb{R}^{K \times K}$ are the eigenvectors corresponding to the eigenvalues in Λ. The matrix Q can be expressed as

$$Q = [q_1, q_2, ..., q_K], \tag{4.43}$$

where $q_n \in \mathbb{R}^{K \times 1}$ is the eigenvector corresponding to λ_n.

In Section 4.5.2 it was shown that for a low-pass reconstruction filter characteristic, the eigenvalues of R appear roughly in two groups: those close to unity and those close to zero. Suppose a threshold value, ε, is set such that

$$\lambda_1 \geq \lambda_2 \geq \lambda_3 \ldots \geq \lambda_N > \varepsilon \geq \lambda_{N+1} \ldots \geq \lambda_K . \tag{4.44}$$

Equation (4.41) can now be written as

$$\begin{aligned} R &= Q(\Lambda_N + \Lambda_{K-N})Q^T \\ &= Q\Lambda_N Q^T + Q\Lambda_{K-N}Q^T, \end{aligned} \tag{4.45}$$

where

$$\Lambda_N = \begin{bmatrix} \Sigma_N & 0 \\ 0 & 0 \end{bmatrix}$$

and

$$\Lambda_{K-N} = \begin{bmatrix} 0 & 0 \\ 0 & \Sigma_{K-N} \end{bmatrix}, \tag{4.46}$$

and where

$$\Sigma_N = \mathrm{diag}(\lambda_1, \lambda_2, \ldots, \lambda_N)$$

and

$$\Sigma_{K-N} = \mathrm{diag}(\lambda_{N+1}, \lambda_{N+2}, \ldots, \lambda_K). \tag{4.47}$$

Letting

$$R_N = Q\Lambda_N Q^T$$

and

$$R_{K-N} = Q\Lambda_{K-N}Q^T \tag{4.48}$$

the cost function in (4.11) can be rewritten as

$$\begin{aligned} J(g) &= d - 2g^T p + g^T (R_N + R_{K-N}) g \\ &= d - 2g^T p + g^T R_N g + g^T R_{K-N} g \end{aligned} \tag{4.49}$$

If the threshold value, ε, in (4.44) is chosen so that the matrix Λ_{N-K} contains only the group of $N - K$ eigenvalues close to zero then

$$g^T R_{N-K} g \ll g^T R_N g \tag{4.50}$$

and the cost function is closely approximated by

$$J(g) \cong d - 2g^T p + g^T R_N g \tag{4.51}$$

Defining the new cost function

$$J_N(g) = d - 2g^T p + g^T R_N g$$
$$\cong J(g)$$

(4.52)

the vector $\breve{g}_N$ is found that minimises $J_N(g)$ using the approach described in Section 4.3. The vector $\breve{g}_N$ is found by solving the set of linear equations given by

$$R_N \breve{g}_N = p.$$

(4.53)

Since R_N is not full rank the system of equations defined by (4.53) has an infinite number of solutions. However, as described in Section 4.3 a unique solution of minimum Euclidean norm can be found using the pseudoinverse and is given by

$$\breve{g}_N = R_N^+ p$$

(4.54)

where R_N^+ is the pseudoinverse matrix given by

$$R_N^+ = \left(R_N^T R_N\right)^{-1} R_N^T.$$

(4.55)

Alternatively, the pseudoinverse, R_N^+, can be expressed in terms of the largest N eigenvalues and their corresponding eigenvectors of the R matrix as [74]

$$R_N^+ = Q \Gamma_N^+ Q^T,$$

(4.56)

where

$$\Gamma_N^+ = \mathrm{diag}\left(\frac{1}{\lambda_1}, \frac{1}{\lambda_2}, \ldots, \frac{1}{\lambda_N}, 0, \ldots, 0\right) \in \mathbb{R}^{K \times K}.$$

(4.57)

A number of methods are available for the computation of the eigenvalues of the R matrix, [74, 80, 81]. In the simulation studies in Section 4.8 and the implementation presented in Chapter 6, the eigenvalues and corresponding eigenvectors of the I and Q channel R matrices are computed using the Jacobi method [81]. A re-formulated but mathematically equivalent version of the classical Jacobi method that minimises round-off error is used and details can be found in [81, pp. 503-504].

4.7 Algorithm Summary

The computational steps necessary to determine the I and Q channel FIR digital compensation filter tap-weight vectors are now summarised:

1. Generate the required matrices and vectors.

2. Perform an eigenvalue decomposition of the I and Q channel R matrices.

3. Construct the matrices Γ_i and Γ_q from the N_i and N_q largest eigenvalues.

4. Compute the I and Q channel tap-weight vectors.

These four steps are shown in Table 4.1.

	I-channel	Q-channel
1	Frequency domain: $p_i = \dfrac{1}{\omega_s} \int\limits_{\Omega} s_R \left(D_R H_{R,i} + D_I H_{I,i}\right) d\omega$ $+ \dfrac{1}{\omega_s} \int\limits_{\Omega} s_I \left(D_I H_{R,i} - D_R H_{I,i}\right) d\omega$ $R_i = \dfrac{1}{\omega_s} \int\limits_{\Omega} \left(s_R s_R^T + s_I s_I^T\right) \left\| H_i'\left(e^{j\omega T}\right)\right\|^2 d\omega$ Time domain: $\left[p_i\right]_k = \sum\limits_{m=-\infty}^{\infty} h_i'(mT) d\left((m-k+1)T\right);$ $k = 1,2,\ldots,K$ $\left[R_i\right]_{k,l} = \sum\limits_{m=-\infty}^{\infty} h_i'(mT) h_i'\left((m-k+l)T\right);$ $k,l = 1,2,\ldots,K$	Frequency domain: $p_q = \dfrac{1}{\omega_s} \int\limits_{\Omega} s_R \left(D_R H_{R,q} + D_I H_{I,q}\right) d\omega$ $+ \dfrac{1}{\omega_s} \int\limits_{\Omega} s_I \left(D_I H_{R,q} - D_R H_{I,q}\right) d\omega$ $R_q = \dfrac{1}{\omega_s} \int\limits_{\Omega} \left(s_R s_R^T + s_I s_I^T\right) \left\| H_q'\left(e^{j\omega T}\right)\right\|^2 d\omega$ Time domain: $\left[p_q\right]_k = \sum\limits_{m=-\infty}^{\infty} h_q'(mT) d\left((m-k+1)T\right);$ $k = 1,2,\ldots,K$ $\left[R_q\right]_{k,l} = \sum\limits_{m=-\infty}^{\infty} h_q'(mT) h_q'\left((m-k+l)T\right);$ $k,l = 1,2,\ldots,K$
2	$R_i = Q_i \Lambda_i Q_i^T$	$R_q = Q_q \Lambda_q Q_q^T$
3	$\Gamma_i = \text{diag}\left(\dfrac{1}{\lambda_{i,1}}, \dfrac{1}{\lambda_{i,2}}, \ldots, \dfrac{1}{\lambda_{i,N_i}}, 0, \ldots, 0\right)$	$\Gamma_q = \text{diag}\left(\dfrac{1}{\lambda_{q,1}}, \dfrac{1}{\lambda_{q,2}}, \ldots, \dfrac{1}{\lambda_{q,N_q}}, 0, \ldots, 0\right)$
4	$\breve{g}_{i,N_i} = Q_i \Gamma_i Q_i^T p_i$	$\breve{g}_{q,N_q} = Q_q \Gamma_q Q_q^T p_q$

Table 4.1. Determining the I and Q channel digital FIR compensation filter tap-weight vectors.

Note in step 1 of Table 4.1 that the following abbreviations have been made for compactness:

$$s_R = s_R\left(e^{j\omega T}\right), s_I = s_I\left(e^{j\omega T}\right)$$
$$D_R = D_R\left(e^{j\omega T}\right), D_I = D_I\left(e^{j\omega T}\right)$$
$$H_{R,i} = \mathrm{Re}\left[H_i'\left(e^{j\omega T}\right)\right], H_{I,i} = \mathrm{Im}\left[H_i'\left(e^{j\omega T}\right)\right]$$
$$H_{R,q} = \mathrm{Re}\left[H_q'\left(e^{j\omega T}\right)\right], H_{I,q} = \mathrm{Im}\left[H_q'\left(e^{j\omega T}\right)\right]$$

$$(4.58)$$

A number of assumptions have been made in presenting the algorithm shown in Table 4.1:

1. The I and Q channel frequency domain parameters, $H_i'\left(e^{j\omega T}\right)$ and $H_q'\left(e^{j\omega T}\right)$, or time domain parameters, $h_i'(nT)$ and $h_q'(nT)$, are known.

2. The desired channel transfer function, $D\left(e^{j\omega T}\right)$, or impulse response, $d(nT)$, is known.

3. The eigenvalue threshold parameters, N_i and N_q, are known.

The identification of the I and Q channel frequency-domain or time-domain parameters (point number 1 above) is the subject of the next chapter.

The choice of desired response, $D\left(e^{j\omega T}\right)$, was discussed in Section 4.4 however the choice of the optimum desired delay parameter, $\breve{\tau}_0$, remained unresolved. In the next section it is shown, for a given set of modulator parameters and FIR filter lengths, that the cost function is not sensitive (within a range of delay values) to the choice of $\breve{\tau}_0$ and a simple technique is proposed for obtaining an acceptable estimate of $\breve{\tau}_0$.

The choice of the I and Q channel eigenvalue thresholds, N_i and N_q, is a trade-off between

A. including enough of the smaller eigenvalues in the solution that the cost $J_N(\boldsymbol{g})$ is not significantly greater than $J(\boldsymbol{g})$ thus degrading the quality of compensation achieved, and

B. excluding enough of the smaller eigenvalues to ensure that the P-condition number of the matrix $\boldsymbol{\varSigma}_N$ is small enough that the solution is not sensitive to coefficient error and finite numerical precision effects in the chosen DSP platform.

4.8 Simulation Studies

In this section a computer model of the IQ modulator system shown in Figure 4.1 is used to investigate the application of the digital compensation techniques developed in the preceding sections. The IQ modulator system parameters are selected for the generation of a 4-PAM/CPFSK modulator output signal that conforms to the ERMES signal standard that was described in detail in Chapter 2.

Specifically, the following issues are addressed in regard to the digital compensation techniques developed:

- Methods for choosing the optimum desired channel delay parameters, $\breve{\tau}_0^i$ and $\breve{\tau}_0^q$.

- The effect of the length of the two FIR digital compensation filters on the quality of compensation.

- The effect of the desired channel response on the solution to the optimisation problem and the quality of compensation.

- The impact of the proposed sub-space approach to the solution of the optimisation problems on the quality of compensation.

In the latter three cases the quality of compensation is measured in terms of the reduction in envelope ripple from the uncompensated system.

4.8.1 Simulation Parameters

The two low-pass reconstruction filters, LPF 1 and LPF 2, in Figure 4.1 have a nominal 6th order Butterworth response with a 3 dB bandwidth of 20 kHz. The

magnitude and group delay responses of the I and Q channel reconstruction filters are shown in Figure 3.15 and Figure 3.16 respectively. These responses correspond to two particular realisation of the filter circuit resulting from perturbations of the component values about their nominal values. For reference, the nominal or design magnitude and group delay responses are also plotted in Figures 3.15 and 3.16 respectively.

In Sections 4.8.2, 4.8.3 and 4.8.5 the desired response, $D\left(e^{j\omega T}\right)$, is chosen to have the same magnitude characteristic as the nominal response of the reconstruction filters but is constrained to have linear phase (as proposed in Section 4.4). The function $D\left(e^{j\omega T}\right)$ can therefore be expressed as

$$D\left(e^{j\omega T}\right) = \left|H(j\omega)\right|e^{-j\omega\tau_0}, \quad -\omega_s/2 \le \omega \le \omega_s/2, \tag{4.59}$$

where $H(j\omega)$ is the frequency response of the nominal 6th order Butterworth analogue filter given by

$$H\left(j\omega\right) = \prod_{i=1}^{3}\frac{\omega_0}{\omega_0^2 - \omega^2 + j\left(\omega_0/Q_i\right)\omega}. \tag{4.60}$$

The parameters ω_0 and $\{Q_i\}, i = 1,2,3$ are found from the standard formulae [82]

$$\omega_0 = \frac{\omega_c}{\left(10^{-\rho/10} - 1\right)^{1/12}}$$

and

$$Q_i = \frac{1}{2\cos\psi_i}, i = 1,2,3, \tag{4.61}$$

and the parameters ω_c, ρ and $\{\psi_i\}$ are given by

$$\omega_c = 2\pi f_c = 2\pi \times 20 \times 10^3$$

$$\rho = -3\text{dB} \tag{4.62}$$

$$\{\psi_i\} = \left\{\frac{\pi}{12}, \frac{\pi}{4}, \frac{5\pi}{12}\right\}.$$

Note that $\omega_s = 2\pi f_s$ in (4.59) where $f_s = 200\,\text{kHz}$ is the system sampling frequency. The parameter, τ_0, is the compensated channels desired group-delay and is yet to be determined.

For ease of comparison with the results of presented in Chapter 3, the same test input symbol sequence to the modulator shown in Figure 3.2 is used.

4.8.2 The Optimum Delay Parameter

In this example it is shown that the *quality* of digital compensation, measured in terms of the cost $J(g,\tau_0)$, is relatively insensitive to the choice of the desired channel delay parameter, τ_0, for a given FIR compensation filter length and range of delay values.

One technique to determine the optimum value of the desired channel delay, $\breve{\tau}_0$, is to use an exhaustive search over a discrete grid. However, it has been found empirically that a good estimate of $\breve{\tau}_0$ can be calculated using a simple formula and requiring only knowledge of the nominal or design group delay response of the reconstruction filters.

In Section 4.4 an extended, generic optimisation problem given by (4.25) was formulated to include the desired channel delay, τ_0. Equation (4.25) is reformulated in terms of the individual I and Q channel parameters as follows:

I-channel
$$\min_{\tau_0^i} \min_{g_i} J_i\left(g_i, \tau_0^i\right) = d\left(\tau_0^i\right) - 2g_i^T p_i\left(\tau_0^i\right) + g_i^T R_i g_i \tag{4.63}$$

Q-channel
$$\min_{\tau_0^q} \min_{g_q} J_q\left(g_q, \tau_0^q\right) = d\left(\tau_0^q\right) - 2g_q^T p_q\left(\tau_0^q\right) + g_q^T R_q g_q \tag{4.64}$$

For given τ_0^i and τ_0^q it has been shown that the inner minimisation problems can be solved by finding the solution to the following sets of simultaneous equations

$$R_i \breve{g}_{i,\tau_0^i} = p_i\left(\tau_0^i\right). \tag{4.65}$$

$$R_q \breve{g}_{q,\tau_0^q} = p_q\left(\tau_0^q\right) \tag{4.66}$$

The following figures were obtained by calculating $\breve{g}_{i,\tau_0^i}$ and $\breve{g}_{q,\tau_0^q}$ from (4.65) and

(4.66) for a range of τ_0^i and τ_0^q then computing the values of the cost functions

$J_i\left(\breve{g}_{i,\tau_0^i},\tau_0^i\right)$ and $J_q\left(\breve{g}_{q,\tau_0^q},\tau_0^q\right)$ from (4.63) and (4.64).

Plots of the cost functions, $J_i\left(\breve{g}_{i,\tau_0^i},\tau_0^i\right)$ and $J_q\left(\breve{g}_{q,\tau_0^q},\tau_0^q\right)$ as the delays, τ_0^i and τ_0^q,

are varied are shown in the figures below. Figures 4.6, 4.7 and 4.8 correspond to FIR
compensation filter lengths of 100-taps, 50-taps and 30-taps respectively and all
results were obtained using ERMES modulation system parameters. (In some figures
in this thesis the values of two or more plots are so close that they can not be visually
separated on the chosen scale. An example of this appears in Figures 4.6 to 4.8 where
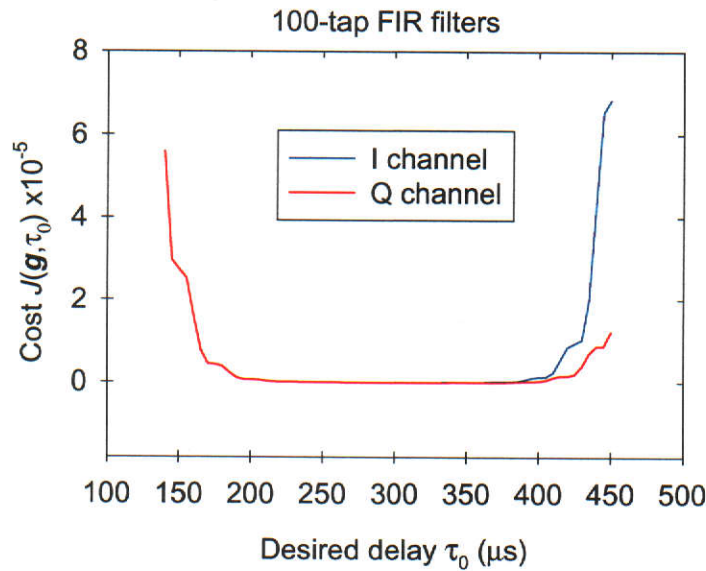the blue plot lies underneath the red plot in parts of the figures.)

Figure 4.6. Least-squares cost as a function of desired delay: 100-tap FIR
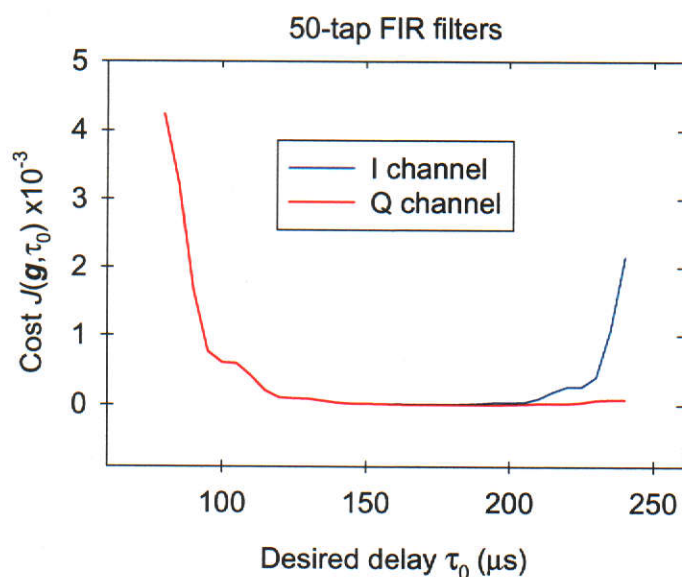filters.

Figure 4.7. Least-squares cost as a function of desired delay: 50-tap FIR filters.
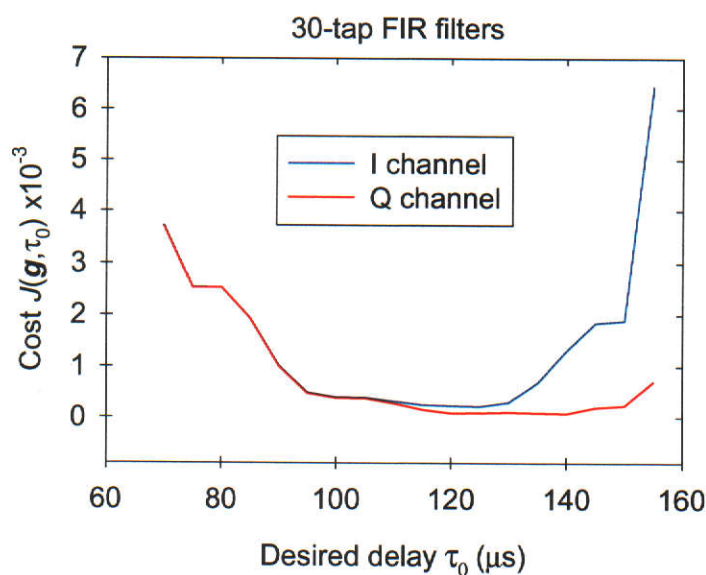

Figure 4.8. Least-squares cost as a function of desired delay: 30-tap FIR filters.

As can be seen from the plots of the cost vs. delay in the three figures above, the optimisation is quite insensitive to the choice of delay for a range of delay values for each of the filter lengths considered. It is also important to note that the differences between the I and Q channel reconstruction filters produce little or no difference between the optimum delay values for each channel (for a given FIR compensation

filter length). However, the range of τ_0^i and τ_0^q values for which there is little change in the cost is narrower and the overall cost is higher as the filter length is reduced.

To better appreciate the trends in the desired delay characteristics as the FIR filter length is varied, it is also helpful to view the three figures above with the cost plotted on a log scale as shown in Figure 4.9.
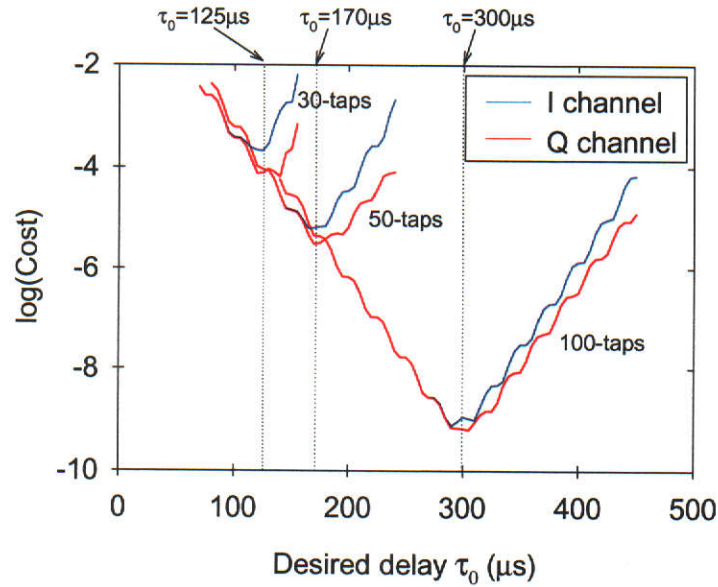

Figure 4.9. Least-squares cost as a function of desired delay for 100, 50 and 30-tap FIR filters.

This figure clearly illustrates the increasing trend in least squares cost and sensitivity to reconstruction filter variation as the FIR filter length is reduced. The vertical dotted lines in Figure 4.9 mark the approximate values of delay that result in the lowest cost for each FIR filter length. These values are therefore good estimates of the optimum desired channel delay, $\breve{\tau}_0$. (Recall from Section 4.3 that for balance in the group delay response of the I and Q channels, the desired channel delay parameter must be the same for both channels.)

While the exhaustive search approach employed above can be used to determine the optimum delay parameter, $\breve{\tau}_0$, it has been found empirically that a good estimate of the optimum delay value can be found using the simple formula

$$\breve{\tau}_0 \cong \frac{KT}{2} + \tau_{n,\max} \qquad (4.67)$$

where

- K is the length of the FIR compensation filters,

- T is the digital system sampling period, and

- $\tau_{n,\max}$ is the peak value of the group delay response of the nominal reconstruction filters.

For ERMES, the digital system sampling period is $T = 1/(200 \times 10^3) = 5\mu s$ and from Figure 3.16 the maximum value of the nominal filter group delay response is $\tau_{n,\max} \cong 50\mu s$. Equation (4.67) gives the following estimates of $\breve{\tau}_0$ for the three FIR filter lengths used in this example:

$$
\begin{aligned}
100\text{-taps}:\hat{\tau}_0 &= 300\mu s \\
50\text{-taps}:\hat{\tau}_0 &= 175\mu s \\
30\text{-taps}:\hat{\tau}_0 &= 125\mu s
\end{aligned}
\tag{4.68}
$$

Note that the estimated desired channel delay values in (4.68) closely match those determined using the exhaustive search and shown plotted in Figure 4.9.

4.8.3 FIR Filter Length

In this section the length of the two digital FIR filters required to provide adequate compensation and hence reduction of the envelope ripple is investigated. Again the modulator parameters for ERMES signals are used in the examples presented here.

The optimum digital FIR compensation filter impulse responses for 100-tap, 50-tap and 30-tap filters are shown in Figure 4.10, Figure 4.11 and Figure 4.12 respectively. (The optimum desired channel delay parameter, $\breve{\tau}_0$, for each filter length is determined as outlined in Section 4.8.2.)

Note that samples of the FIR compensation filter impulse responses shown in the figures are joined by straight lines for ease of comparison.
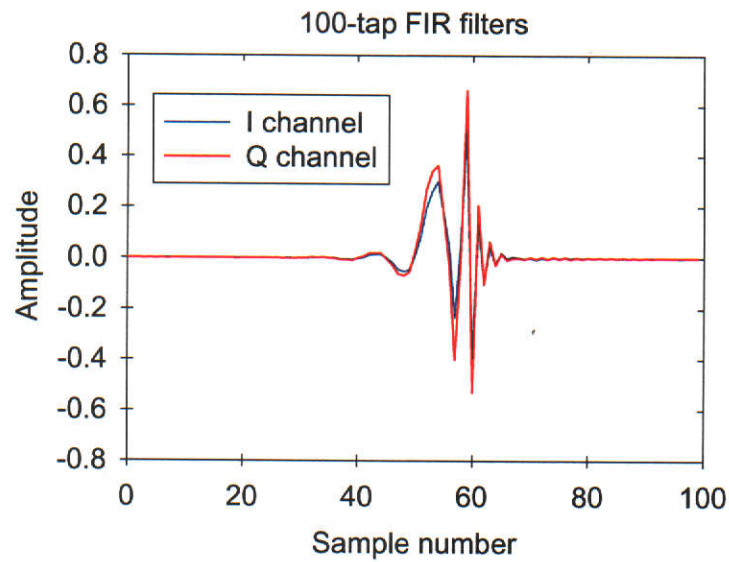
Figure 4.10. Impulse responses of optimum I and Q channel 100-tap FIR compensation filters.
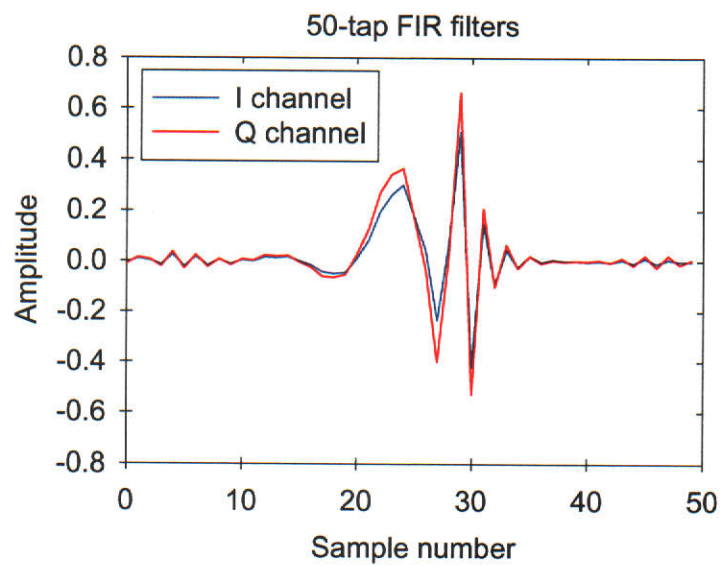
Figure 4.11. Impulse responses of optimum I and Q channel 50-tap FIR compensation filters.
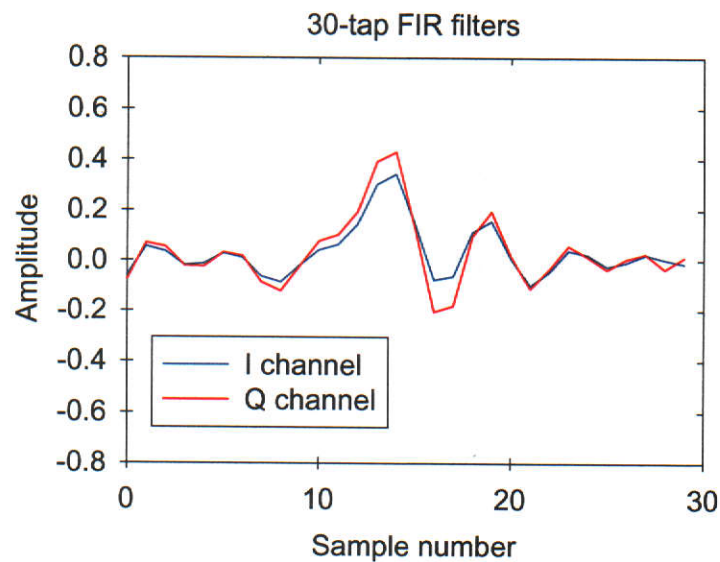
Figure 4.12. Impulse responses of optimum I and Q channel 30-tap FIR
compensation filters.

For the three filter lengths investigated, the resulting envelope functions of the vector
modulator output signal (with the FIR compensation filters present in the modulator)
are shown in Figure 4.13. For reference the envelope function produced by the
uncompensated modulator is also shown.
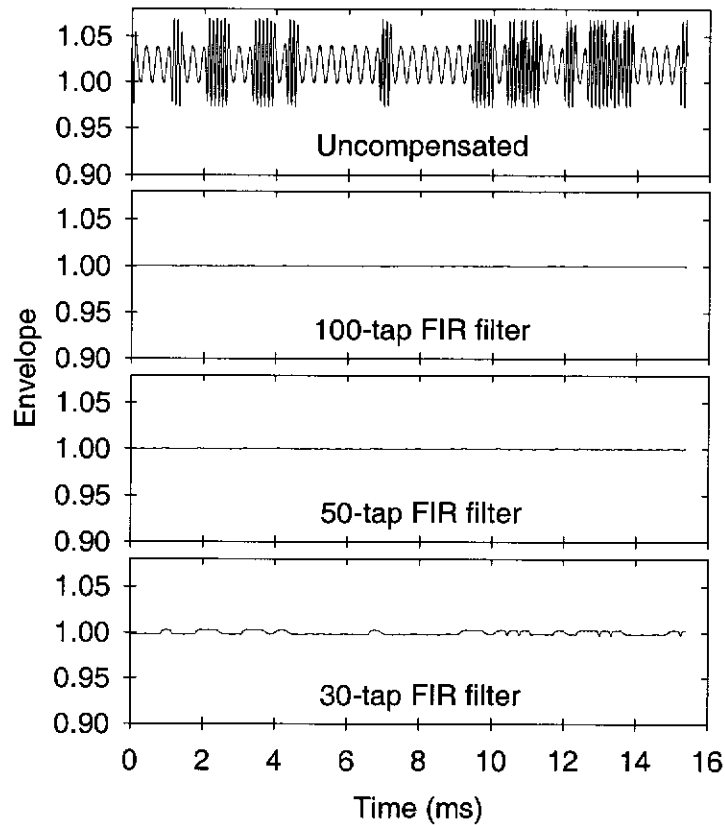
Figure 4.13. Envelope functions for the uncompensated and compensated modulator system.

The envelope functions for the digitally compensated system using the 100, 50 and 30-tap FIR filters (lower three plots in Figure 4.13) are shown with expanded vertical axes in Figure 4.14, Figure 4.15 and Figure 4.16 respectively.

Figure 4.14. Envelope function for the vector modulator output signal:
100-tap FIR compensation filters.

Figure 4.15. Envelope function for the vector modulator output signal:
50-tap FIR compensation filters.

Figure 4.16. Envelope function for the vector modulator output signal:
30-tap FIR compensation filters.

The RMS values of the envelope ripple in the three figures above are given in Table 4.2. Also shown for reference is the RMS value of the envelope ripple for the uncompensated system.

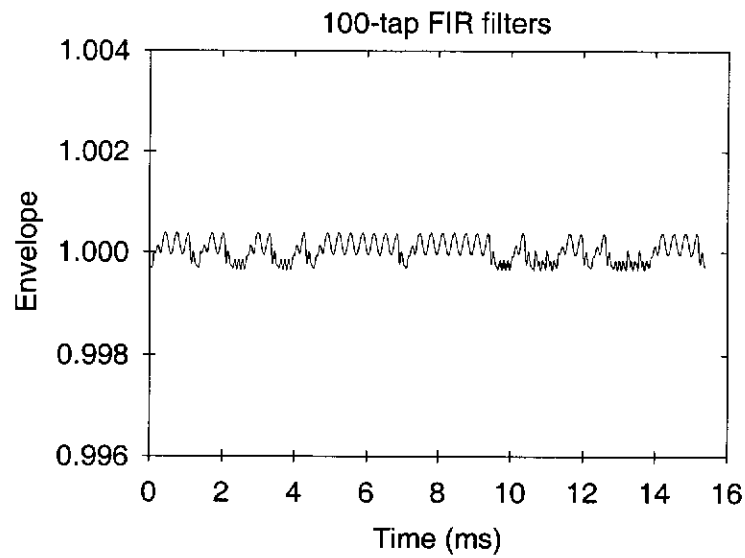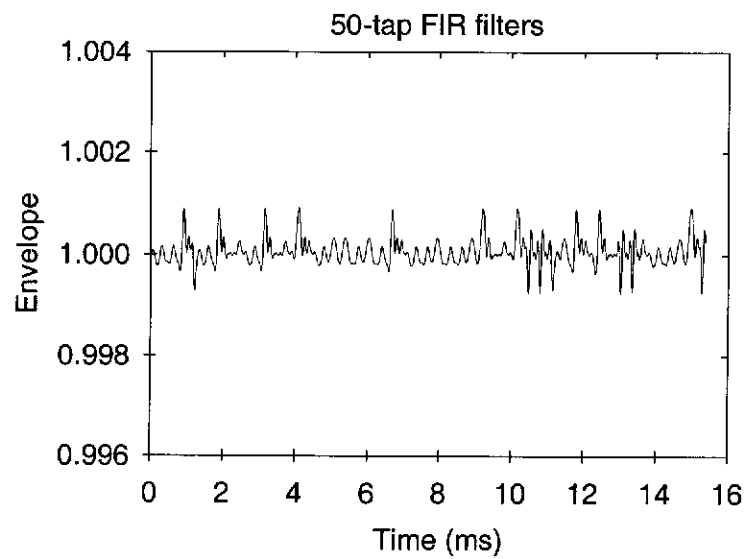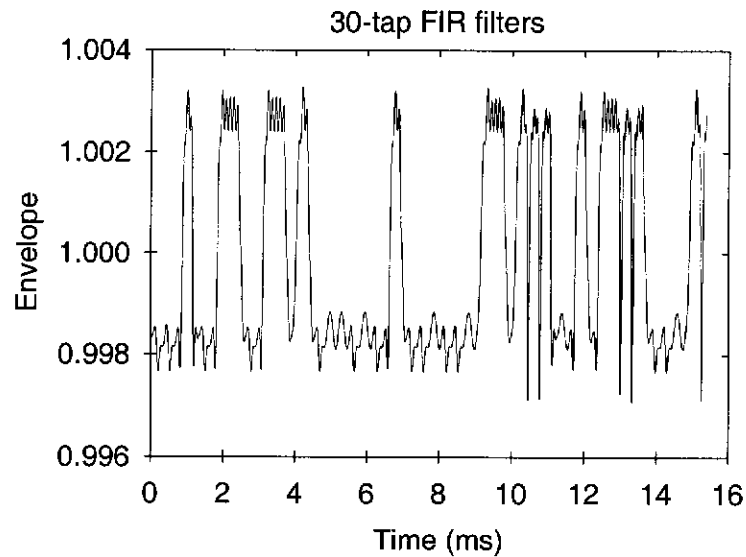| FIR filter length	RMS envelope ripple	Ripple reduction factor
100-taps	26 μV	111
50-taps	32 μV	90
30-taps	247 μV	12
Uncompensated	2.88 mV	1

Table 4.2. RMS envelope ripple for different FIR filter lengths.

From Table 4.2 and the three envelope function plots above it can be seen that the 100-tap and 50-tap digital FIR compensation filters perform similarly well in reducing envelope ripple in the vector modulator output signal. Note also that the RMS ripple values for the 100-tap and 50-tap filters are actually lower than the 44 μV RMS value obtained for the brick-wall, linear phase reconstruction filter in Section 3.3.1 in Chapter 3. This can be attributed to the fact that the optimum digital FIR filters not only compensate for the errors and imbalances in the reconstruction filters but they also implicitly compensate for the $\sin(x)/x$ magnitude response effect of the two zero-order hold D/A converters also present in the I and Q channels. In

Chapter 3 the D/A converter characteristic were identified as a contributor to the $44\mu V$ RMS residual ripple in this case.

From Figure 4.16 and Table 4.2, the 30-tap FIR filters result in a noticeable increase in envelope ripple characterised by a 8-fold increase in the RMS value from the 50-tap filter. The 30-tap FIR filters, however still provide quite acceptable compensation as can be seen from Figure 4.13 and result in a reduction in envelope ripple by a factor of approximately 12.

The effect of digital compensation on the I and Q channel frequency response characteristics is shown in Figure 4.17, Figure 4.18 and Figure 4.19. Here the magnitude and group delay response characteristics of the 50-tap optimum compensation filters shown in Figure 4.11 in cascade with their corresponding I and Q channel D/A, low-pass filter and A/D are shown. (Note that the frequency responses of the I and Q discrete-time channels are periodic with period $f_s = 200\text{kHz}$. Only a small section of the frequency response characteristics are shown in the figures below thus allowing details of the effect of digital compensation to be seen more clearly.)
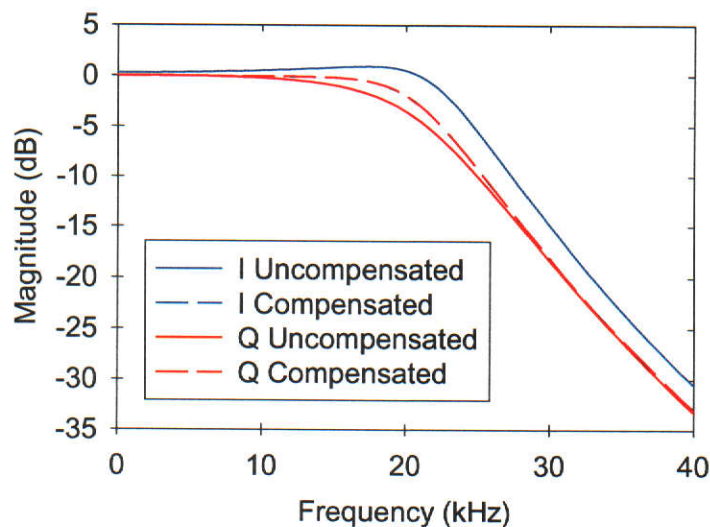
Figure 4.17. Effect of digital compensation on the I and Q channel magnitude responses: 50-tap FIR compensation filters. (The "I Compensated" plot lies under the "Q Compensated" plot.)
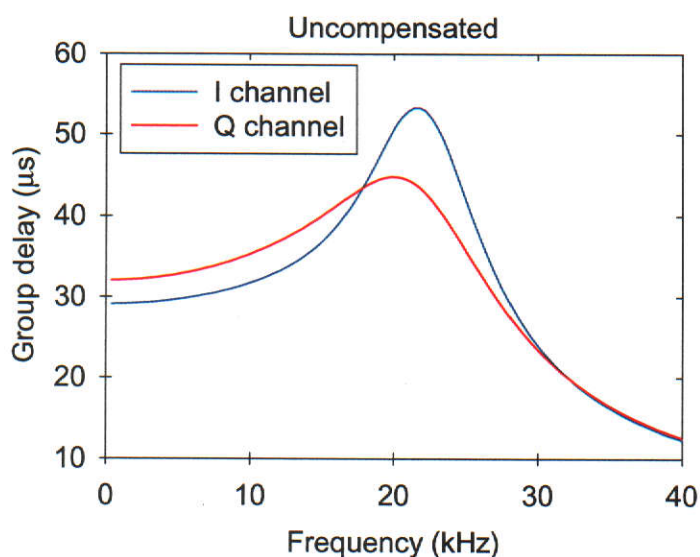
Figure 4.18. I and Q channel group delay responses: **uncompensated system**.
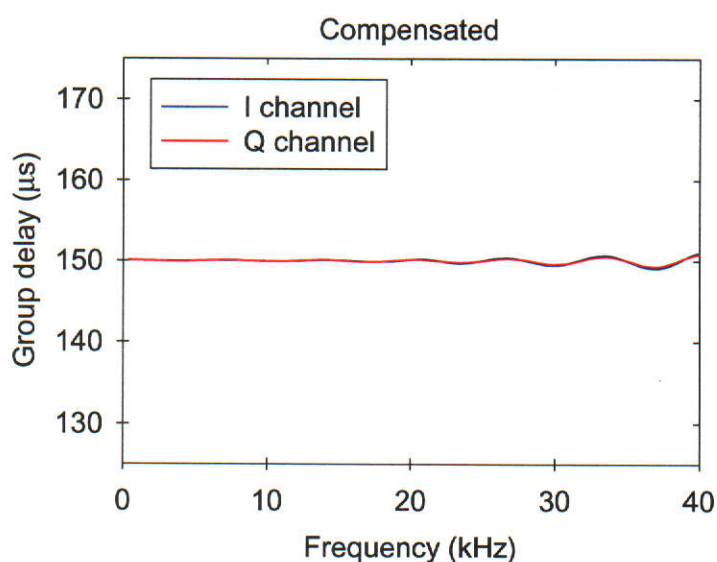
Figure 4.19. Effect of digital compensation on the I and Q channel group delay responses: 50-tap FRI compensation filters.

4.8.4 Desired Channel Response

In this section the significant advantages gained in using the desired channel response proposed in Section 4.4 are highlighted. The quality of compensation obtained using the "same magnitude", linear phase desired channel response proposed in Section 4.4 is compared with that obtained using a brick-wall, linear phase desired response.

The effects are investigated for two FIR compensation filter lengths:

1. 50-taps, and

2. 30-taps.

The "same magnitude", linear phase desired response is given by (4.59) and (4.60) with the optimum desired delay parameter, $\check{\tau}_0$, determined using (4.67) and given by (4.68) for the 50 and 30 tap lengths.

The brick-wall, linear phase response is given by

$$D_{br}\left(e^{j\omega T}\right) = \begin{cases} e^{j\omega\tau_0} & |\omega| \le \omega_c \\ 0 & \omega_c < \omega < \omega_s \end{cases}, \tag{4.69}$$

where

$$\begin{aligned} \omega_c &= 2\pi \times 20 \times 10^3 \\ \omega_s &= 2\pi \times 200 \times 10^3 \end{aligned}. \tag{4.70}$$

The optimum desired channel delay parameters for the two filter lengths are the same as those for the "same magnitude", linear phase desired response.

The optimum I and Q channel FIR compensation filter impulse responses resulting from the optimisation problems using the brick-wall, linear phase desired responses are shown in Figure 4.20 and Figure 4.21. (The corresponding impulse responses computed using the "same magnitude", linear phase desired response are shown in Figure 4.11 and Figure 4.12 respectively.)
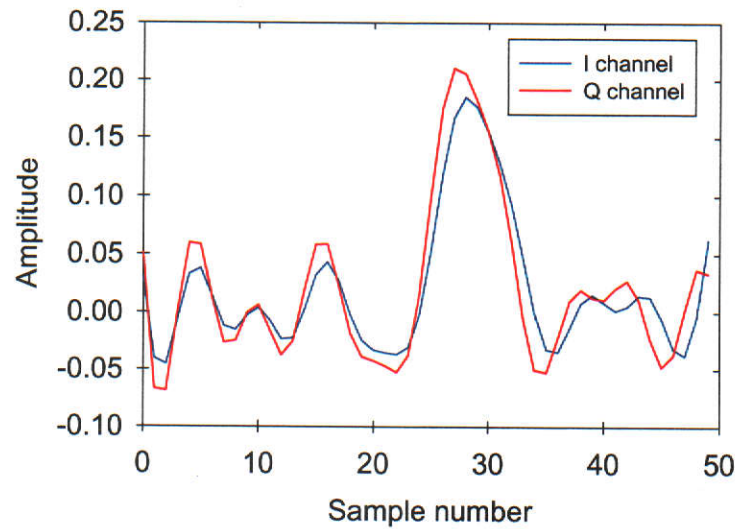
Figure 4.20. Optimum 50-tap I and Q channel compensation filters: brick-wall, linear phase desired response.
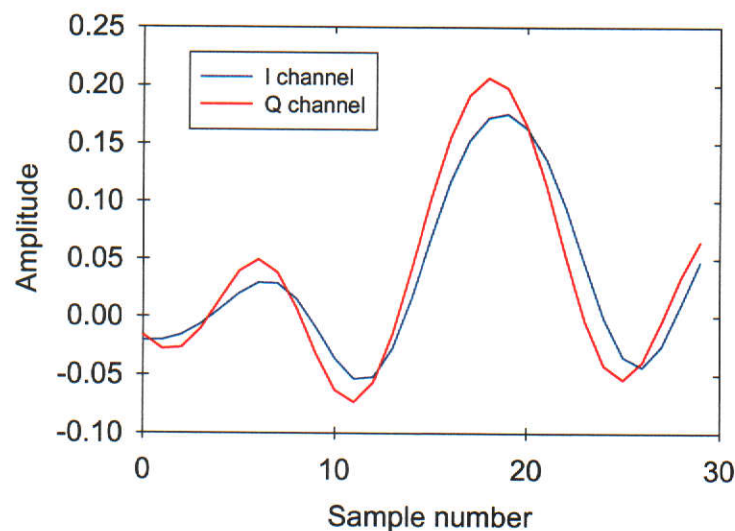
Figure 4.21. Optimum 30-tap I and Q channel compensation filters: brick-wall, linear phase desired response.

The envelope functions of the vector modulator output signals produced by the digital modulator with the optimum 50 and 30-tap FIR filters shown in Figure 4.20 and Figure 4.21 in place are shown in Figure 4.22 and Figure 4.23 respectively (lower plots). Also shown for reference are the envelope functions for the uncompensated system (upper plots) and for the modulator compensated using the "same magnitude", linear phase desired channel responses.
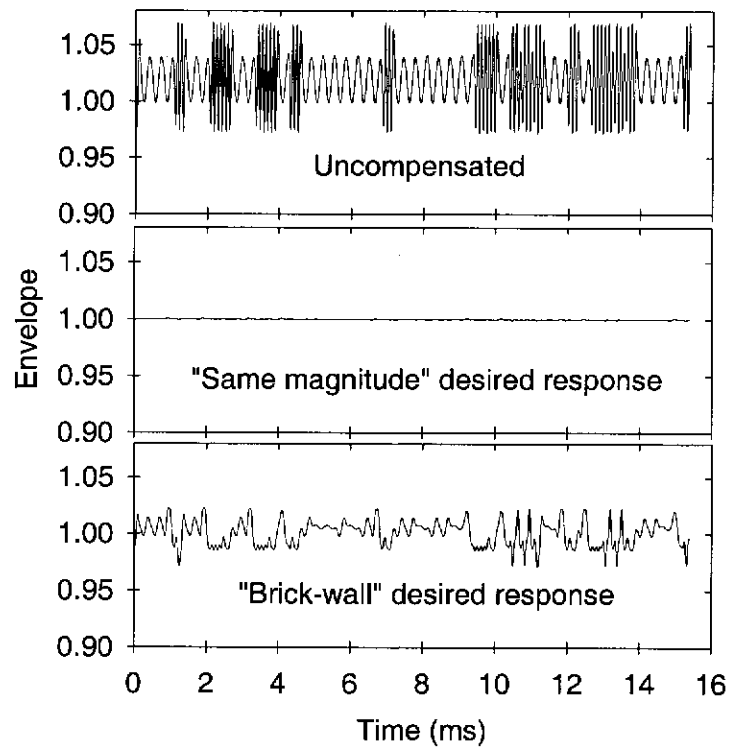
Figure 4.22. Vector modulator output signal envelope: 50-tap FIR compensation filters.
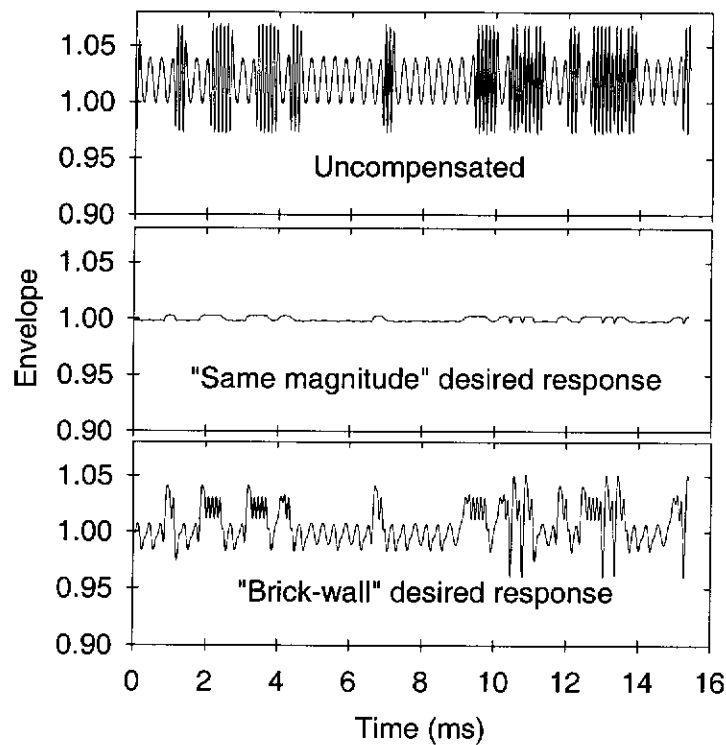
Figure 4.23. Vector modulator output signal envelope: 30-tap FIR compensation filters.

The RMS values of the envelope ripple in Figure 4.22 and Figure 4.23 are summarised in Table 4.3

		RMS ripple (mV)	Reduction Factor
50-Taps	Uncompensated	2.88	1
	"same magnitude", linear phase	0.032	90
	Brick-wall, linear phase	1.353	2.1
30-Taps	Uncompensated	2.88	1
	"same magnitude", linear phase	0.247	12
	Brick-wall, linear phase	2.096	1.4

Table 4.3. RMS envelope ripple and ripple reduction factors for different desired channel responses and different FIR compensation filter lengths.

From the results presented in this section it is clear that the proposed "same magnitude", linear phase desired channel response that only compensates for critical channel characteristics offers significant advantages over a response that attempts to compensate for additional non-critical channel characteristics.

4.8.5 Eigenvalue Decomposition

In Section 4.6 an algorithm based on the eigenvalue decomposition of the I and Q channel matrices R_i and R_q was developed to improve the robustness of the I and Q channel tap-weight solution vectors to coefficient errors and finite numerical precision effects in the DSP platform. In this section the algorithm, which is summarised in Table 4.1, is investigated in terms of its effect on the quality of compensation achieved.

In the example presented here a computer model of the IQ modulator shown in Figure 4.1 with ERMES signal parameters is again used and a digital FIR compensation filter length of 50 taps is assumed.

Figure 4.24 shows the 50 eigenvalues of the R matrix for one of the channels (I or Q) in decreasing order of magnitude. Note that the eigenvalues of R closely correspond to 50 equally spaced points along the squared magnitude response of the actual

discrete-time equivalent channel which is also plotted in this figure. This is in line with the theoretical findings of Section 4.5.2.
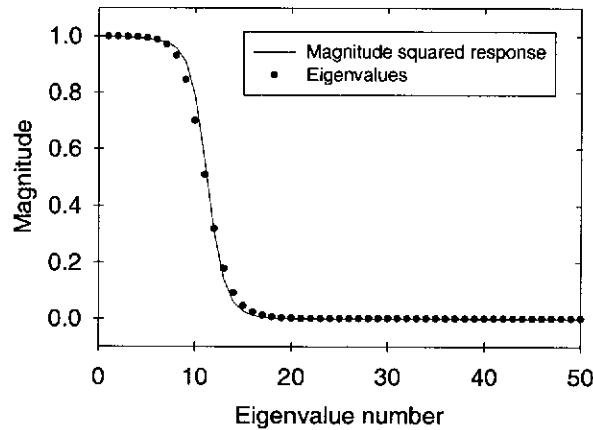
Figure 4.24. Ordered eigenvalues of the R matrix.

A critical factor in implementing the algorithm in Table 4.1 is the choice of the parameters N_i and N_q. These parameters determine, for each channel, the number of the smallest eigenvalues that are discarded before computing the minimum norm solutions in step 4 of the algorithm. As discussed in Section 4.7, the choice of N_i and N_q involve a trade-off between

A. **Higher cost,** $J(g)$, and hence unacceptable degradation in the quality of compensation, and

B. **Poorer conditioning,** characterised by sensitivity of the solution vectors to coefficient errors and finite numerical effects in the chosen DSP platform.

Figure 4.25 shows the I and Q channel cost functions, $J_{N_i}(g)$ and $J_{N_q}(g)$, as N_i and N_q are decreased (i.e., as more of the smallest eigenvalues are discarded from the solutions).
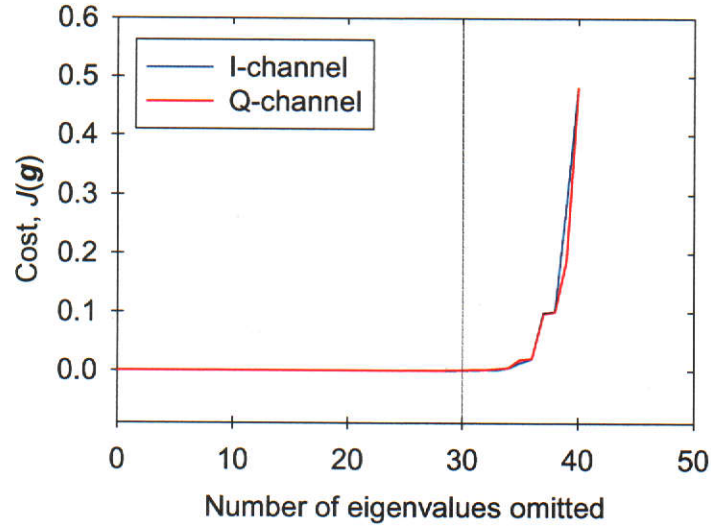
Figure 4.25. I and Q channel cost as the number of the smallest eigenvalues that are discarded from the solution is increased.

From Figure 4.25 it can be seen that the I and Q channel costs start to increase appreciably when more than about 30 of the smallest eigenvalues are discarded.

An indication of the condition of the I and Q channel problems is given by the P-condition numbers of the sub-matrices, $\boldsymbol{\Sigma}_{N_i}$ and $\boldsymbol{\Sigma}_{N_q}$ defined by (4.47). The P-condition numbers of these two matrices are shown plotted in Figure 4.26.
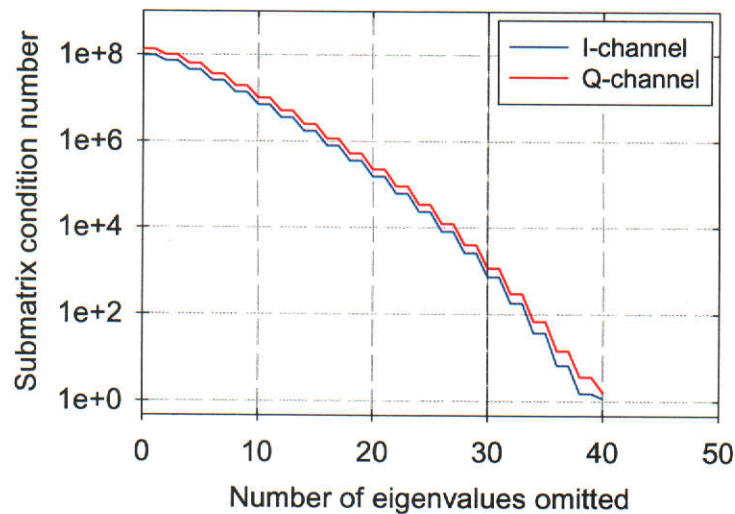
Figure 4.26. P-condition number of the I and Q channel matrices $\boldsymbol{\Sigma}_{N_i}$ and $\boldsymbol{\Sigma}_{N_q}$.

From Figure 4.25 and Figure 4.26 the value

$$N_i = N_q = 20 \qquad (4.71)$$

is chosen. This value is indicated on the two figures by the dashed vertical line and corresponds to I and Q channel P-condition numbers of the order of 1×10^3 which are acceptable for a 32-bit single precision floating point environment that is readily available on many commercial DSP platforms. From Figure 4.25 it can be seen that the I and Q channel costs are not significantly increased by discarding the 30 smallest eigenvalues.

Using the algorithm summarised in Table 4.1, the digital compensation FIR filter tap-weights are calculated giving the FIR filter impulse responses shown in Figure 4.27. (Again the samples are joined by straight lines to aid visual comparison of the impulse responses.)
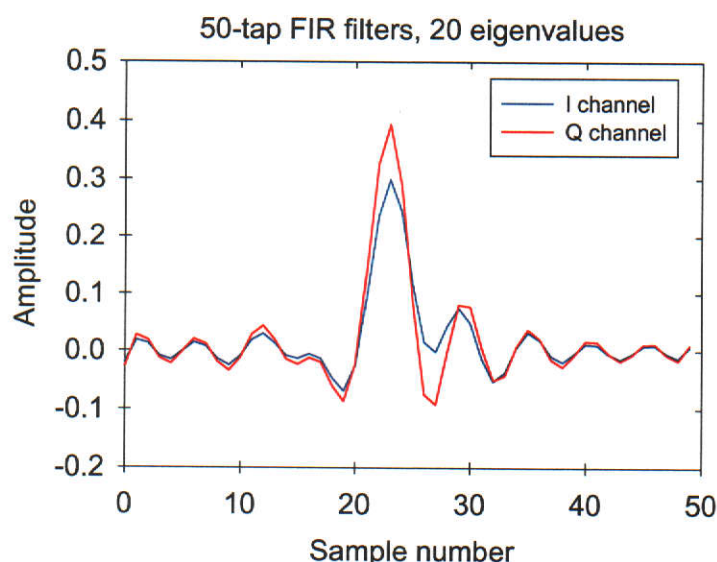
Figure 4.27. Impulse responses of the I and Q channel 50-tap FIR compensation filters computed using 20 eigenvalues.

With the I and Q channel FIR filters in Figure 4.27 present in the IQ modulator system, the envelope function produced when the test input sequence is applied to the system is shown in Figure 4.28. For reference the envelope function produced by the uncompensated modulator is also shown.
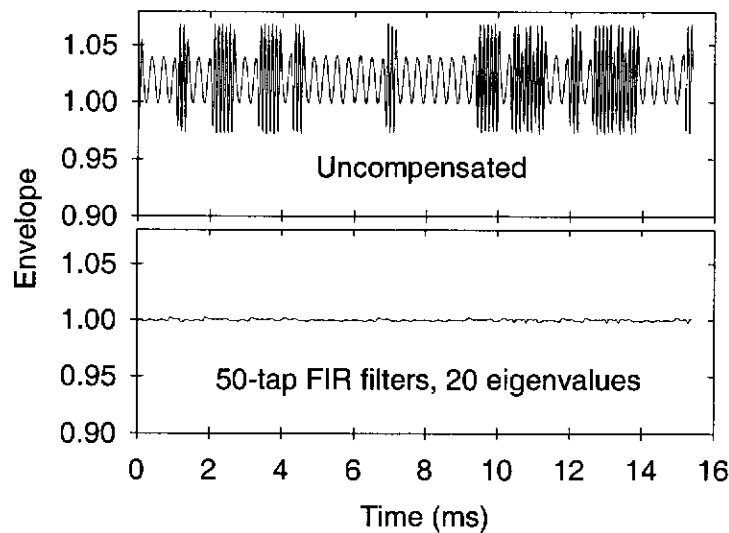
Figure 4.28. Envelope functions of the vector modulator output signal.

Upper plot: uncompensated system

Lower plot: 50-tap FIR compensation filters computed using 20

eigenvalues.

From the envelope plots in Figure 4.28 it can be seen that the quality of digital compensation is not significantly degraded with the use of the sub-space approach summarised in the algorithm in Table 4.1. Use of this approach, therefore has allowed improvements in the condition of the I and Q channel optimisation problems by approximately five orders of magnitude while maintaining a high quality of channel compensation.

As will be seen in subsequent chapters, this is a critical factor in successfully implementing these techniques on a DSP system.

4.9 Conclusion

In this chapter it has been shown that ripple in vector modulator output envelope caused by the reconstruction filters can be substantially reduced by introducing digital compensation FIR filters into the I and Q channels optimised according to a least squares optimality criterion.

A significant contribution of this chapter is the approach taken to digital compensation through the choice of the desired channel response. Specifically, it has been shown that compensating for deviations from constant group delay *only*, in each

of the channels and for group delay and magnitude imbalance between the channels provides effective reduction of ripple in the envelope function.

Another important contribution of this chapter is the formulation of an optimisation problem in the digital FIR compensation filter tap-weights and the characterisation of the solution. This has allowed establishment of a numerical framework for implementing the digital compensation technique on a DSP platform by identifying a method for finding a stable solution in a finite numerical precision environment.

Chapter 5. Automatic Digital Compensation

5.1 Introduction

The optimum digital compensation scheme developed in Chapter 4 was shown to significantly reduce AM present in the envelope function of the vector modulator output signal. Determining the optimum tap-weights of the two digital FIR compensation filters, however, requires knowledge of the frequency or time domain parameters of the I and Q channel analogue reconstruction filters.

The work presented in this chapter is motivated by two key issues concerning the I and Q channel reconstruction filters:

1. Different realisations of the same nominal filter circuit will have different errors and hence different filter characteristics due to manufacturing tolerances.

2. The characteristics of the two filters change with time (for example due to temperature fluctuations or component aging).

The focus of this chapter is the development of channel parameter identification techniques that can be used to establish initial estimates of the optimum digital compensation filters and to periodically update the estimates to reflect changes in the I and Q channel characteristics. Ideally the I and Q channel compensation filters would be *adapted* on a continuous basis using real modulator input data, however this remains a challenging problem because it is difficult to achieve the tight constraints on adjacent channel power in a continuous adaptive scheme.

The problem addressed in this chapter is essentially one of estimating the parameters of the optimisation problem (the matrices and vectors outlined in Chapter 4) with sufficient accuracy that the resulting digital compensation filters are effective in reducing AM in the envelope of the vector modulator output signal.

Two methods are proposed to identify the required parameters. One is for the time domain, the other for the frequency domain parameters of the I and Q channels.

The key contributions of this chapter are

- A frequency domain algorithm for automatic digital compensation that is shown to work effectively in reducing AM in the envelope function of the vector modulator output signal.

- A time domain algorithm for automatic digital compensation that is also shown to work effectively in reducing AM in the envelope function of the vector modulator output signal.

- A characterisation of the effects of quantisation and system noise on the effectiveness of the frequency and time domain methods in an implementation of the techniques.

This chapter is organised into seven sections. In the next section, two parameter estimation problems are defined: one based on the frequency domain formulation of the optimisation problem and one based on the time domain formulation. The definition of the frequency domain estimation problem motivates the frequency domain channel identification technique proposed in Section 5.3, while the time domain estimation problem motivates the time domain technique proposed in Section 5.4. The effects of quantisation on the frequency and time domain methods are investigated from a theoretical standpoint in Section 5.5 and in Section 5.6 the effects of quantisation and additive system noise on the two techniques are characterised using computer simulations. The simulation results presented in Section 5.6 highlight the effectiveness of both methods in providing compensation under both practical and extreme conditions. Section 5.7 contains conclusions from the work presented in this chapter.

5.2 Estimation Problem

The algorithm for determining the optimum sets of I and Q channel digital FIR compensation filter tap-weights is summarised in Table 4.1. From the algorithm summary it can be seen that two quantities need to be determined for each channel before the compensation filter tap-weights can be found:

1. The matrices R_i and R_q.

2. The vectors p_i and p_q.

It was shown in Chapter 4 that the matrices R_i and R_q and the vectors p_i and p_q could be formulated equivalently in terms of their corresponding channels' frequency or time domain parameters. The frequency-domain formulations are given by (4.13) and (4.14), while the time-domain formulations are given by (4.26) and (4.27).

Frequency domain:

From (4.13) and (4.14) the I and Q channel R matrices and p vectors are given by integrals over a frequency range. One approach for estimating R and p for each channel is to approximate the integrals with summations by discretising the frequency interval into enough frequency points that the summations closely approximate the integrals. An alternative approach is to formulate a discrete-frequency version of the optimisation problem as follows.

The cost function for the new discrete-frequency version of the optimisation problem is defined, in terms of the generic optimisation structure in Figure 4.3, as

$$\tilde{J}(g) = \sum_{k=1}^{N}\left| D\!\left(e^{j\omega_k T}\right) - g^T s\!\left(e^{j\omega_k T}\right) H'\!\left(e^{j\omega_k T}\right)\right|^2 \tag{5.1}$$

Using the same approach of Section 4.3, the vector, $\hat{g}$, that minimises the cost function in (5.1) is given by

$$\tilde{R}\hat{g} = \tilde{p} \tag{5.2}$$

where
$$\tilde{R} = \sum_{k=1}^{N} \left(s_R \left(e^{j\omega_k T} \right) s_R^T \left(e^{j\omega_k T} \right) + s_I \left(e^{j\omega_k T} \right) s_I^T \left(e^{j\omega_k T} \right) \right) \left| H' \left(e^{j\omega_k T} \right) \right|^2 \qquad (5.3)$$

and
$$\tilde{p} = \sum_{k=1}^{N} s_R \left(e^{j\omega_k T} \right) \left(D_R \left(e^{j\omega_k T} \right) H_R \left(e^{j\omega_k T} \right) + D_I \left(e^{j\omega_k T} \right) H_I \left(e^{j\omega_k T} \right) \right) \\ + \sum_{k=1}^{N} s_I \left(e^{j\omega_k T} \right) \left(D_I \left(e^{j\omega_k T} \right) H_R \left(e^{j\omega_k T} \right) - D_R \left(e^{j\omega_k T} \right) H_I \left(e^{j\omega_k T} \right) \right) \qquad (5.4)$$

Note that the quantities $\left\{ s_R \left(e^{j\omega T} \right), s_I \left(e^{j\omega T} \right) \right\} \in \mathbb{R}^{K \times 1}$ and $\left\{ D_R \left(e^{j\omega T} \right), D_I \left(e^{j\omega T} \right) \right\} \in \mathbb{R}$, which are defined in (4.15), are known *a priori*.

Recall from Section 4.3 that $H' \left(e^{j\omega T} \right)$ is the transfer function of the discrete-time system formed by the D/A converter, analogue low-pass reconstruction filter and A/D converter for the generic optimisation problem. From (4.15) the quantities $\left\{ H_R \left(e^{j\omega T} \right), H_I \left(e^{j\omega T} \right) \right\} \in \mathbb{R}$ are defined in terms of the generic optimisation problem to be

$$H_R \left(e^{j\omega T} \right) = \mathrm{Re} \left[H' \left(e^{j\omega T} \right) \right] \\ H_I \left(e^{j\omega T} \right) = \mathrm{Im} \left[H' \left(e^{j\omega T} \right) \right] \qquad (5.5)$$

In practice the I and Q channel reconstruction filters will be different in general and the matrix $\tilde{R}$ and vector $\tilde{p}$ given by (5.3) and (5.4) will need to be estimated for each channel using the substitutions

$$H' \left(e^{j\omega T} \right) = \begin{cases} H_i' \left(e^{j\omega T} \right) & \text{I channel optimisation} \\ H_q' \left(e^{j\omega T} \right) & \text{Q channel optimisation} \end{cases} \qquad (5.6)$$

$$H_R' \left(e^{j\omega T} \right) = \begin{cases} \mathrm{Re} \left[H_i' \left(e^{j\omega T} \right) \right] & \text{I channel optimisation} \\ \mathrm{Re} \left[H_q' \left(e^{j\omega T} \right) \right] & \text{Q channel optimisation} \end{cases} , \qquad (5.7)$$

and
$$H_I' \left(e^{j\omega T} \right) = \begin{cases} \mathrm{Im} \left[H_i' \left(e^{j\omega T} \right) \right] & \text{I channel optimisation} \\ \mathrm{Im} \left[H_q' \left(e^{j\omega T} \right) \right] & \text{Q channel optimisation} \end{cases} . \qquad (5.8)$$

Since the transfer functions of the I and Q discrete-time channels, $H_i'\left(e^{j\omega T}\right)$ and $H_q'\left(e^{j\omega T}\right)$ respectively, are not known *a priori* they must be measured before the algorithm in Table 4.1 can be used to compute the digital compensation filter tap-weights.

The frequency-domain estimation problem can therefore be stated as follows:

- Find estimates of the required matrices, $\tilde{R}_i$ and $\tilde{R}_q$, and the vectors, $\tilde{p}_i$ and $\tilde{p}_q$ by making N measurements of the I and Q channel transfer functions, $\left\{H_i'\left(e^{j\omega_k T}\right), H_q'\left(e^{j\omega_k T}\right)\right\}; k = 1, 2, \ldots, N$. The estimates of $\tilde{R}_i, \tilde{R}_q, \tilde{p}_i$ and $\tilde{p}_q$ must be sufficiently accurate to allow the calculation of digital compensation filters that provide effective reduction in the envelope ripple of the vector modulator output signal.

Time domain:

From (4.27) the R matrix for each channel is constructed from segments of the auto-correlation sequence of the channels' discrete-time impulse response, $h'(nT)$. From (4.26) the p vector for each channel is a segment of the cross-correlation between the desired channel impulse response, $d(nT)$, and the actual channel impulse response, $h'(nT)$.

Since $d(nT)$ is known *a priori* the time-domain estimation problem can be stated as follows:

- Find estimates of the required matrices, R_i and R_q, and the vectors, p_i and p_q, by making measurements of the I and Q channel impulse responses, $h_i'(nT)$ and $h_q'(nT)$. The estimates of R_i, R_q, p_i and p_q must be sufficiently accurate to allow the calculation of digital compensation filters that provide effective reduction in the envelope ripple of the vector modulator output signal.

5.3 Frequency Domain Approach

In this section a method for measuring the discrete-time transfer functions of the I and Q channels, $H_i'\left(e^{j\omega T}\right)$ and $H_q'\left(e^{j\omega T}\right)$, is proposed. The method involves the use of a set of sinusoidal test input signals and a least-squares fitting of a sinusoidal function to the output signal of the channel under test. A model for the generic channel is given in Figure 5.1 below.
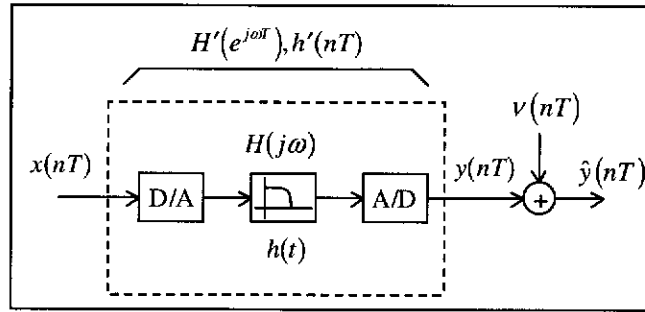
Figure 5.1. Model of the generic channel.

The channel model in Figure 5.1 is similar to that of Figure 4.4 with the inclusion here of the additive noise source $v\left(nT\right)$.

It is assumed that the additive noise, $v\left(nT\right)$, is made up of two components:

1. equivalent quantisation noise, $v_Q\left(nT\right)$, and

2. other additive system noise, $v_s\left(nT\right)$.

Hence, it is assumed that $v\left(nT\right)$ is given by

$$v\left(nT\right) = v_s\left(nT\right) + v_Q\left(nT\right). \tag{5.9}$$

From (5.3) and (5.4) the matrix $\tilde{R}$ and vector $\tilde{p}$ (for each channel) are calculated using N measurements of the channel transfer function, $\left\{H'\left(e^{j\omega_k T}\right)\right\}; k = 1, 2, \ldots, N$ where the number, N, and distribution of the frequency points, $\left\{\omega_k\right\}; k = 1, 2, \ldots, N$, is yet to be determined.

In practice the number of points, N, is determined by how effective the solution to the optimisation problem in (5.1) is in reducing ripple in the envelope of the vector modulator output signal (and hence in reducing adjacent channel power in the transmitter output signal).

Note, however, that a sufficient condition on the number of frequency points for $\tilde{R}$ to be full rank can be derived (see Appendix C) and is given by:

$$N = K \tag{5.10}$$

where:

(1) The N frequency points $\{\omega_k\}$; $k = 1, 2, \ldots, N$ are distinct.

(2) The difference between any pair of frequency points must not be an integer multiple of the sampling frequency, i.e.,

$$\begin{array}{c} \omega_m - \omega_n \neq l\omega_s \\ l = \pm 1, \pm 2, \ldots \\ N \geq m > n \geq 1 \end{array} \tag{5.11}$$

(3) The function $H'\left(e^{j\omega_k T}\right)$ is non-zero at the frequency points $\{\omega_k\}$; $k = 1, 2, \ldots, N$.

In Appendix C it is shown that if a particular uniform distribution of frequency sample points is chosen then a full-rank $\tilde{R}$ matrix can be constructed using

$$N = \frac{K}{2} + 1 \tag{5.12}$$

frequency sample points (K even). It is also shown in Appendix C that $\tilde{R}$ does not have full rank if

$$N < \frac{K}{2}. \tag{5.13}$$

It has been found empirically that under certain conditions $\tilde{R}$ can have full rank if $N = K/2$ (K even). However, for the FIR filter lengths of practical interest here the value $N = K/2$ results in a solution to the optimisation problem that does not adequately reduce envelope ripple in the vector modulator output signal and is of no practical use in this application.

One method for measuring the set of points $\left\{ H'\left(e^{j\omega_k T}\right)\right\}; k = 1, 2, \ldots, N$ is to apply N sinusoids to the channel under test one at a time and, after allowing initial transients to subside, measure the magnitude and phase of the output [83-86].

Let the nth input signal to the system in Figure 5.1, $x(nT)$, be discrete-time samples of a sinusoid of amplitude, $\rho > 0$, and frequency ω_k, i.e.,

$$x_k(nT) = \rho \sin(\omega_k nT),$$
$$k = 1, 2, \ldots, N. \tag{5.14}$$

After waiting for initial transients to subside, the discrete-time output, $\hat{y}_k(nT)$, of the system in Figure 5.1 for the kth input sinusoid is given by

$$\hat{y}_k(nT) = A_k \rho \sin(\omega_k nT + \phi_k) + v_k(nT)$$
$$= A_k \rho \cos \phi_k \sin(\omega_k nT) + A_k \rho \sin \phi_k \cos(\omega_k nT) + v_k(nT), \tag{5.15}$$

where $A_k \geq 0$ is the magnitude and ϕ_k is the phase of the frequency response of the system at the radian frequency ω_k.

The notation $v_k(nT)$ represents the total noise present in the output signal for the kth input sinusoidal test signal.

The function $\zeta_k(nT)$ given by

$$\zeta_k(nT) = \breve{A}_k \sin(\omega_k nT + \breve{\phi}_k)$$
$$= \breve{A}_k \cos(\breve{\phi}_k)\sin(\omega_k nT) + \breve{A}_k \sin(\breve{\phi}_k)\cos(\omega_k nT), \tag{5.16}$$

is fitted to the measured output data, $\hat{y}(nT)$, by finding the parameters $\breve{A}_k$ and $\breve{\phi}_k$ such that the difference between $\hat{y}_k(nT)$ and $\zeta_k(nT)$ is minimised in the least-squares sense.

Let

$$\alpha_k = \breve{A}_k \cos\left(\breve{\phi}_k\right)$$
$$\text{and}$$
$$\beta_k = \breve{A}_k \sin\left(\breve{\phi}_k\right)$$
$$k = 1, 2, \ldots, N.$$

(5.17)

The cost function, $J\left(\alpha_k, \beta_k\right)$, is defined as

$$
\begin{aligned}
J\left(\alpha_k, \beta_k\right) &= \frac{1}{L - l_0} \sum_{n=l_0}^{L} \left(\hat{y}_k(nT) - \zeta_k(nT)\right)^2 \\
&= \frac{1}{L - l_0} \sum_{n=l_0}^{L} \left(\hat{y}(nT) - \alpha_k \sin\left(\omega_k nT\right) - \beta_k \cos\left(\omega_k nT\right)\right)^2, \\
k &= 1, 2, \ldots, N.
\end{aligned}
$$

(5.18)

(Note in (5.18) that the lower limit of the summation, l_0, is chosen such that the initial condition transients are sufficiently small.)

The $2N$ parameters α_k and β_k are chosen to minimise $J(\alpha_k, \beta_k)$, that is,

$$\min_{\alpha_k, \beta_k}\left[J\left(\alpha_k, \beta_k\right)\right], k = 1, 2, \ldots, N.$$

(5.19)

Closed-form expressions for the optimum values, $\breve{\alpha}_k$ and $\breve{\beta}_k$, that minimise $J\left(\alpha_k, \beta_k\right)$ in (5.18) are derived using standard optimisation theory in Appendix D.

With the values $\breve{\alpha}_k$ and $\breve{\beta}_k$ thus determined, the estimated magnitude, $\breve{A}_k$, and phase, $\breve{\phi}_k$, of the kth output signal are found from (5.17) and the $2N$ estimates, $\left\{\breve{A}_k, \breve{\phi}_k\right\}; k = 1, 2, \ldots, N$ give the required N estimates of the complex transfer function $\left\{H'\left(e^{j\omega_k T}\right)\right\}; k = 1, 2, \ldots, N$.

The length L of the summations in (5.18) is determined by the characteristics of the noise, $v_k(nT)$, and the accuracy required in the estimates of the magnitude, A_k, and phase, ϕ_k. In Appendix D it is shown that $\breve{\alpha}_k$ and $\breve{\beta}_k$ can be expressed as

$$\breve{\alpha}_k = A_k \rho \cos(\phi_k) + \varepsilon_{\alpha,k} \tag{5.20}$$

and

$$\breve{\beta}_k = A_k \rho \cos(\phi_k) + \varepsilon_{\beta,k} \tag{5.21}$$

where

$$\varepsilon_{\alpha,k} = \Gamma_k \left(C_k \sum_{n=l_0}^{L} v_k(nT)\sin(\omega_k nT) - B_k \sum_{n=l_0}^{L} v_k(nT)\cos(\omega_k nT) \right) \tag{5.22}$$

and

$$\varepsilon_{\beta,k} = \Gamma_k \left(S_k \sum_{n=l_0}^{L} v_k(nT)\cos(\omega_k nT) - B_k \sum_{n=l_0}^{L} v_k(nT)\sin(\omega_k nT) \right). \tag{5.23}$$

For the kth input test signal the parameters Γ_k, C_k, S_k and B_k are constants and are defined in Appendix D.

If the additive noise, $v_k(nT)$, is a zero-mean stochastic signal then

$$E\left[v_k(nT)\right] = 0 \tag{5.24}$$

and in Appendix D it is shown that the expected values of the parameter estimates $\breve{\alpha}_k$ and $\breve{\beta}_k$ in (5.20) and (5.21) are given by

$$E\left[\breve{\alpha}_k\right] = A_k \rho \cos(\phi_k), \tag{5.25}$$

and

$$E\left[\breve{\beta}_k\right] = A_k \rho \sin(\phi_k), \tag{5.26}$$

i.e., the estimators $\breve{\alpha}_k$ and $\breve{\beta}_k$ are unbiased.

If the additive noise, $v_k(nT)$, is white with variance $\sigma_{v_k}^2$ then it is also shown in Appendix D that

$$\text{var}\left[\breve{\alpha}_k\right] = \Gamma_k^2 \sigma_{v_k}^2 \sum_{n=l_0}^{L} \left(C_k \sin\left(\omega_k nT\right) - B_k \cos\left(\omega_k nT\right)\right)^2 \tag{5.27}$$

and
$$\text{var}\left[\breve{\beta}_k\right] = \Gamma_k^2 \sigma_{v_k}^2 \sum_{n=l_0}^{L} \left(S_k \cos\left(\omega_k nT\right) - B_k \sin\left(\omega_k nT\right)\right)^2 . \tag{5.28}$$

Since the quantities Γ_k, S_k, C_k and B_k are all functions of L, the expressions in (5.27) and (5.28) do not give a clear indication of how the variance in the estimates $\breve{\alpha}_k$ and $\breve{\beta}_k$ changes with increasing L. Figure 5.2 shows the variance in the parameter estimates, $\breve{\alpha}_k$ and $\breve{\beta}_k$, for three separate sinusoids in noise as the sample length L is increased. The results were determined numerically with the following parameters:

- Sinusoid frequencies = 10 kHz, 30 kHz and 70 kHz
- Sinusoid amplitude = 1 volt
- Digital system sampling frequency = 200 kHz
- Additive noise: Gaussian distributed white noise with variance = -20 dB (relative to the square of the sinusoid amplitude)

These parameters represent typical operating conditions for the ERMES system example considered in Section 5.6. The three sinusoidal frequencies represent low, mid and high frequency regions in the I and Q channel frequency response characteristics.
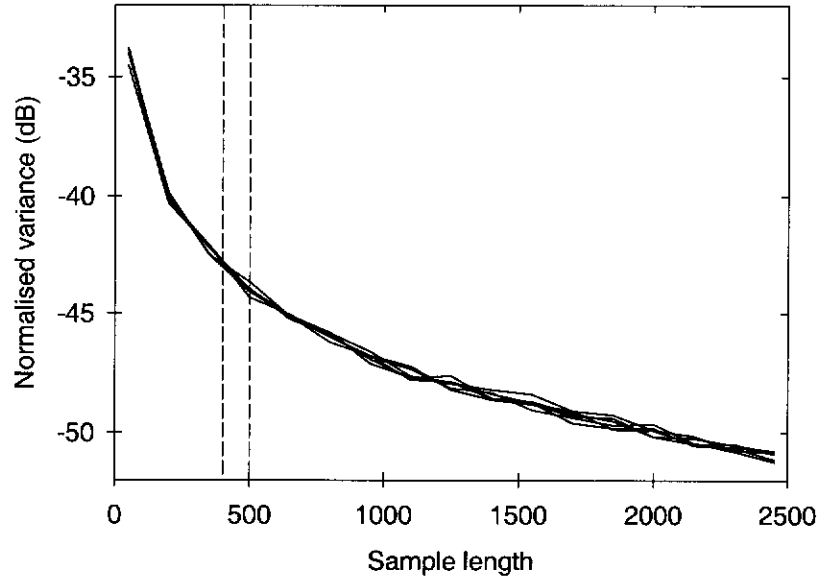

Figure 5.2. Normalised variance in the parameters $\breve{\alpha}_k$ and $\breve{\beta}_k$ as the

sample length is increased.

Note that the *normalised variance* shown in Figure 5.2 is calculated as follows

$$
\begin{aligned}
\text{var}_{norm}\left[\breve{\alpha}_k\right] &= 10 \log_{10}\left[\frac{\text{var}\left[\breve{\alpha}_k\right]}{\tilde{\alpha}_k^2 + \tilde{\beta}_k^2}\right] \\
\text{var}_{norm}\left[\breve{\beta}_k\right] &= 10 \log_{10}\left[\frac{\text{var}\left[\breve{\beta}_k\right]}{\tilde{\alpha}_k^2 + \tilde{\beta}_k^2}\right].
\end{aligned}
\tag{5.29}
$$

where $\left\{\tilde{\alpha}_k\right\}, \left\{\tilde{\beta}_k\right\}; k = 1, 2, 3$ are the exact parameter values corresponding to the

three test sinusoids listed above.

From Figure 5.2 it can be seen that the variance decreases rapidly initially as the sample length is increased. Note also that there is no significant difference in the variance characteristics for the three frequencies considered. Typical sample lengths (for each sinusoidal test frequency) that are considered in Section 5.6 range between 400 and 500 (shown by the vertical dashed lines in Figure 5.2)

The algorithm for estimating the I and Q channel parameters R_i, R_q, p_i and p_q based on the frequency domain approach using sinusoidal test signals is summarised in the following table.

---

1. Apply N sinusoids consecutively to the inputs the I and Q channels and compute the parameters

$$\left\{ \breve{\alpha}_k^i, \breve{\alpha}_k^q, \breve{\beta}_k^i, \breve{\beta}_k^q \right\}; k = 1, 2, \ldots, N$$

from measurements of the output signals, $\left\{ \hat{y}_k^i(nT), \hat{y}_k^q(nT) \right\}; k = 1, 2, \ldots, N$ and the formulas given in Appendix D.

2. Calculate estimates of the I and Q channel magnitude and phase responses,

$$\left\{ \breve{H}_i\left(e^{j\omega_k T}\right) = \breve{A}_k^i e^{j\phi_k^i} \right\}; k = 1, 2, \ldots, N,$$

and

$$\left\{ \breve{H}_q\left(e^{j\omega_k T}\right) = \breve{A}_k^q e^{j\phi_k^q} \right\}; k = 1, 2, \ldots, N,$$

at the N frequency points using the formulas given in Appendix D.

3. From, (5.3) and (5.4) construct the estimated matrices and vectors

$$\hat{R}_i, \hat{R}_q$$

and

$$\hat{p}_i, \hat{p}_q$$

required for the computation of the I and Q channel optimum FIR compensation filters, $\breve{g}_i$ and $\breve{g}_q$ according to the algorithm in Table 4.1.

Table 5.1. Frequency domain estimation algorithm.

5.4 Time Domain Approach

In this section a technique based on the time domain formulation in Section 4.5.1 for estimating the required matrices and vectors is proposed.

The technique described in the following two sections uses cross-correlation and pseudo-random noise test signals to identify the impulse responses of the I and Q channels and is well known in system identification [83-86, 87-90].

5.4.1 Cross-correlation

Consider the system in Figure 5.3. The components shown in the dotted rectangle are the D/A converter, analogue low-pass filter and A/D converter of the channel under test.
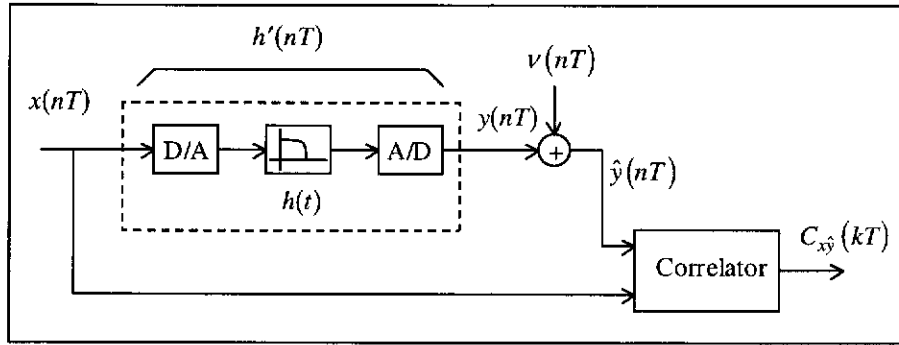

Figure 5.3. System identification using cross-correlation.

As in Section 5.3, the term $v(nT)$ accounts for additive equivalent quantisation noise and other additive system noise in the output signal $\hat{y}(nT)$, and is given by (5.9).

Estimates of the discrete-time impulse responses for the I and Q channels, $h_i'(nT)$ and $h_q'(nT)$, are required so that the quantities R_i, R_q, p_i and p_q given in Section 4.5.1 by (4.26) and (4.27) can be determined.

It is assumed that the impulse responses, $h_i'(nT)$ and $h_q'(nT)$, are negligibly small outside a finite range of samples and therefore the quantities R_i, R_q, p_i and p_q

given by infinite summations in (4.26) and (4.27) can be approximated by summations over finite ranges, N_i and N_q. For the generic time-domain optimisation, the R matrix and p vector are approximated as follows

$$\left[\hat{R}\right]_{k,l} = \sum_{n=0}^{N-|k-l|-1} h'(nT)h'\left((n+|k-l|)T\right),$$

$$k = 1, 2, \ldots, K,$$

(5.30)

and

$$\left[\hat{p}\right]_{k} = \sum_{n=k-1}^{N+k-2} d(nT)h'\left((n-k+1)T\right),$$

$$k = 1, 2, \ldots, K.$$

(5.31)

The signal $\hat{y}(nT)$ in Figure 5.3 is given by

$$\hat{y}(nT) = x(nT) * h'(nT) + v(nT)$$

$$= \sum_{m=-\infty}^{\infty} h'(mT)x\left((n-m)T\right) + v(nT).$$

(5.32)

The correlator shown in Figure 5.3 produces an estimate of the cross-correlation between the input, $x(nT)$, and the output, $\hat{y}(nT)$. An unbiased estimator of the correlation function is given by [91, 92]

$$C_{x\hat{y}}(kT) = \frac{1}{L_0 - k} \sum_{l=0}^{L_0-k-1} x(lT)\,\hat{y}\left((l+k)T\right).$$

(5.33)

It can be shown that

$$C_{x\hat{y}}(kT) = h'(kT) * C_{xx}(kT) + C_{xv}(kT),$$

(5.34)

where $C_{xx}(kT)$ is the auto-correlation sequence of $x(nT)$ given by

$$C_{xx}(kT) = \frac{1}{L_0 - k} \sum_{l=0}^{L_0-k-1} x(lT)x\left((l+k)T\right),$$

(5.35)

and where $C_{xv}(kT)$ is the cross-correlation between the input and the noise and is given by

$$C_{xv}(kT) = \frac{1}{L_0 - k} \sum_{l=0}^{L_0-k-1} x(lT)v\big((l+k)T\big). \tag{5.36}$$

Hence, from (5.34) the output of the correlator is the convolution between the impulse response of the discrete-time system, $h'(nT)$, and the auto-correlation function of the input sequence plus a term resulting from noise.

Consider a probing signal, $x(nT)$, with

$$E\big[x(nT)\big] = 0 \tag{5.37}$$

and

$$E\big[x(nT)x\big((n+k)T\big)\big] = A^2\delta(kT), \tag{5.38}$$

where

$$\delta(kT) = \begin{cases} 1 & k = 0 \\ 0 & \text{otherwise} \end{cases}. \tag{5.39}$$

and where $E[\cdot]$ is the expected value.

Taking the expected value of both sides of (5.34) gives

$$E\big[C_{x\hat{y}}(kT)\big] = A^2 h'(kT) + E\big[C_{xv}(kT)\big]. \tag{5.40}$$

Assuming the noise, $v(nT)$, is uncorrelated with the input then

$$E\big[C_{xv}(kT)\big] = 0 \tag{5.41}$$

and (5.40) reduces to

$$E\big[C_{x\hat{y}}(kT)\big] = A^2 h'(kT). \tag{5.42}$$

i.e., the correlator output for an input signal with the characteristics given by (5.37) and (5.38) is an unbiased estimator of the discrete-time impulse response of the channel.

If the additive noise, $v(nT)$, is also white with a variance of σ_v^2 then the variance of the estimator $C_{x\hat{y}}(kT)$ is given by

$$\text{var}\left[C_{x\hat{y}}\left(kT\right)\right] = \frac{A^2 \sigma_v^2}{L_0 - k},$$
(5.43)

i.e., the variance of the of the estimator, $C_{x\hat{y}}\left(kT\right)$, is inversely proportional to the correlation length, L_0. Hence, L_0 can be chosen to ensure that the variance in the estimate of the channel impulse response is below a given value.

In practice, the ideal auto-correlation function given by (5.38) can only be approximated. In the next section a class of signals known as *Pseudo-Random Binary Noise (PRBN)* is investigated. These signals have cross-correlation properties that approximate the ideal function given by (5.38) and are simple and efficient to implement in digital hardware.

5.4.2 PRBN Signals

A test signal with cross-correlation properties that approximate the ideal cross-correlation function given by (5.38) is the *pseudo- noise* signal [68, 87, 90, 93-99]. This is a periodic sequence of discrete values where switching between values takes place only at equispaced time intervals [93, 95].

The dynamic range of the D/A converters imposes limitations on the peak input amplitude of the test signal and a class of pseudonoise signals which have the largest signal-to-noise ratio for a given peak amplitude are *Pseudo-Random Binary Noise (PRBN)* signals [93]. A PRBN signal switches between one of two levels, $\pm A$, only at integer multiples of some interval T.

The autocorrelation function of the piecewise-constant signal, $u(t)$, related to the PRBN sequence $x(nT)$ of amplitude A and period $N_{prbn}T$, is defined for the interval $-N_{prbn}T/2 \le \tau \le N_{prbn}T/2$ as, [68]

$$C_{xx}\left(\tau\right) = \begin{cases} A^2\left(1 - \dfrac{N_{prbn}+1}{N_{prbn}T}|\tau|\right), & |\tau| \le T \\ \dfrac{-A^2}{N_{prbn}}, & |\tau| > T. \end{cases}$$
(5.44)

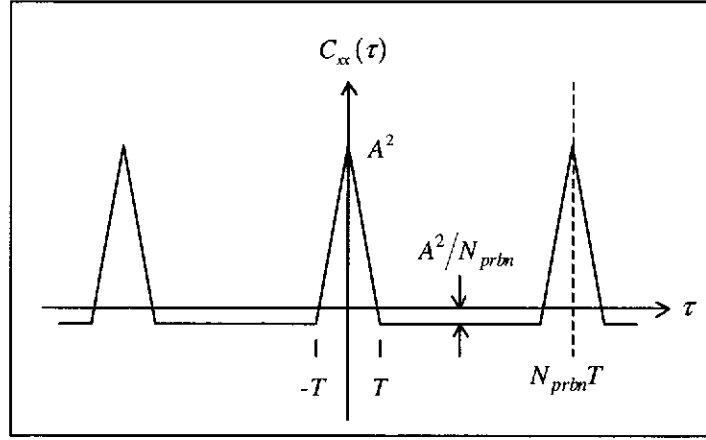The function $C_{xx}(\tau)$ is shown plotted in Figure 5.4.

Figure 5.4. Auto-correlation function of a PRBN signal.

From Figure 5.4 it can be seen that provided the duration, T, of the random pulses is short and the sequence period, N_{prbn}, is large, the auto-correlation function can be made to approximate the ideal auto-correlation function, i.e.,

$$C_{xx}(kT) \cong A^2 \delta(kT).$$
(5.45)

With a PRBN input, $x(nT)$, to the system in Figure 5.3, the output of the correlator given by (5.34) can be written as

$$C_{x\hat{y}}(kT) = h'(kT) * C_{xx}(kT) + C_{xv}(kT)$$
(5.46)

Let

$$\hat{h}(kT) = h'(kT) * C_{xx}(kT),$$
(5.47)

then (5.46) can be rewritten as

$$C_{x\hat{y}}(kT) = \hat{h}(kT)$$
$$\cong A^2 h'(nT).$$
(5.48)

From (5.45) to (5.48) the accuracy of the estimate of the channel impulse response provided at the output of the correlator is influenced by three factors:

1. The characteristics of the auto-correlation function of the PRBN input signal,

2. The characteristics of the additive noise, $v(nT)$, and

3. The correlation length L_0.

Since the auto-correlation function of the PRBN input signal is periodic (see Figure 5.4 and equation (5.44)) with period $N_{prbn}T$, the value N_{prbn} must be chosen such that $N_{prbn}T$ is larger than the duration of the channel impulse response, $h'(nT)$, [89]. For practical channel impulse responses of the IQ modulator considered here, however, this is not the principal consideration in choosing N_{prbn}.

For the application considered here the critical factor in determining N_{prbn} is how closely the autocorrelation function approximates a delta function for lags of the order of the duration of the channel impulse response about the zero-lag point. As can be seen in Figure 5.4 the autocorrelation function has a DC offset that is inversely proportional to the PRBN sequence period. Thus, for larger N_{prbn}, the autocorrelation function more closely approximates the delta function resulting in more accurate estimates of the channel impulse response. In the work presented here N_{prbn} is found empirically.

The algorithm for estimating the I and Q channel parameters R_i, R_q, p_i and p_q based on the time domain approach using PRBN test signals is summarised in Table 5.2.

---

1. Apply PRBN probing signals with period $N_{prbn}T$ to the inputs of the I and Q channels.

2. Measure the I and Q channel outputs and compute the cross-correlations

$$C^i_{x_i \hat{y}_i}(kT) = \frac{1}{L_0 - k} \sum_{l=0}^{L_0 - k - 1} x_i(lT)\, \hat{y}_i\big((l+k)T\big)$$
$$= \hat{h}_i(kT); \quad k = 1,2,\ldots,N_i$$

$$C^q_{x_q \hat{y}_q}(kT) = \frac{1}{L_0 - k} \sum_{l=0}^{L_0 - k - 1} x_q(lT)\, \hat{y}_q\big((l+k)T\big)$$
$$= \hat{h}_q(kT); \quad k = 1,2,\ldots,N_q$$

where N_i and N_q are the duration's of the I and Q channel impulse responses and where L_0 is the correlation length determined by noise and PRBN sequence considerations as discussed above.

3. Construct the required estimates of the matrices R_i, R_q, p_i and p_q according to (5.30) and (5.31) using the estimated I and Q channel impulse responses $\hat{h}_i$ and $\hat{h}_q$.

4. Compute of the I and Q channel optimum FIR compensation filters, $\breve{g}_i$ and $\breve{g}_q$, according to the algorithm in Table 4.1.

Table 5.2. Time domain estimation algorithm.

5.5 Quantisation Effects

Various elements in the digital modulator introduce constraints and errors that limit the accuracy of the estimates that can be obtained. In this section the effects of quantisation in the D/A and A/D converters on the frequency domain and time domain estimation schemes are investigated.

The amplitude quantisation of signals has been the subject of extensive investigation over many years and for a review of the area see [100]. Papers of particular relevance to the work presented in this section are [101-104] where a stochastic approach to the effect of quantisation is used, [105-107] where the subject is treated from a deterministic viewpoint and [108] where both stochastic and deterministic treatments are incorporated.

In the analysis of the effects of amplitude quantisation one approach [103] is to represent the quantised signal, $\hat{y}(nT)$, as the original unquantised signal, $y(nT)$, plus equivalent additive quantisation noise, $v_Q(nT)$. Therefore, from (5.9) the output signal of the channel under test is given by

$$\hat{y}(nT) = y(nT) + v_s(nT) + v_Q(nT) \tag{5.49}$$

To gauge the effects of quantisation on the frequency and time domain methods, the system noise, $v_s(nT)$, is assumed to be zero in the next two sections, i.e.,

$$v_s(nT) = 0. \tag{5.50}$$

5.5.1 Quantisation Effects: Frequency Domain Method

In Appendix D expressions for the expected values and variances of the parameter estimates $\{\breve{\alpha}_k\}$ and $\{\breve{\beta}_k\}$, $k = 1, 2, \ldots, N$ are derived.

If the quantisation noise can be assumed to be uniformly distributed and uncorrelated with the input test signals for each test frequency then the estimates $\breve{\alpha}_k$ and $\breve{\beta}_k$ are unbiased as outlined in Section 5.3. Under these conditions the variances of the

estimates $\breve{\alpha}_k$ and $\breve{\beta}_k$ are given by (5.27) and (5.28) where $\sigma_{v_k}^2$ is the variance of the equivalent quantisation noise for the kth input test signal (since from (5.50) the system noise is assumed to be zero). The value of L can then be chosen to make the variance in the estimates arbitrarily small and $\breve{\alpha}_k$ and $\breve{\beta}_k$ become good approximations of the true values.

Conditions on the input signals and the quantisation characteristics of the A/D and D/A converters are therefore required under which the quantisation noise can be considered to be uniform and uncorrelated with the input test signals.

A number of researchers have presented theoretical approaches to the characterisation of sinusoidal signal quantisation noise [106-108]. The approaches generally focus on characterising the quantisation noise in terms of its power spectral density (PSD) rather than correlation properties and conditions are derived under which the PSD can be considered to be uniform in the band of interest. In [105] an approximate expression is derived for the PSD of the quantisation noise of a quantised continuous-time sinusoidal signal. The result is also extended to cover sampled sinusoids. A similar approach to [105] is followed in [108] however the results are extended further to obtain approximate expressions for the PSD of quantisation noise for a sinusoid plus coloured noise. In [107], expressions are derived for the probability density function and variance of the quantisation noise of quantised sinusoidal signals with additive dither.

However, due to the complexity of the channel model in Figure 5.1 and overly restrictive assumptions required for some of the theoretical results, the effects of quantisation on the channel identification and digital compensation using the frequency-domain approach are gauged empirically.

5.5.2 Quantisation Effects: Time Domain Method

In this section the effects of quantisation in the A/D converters on the channel identification approach using the time-domain, cross-correlation technique are investigated. It is assumed that quantisation in the D/A converter in Figure 5.3 does not impact on the cross-correlation identification technique since the PRBN input is a

two-level signal. Note that other implementation errors in the D/A such as DC offset and slew-rate limiting will in general impact on the cross-correlation technique. It is assumed, however, that the effects of these errors are either small, as is the case with slew-rate limiting or can be compensated for, as is the case for DC offset errors.

From (5.34), (5.47) and (5.50), the output of the correlator in Figure 5.3 is given by

$$C_{x\hat{y}}\left(kT\right) = \hat{h}\left(kT\right) + C_{xv_Q}\left(kT\right),$$ (5.51)

where $C_{xv_Q}\left(kT\right)$ is the cross-correlation between $x(nT)$ and the equivalent quantisation noise, $v_Q\left(nT\right)$, and is given by

$$C_{xv_Q}\left(kT\right) = \frac{1}{L_0 - k}\sum_{l=0}^{L_0-k-1} x\left(lT\right)v_Q\left(\left(l+k\right)T\right).$$ (5.52)

In Appendix E it is shown using the stochastic approach developed in [101-104] that the quantisation noise, $v_Q\left(nT\right)$, is approximately uncorrelated with the signals $y(nT)$ and $x(nT)$ even for coarse quantisation.

Therefore taking the expected value of $C_{x\hat{y}}\left(kT\right)$ in (5.51) gives

$$E\left[C_{x\hat{y}}\left(nT\right)\right] = \hat{h}\left(kT\right)$$ (5.53)

and thus $C_{x\hat{y}}\left(nT\right)$ is an unbiased estimator of $\hat{h}\left(nT\right)$.

From (5.43), the variance of $C_{x\hat{y}}\left(kT\right)$ is given by

$$\mathrm{var}\left[C_{x\hat{y}}\left(kT\right)\right] = \frac{A^2\sigma_{v_Q}^2}{L_0 - k},$$ (5.54)

where A is the amplitude of the input PRBN test signal. The quantity $\sigma_{v_Q}^2$ is the variance of the uniformly distributed quantisation noise and is given by the well-known [101-103] relation

$$\sigma_{v_Q}^2 = \frac{\varDelta_q^2}{12},$$

(5.55)

where $\varDelta_q$ is the quantisation step size of the A/D converter.

From (5.54) and (5.55),

$$\text{var}\left[C_{x\hat{y}}\left(kT\right)\right] = \frac{A^2 \varDelta_q^2}{12\left(L_0 - k\right)}.$$

(5.56)

Equation (5.56) provides a method for estimating the correlation length for a required variance in $C_{x\hat{y}}\left(kT\right)$ and given the quantisation characteristic of the A/D converter.

Examples of the effect of amplitude quantisation on cross-correlation estimation are provided Section 5.6.

5.6 Numerical Studies

In this section the results of computer simulation studies of the frequency and time domain channel identification and parameter estimation techniques described in the previous sections of this chapter are presented. The results are grouped into two *trials* where the effectiveness of the channel identification and parameter estimation is measured in terms of the reduction in AM in the envelope of the vector modulator output signal. The conditions for each trial are summarised below:

1. No quantisation, no system noise.

2. Varying amounts of additive system noise, $v_s(nT)$, together with a range of different quantisation characteristics in the A/D and D/A converters.

For each trail the results for frequency domain technique (summarised by the algorithm in Table 5.1) are presented first followed by the results for the time domain technique (summarised by the algorithm in Table 5.2).

A fundamental difference between the simulation studies in this section and those presented in Section 4.8 is that the matrices and vectors, R_i, R_q, p_i and p_q are *estimated* from measurements of the I and Q channel frequency or time domain parameters rather than assumed to be known exactly *a priori*.

The input test signals for the frequency and time domain techniques are designed such that the total measurement time required per channel for each technique is approximately the same (and equal to 82 mS). This provides a basis for comparison between the two approaches. Details (including the number of samples, signal amplitudes, etc) of the test inputs for the frequency and time domain techniques are given in Sections 5.6.2 and 5.6.3

5.6.1 Simulation Conditions

The model of the system used to study the channel identification methods proposed in Sections 5.3 and 5.4 is shown in Figure 5.5.
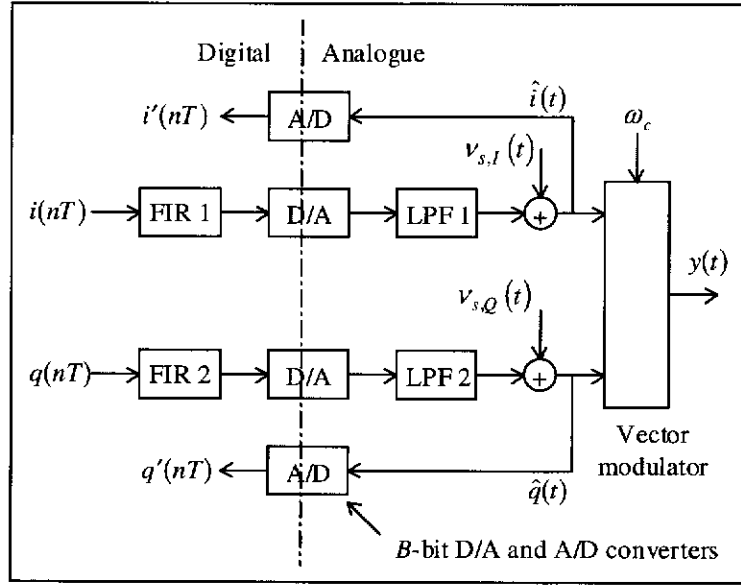
Figure 5.5. Model of the simulated digital IQ modulator system.

This system model is similar to that used in the numerical studies in Section 4.8. However, for the system considered here, the D/A and A/D converters are assumed to be B-bit devices and the I and Q channels are assumed to be contaminated with additive system noise. The additive system noise for the I and Q channels is denoted by $v_{s,I}(t)$ and $v_{s,Q}(t)$ respectively.

ERMES parameters (detailed in Section 2.4.3) are again used for the digital IQ modulator and in all of the numerical trials that follow, the two compensation filters FIR 1 and FIR 2 are 50-tap digital filters, i.e.,

$$K = 50. \tag{5.57}$$

and the digital section sampling frequency is

$$f_s = 200 \times 10^3 \text{ Hz.} \tag{5.58}$$

The I and Q channel low-pass analogue signal reconstruction filters, LPF1 and LPF2, have a nominal 6th order Butterworth characteristic frequency response. The actual I and Q channel reconstruction filters used here are the same realisations of the filter circuit used in the numerical trials in Sections 3.4 and 4.8. The magnitude and group-delay responses of the I and Q channel filters are shown in Figures 3.15 and 3.16.

The same input symbol test sequence shown in Figure 3.2 is used. This allows the digital compensation results presented in the following sections to be compared in terms of reduction in envelope ripple with those in earlier chapters. The ripple in the envelope function of the vector modulator output signal for this particular input test symbol sequence and for the uncompensated modulator system is shown in Figure 5.6.
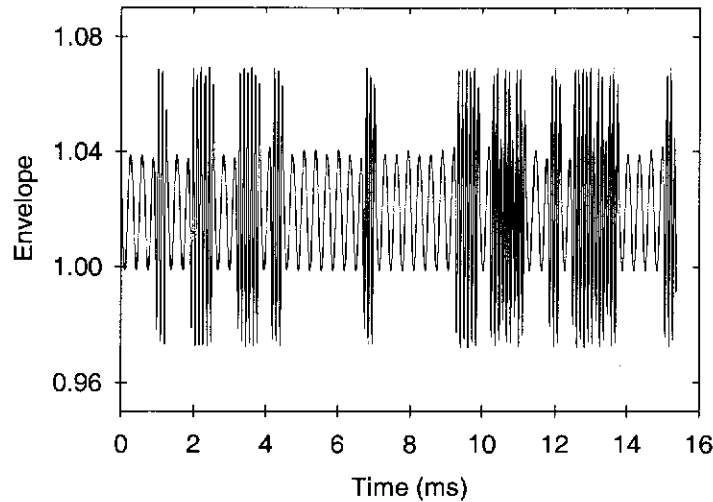

Figure 5.6. Vector modulator output signal envelope function from the uncompensated system.

The ripple present in the envelope function in Figure 5.6 has an RMS value of 2.88 mV. This value, together with the plot in Figure 5.6 will form a basis for quantitative and qualitative evaluation of the effectiveness of digital compensation in the following trials.

As proposed in Section 4.4, the desired channel complex frequency response, $D\!\left(e^{j\omega T}\right)$, for the optimisation is chosen to have the same magnitude response as that of the nominal reconstruction filter (6th order Butterworth characteristic) but is constrained to have linear phase. The desired channel complex frequency response is given in Section 4.8.1 and impulse response required for the time-domain formulation of the optimisation problem is found from an inverse discrete Fourier transform of $D\!\left(e^{j\omega T}\right)$.

5.6.2 Test Signals for the Frequency-Domain Approach

The number of frequency points, N, chosen for the discrete frequency version of the optimisation problem given in (5.1) is

$$N = 50 \tag{5.59}$$

The N frequency points are uniformly distributed in the interval according to

$$f_n \in \left(0, 100 \times 10^3\right) \text{Hz}; \; n = 1, 2, \ldots, N. \tag{5.60}$$

The estimates of the I and Q channel responses presented in the following numerical trials were obtained by applying the 50 sampled sinusoidal input signals, one frequency at a time and to one channel at a time, and measuring the corresponding channels' magnitude and phase responses. The least-squares curve-fitting method described in Section 5.3 was used to estimate the amplitude and phase-shift of the output signals. Each sinusoidal test signal was applied to the system for a duration of $2.15ms$. The channel impulse responses have a duration of approximately $250\mu s$ and, in order to ensure that initial transients are sufficiently small before measurements are made, the first $500\mu s$ of the outputs are discarded.

For a sampling frequency given by (5.58) the values $2.15ms$ and $500\mu s$ correspond to sample lengths of 430 and 100 respectively and the values L and l_0 in (5.18) are therefore given by

$$\begin{aligned} L &= 430 \\ l_0 &= 100 \end{aligned} \tag{5.61}$$

From (5.59) and (5.61), the total effective measurement time in samples per channel is given by

$$\begin{aligned} L_{eff} &= 50 \times \left(L - l_0\right) \\ &= 16500. \end{aligned} \tag{5.62}$$

Note that the value $L = 430$ in (5.61) was chosen to give the effective per-channel measurement length in (5.62) that approximately matched the per-channel

measurement length of $L_0 = 16383$ for the time domain technique test signals detailed in the next section. This was done so that the results of the frequency and time domain approaches could be compared on the basis of comparable measurement times.

5.6.3 Test Signals for the Time-Domain Approach

In Section 5.4.2 the use of pseudorandom binary noise (PRBN) sequences as test signals for the estimation of the I and Q channel discrete-time impulse responses was proposed.

For the IQ modulator system with ERMES parameters considered here, the value of N_{prbn} that results in effective reduction in ripple in the envelope of the vector modulator output signal is found empirically to be

$$N_{prbn} = 16383.$$
(5.63)

It was found that sequences with shorter periods (i.e. $N_{prbn} = 8191, 4095, \ldots$) resulted in a significant DC offset or bias in the estimates of the I and Q channel impulse responses. This in turn resulted in digital compensation filters that were ineffective in reducing AM in the envelope of the vector modulator output signal.

Equation (5.43) gives a value, L_0, of the number of samples required for the cross-correlation calculations to achieve a certain variance in the estimate $C_{x\hat{y}}(kT)$ for lag k, given the additive noise variance, σ_v^2. Assuming $L_0 \gg k$ (i.e. L_0 much larger than the duration in samples of the channel impulse response) then for the severe case of -10dB additive noise and a requirement for the variance to be less than -40 dB, equation (5.43) gives

$$L_0 \cong 1000 \text{ samples.}$$
(5.64)

From (5.63) and (5.64), the correlation length, L_0, in (5.33) is chosen to be

$$L_0 = N_{prbn} = 16383,$$
(5.65)

as discussed in Section 5.4.2.

The PRBN test sequence used in the following trials was a 14th order m-sequence [90, 97] with a generator polynomial defined by

$$X^{14} \oplus X^{10} \oplus X^6 \oplus X \oplus 1, \tag{5.66}$$

where $\oplus$ represents modulo-2 addition.

5.6.4 No Quantisation, No System Noise.

In this trial it is assumed that the D/A and A/D converters in Figure 5.5 produce negligible quantisation of the I and Q channel signals and that no device saturation occurs. It is also assumed that the measurements of the low-pass filter outputs are not corrupted by noise, i.e.,

$$V_{s,I}(t) = V_{s,Q}(t) = 0. \tag{5.67}$$

Frequency Domain Technique

The magnitude and group delay responses estimated using the frequency-domain method summarised in the algorithm in Table 5.1 are shown in Figures 5.7 to 5.10. (Note that the frequency response characteristics of the compensated and uncompensated I and Q discrete-time channels shown in the following figures are periodic with period $f_s = 200\,\text{kHz}$. However, only a small section of the frequency response characteristics are shown thus allowing details of the effectiveness of the channel identification and digital compensation to be seen more clearly.)
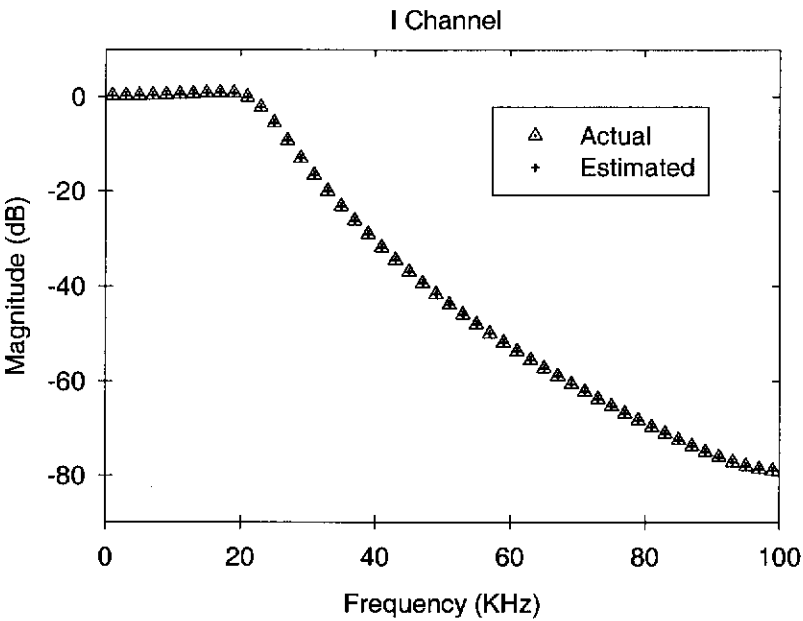
I Channel

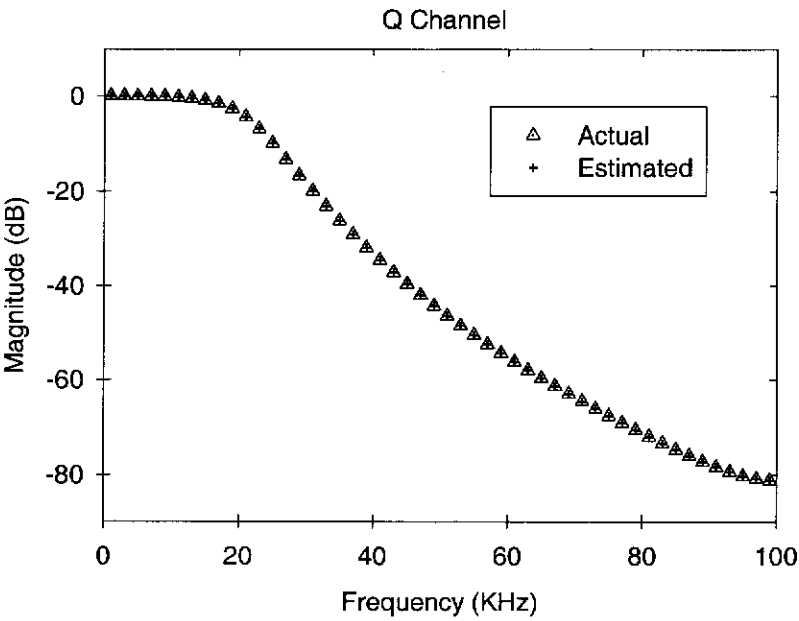**Figure 5.7.** I channel magnitude response.

Q Channel

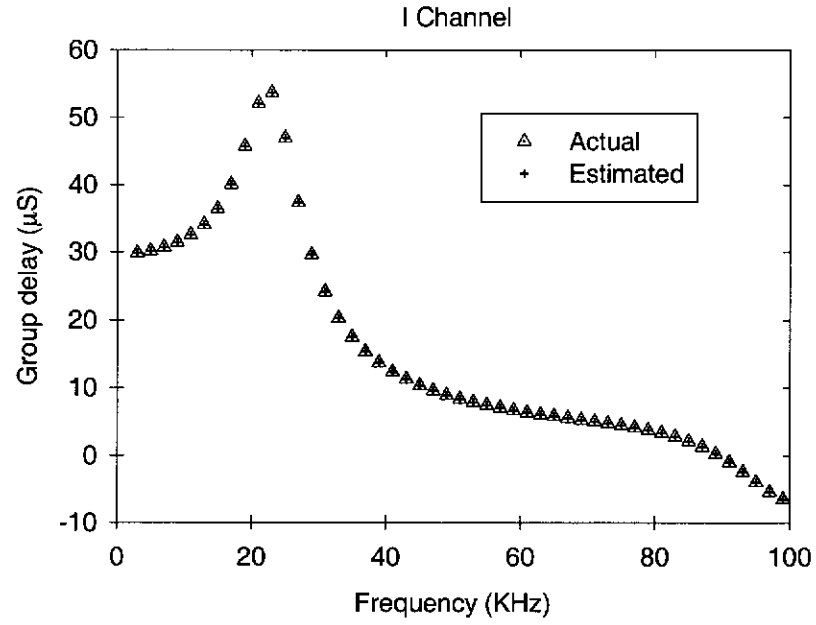**Figure 5.8.** Q channel magnitude response.

Figure 5.9. I channel group delay response.
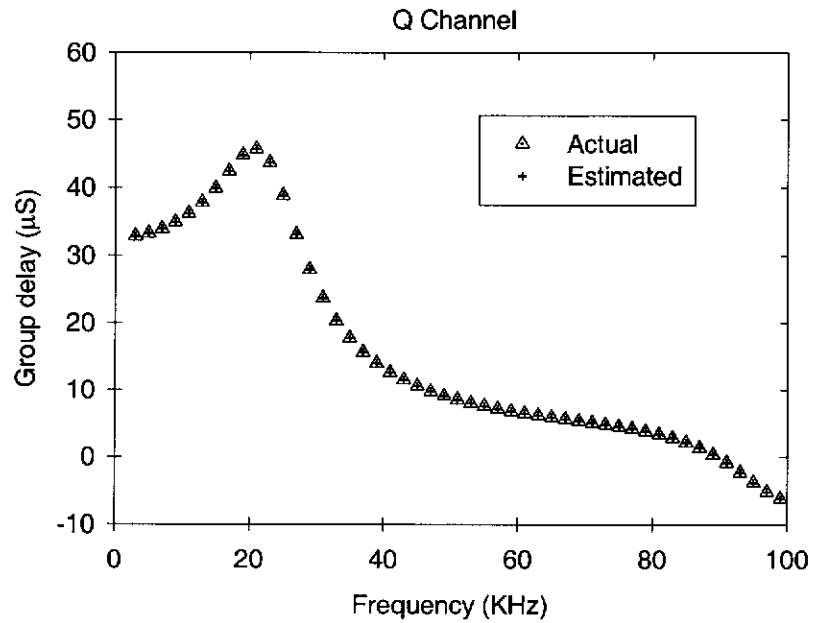

Figure 5.10. Q channel group delay response.

With the measurements of $\left\{H'\left(e^{j\omega_n T}\right)\right\}; n = 1, 2, \ldots, N$ above, estimates of the quantities R_i, R_q, p_i and p_q are calculated using (5.3) and (5.4). The optimum I and Q channel digital FIR compensation filters are found using the algorithm in Table 4.1. The impulse responses of these FIR filters are shown in Figure 5.11.

(Note that samples of the FIR compensation filter impulse responses shown in Figure 5.11 are joined by straight lines for ease of visual comparison.)
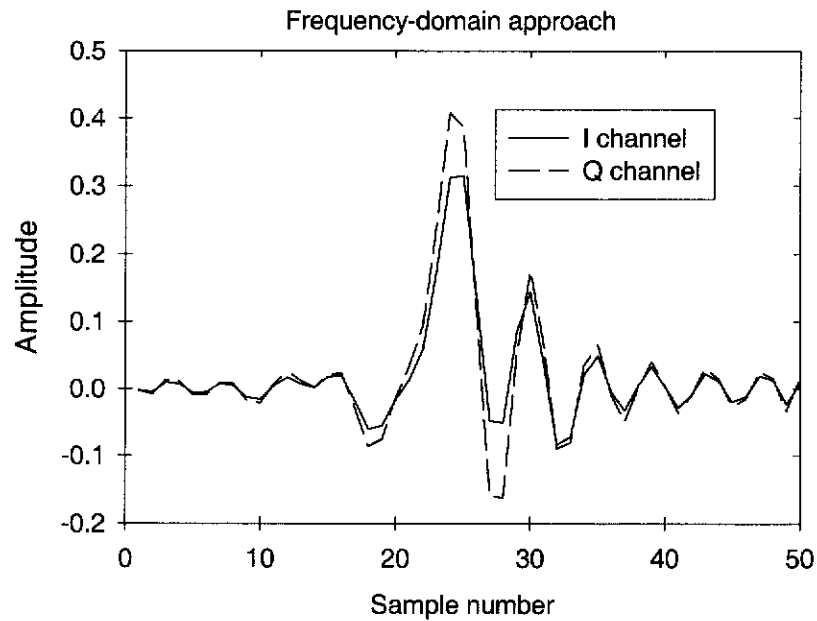

Figure 5.11. Optimum digital compensation filter impulse responses.

The magnitude responses for the compensated and uncompensated I and Q channels are compared in Figure 5.12 and Figure 5.13 while the compensated and uncompensated I and Q channel group delay responses are compared in Figure 5.14 and Figure 5.15. and The compensated I and Q channel characteristics are computed by multiplying the discrete Fourier transforms (DFTs) of the digital FIR compensation filter impulse responses shown in Figure 5.11 with the estimated I and Q channel frequency responses shown in Figures 5.7 to 5.10.
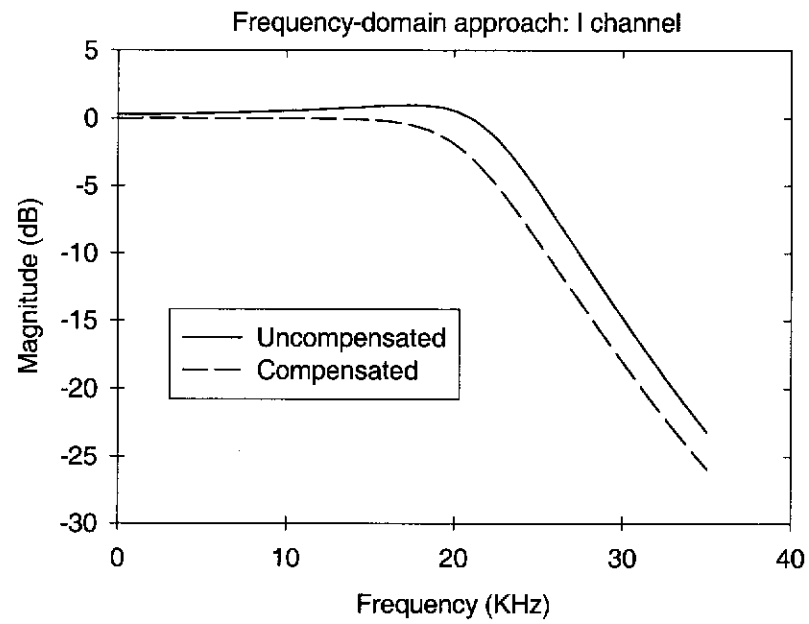
Frequency-domain approach: I channel

Figure 5.12. I channel magnitude response comparison between compensated and uncompensated systems.

Frequency-domain approach: Q channel
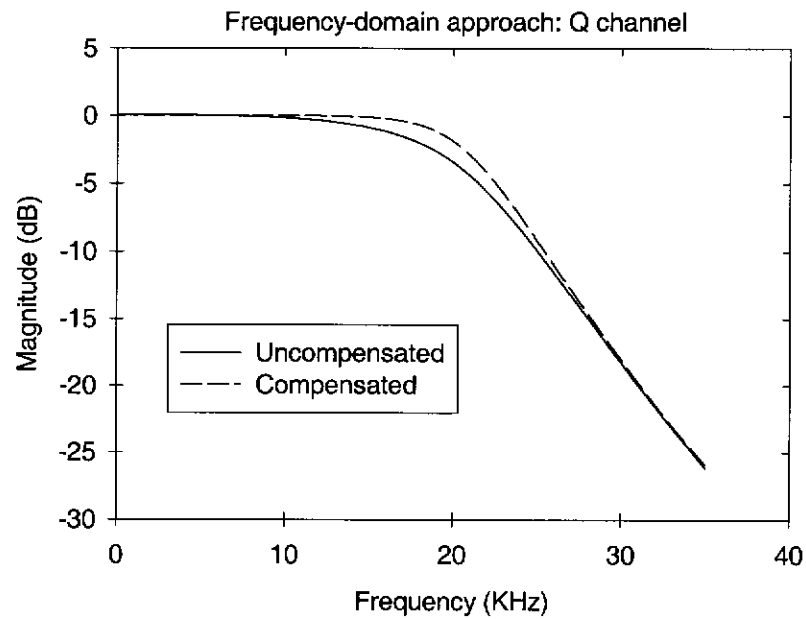
Figure 5.13. Q channel magnitude response comparison between compensated and uncompensated systems.
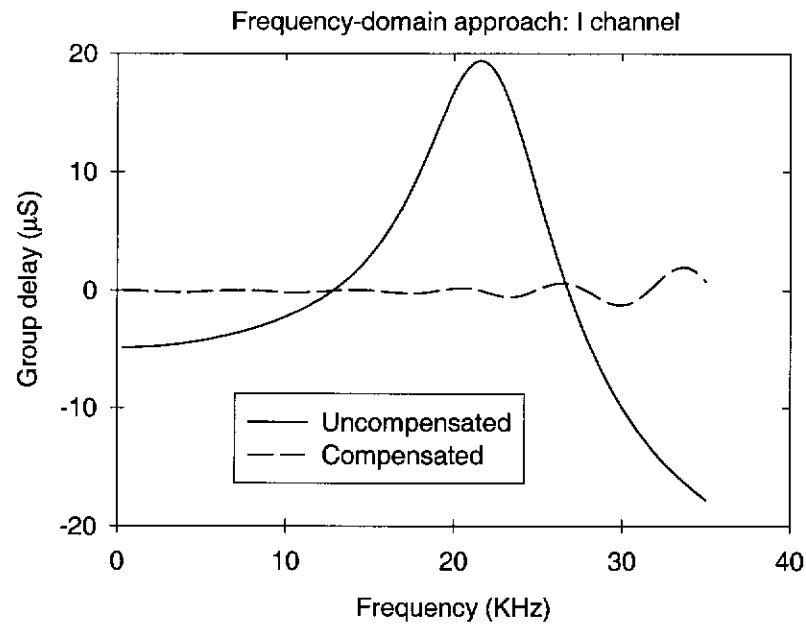
Frequency-domain approach: I channel

Figure 5.14. I channel group delay response comparison between compensated and uncompensated systems (mean delay removed).
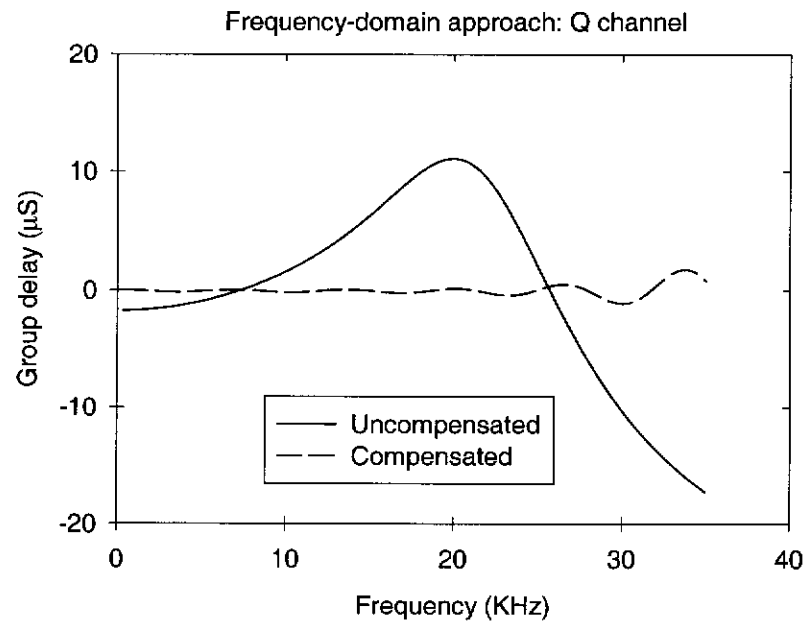
Frequency-domain approach: Q channel

Figure 5.15. Q channel group delay response comparison between compensated and uncompensated systems (mean delay removed).

The effectiveness of the digital compensation employing the frequency domain channel identification technique in reducing ripple in the vector modulator output signal is now tested by applying the 50-symbol test sequence of Figure 3.2 to the

digital IQ modulator input. The resulting envelope of the vector modulator output signal is calculated for the system with the digital compensation filters in place and is shown in Figure 5.16. (Note that the vertical scale in the plot below is chosen so that the envelope function can be visually compared with that of the uncompensated system in Figure 5.6.)
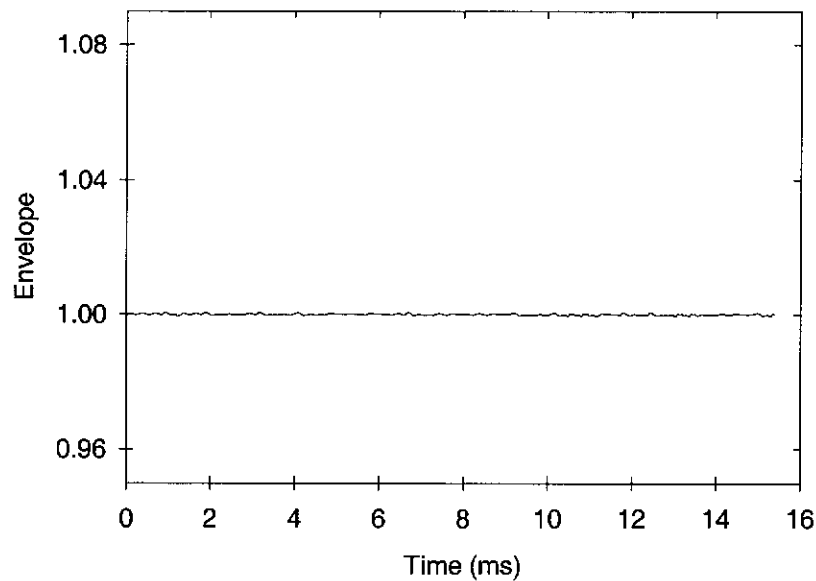

Figure 5.16. Vector modulator output envelope.

The RMS value of the ripple present on the envelope function in Figure 5.16 is $29.0 \mu V$. This represents a significant reduction in envelope ripple when compared with the RMS value of 2.88mV for the uncompensated system.

∎

Time Domain Technique

The impulse responses of the I and Q channels are shown in Figure 5.17 and Figure 5.18 respectively. The plots labelled "Estimated" are the impulse responses determined using the time domain technique based on cross-correlation with the PRBN test signal outlined in Section 5.6.3. The plots labelled "Actual" are included for reference and are the impulse responses of the I and Q channels calculated from the actual channel parameters (reconstruction filter component values and system sampling rate).

Note that impulse responses shown in Figure 5.17 and Figure 5.18 are discrete-time functions and the sample values are joined by straight lines for ease of visual comparison.
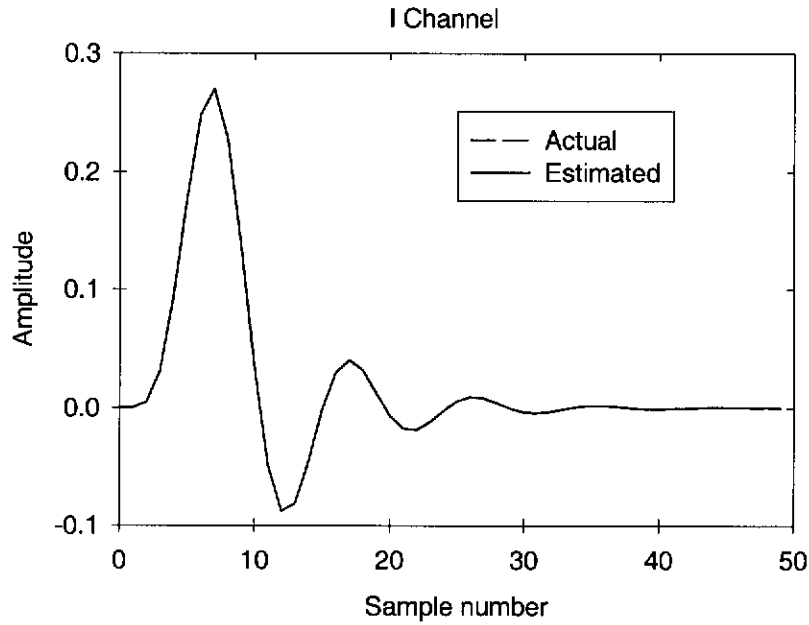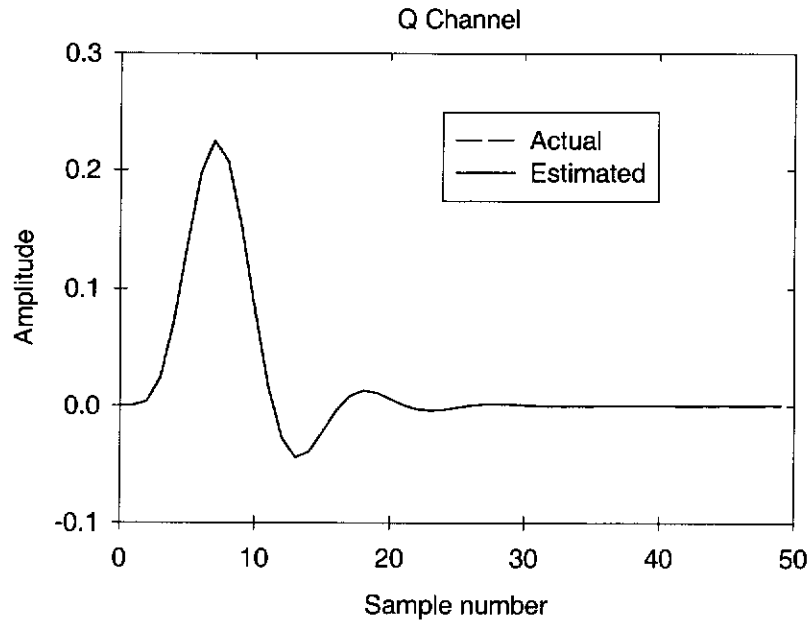

Figure 5.17. I channel impulse response.

Figure 5.18. Q channel impulse response.

With the measurements of $h_i'(nT)$ and $h_q'(nT)$ shown in Figure 5.17 and Figure 5.18, estimates of the matrices and vectors required for the optimisation are

calculated using (5.30) and (5.31). The optimum I and Q channel digital FIR compensation filters are found using the algorithm in Table 4.1. The impulse responses of these FIR filters are shown in Figure 5.19.
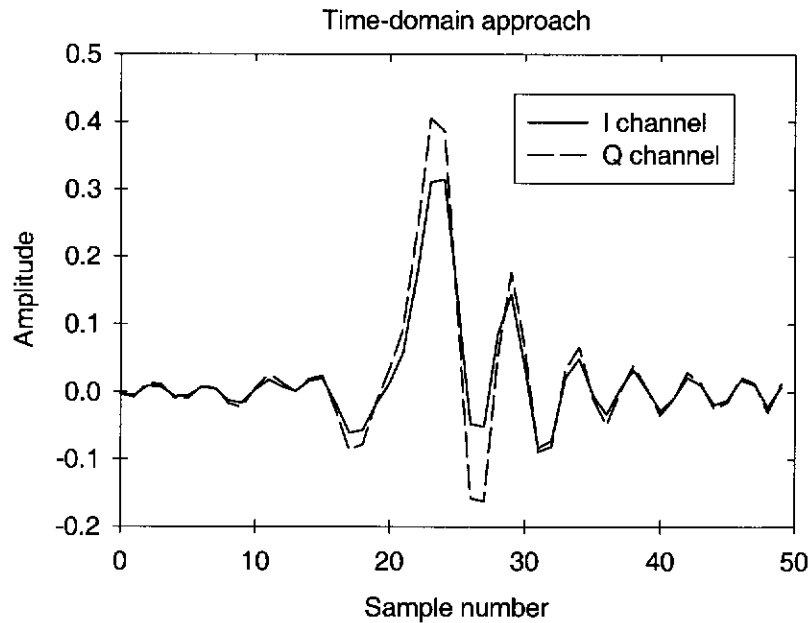

Figure 5.19. Optimum digital compensation filter impulse responses.

The magnitude responses for the compensated and uncompensated I and Q channels are shown in Figure 5.20 and Figure 5.21 while the compensated and uncompensated I and Q channel group delay responses are compared in Figure 5.22 and Figure 5.23. The compensated I and Q channel characteristics are computed by multiplying the DFTs of the digital FIR compensation filter impulse responses in Figure 5.19 with the DFTs of the estimated I and Q channel discrete-time impulse responses shown in Figure 5.17 and Figure 5.18.
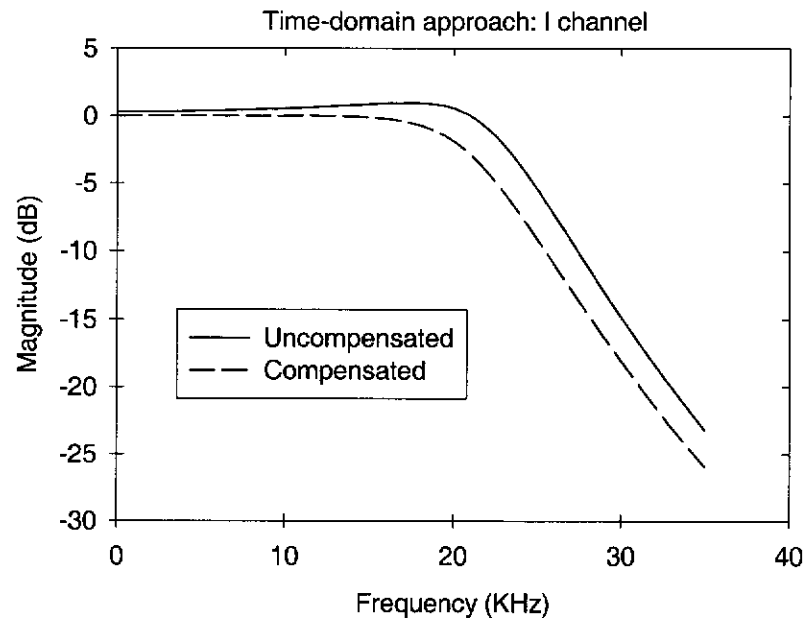
Figure 5.20. I channel magnitude response comparison between
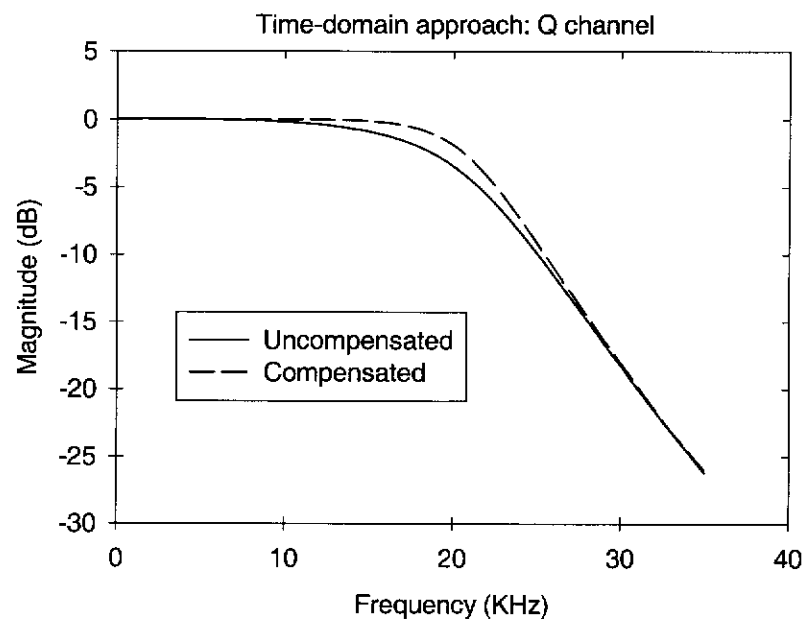compensated and uncompensated systems.

Figure 5.21. Q channel magnitude response comparison between
compensated and uncompensated systems.

Time-domain approach: I channel

Figure 5.22. I channel group delay response comparison between compensated and uncompensated systems (mean delay removed).

Time-domain approach: Q channel

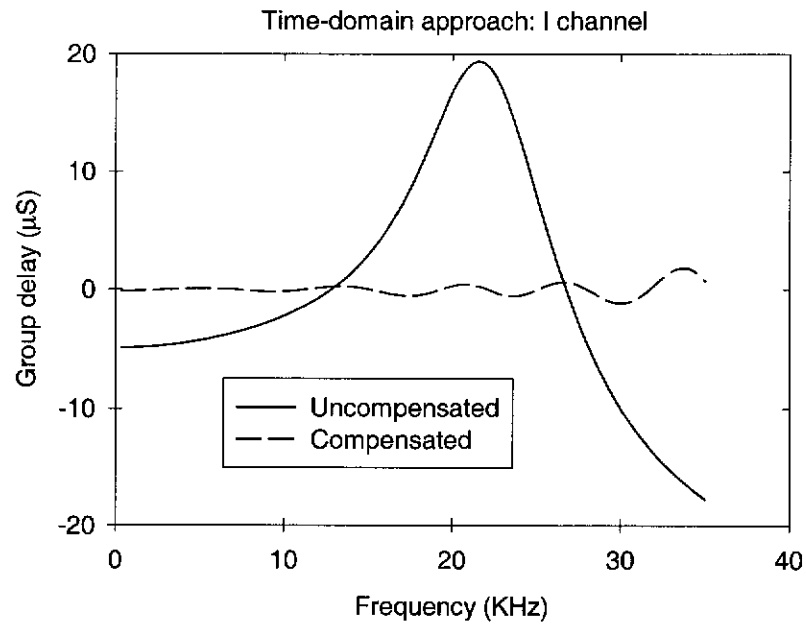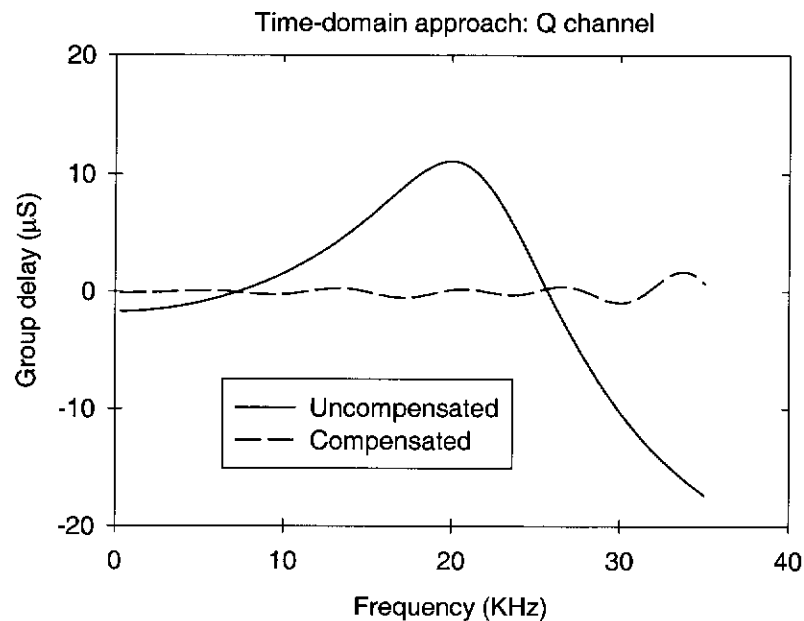**Figure 5.23.** Q channel group delay response comparison between compensated and uncompensated systems (mean delay removed).

The effectiveness of the digital compensation employing the time domain channel identification technique in reducing ripple in the vector modulator output signal is tested by applying the 50-symbol test sequence of Figure 3.2 to the digital IQ

modulator input. The resulting envelope of the vector modulator output signal for the system with the digital compensation filters in place is shown in Figure 5.24.
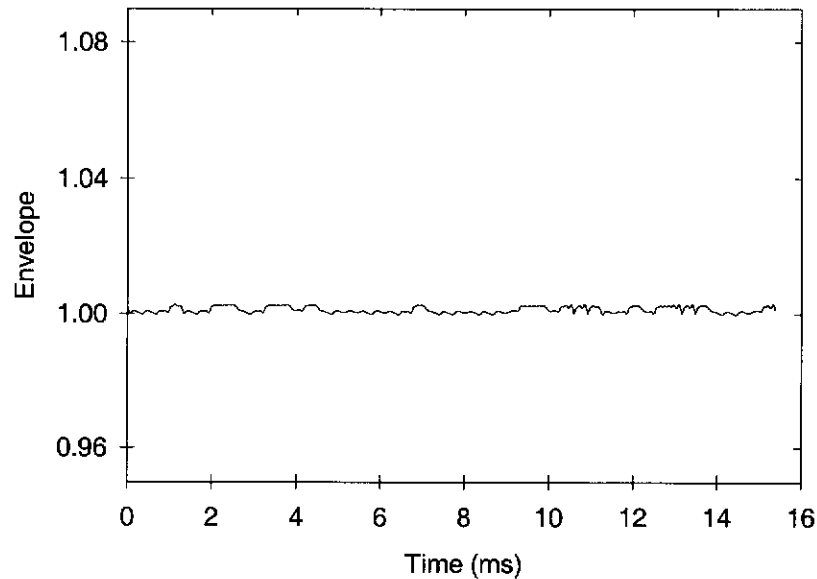

Figure 5.24. Vector modulator output envelope.

The RMS value of the ripple present on the envelope function in Figure 5.24 is $128.4\mu V$. This figure represents a substantial reduction in envelope ripple when compared with the RMS value for the uncompensated system of 2.88mV.

■

The envelope functions shown in Figure 5.16 and Figure 5.24 give a clear indication that both channel identification approaches provide sufficiently accurate estimates of the I and Q channel parameters (under the conditions of this trial) to enable good compensation and reduction of the envelope ripple. Table 5.3 provides a quantitative comparison between the two approaches for this trial.

	Frequency-domain approach	Time-domain approach
Reduction factor	110.7	25.0

Table 5.3. Factor reduction in RMS ripple in the envelope functions for Figure 5.16 and Figure 5.24.

The "Reduction factor" in Table 5.3 is calculated as follows

$$\text{Reduction factor} = \frac{\text{uncompensated RMS ripple}}{\text{compensated RMS ripple}}$$
$$= \frac{2.88mV}{\text{compensated RMS ripple}} \quad . \tag{5.68}$$

5.6.5 Effects of Additive System Noise Plus Quantisation on Channel Identification Performance.

In this example the impact of additive system noise, $v_{s,I}(t)$ and $v_{s,Q}(t)$, combined with various degrees of quantisation in the D/A and A/D converters on the system identification methods is investigated in terms of the resulting effectiveness of the digital compensation.

Four quantisation scenarios are considered:

1. Negligible quantisation.
2. 8-bit.
3. 6-bit.
4. 4-bit.

It is assumed that the D/A and A/D converters are all B-bit devices as shown in Figure 5.5 and that the input signals to the devices are correctly scaled to ensure that the dynamic ranges of the converters is not exceeded.

For each quantisation scenario four different levels of zero-mean, Gaussian distributed system noise is added to the I and Q channels before the A/D converters (see Figure 5.5):

1. No additive system noise, $v_{s,I}(t) = v_{s,Q}(t) = 0$.

2. $\text{var}\left[v_{s,I}(t)\right] = \text{var}\left[v_{s,Q}(t)\right] = -30\,\text{dB}$.

3. $\text{var}\left[v_{s,I}(t)\right] = \text{var}\left[v_{s,Q}(t)\right] = -20\,\text{dB}$.

4. $\text{var}\left[v_{s,I}(t)\right] = \text{var}\left[v_{s,Q}(t)\right] = -10\,\text{dB}$.

The variance of the system noise is relative to the square of the peak value of the nominal impulse response of the I and Q channel analogue filters.

Note that the case of negligible quantisation and zero additive system noise has already been considered in Section 5.6.4.

Frequency Domain Technique

The matrices and vectors required for the optimisation are estimated using the frequency-domain algorithm in Table 5.1 and the optimum I and Q channel digital compensation filters are calculated using the algorithm in Table 4.1. The envelope functions for outputs of the digitally compensated vector modulator for the four quantisation scenarios listed above are shown in Figures 5.25 to 5.28. (Note that in the following figures the noise captions on each plot and the quantisation levels in the figure captions describe the system noise and quantisation present during the channel identification process only. System noise and quantisation are not present for the measurements of the envelope functions shown.)
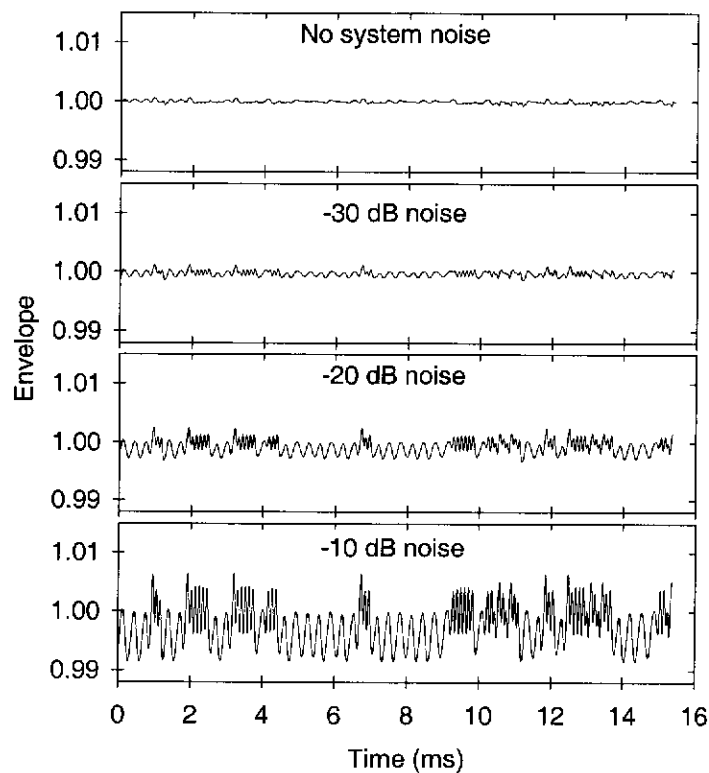

Figure 5.25. Vector modulator output envelope functions:

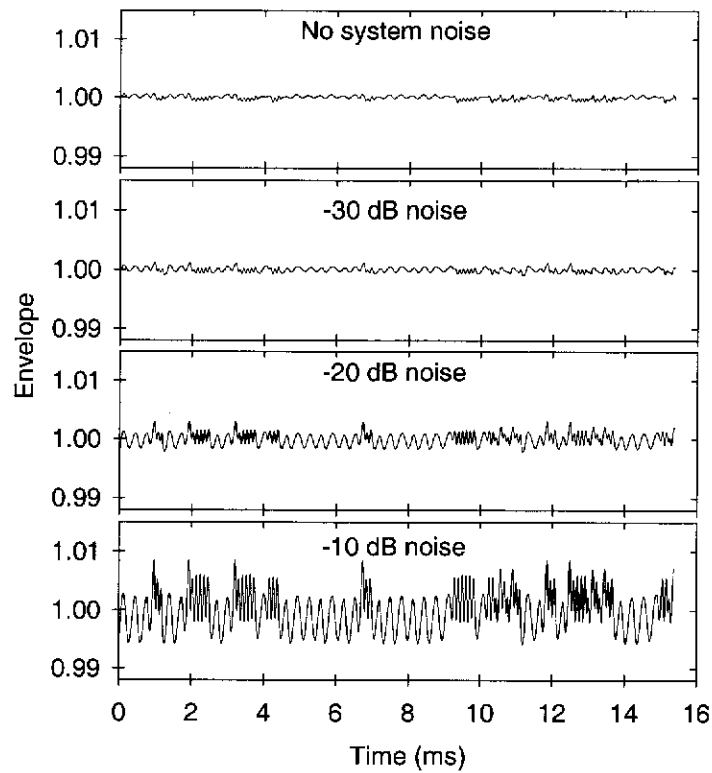negligible quantisation, varying system noise.

Figure 5.26. Vector modulator output envelope functions:
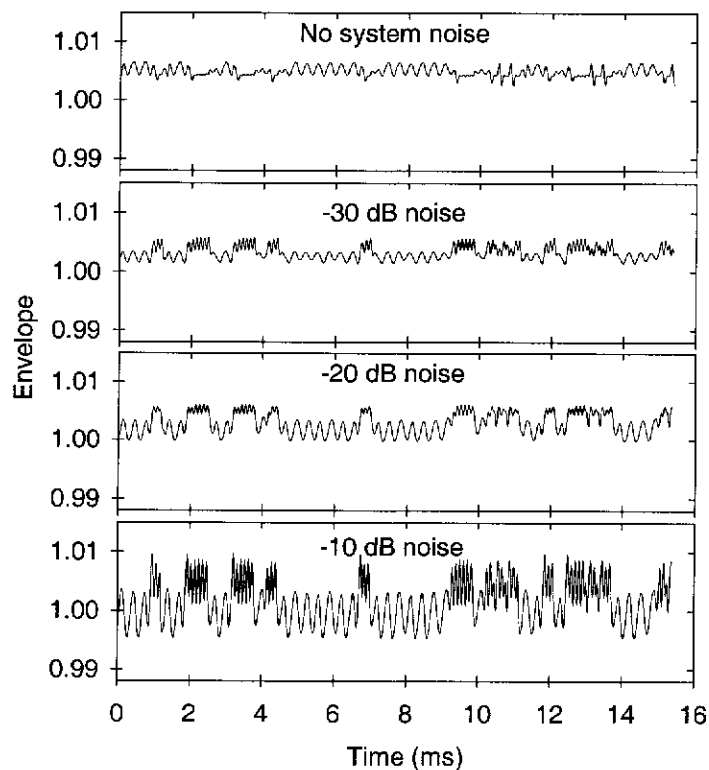
8-bit quantisation, varying system noise.

Figure 5.27. Vector modulator output envelope functions:

6-bit quantisation, varying system noise.

Figure 5.28. Vector modulator output envelope functions:

4-bit quantisation, varying system noise.

From the four figures above a number of observations can be made:

- For the cases of no quantisation, 8-bit and 6-bit quantisation (Figures 5.25, 5.26 and 5.27), the effectiveness of the frequency domain technique in reducing envelope ripple is degraded more as the additive system noise level is increased.

- For the case of severe 4-bit quantisation (Figure 5.28), additive noise appears to improve the frequency domain technique.

- From all four quantisation scenarios, the frequency domain technique is degraded as the severity of the quantisation is increased, however, there is a marked reduction in the effectiveness of the technique for the extreme case of 4-bit quantisation.

Time Domain Technique

The matrices and vectors required for the optimisation are estimated using the time-domain algorithm in Table 5.2 and the optimum I and Q channel digital compensation filters are calculated using the algorithm in Table 4.1. The envelope functions for outputs of the digitally compensated vector modulator for the four quantisation scenarios are shown in Figures 5.29 to 5.32.

Figure 5.29. Vector modulator output envelope functions:

no quantisation, varying system noise.
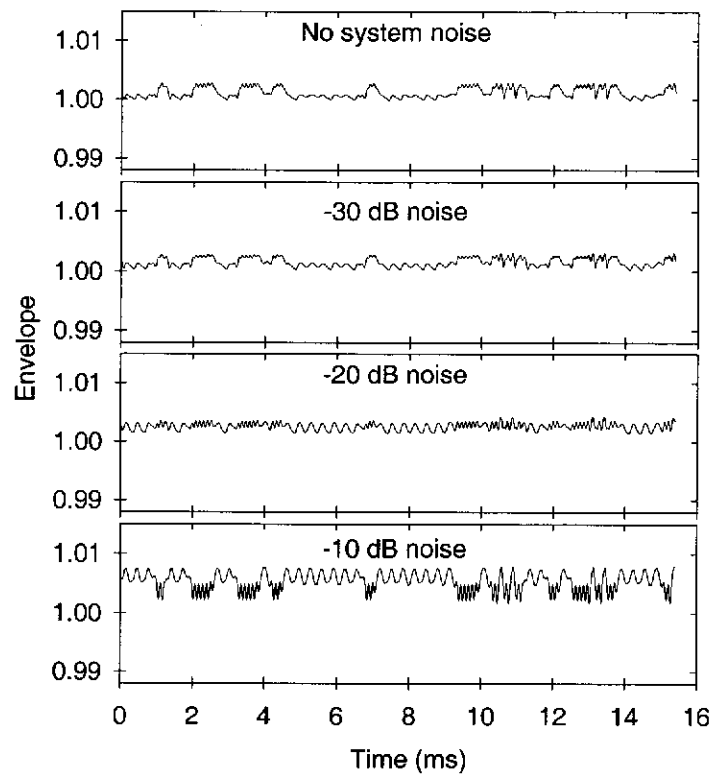
Figure 5.30. Vector modulator output envelope functions:

8-bit quantisation, varying system noise.
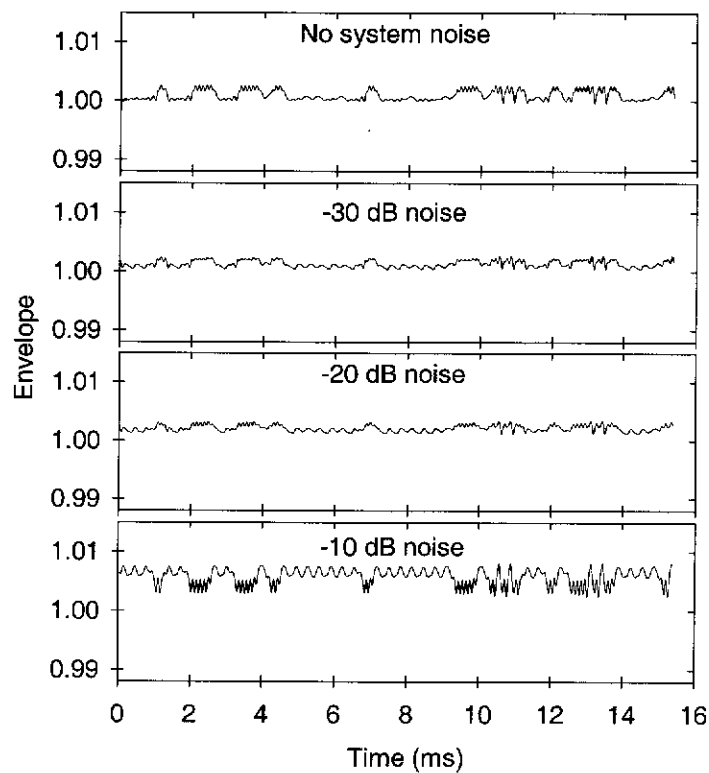
Figure 5.31. Vector modulator output envelope functions:
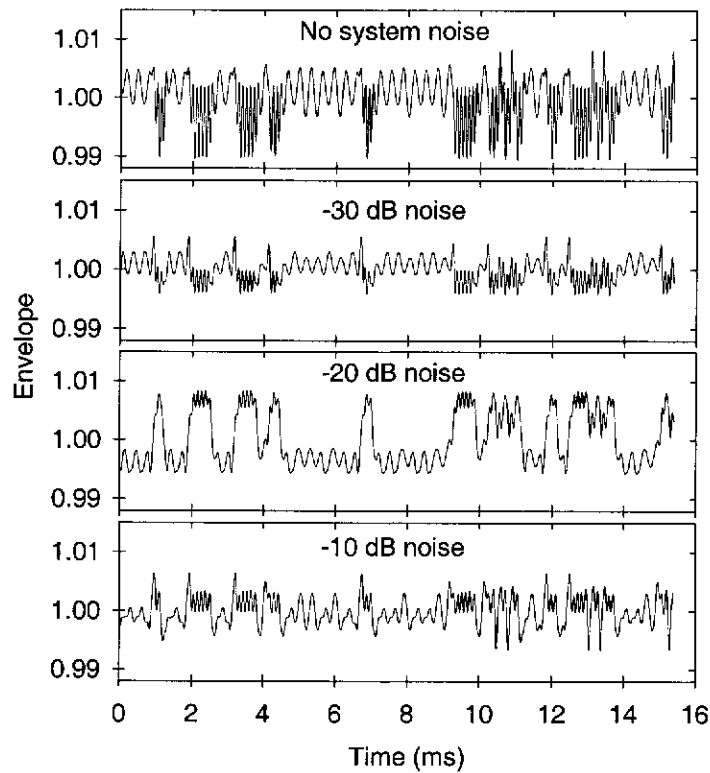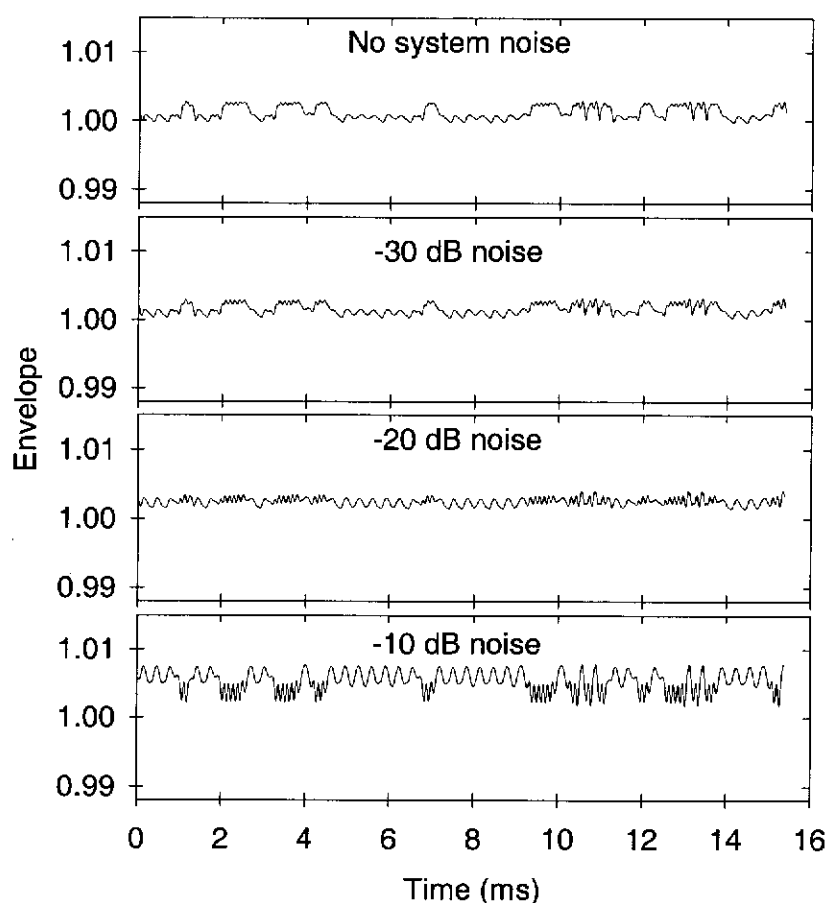
6-bit quantisation, varying system noise.
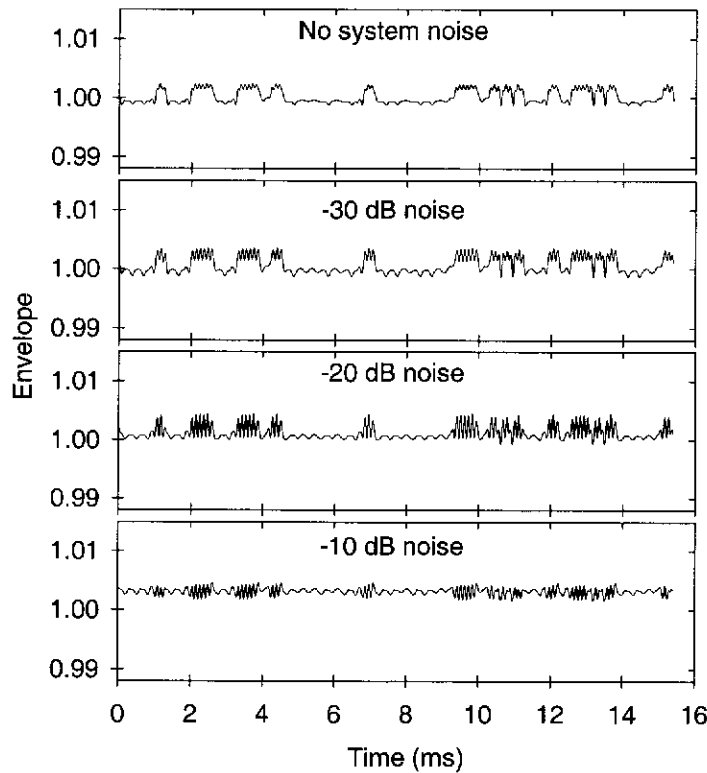
Figure 5.32. Vector modulator output envelope functions:

4-bit quantisation, varying system noise.

The following observations can be made regarding the results presented in Figures 5.29 to 5.32:

- For the cases of no quantisation, 8-bit and 6-bit quantisation, additive noise with levels of −30 dB or −20 dB appear to improve the effectiveness of the time domain technique in reducing envelope ripple. In each of these three cases, however the effectiveness of the technique is degraded when the noise level is increased to −10 dB.

- For the case of 4-bit quantisation the effectiveness of the technique appears to be improved by higher noise levels (-20 dB and −10 dB).

- For all four quantisation scenarios, the effectiveness of the time domain technique in reducing envelope ripple is not significantly degraded as the severity of the quantisation is increased and the technique performs well even under extreme 4-bit quantisation.

Given the basis of common measurement times as described in Sections 5.6.2 and 5.6.3 the following comparisons can be made between the frequency domain technique results (Figures 5.25 to 5.28) and the time domain technique results (Figures 5.29 to 5.32):

- The frequency domain technique performs better than the time domain technique for the combination of finer quantisation (negligible and 8-bit) and low additive system noise (-30 dB to -20 dB).

- For scenarios where the quantisation environment is severe (6-bit or 4-bit) or where higher additive system noise (-20 dB or -10 dB) is present the time domain technique provides better performance in terms of reduction in envelope ripple.

The qualitative results and observations are supported by the quantitative results in Table 5.4 where the reduction factors in RMS envelope ripple (calculated according to (5.68)) for the envelope functions shown in Figures 5.25 to 5.32 are provided.

Reduction factor		Additive system noise							
		No noise		-30 dB		-20 dB		-10 dB	
Quantisation	None	111	25	53	31	20	43	7	16
	8-bit	75	27	60	31	23	38	7	15
	6-bit	29	27	21	40	13	43	6	17
	4-bit	6	20	12	17	5	21	10	39

Table 5.4. Quantitative summary of the effects of noise and quantisation on the frequency and time domain techniques:

Unshaded: Reduction factor, frequency domain method.

Shaded: Reduction factor, time domain method.

It has been found empirically that reduction factors of greater than 15 in the envelope ripple (given poor I and Q channel reconstruction filter characteristics) are sufficient to provide effective reduction in the adjacent channel power in the transmitted RF signal.

The results of the computer simulation studies presented in this section show that both the frequency and time domain methods provide sufficiently high reduction factors under typical operating conditions; i.e. 8-bit (or better) quantisation in the

D/A and A/D converters and less than −20 dB additive system noise. For environments with low system noise (-30 dB) and D/A's and A/D's with bit-numbers of 8 or higher, the frequency domain technique performs significantly better in terms of envelope reduction factor. For environments where system noise is higher or applications where a low number of bits are necessary (eg. high frequency applications) the results of this section indicate that the time domain technique will perform better than the frequency domain technique for a given measurement time.

Improvements in compensation resulting from the addition of system noise were noted in the frequency domain technique for 4-bit quantisation and for the time domain technique in all quantisation scenarios. This is most likely attributable to the well known [100, 107, 109-111] *dithering* effect of noise in quantised signals.

5.7 Conclusion

From the material presented in this chapter it can be seen that the two methods for identifying the I and Q channel frequency or time-domain parameters supply sufficiently accurate estimates of the required channel parameters for effective digital compensation under typical operating conditions. Either method provides a means by which *automatic* digital compensation can be implemented and, as the reconstruction filter characteristics drift relatively slowly with time, "re-training" the FIR compensation filters using the test input signals need only be done at infrequent intervals.

The comparisons made here between the two channel identification methods are on the basis of approximately equivalent measurement times. Naturally, one method may out-perform the other for different measurement times and the performance of both methods in the presence of system noise can be improved by averaging the parameter estimates for longer. However, this is at the expense of longer measurement and identification times.

While both methods provide acceptable reduction of ripple in the envelope function of the vector modulator output signal, the time domain technique is attractive for implementation for a number of reasons:

1. Robustness against system noise and quantisation.

2. The practical simplicity of generating the input test signals. A PRBN test signal simply takes on values of ± 1, while relatively complex look-up tables must be used to generate the sinusoidal functions for the frequency-domain identification approach.

3. Many DSP architectures have efficient structures for implementing the correlation calculations required for the time domain technique.

Chapter 6. Implementation of Digital Compensation

6.1 Introduction

While both frequency and time domain automatic digital compensation approaches were shown in Chapter 5 to work effectively, the time domain approach had certain advantages for a low number of bits and in the presence of noise. Furthermore, the construction of the test signals is much simpler for the time domain approach. Hence, the time domain approach was selected for implementation.

This chapter describes the implementation of an IQ modulator, incorporating the time domain automatic compensation algorithm, on a DSP platform and presents the results of experiments performed using the digitally compensated modulator.

The key contributions of this chapter are:

1. A demonstration that effective automatic digital compensation can be implemented on a practical DSP platform.

2. The identification of some additional implementation issues not addressed in Chapter 5 that need to be considered in order for automatic digital compensation to be successful on a DSP platform.

3. A practical demonstration of the significant improvements in modulator performance that can be obtained by using the digital compensation technique.

The characteristics of real hardware components impose additional constraints and introduce sources of error beyond those considered in Chapter 5 that can not be easily modelled or simulated. These additional conditions require special attention, for example in the scaling of signals. In this chapter we detail techniques that need to be adopted to implement the automatic digital compensation in hardware and software on a practical DSP-based IQ modulator system.

This chapter is organised into four main sections. In Section 6.2 an outline of the DSP platform structure is provided showing the key elements required for automatic

digital compensation and modulator operation. Also in Section 6.2, four separate hardware specific issues are considered in terms of their impact on the automatic digital compensation technique. One of these issues is the subject of the first of the experimental results presented in Section 6.3. Section 6.3 also contains details of the complete IQ modulator system tested and information about the measurements that were made to obtain the experimental results that are presented. The experimental results presented in the final two parts of Section 6.3 characterise the performance of the automatic digital compensation technique under practical operating conditions. Finally, Section 6.4 contains conclusions from the work presented in this chapter.

6.2 DSP Based Digital Compensation Structure

The main elements of the DSP based IQ modulator and automatic digital compensation structure are shown in Figure 6.1.
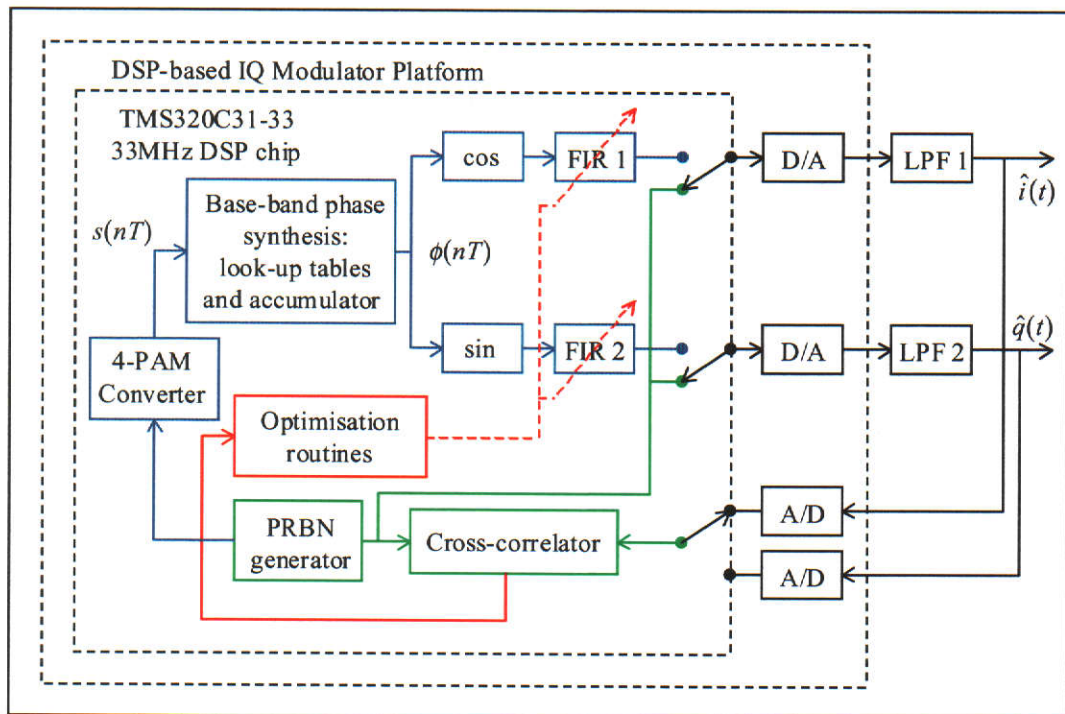

Figure 6.1. Structure of the DSP based IQ modulator with automatic digital compensation.

The DSP based modulator platform shown in Figure 6.1 consists of a DSP chip and D/A and A/D converters and existed as part of a larger project on digital modulators for ERMES signal generation. From Figure 6.1 it can be seen that the core of the

digitally compensated IQ modulator system is a Texas Instruments TMS320C31-33 (abbreviated 'C31) 32-bit floating point DSP chip operating at a clock frequency of 33 MHz.

The elements within the DSP in Figure 6.1 are colour-coded to highlight their function in the automatic digital compensation scheme:

Green: identification of the I and Q channel impulse responses. The time domain channel identification and parameter estimation algorithm is summarised in Table 5.2.

Red: computation of the optimum digital FIR compensation filter weights. The optimisation algorithm for computing the optimum I and Q channel FIR filter tap weights is summarised in the algorithm in Table 4.1.

Blue: operation of the IQ modulator (generating base-band components of the CPFSK signal).

Four important considerations with respect to the implementation of automatic digital compensation on the DSP platform in Figure 6.1 are:

- arithmetic operations and number representation in finite precision,
- sampling rate for input/output operations,
- computation time,
- dynamic distortion in the two reconstruction filters.

These matters were not covered in the implementation issues or the numerical studies sections of Chapter 5 because either

1. they can not be easily modelled or simulated, as is the case with finite precision and dynamic distortion effects, or

2. they are issues that arise from the particular DSP platform used for the implementation described in this chapter, as is the case with sampling rate and computation time.

The four issues listed above are now covered separately in the following four sections.

6.2.1 Finite Precision Effects of the DSP

The 'C31 DSP chip has three floating-point formats: short, single-precision and extended precision (see [112, pp. 4-1 to 4-24] for details). If the extended-precision registers are used, a number, α, is represented as

$$\alpha = \begin{cases} 01.m \times 2^e & s = 0 \\ -10.m \times 2^e & s = 1 \\ 0 & e = -128 \end{cases}, \tag{6.1}$$

where m is a 32-bit binary mantissa, e is an 8-bit exponent and s is the sign bit.

In the case of $\alpha = \text{floating-point}(1.0)$, the smallest number (in magnitude) that will still change α in 'C31 extended precision floating-point addition can be found from

$$\begin{aligned} & 01.0000000000000000000000000000000 \times 2^0 \\ +\, & 00.0000000000000000000000000000001 \times 2^0 \\ =\, & 01.0000000000000000000000000000001 \times 2^0 \end{aligned} \tag{6.2}$$

Hence, the machine accuracy [80] is

$$\varepsilon_m = 1.0 \times 2^{-31} = 4.6566 \times 10^{-10}. \tag{6.3}$$

Finite numerical precision impacts on the algorithm in Table 4.1 used to compute the I and Q channel FIR compensation tap-weight vectors. Techniques proposed in Chapter 4 for determining the I and Q channel FIR compensation filter coefficients were selected for their robustness in the presence of finite numerical precision. Recall that these included:

- decomposition of the I and Q channel R matrices into their eigenvalues and eigenvectors, and

- a modified Jacobi algorithm for implementing the eigenvalue decomposition.

6.2.2 System Sampling Rate Considerations

Two factors that significantly impact on the maximum sampling rate of the digital system are:

1. conversion time constraints on the D/A and A/D converters, and

2. DSP computation time, i.e., the time required to perform all the operations necessary for the generation of the next I and Q channel output samples.

The first of these factors is dealt with in this section while the DSP computation time is the subject of the next section.

An important parameter in the specification of D/A and A/D converters is the time required to convert the quantity at the devices' input at the current sample instant (digital number or voltage/current) to an output representation of that quantity (voltage/current or digital number).

For the DSP platform shown in Figure 6.1 the two D/A converters have a typical conversion time of $3 \mu s$ thus allowing maximum sampling rates of approximately 330 kHz. The A/D converters available at the time of implementation, however, have typical conversion times of $50 \mu s$ therefore restricting the maximum system sampling rate to 20 kHz.

As outlined in Chapter 2, the digital synthesis of the ERMES base-band I and Q signals requires a system sampling rate of 200 KHz. Therefore, in the implementation and experimental results presented in this chapter, the frequency-domain system parameters that are required to meet the ERMES specifications are scaled by a factor of ten so that the conversion-time constraints on the A/D converters are met. It is noted, however, that A/D converters are commercially available which allow a full-rate implementation of the ERMES system.

6.2.3 Computation Time Considerations

The inclusion of the digital FIR compensation filters only adds two significant real-time constraints, namely the realisation of the two compensation FIR filters and the sampling of the analogue filter outputs during the identification stage. Note that the latter operation is "offline" and does not involve the operation of other elements of the digital modulator and hence does not represent a significant challenge.

While there is a requirement to keep the time to compute the optimal FIR coefficients short (since the system is out of use during this time) it need not be done in real time. For instance, in the implementation presented here (which has not been optimised for speed), the time taken for the algorithm to measure the I and Q channel impulse responses and compute the I and Q channel optimum FIR compensation filters is approximately 20 seconds.

Implementing two, K-tap FIR filters is computationally demanding and must be carried out to meet the real-time constraints. Most DSP chips have specialised architectures for implementing FIR filters.

The code fragment shown in Figure 6.2 is based on the FIR implementation suggested in [112 , pp.11-58 to 11-60] and is indicative of the efficiencies gained through the specialised DSP hardware. It incorporates two circularly addressed arrays, a parallel (single-cycle) floating-point multiply and add and a zero-overhead block repeat.

```
       LDI    @CONSTS+5,BK      ;block size register (BK) = FIR length
       LDI    @IF_PNT,AR0       ;load pointer to filter coefficients
       LDI    @ID_PNT,AR1       ;load current pointer to filter data
       STF    R3,*AR1++(1)%     ;store new data point (circularly)
       MPYF3  AR0++(1),AR1++(1)%,R0   ;h(N-1)x(n-(N-1)) -> R0
       LDF    0.0,R2            ;initialise R2

       RPTS   @CONSTS+6         ;initialise repeat cycle
       MPYF3  AR0++(1),AR1++(1)%,R0   ;h(N-1-i)x(N-(N-1-I)) -> R0
||     ADDF3  R0,R2,R2          ;parallel multiply and add operation
       ADDF3  R0,R2,R3          ;add last product
       STI    AR1,@ID_PNT       ;save last pointer to filter data
```

Figure 6.2. FIR filter implementation.

Typically, the number of machine cycles required for a single execution of routines such as this (i.e., to generate one new FIR filter output sample) is given by

$$\text{FIR}_{\text{cycles}} = C_0 + K \times C_1, \tag{6.4}$$

where K is the FIR filter length and C_0 and C_1 are constant values.

For the 'C31 FIR filter implementation shown in Figure 6.2, C_0 and C_1 are given by

$$\begin{aligned} C_0 &= 10 \\ C_1 &= 1. \end{aligned} \tag{6.5}$$

Hence from (6.4) and (6.5), and for say 50-tap FIR compensation filters the number of cycles required per filter is $\text{FIR}_{\text{cycles}} = 60$. Therefore output samples from both of the 50-tap FIR compensation filters implemented on a 'C31 DSP chip operating at a clock frequency of 33 MHz can be computed in approximately $3.64\,\mu s$. On a 33 MHz DSP it would be tight to include the other modulation functions within the $5\,\mu s$ sampling period of a full-rate ERMES system. However on a 50 or 100 MHz DSP the digital compensation FIR filters would easily be accommodated together with the other modulation functions.

6.2.4 Dynamic Distortion in the Reconstruction Filters

The linear, frequency-domain characteristics of the analogue signal reconstruction filters were investigated in Chapter 3. An additional hardware characteristic of these filters that must also be considered in the implementation of the IQ modulator is dynamic (non-linear) distortion.

Dynamic distortion is caused by non-linear characteristics within the filter such as slew-rate limiting and typically increases with increasing input signal level.

An example of dynamic distortion occurring in one of the filters used in the implementation described in Section 6.3 is given below. Here, three sinusoidal signals are applied consecutively to the input of a 4th order Chebyshev filter with a -3 dB point of approximately 2 KHz. Two input signal level scenarios are considered:

1. Input signal level is 65% of the filter supply rails.

2. Input signal level is 75% of the filter supply rails.

The spectrum of each corresponding filter output signal is measured and shown plotted (for the two input level scenarios) in Figure 6.3 and Figure 6.4. (Note that the attenuation of the 2 kHz and 3 kHz signals is due to the roll-off of the filter.)
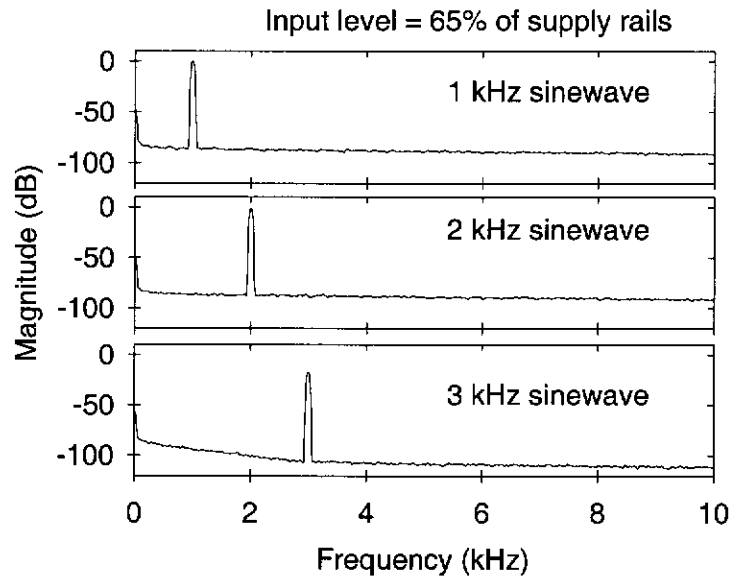

Figure 6.3. Analogue filter magnitude response: Input signal level is 65% of supply rails.
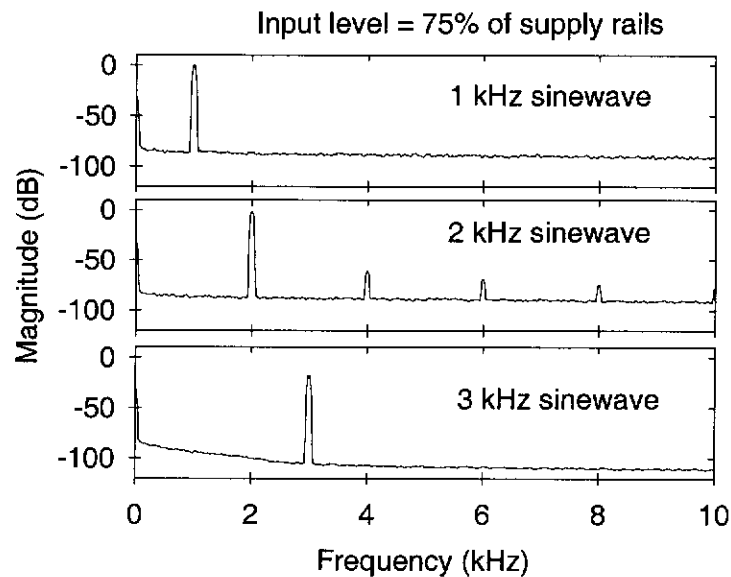

Figure 6.4. Analogue filter magnitude response: Input signal level is 75% of supply rails.

Note the appearance of harmonic products in the output spectrum for the 2 kHz case when the input level is increased.

As illustrated in Section 6.3.3 dynamic distortion can have significant adverse effects on channel identification and ultimately on the quality of compensation achieved. Consequently, particular attention must be paid to peak-to-peak signal values, correct signal scaling and reconstruction filter design. The selection of amplifiers with suitable dynamic performance is critical in building reconstruction filters that produce minimal dynamic distortion of the signal.

6.3 Experimental Results

In this section measurements made on the experimental IQ modulation system are presented that highlight the effectiveness of the automatic digital compensation technique under typical operating conditions.

Section 6.3.1 provides details of the system tested while Section 6.3.2 describes the measurements made. In Sections 6.3.3, 6.3.4, 6.3.5 and 6.3.6 the results of four separate experiments are given that highlight, respectively:

1. The impact of dynamic distortion in the I or Q channels on the automatic digital compensation technique.

2. The effectiveness of automatic digital compensation for nominal Chebyshev characteristic reconstruction filters.

3. The effectiveness of automatic digital compensation for nominal Butterworth characteristic reconstruction filters.

4. The effect on the digital compensation of using a desired channel magnitude response that differs from the nominal Chebyshev response of the reconstruction filters used in Sections 6.3.3 and 6.3.4.

6.3.1 System Tested

A block diagram of the IQ modulator system used to produce the experimental results in the following sections is shown in Figure 6.5.
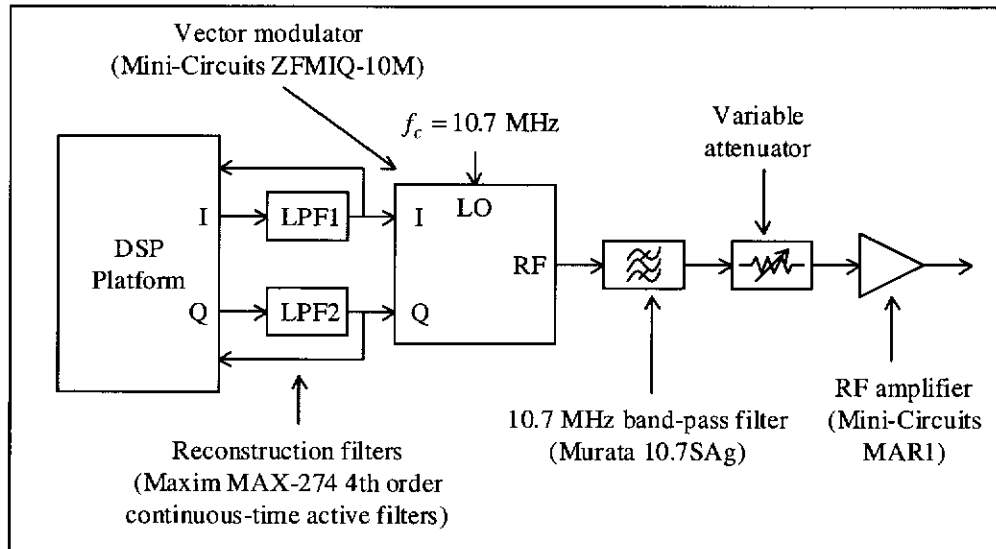

Figure 6.5. Digitally compensated IQ modulator system structure.

The internal structure of the "DSP Platform" block is shown in Figure 6.1. Relevant parameters of the DSP Platform block are listed below:

- System sampling rate $f_s = 20$ kHz.

- Length of digital compensation filters (FIR 1 and FIR 2) $K = 50$ taps.

- PRBN probing sequence for identification of the I and Q channels: 14th order m-sequence, period $= 16383$ (see Section 5.6.3 for more details).

- Modulator input test data symbol sequence: internally generated pseudo-random sequence of period 8192 symbols.

- D/A converters: Analogue Devices AD667 12-bit.

- A/D converters: Analogue Devices AD7580 10-bit.

The two analogue reconstruction filters have 4th order low-pass characteristics and are implemented using a single Maxim MAX274 continuous-time active filter chip. For the experimental results presented in Sections 6.3.3, 6.3.4 and 6.3.6 the nominal design response of the two reconstruction filters is a Chebychev 4th order

characteristic while for the results presented in Section 6.3.5 the nominal filter design is a 4th order Butterworth characteristic. Details of the filter designs are given below:

The I and Q channel Chebyshev response reconstruction filters in Section 6.3.3, 6.3.4 and 6.3.6 are designed with the following parameters:

- Cut-off frequency $f_c = 2$ KHz

- Pass-band ripple = 0.1 dB

- First 2nd order section: $f_0 = 1901.36$ Hz, $Q = 2.18293$

- Second 2nd order section: $f_0 = 1301.22$ Hz, $Q = 0.61801$

To demonstrate the digital compensation technique, the I and Q channel filters are deliberately mismatched by perturbing the f_0 and Q values as shown in Table 6.1.

	First 2nd order section		Second 2nd order section	
	f_o	Q	f_o	Q
I Channel	1996.43	2.2921	1236.16	0.5879
Q Channel	1806.29	2.0738	1366.28	0.6497

Table 6.1. Perturbed 2nd order section parameters for Chebyshev filter implementation.

In Section 6.3.5 the two reconstruction filters have a nominal 4th order Butterworth characteristic with the following parameters:

- Cut-off frequency, $f_c = 2$ kHz

- First 2nd order section: $f_0 = 2001.2$ Hz, $Q = 1.3066$

- Second 2nd order section: $f_0 = 2001.2$ Hz, $Q = 0.5412$.

Again to demonstrate the effectiveness of the digital compensation technique, the I and Q channel responses are deliberately mismatched by perturbing the cut-off frequencies of the two filters as follows:

$$I \text{ channel:} \quad f_c = 1.8 \text{ kHz}$$
$$Q \text{ channel:} \quad f_c = 2.1 \text{ kHz.}$$

DC offsets in the two analogue reconstruction filters can be quite considerable: of the order of hundreds of millivolts [113]. In this implementation, the DC offsets are

removed by manual adjustment of offset-null circuits on each filter. Specific details of the offset-null circuit can be found in [113]. Recall however, that an effective technique to remove the DC offsets in the D/A converters and signal reconstruction filters has already been investigated and implemented [44].

The band-pass filter shown in Figure 6.5 is required at the output of the vector modulator to remove harmonic products generated within the vector modulator.

The variable attenuator shown in Figure 6.5 allows the RF amplifier transfer characteristic to be varied from approximately linear to heavily saturated (non-linear) by controlling the ratio of input drive to power supply level of the RF amplifier. The effect of varying the severity of the RF amplifier non-linearity on the compensated and uncompensated output RF signals is investigated in Section 6.3.5.

6.3.2 Description of Measurements

The following measurements were made for each of the four experiments (reported separately in Sections 6.3.3, 6.3.4, 6.3.5 and 6.3.6).

- **I and Q channel impulse responses.** These time-domain measurements were made as part of the automatic digital compensation algorithm (using the DSP's internal cross-correlation technique). Recall that the time-domain identification technique using cross-correlation provides estimates of the impulse responses of the I and Q discrete-time channels from the D/A converter inputs to the A/D converter outputs shown in Figure 6.1.

- **I and Q channel analogue reconstruction filter magnitude and phase characteristics.** These frequency-domain estimates of the actual I and Q channel analogue reconstruction filters themselves were made by direct, "out-of-circuit" measurements of the filter frequency responses using a HP 3566A Dynamic Signal Analyser.

- **Signal envelope function.** The envelope function measurements were made directly from the output signals of the I and Q channel analogue reconstruction filters using a HP 89441A Vector Signal Analyser (VSA).

For the experimental results presented in Sections 6.3.4 and 6.3.5 the following addition measurements were made:

- **RF amplifier output Power-spectrum.** These measurements were also made using the VSA.

The experimental results presented in Sections 6.3.3, 6.3.4 and 6.3.5 follow the format listed below:

1. Results from the system identification stage:

   A. I and Q channel impulse responses

   B. I and Q channel Magnitude responses

   C. I and Q channel group delay responses

2. Results from the optimisation stage:

   A. I and Q channel optimum compensation filter impulse responses

   B. Compensated I and Q channel magnitude responses

   C. Compensated I and Q channel group delay responses

3. Operational results from the digitally compensated IQ modulator:

   A. Envelope function for the compensated and uncompensated signals

   B. RF amplifier output power spectrum for the compensated and uncompensated signals (Sections 6.3.4 and 6.3.5 only).

For the experimental results reported in Section 6.3.6, only the measurements corresponding to points 2 and 3 above are presented. The results from the system identification stage are the same as those presented in Section 6.3.4 and are therefore not duplicated.

For the system identification stage, three separate impulse responses are shown for each channel and are labelled "DSP-TD", "DSA-TD", and "Theoretical-TD". These results are explained below:

- **"DSP-TD"** - measured in the DSP using the cross-correlation system identification technique.

- **"DSA-TD"** - calculated using an inversed DFT (Discrete Fourier Transform) of the I and Q channel filter frequency responses that were measured using a HP 35665A Dynamic Signal Analyser as described earlier.

- **"Theoretical-TD"** - computed by taking an inverse Fourier transform of the filter transfer function and substituting the actual component values used in the I and Q channel filters.

Note that in all of the figures showing the I and Q channel impulse responses and also showing the I and Q channel FIR compensation filter impulse responses, the sample values are joined by straight lines for ease of visual comparison.

Three sets of data are also shown for the magnitude and group delay results presented in the identification stage and are labelled "DSP-FD", "DSA-FD" and "Theoretical-FD". The results presented were obtained as follows.

- **"DSP-FD"** – I and Q channel magnitude and phase responses calculated from a DFT of the corresponding channels' impulse response as measured by the DSP.

- **"DSA-FD"** – magnitude and phase responses of the I and Q channel analogue filters measured directly using a HP 35665A Dynamic Signal Analyser.

- **"Theoretical-FD"** – magnitude and phase responses calculated from the filter transfer function using the actual I and Q channel filter component values.

For the optimisation stage the magnitude and group delay results shown for each channel were obtained as follows:

- **"Uncompensated"** – magnitude and group delay responses calculated from the inverse DFT of the I and Q channel impulse responses as measured by the DSP time-domain identification algorithm.

- **"Compensated"** – magnitude and group delay responses obtained by multiplying the DFT of the I and Q channel impulse responses (measured using the DSP) with the DFT of the corresponding channels' optimum FIR compensation filter.

Note that the frequency responses of the compensated and uncompensated I and Q discrete-time channels are periodic with period $f_s = 20\,\text{kHz}$. Only a small section of the frequency response characteristics of magnitude and group delay are shown in the figures in Sections 6.3.3, 6.3.4, 6.3.5 and 6.3.6. This allows important details of the pass-band characteristics of the I and Q channel responses to be seen more clearly.

Note also that all of the group delay results presented in the following four sections are computed from the phase responses by calculating the gradients of the lines joining consecutive points on the phase response. In all of the group delay plots, the mean delay is removed from the data. This allows comparison of the compensated and uncompensated channels where the mean delay is considerably different due to the introduction of the two FIR compensation filters.

In the results presented for the optimisation stage, the desired response, $d(nT)$, (discussed in Section 4.4) is the discrete-time impulse response of a filter with a frequency response given by

$$D\left(e^{j\omega T}\right) = \left|H\left(j\omega\right)\right| e^{-j\omega\tau_0}, -\omega_s/2 \le \omega \le \omega_s/2. \tag{6.6}$$

where $f_s = \omega_s/2\pi$ is the system sampling frequency. The desired channel delay parameter, τ_0, in (6.6) is determined as described in Section 4.8.4 to be

$$\tau_0 = 1.4\,\text{ms}. \tag{6.7}$$

In Sections 6.3.3 and 6.3.4 the function $H\left(j\omega\right)$ is the frequency response of a 4th order Chebyshev characteristic analogue filter given by

$$H\left(j\omega\right) = \prod_{i=1}^{2} \frac{\omega_i}{\omega_i^2 - \omega^2 + j\left(\omega_i/Q_i\right)}, \tag{6.8}$$

where
$$\begin{aligned}\left\{\omega_i\right\} &= \left\{2\pi \times 1901.36, 2\pi \times 1301.22\right\} \\ \left\{Q_i\right\} &= \left\{2.18293, 0.61801\right\}.\end{aligned} \tag{6.9}$$

In Sections 6.3.5 and 6.3.6 the function $H\left(j\omega\right)$ is the frequency response of a 4th order Butterworth characteristic analogue filter given by

$$H(j\omega) = \prod_{i=1}^{2} \frac{\omega_0}{\omega_0^2 - \omega^2 + j(\omega_0/Q_i)}, \tag{6.10}$$

where
$$\begin{aligned} \omega_0 &= 2\pi \times 2001.2 \\ \{Q\} &= \{1.3066, 0.5412\} \end{aligned} \tag{6.11}$$

6.3.3 Effect of Dynamic Distortion on Digital Compensation

This experiment demonstrates the detrimental effect of dynamic distortion in the reconstruction filters on the automatic digital compensation technique.

Chebyshev characteristic reconstruction filters described in Section 6.3.1 are used and, in this experiment the filter input signals are scaled so that the peak value of the input signal is greater than 75% of the filter supply rails. This results in the dynamic distortion shown in Figure 6.3.

Identification

The impulse responses measured using the cross-correlation technique are shown for each channel in Figure 6.6 and Figure 6.7.
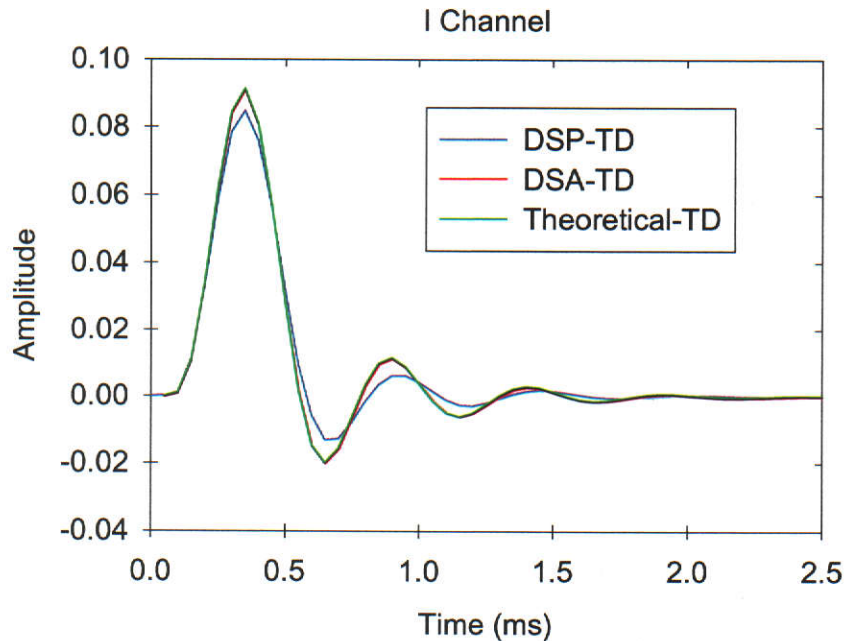

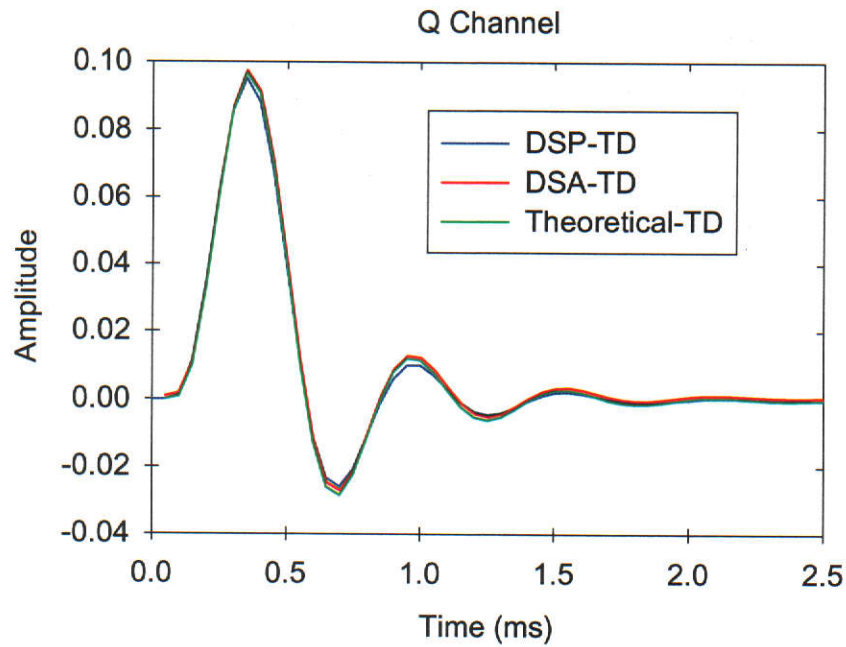**Figure 6.6.** I channel impulse responses.

Figure 6.7. Q channel impulse responses.

From Figure 6.6 it can be seen that the I channel impulse response as measured by the DSP departs from the actual response. The effect is not as noticeable in the measured Q channel impulse response since the gain values of the two stages of this filter are lower and the dynamic distortion is not as severe. Error in the impulse response estimation above is reflected in the magnitude responses of Figure 6.8 and Figure 6.9, and the group delay responses of Figure 6.10 and Figure 6.11.
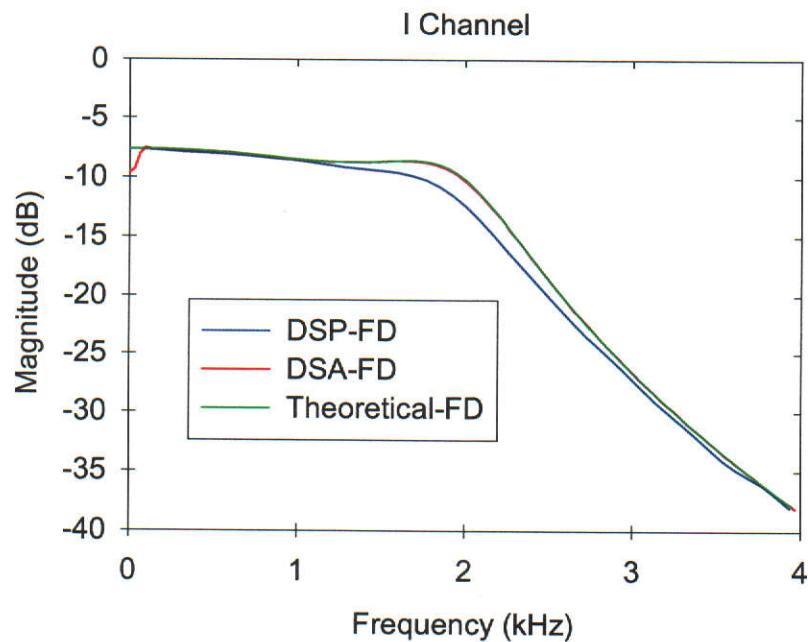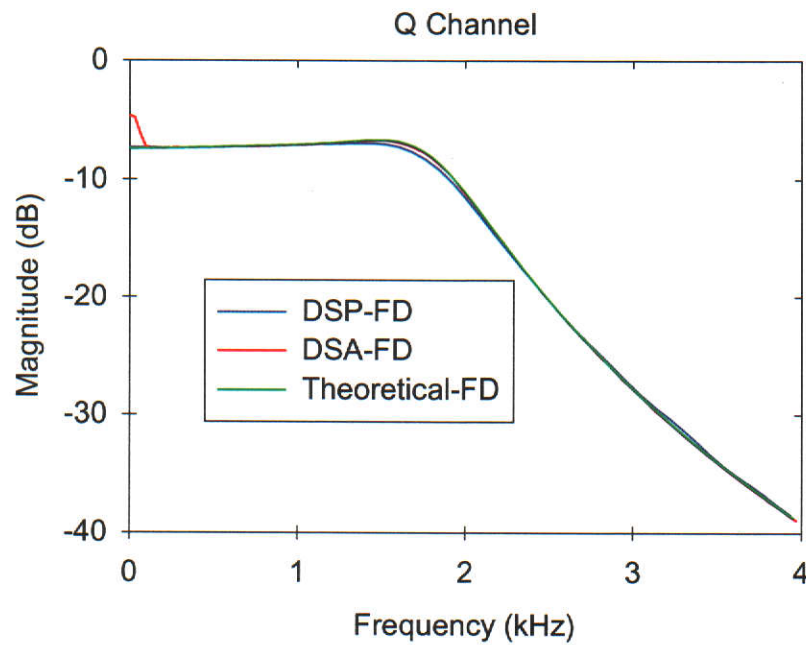

Figure 6.8. I channel magnitude responses.

Figure 6.9. Q channel magnitude responses.

The departures in the red plots in Figures 6.8 and 6.9 above and also in Figures 6.10 and 6.11 below for frequencies close to DC are measurement artefacts of the HP 35665A Dynamic Signal Analyser.
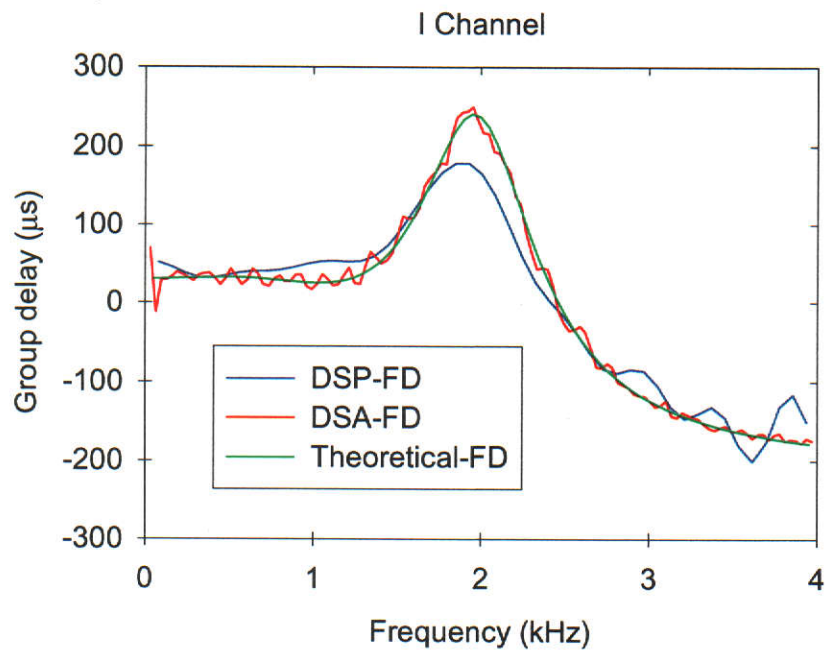

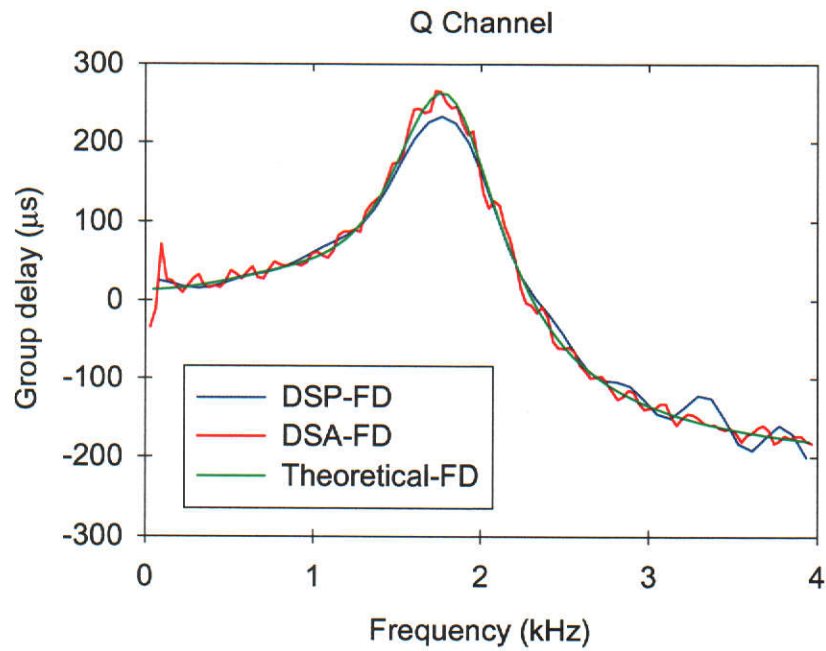**Figure 6.10.** I channel group-delay responses (mean delay removed).

Figure 6.11. Q channel group-delay responses (mean delay removed).

Optimisation

The measured I and Q channel impulse responses are used to computer the optimum sets of I and Q channel FIR filter weights which are shown in Figure 6.12.
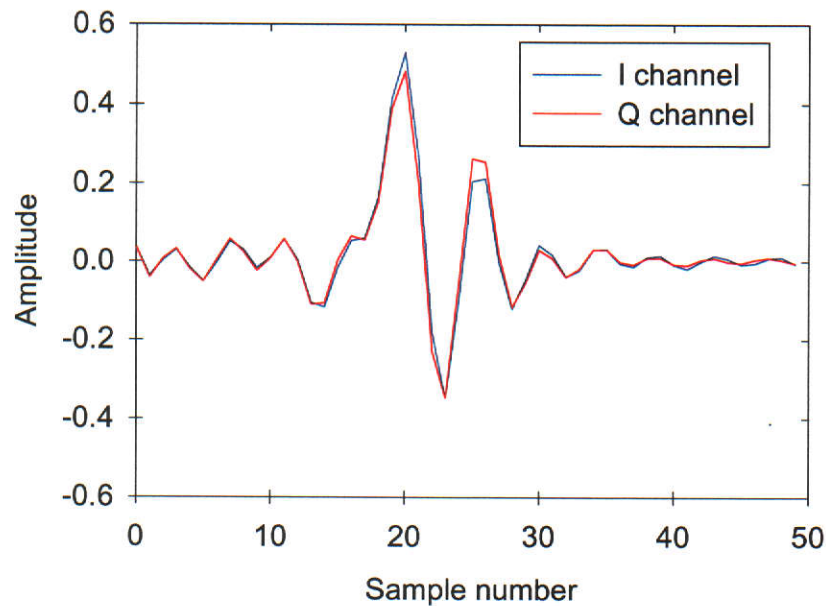

Figure 6.12. I and Q channel FIR digital compensation filter impulse responses.

Figure 6.13 and Figure 6.14 show the result of digital compensation on the I and Q channel magnitude and group delay characteristics respectively. Note that in Figure 6.13 the "I compensated" and "Q compensated" plot values are so close that they can not be separated on the vertical scale chosen. Note also that the measured magnitude responses in Figure 6.13 ("Uncompensated" plots) roll-off earlier than the compensated channel magnitude responses. This is due to two factors:

1. The particular realisations of the two Chebyshev analogue low-pass filters result in cut-off (-3 dB) frequencies that are lower than the nominal filter cut-off frequency.

2. The dynamic distortion in the analogue filters has caused the channel identification technique to return estimates of the I and Q channel responses that are significantly in error.
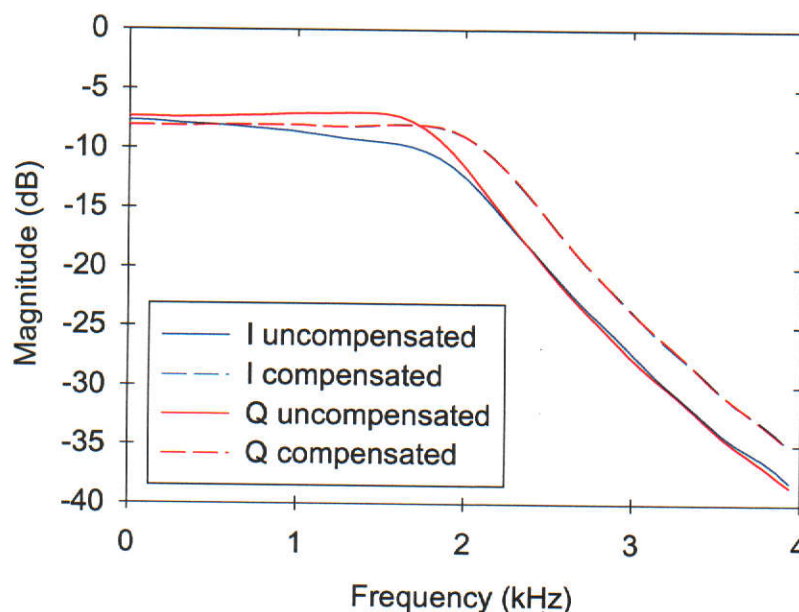

Figure 6.13. Effect of digital compensation on I and Q channel magnitude responses.
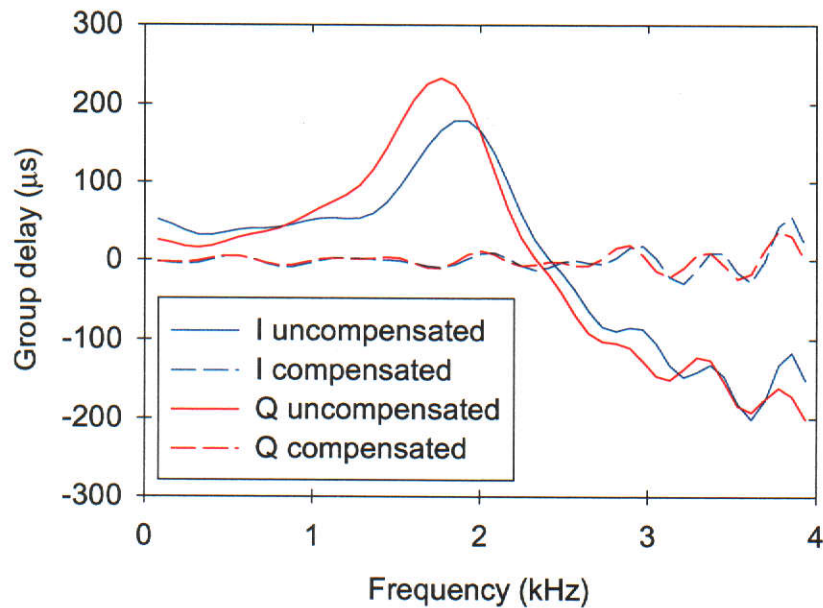
Figure 6.14. Effect of digital compensation on I and Q channel group delay responses (mean delay removed).

IQ Modulator Operation

The effect of dynamic distortion on the quality of digital compensation can be seen clearly in Figure 6.15 which shows the CPFSK signal envelope for the IQ modulator system with and without the digital compensation FIR filters in Figure 6.12 in place. As can be seen there is only slight improvement in the reduction of the envelope ripple.
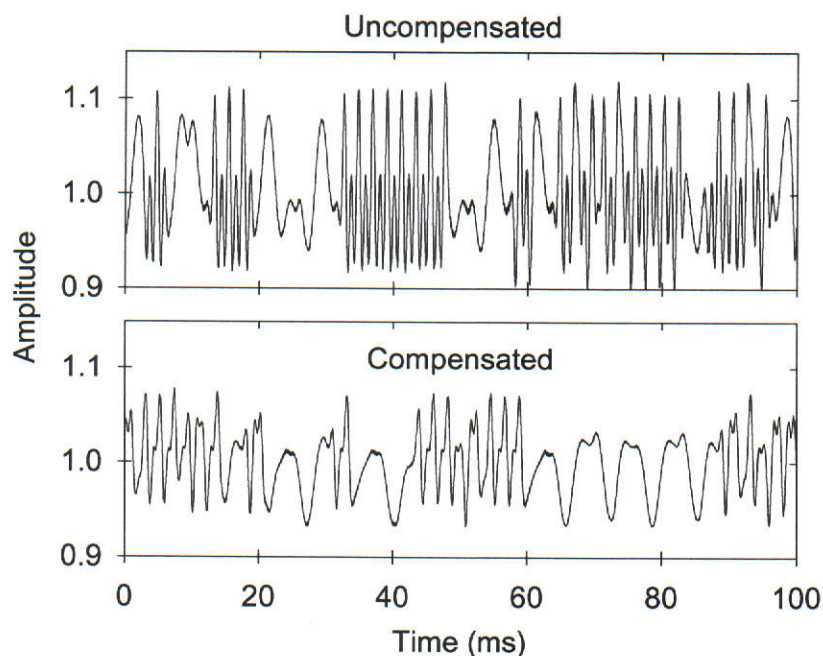

Figure 6.15. Envelope ripple without and with digital compensation.

The envelope function measurements shown in Figure 6.15 are quantified in Table 6.2 where a reduction by a factor of approximately 1.7 in the RMS value of the envelope ripple is reported (significantly lower than the AM reductions reported in the following experiments).

	RMS value (mV)
Uncompensated system	18.6
With digital compensation	11.9
Reduction factor	1.6

Table 6.2. RMS values of AM present in the CPFSK signal envelope: Effects of dynamic distortion.

6.3.4 Chebyshev Response Reconstruction Filters

For the results presented in this section the I and Q channel analogue reconstruction filters have a nominal 4th order Chebyshev characteristic and are implemented as described in Section 6.3.1. In contrast to the experimental results presented in the previous section, however, the input signal level to the filters, while still maintained at practically useful levels, is designed to ensure minimal dynamic distortion of the I and Q channel signals.

Identification

The results of the channel identification stage of the automatic compensation algorithm are shown in the impulse responses in Figure 6.16 and Figure 6.17, and in the frequency domain characteristics of magnitude in Figure 6.18 and Figure 6.19 and group delay in Figure 6.20 and Figure 6.21. A description of these measurements is given in Section 6.3.2.
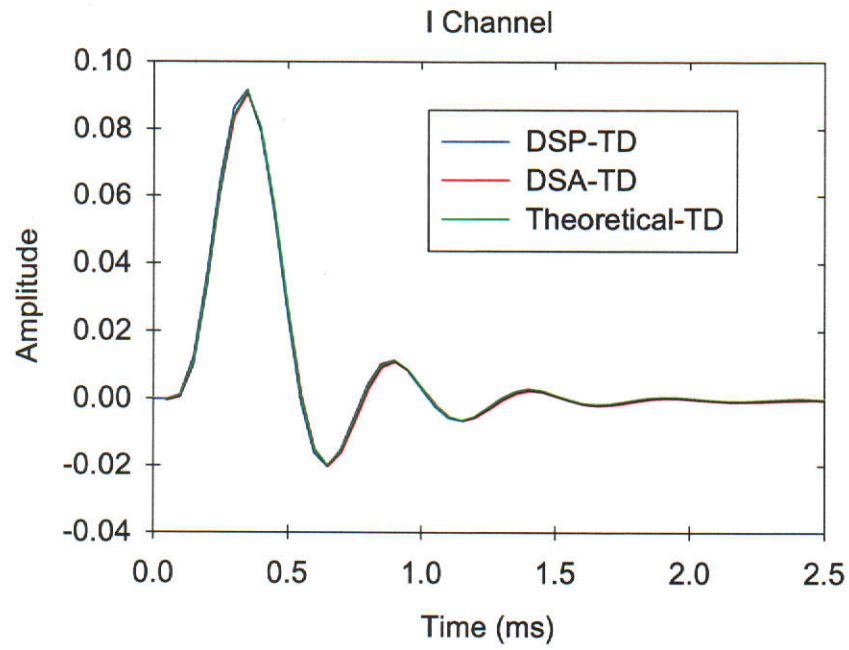
Figure 6.16. I channel impulse responses.
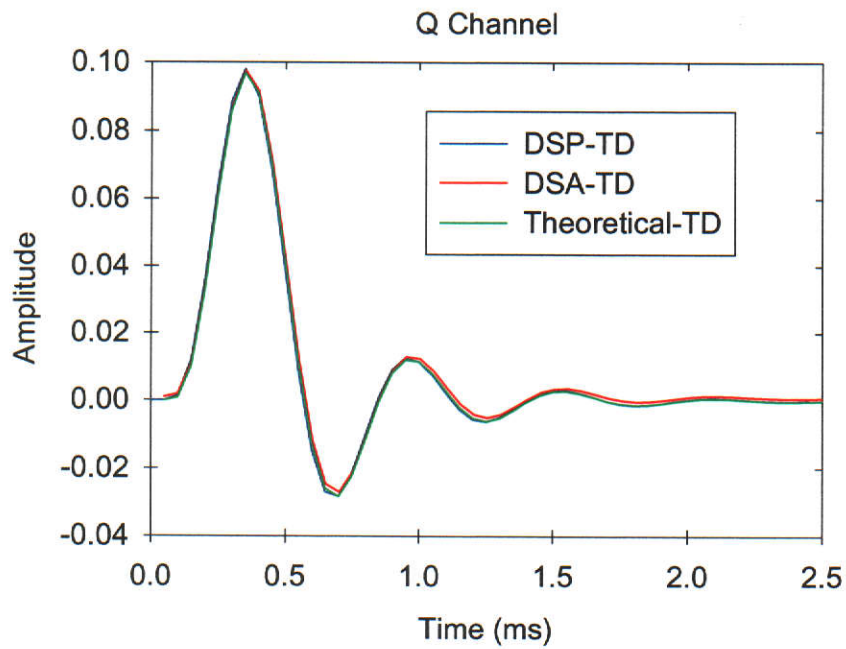
Figure 6.17. Q channel impulse responses.
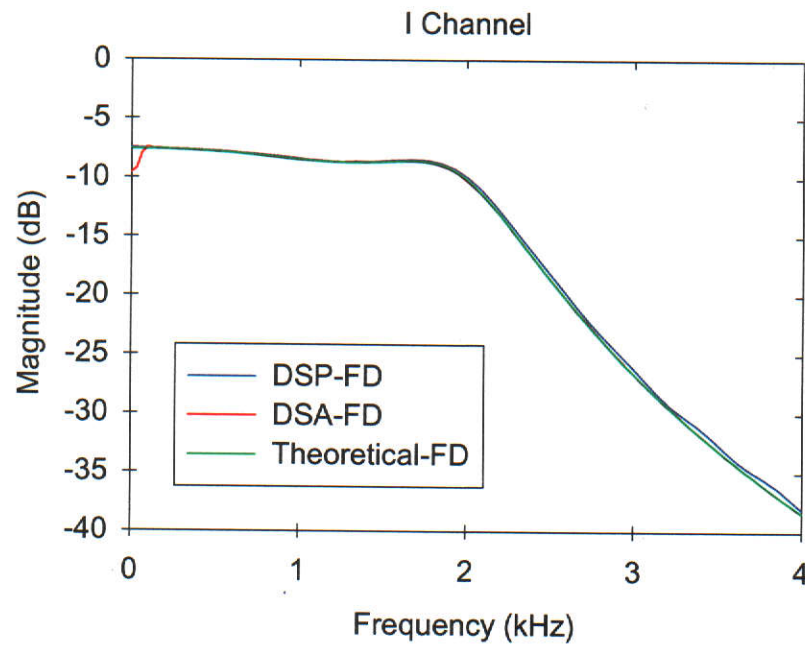
Figure 6.18. I channel magnitude responses.
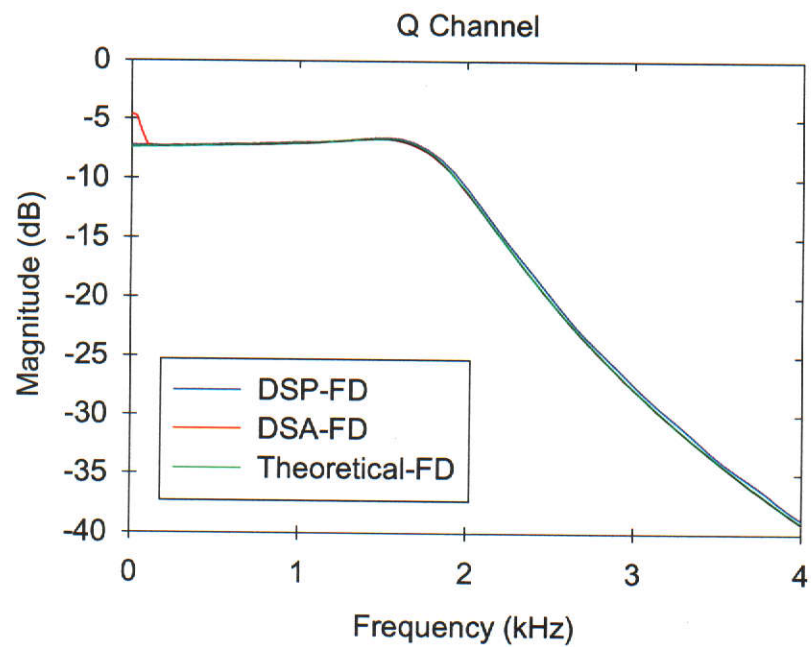
Figure 6.19. Q channel magnitude responses.
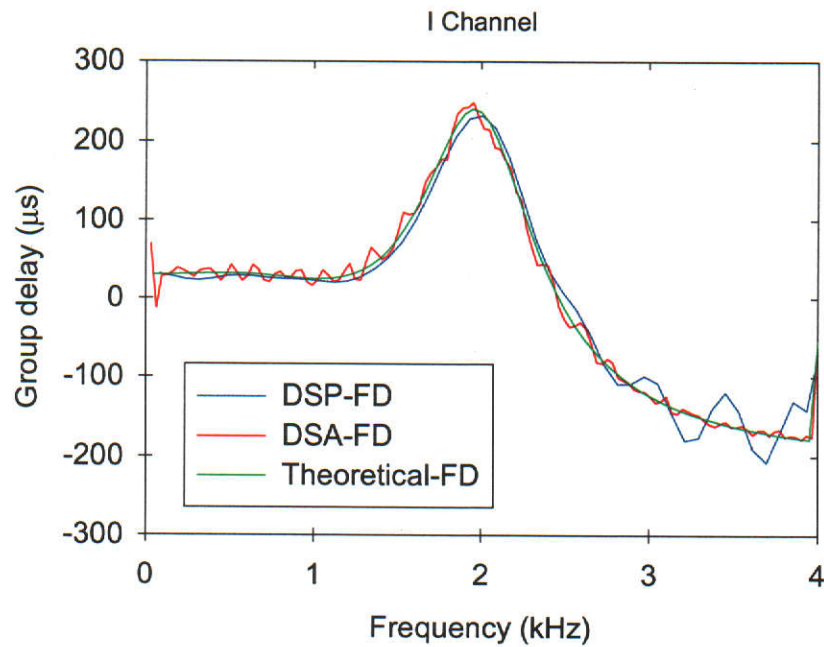
I Channel

Figure 6.20. I channel group delay responses (mean delay removed).
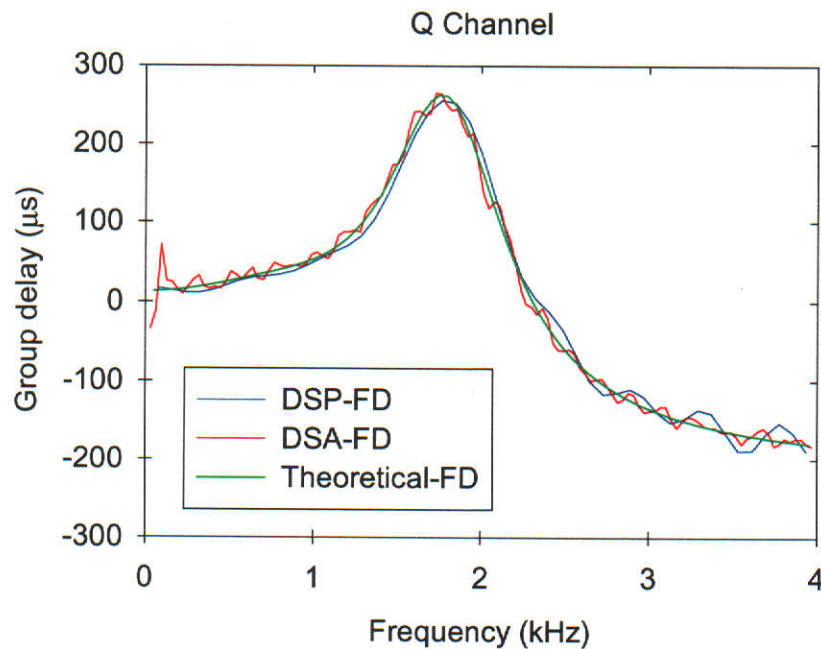
Q Channel

Figure 6.21. Q channel group delay responses (mean delay removed).

Note from Figure 6.16, Figure 6.18 and Figure 6.20 that the system identification technique performs well and gives estimates of the I and Q channels that closely match both the independent measurements from the DSA and the theoretically predicted responses.

Optimisation

The measured impulse responses shown in Figure 6.16 and Figure 6.17 are used by the optimisation routines to find the optimum digital compensation FIR filters. The impulse responses of these compensation filters (for the I and Q channels) are shown in Figure 6.22 and the frequency domain characteristics of the compensated I and Q channels are compared with the uncompensated channel characteristics in Figure 6.23 and Figure 6.24. (Note that the same comments made in Section 6.3.3 regarding the roll-off characteristics of the plots in Figure 6.13 also apply to the plots in Figure 6.24.)
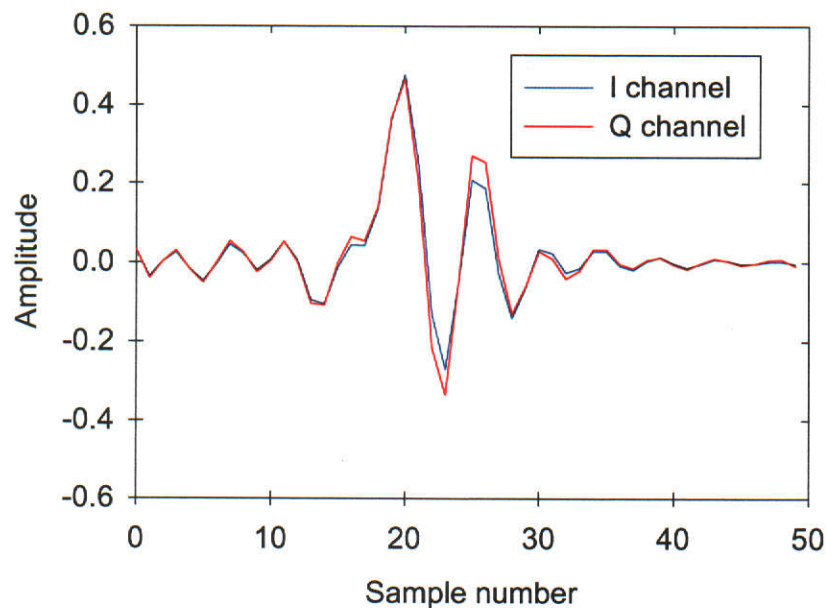
Figure 6.22. I and Q channel FIR digital compensation filter impulse responses.
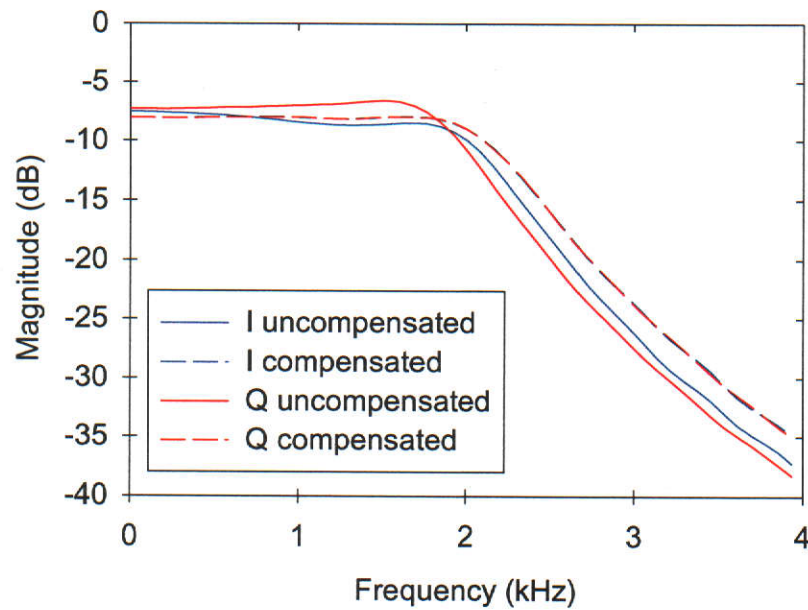
Figure 6.23. Effect of digital compensation on I and Q channel magnitude responses.
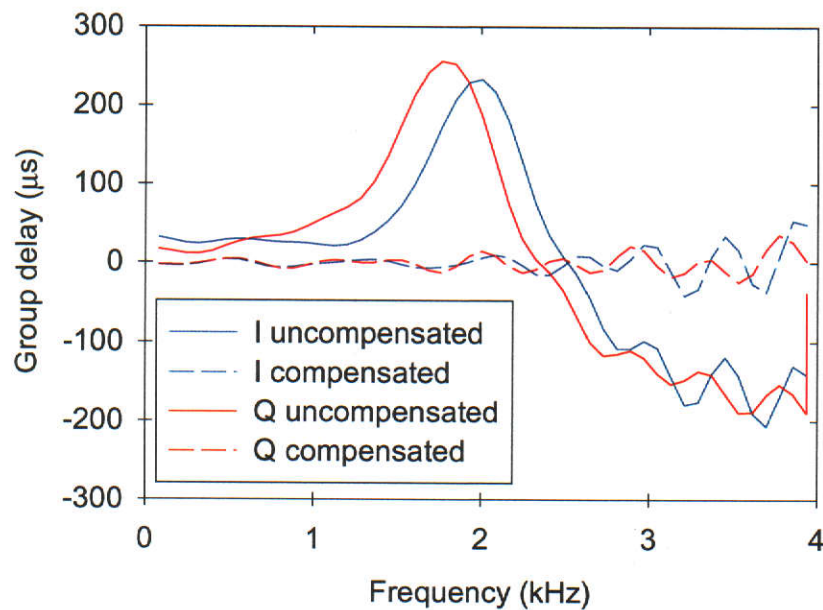
Figure 6.24. Effect of digital compensation on I and Q channel group delay responses (mean delay removed).

From Figure 6.23 and Figure 6.24 it is clear that the I and Q channel frequency response characteristics are improved significantly with the inclusion of the FIR compensation filters: mismatch is removed from the magnitude responses and the group delay of the compensated channels is virtually flat through the pass-band.

IQ Modulator Operation

The digital compensation filters shown in Figure 6.22 are now integrated into the IQ modulator. Figure 6.25 shows the envelope function resulting from the modulation system with and without the digital compensation filters in place.
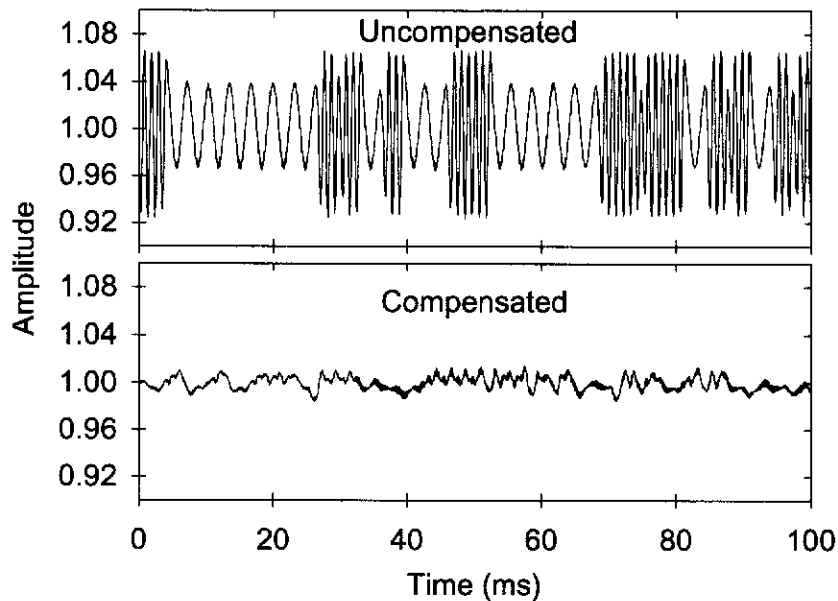
Figure 6.25. Envelope ripple without and with digital compensation.

The RMS values of the signals shown in Figure 6.25 are given in Table 6.3 and provide a quantitative insight into the effectiveness of this technique.

	RMS value (mV)
Uncompensated system	13.06
With digital compensation	2.07
Reduction factor	6.3

Table 6.3. RMS values of AM present in the CPFSK signal envelope:
Chebyshev response reconstruction filters.

From the figures given in Table 6.3 we can determine a reduction in RMS ripple by a factor of approximately 6.

Figure 6.26 shows the output power spectrum of the RF amplifier for the uncompensated and compensated signals. The measurements for this figure were obtained by adjusting the variable attenuator shown in Figure 6.5 so that the RF amplifier was operating approximately at its 1dB compression point.
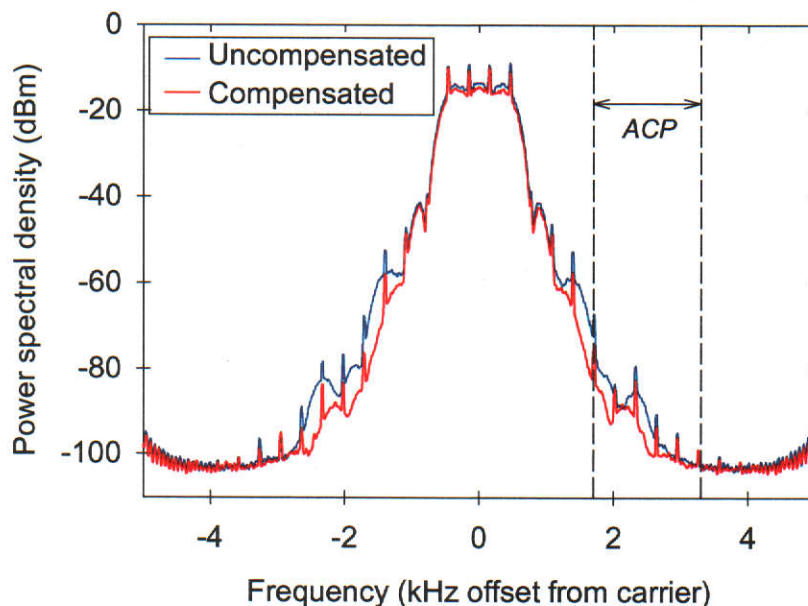
Figure 6.26. RF amplifier output power spectrum.

From the output signal power spectrum plots in Figure 6.26 there is an obvious improvement in the signal spectrum for the digitally compensated modulator. Note the increased side-lobes in the spectrum of the uncompensated signal, particularly in the adjacent channel region indicated by the *ACP (Adjacent Channel Power)* markers. The ACP is defined by the ERMES standard [11] as the power in the band 17 kHz to 33 kHz either side of the carrier and referenced to the carrier power. For the scaled signal scenario considered in this chapter, this corresponds to the power in the band 1.7 kHz and 3.3 kHz either side of the carrier. The ACP values measured for the spectrum plots in Figure 6.26 are given in Table 6.4.

	ACP value (dBc)
Uncompensated system	-67.2
Digitally compensated system	-71.7
Improvement	4.5

Table 6.4. ACP measurements for the uncompensated and compensated modulator systems: Chebyshev response reconstruction filters.

6.3.5 Butterworth Response Reconstruction Filters

For the results presented in this section the I and Q channel analogue reconstruction filters have a nominal 4th order Butterworth characteristic and are implemented as described in Section 6.3.1. As in the previous section the input signal level to the filters is designed to ensure minimal dynamic distortion of the I and Q channel signals.

Identification

The results of the channel identification stage of the automatic compensation algorithm are shown in the impulse responses in Figure 6.27 and Figure 6.28, and in the frequency domain characteristics of magnitude in Figure 6.29 and Figure 6.30 and group delay in Figure 6.31 and Figure 6.32. A description of these measurements is given in Section 6.3.2.
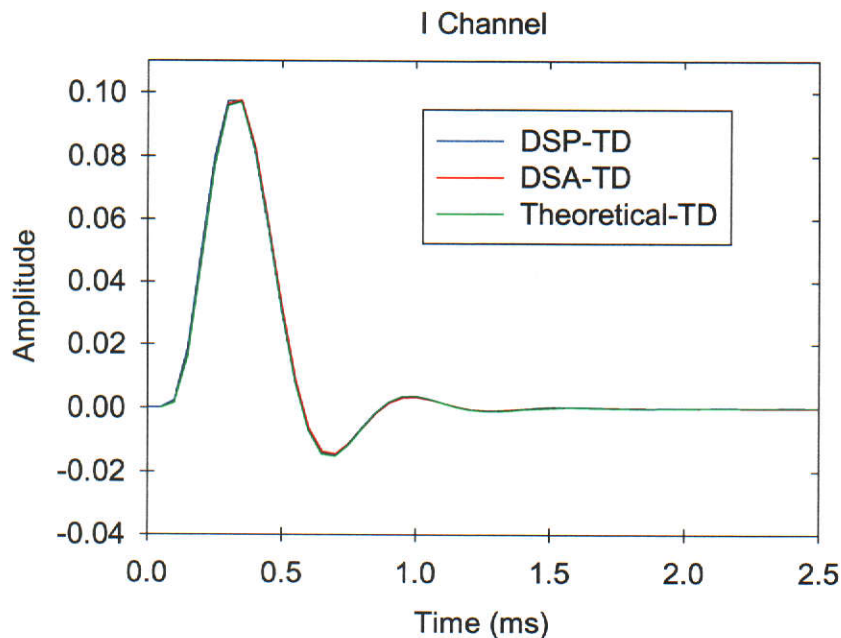
Figure 6.27. I channel impulse responses.
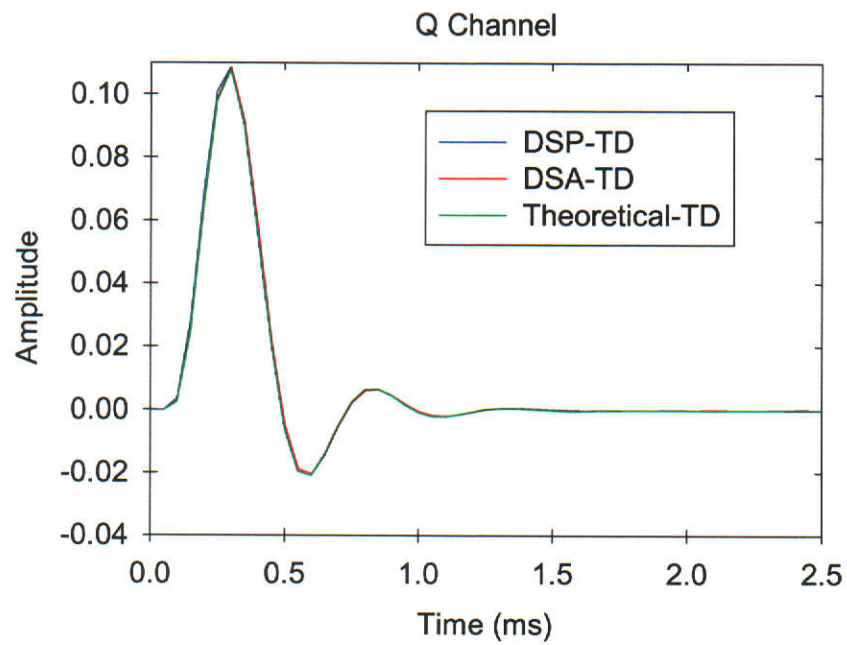
Q Channel

Figure 6.28. Q channel impulse responses.
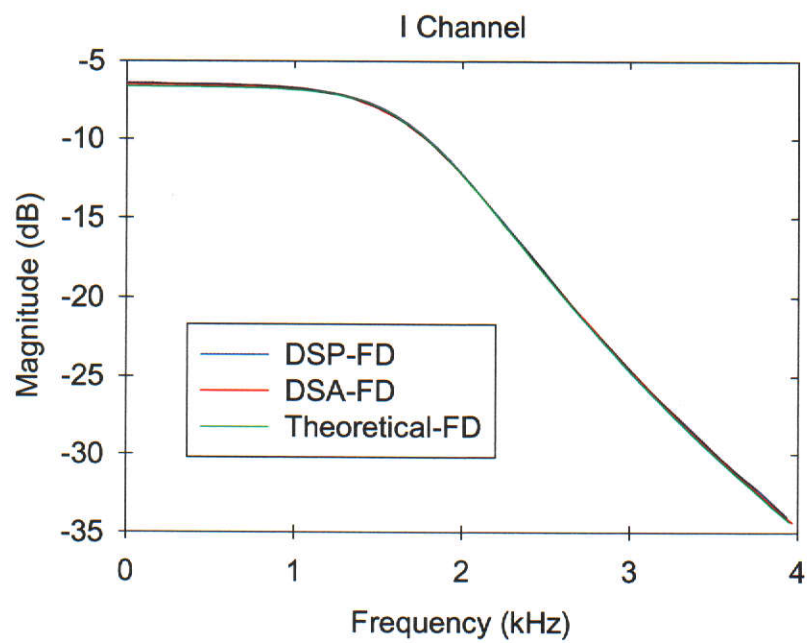
I Channel

Figure 6.29. I channel magnitude responses.
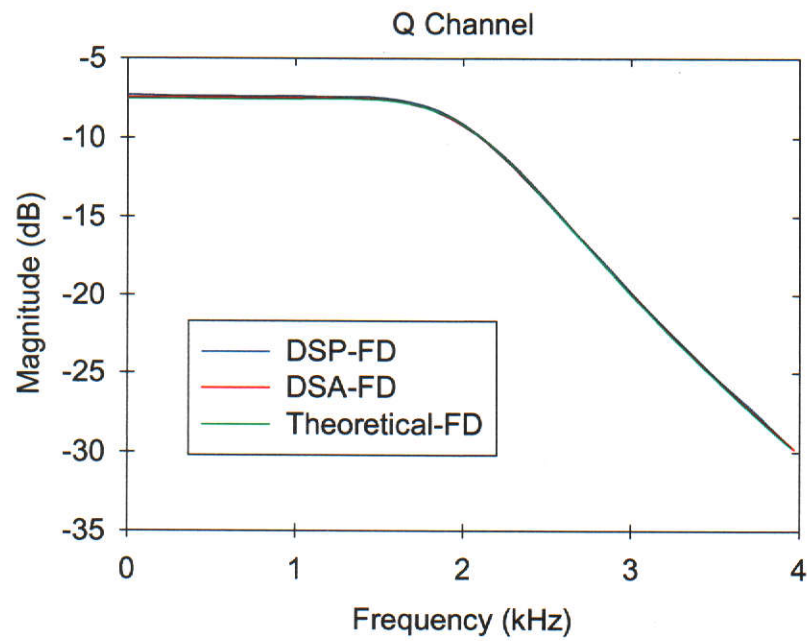
Figure 6.30. Q channel magnitude responses.
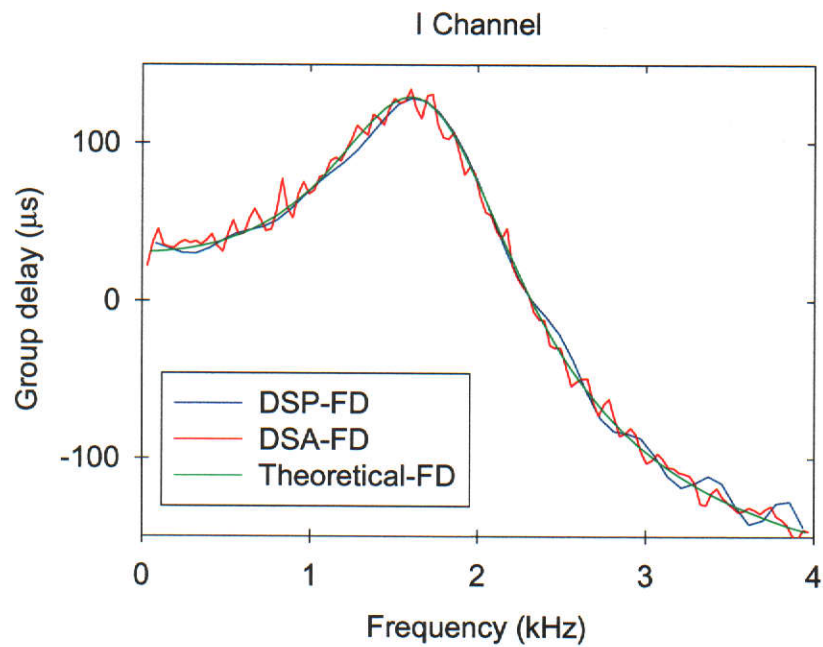
Figure 6.31. I channel group delay responses (mean delay removed).
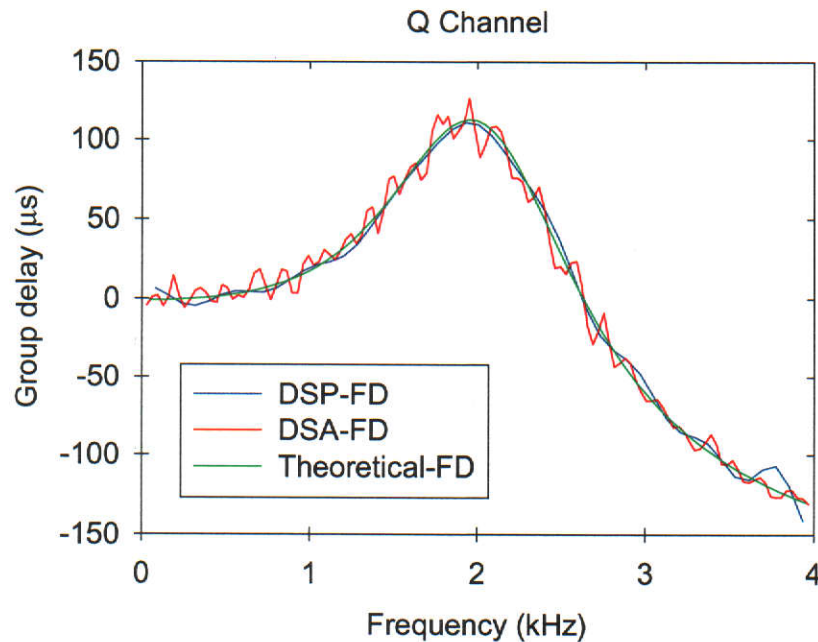
Figure 6.32. Q channel group delay responses (mean delay removed).

From Figures 6.27 to 6.32 it is again clear that the system identification technique provides good estimates of the channel parameters.

Optimisation

The optimum I and Q channel digital FIR compensation filters are computed using the impulse response measurements shown in Figure 6.27 and Figure 6.28. The impulse responses of the optimum compensation filters are shown in Figure 6.33 and the frequency domain characteristics of the compensated I and Q channels are compared with the uncompensated channel characteristics in Figure 6.34 and Figure 6.35. (Note that the values for the "I compensated" and "Q compensated" plots in Figure 6.34 are so close that they can not be separated on the vertical scale chosen. Note also that the difference between the roll-off characteristic of the blue "I uncompensated" plot and the other three plots in Figure 6.34 is due to differences in cut-off frequencies. The actual I-channel filter has a cut-off frequency of approximately 1.8 kHz while the cut-off frequencies of the Q-channel filter and the desired channel response are 2.1 kHz and 2.0 kHz respectively.)
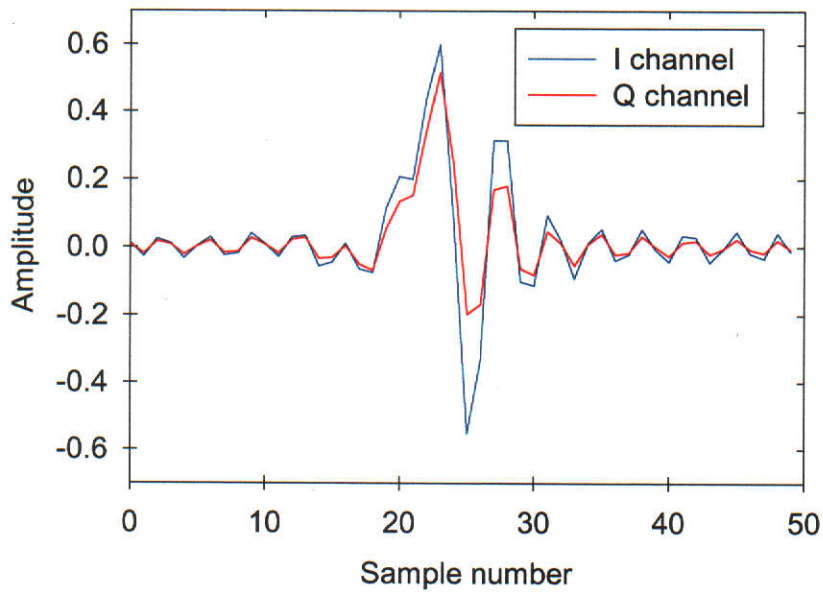
Figure 6.33. FIR digital compensation filter impulse responses.
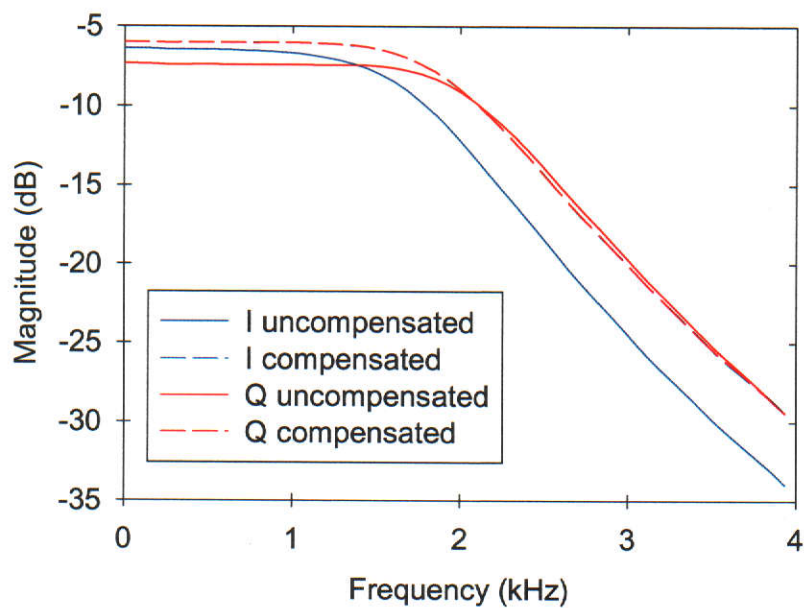
Figure 6.34. Effect of digital compensation on I and Q channel magnitude responses.
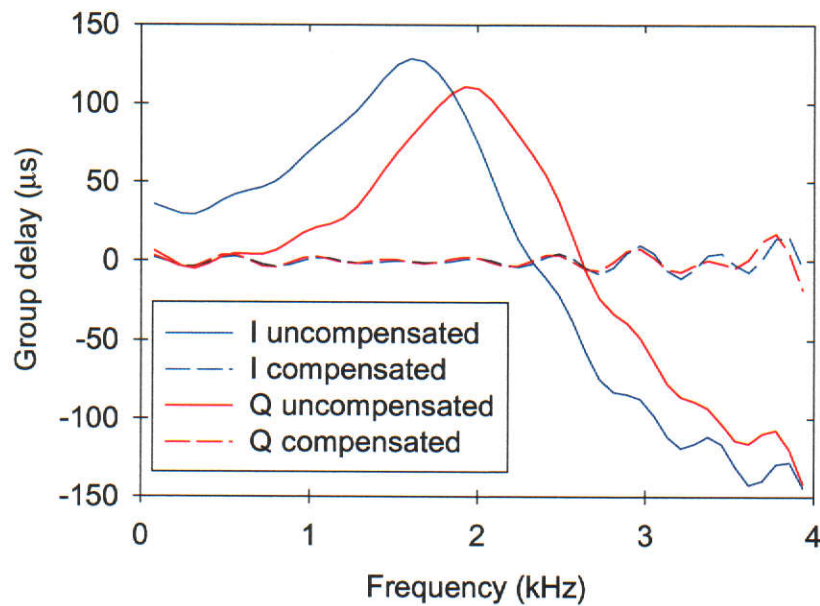
Figure 6.35. Effect of digital compensation on I and Q channel group
delay responses (mean delay removed).

From Figure 6.34 and Figure 6.35 it is again clear that the digital compensation filters provide significant improvement in the I and Q channel frequency-domain characteristics.

IQ Modulator Operation

Envelope measurements made on the system with and without the digital compensation filters in place are shown in Figure 6.36, and again, demonstrate the effectiveness of the digital compensation technique.
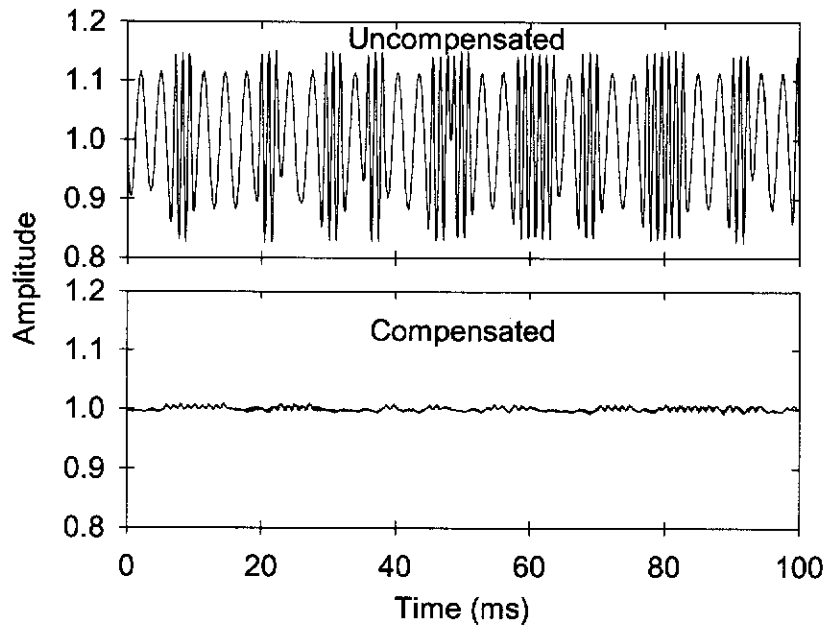
Figure 6.36. Envelope ripple without and with digital compensation.

The measurements plotted in Figure 6.36 are a clear indication that the digital compensation technique provides a significant reduction of AM in the CPFSK signal envelope function. The RMS values of the signals in Figure 6.36 are provided in Table 6.5.

	RMS value (mV)
Uncompensated system	29.29
With digital compensation	1.14
Reduction factor	26

Table 6.5. RMS values of AM present in the CPFSK signal envelope: Butterworth reconstruction filters.

From Table 6.5 the RMS value of the residual AM in the CPFSK signal envelope is reduced by a factor of approximately 26.

Figure 6.37 shows the output power spectrum of the RF amplifier for the uncompensated and compensated signals. The measurements for this figure were obtained by adjusting the variable attenuator shown in Figure 6.5 so that the RF amplifier was operating approximately at its 1dB compression point.
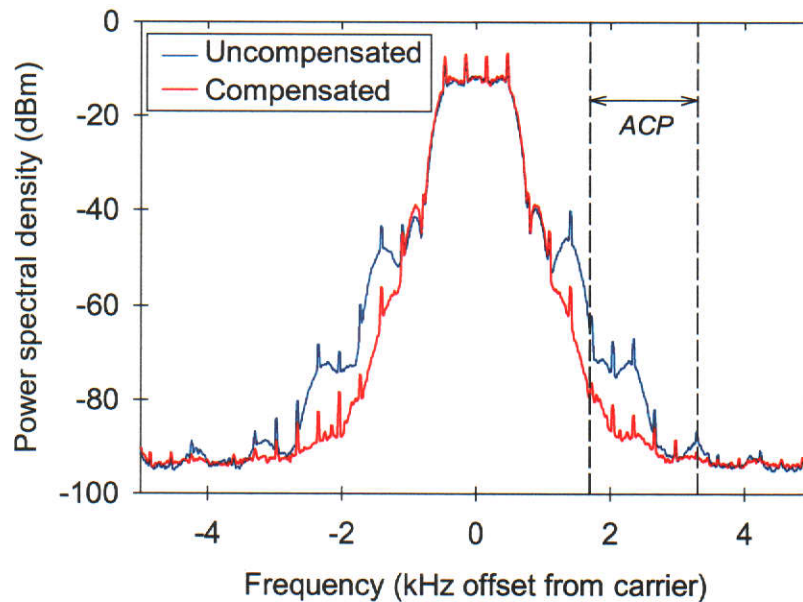
Figure 6.37. RF amplifier output power spectrum.

From the output signal power spectrum plots in Figure 6.37 there is significant reduction in the side-lobe levels for the signal generated by the digitally compensated system. The ACP (see Section 6.3.4) values measured for the spectrum plots in Figure 6.37 are given in Table 6.6.

	ACP value (dBc)
Uncompensated system	-59.3
Digitally compensated system	-72.3
Improvement	13.0

Table 6.6. ACP measurements for the uncompensated and compensated modulator systems: Butterworth response reconstruction filters.

As outlined in Section 3.5, RF power amplifiers with highly non-linear transfer characteristics are often used for the transmission of constant envelope signals such as CPFSK. In the final part of this experiment the effectiveness of the automatic

digital compensation in reducing adjacent channel interference (measured as ACP) for varying degrees of non-linearity in the RF amplifier is investigated.

Figure 6.38 shows the ACP values measured from the RF amplifier output signal spectrum for a number of amplifier RF input drive levels and for the compensated and uncompensated modulator systems. A range of amplifier RF input drive levels are chosen that result in corresponding amplifier transfer characteristics that range from relatively linear to highly non-linear.
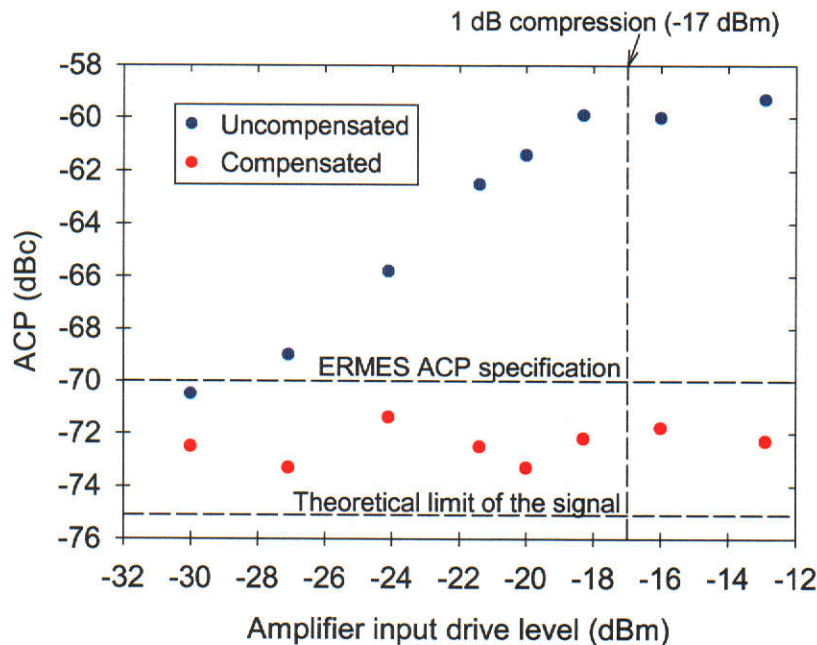
Figure 6.38. ACP measurements for a number of RF amplifier input drive levels.

From the results in Figure 6.38 it can be seen that the reduction in envelope ripple using the digital compensation technique results in output signals from the modulator system that meet ACP requirements even when RF amplifier non-linearity is significant. Thus, one need not use power amplifier *back-off* in the transmitter section to meet requirements on spectral emissions. It is also important to note that the ACP measurements for the compensated system never exceed the upper ACP bound specification for ERMES signals of −70 dBc thus meeting the adjacent channel emission requirements for all cases considered.

6.3.6 Effect of Different Desired Magnitude Response

An underlying assumption in Sections 6.3.3, 6.3.4 and 6.3.5 is that the desired channel response has the same magnitude characteristic as that of the nominal analogue reconstruction filter response. Recall from Section 4.4 that this approach was proposed to ensure that the degrees of freedom in the optimisation are used effectively in meeting the objective of reducing envelope ripple. However, it is assumed in this approach that the nominal reconstruction filter response is sufficiently flat through the pass-band to produce acceptable envelope ripple levels. In the case where the nominal reconstruction filter response does not meet this requirement a different desired channel response must be chosen.

In this section the effect of using a desired channel response that has a magnitude characteristic that is not the same as that of the nominal analogue filter response is briefly considered. However, a full investigation into this issue is left for future work.

The I and Q channel reconstruction filters used to produce the results in this section have the same 4th order Chebyshev response as those in Sections 6.3.3 and 6.3.4. The desired channel response is given by (6.6), (6.7), (6.10) and (6.11) (4th order Butterworth low-pass magnitude characteristic, linear phase).

The results of the system identification stage are the same as those presented in Section 6.3.4 and are therefore not duplicated here.

<u>**Optimisation**</u>

With the I and Q channel impulse responses estimated from the channel identification stage and shown in Figure 6.16 and Figure 6.17 the optimum I and Q channel FIR digital compensation filters are computed. The impulse responses of the FIR compensation filters are shown in Figure 6.39 while the frequency domain characteristics of the compensated I and Q channels are compared with the uncompensated channel characteristics in Figure 6.40 and Figure 6.41
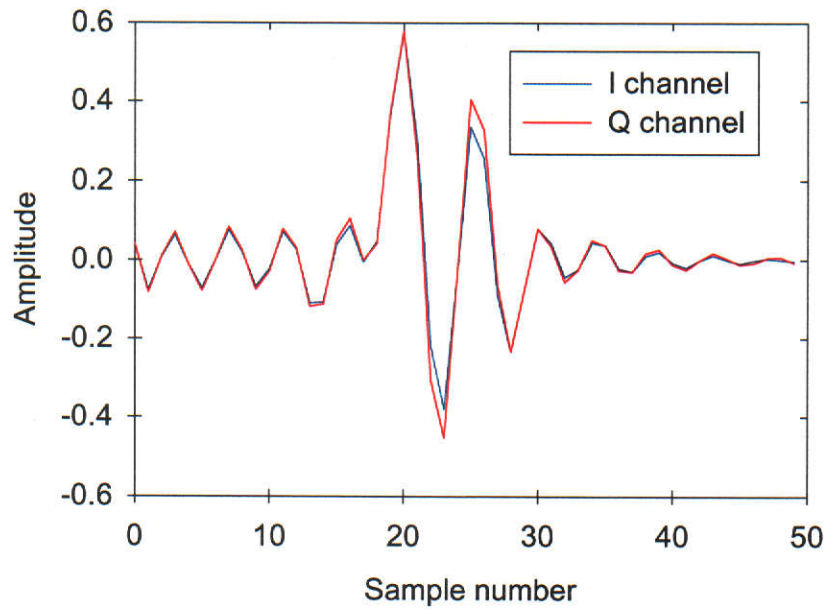
Figure 6.39. FIR digital compensation filter impulse responses.
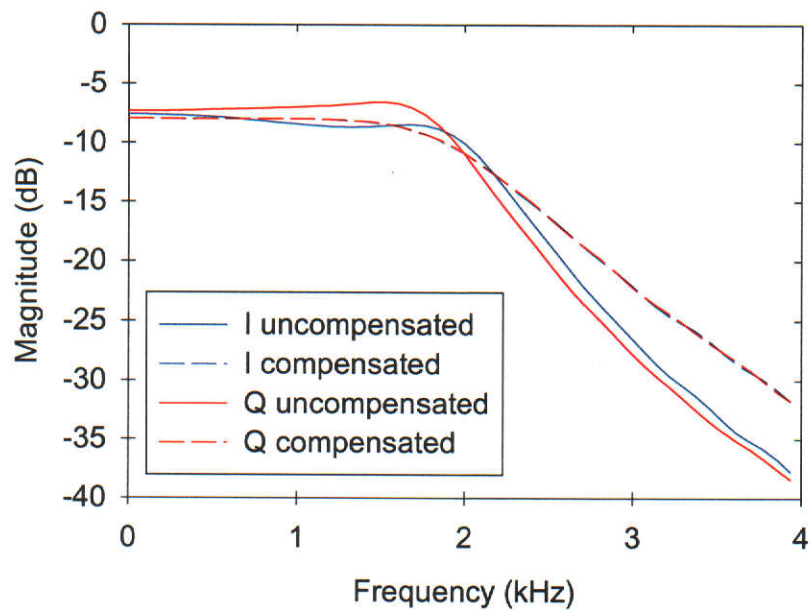
Figure 6.40. Effect of digital compensation on I and Q channel magnitude responses.
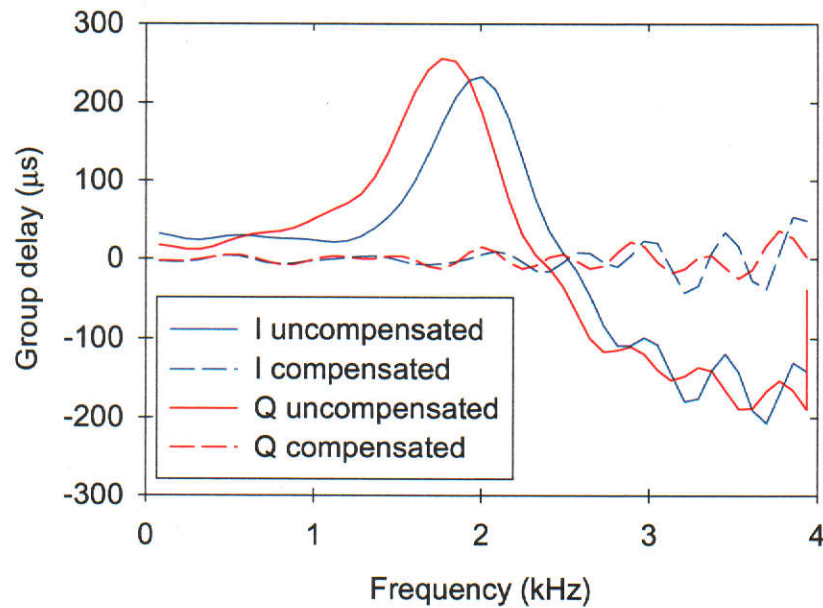
Figure 6.41. Effect of digital compensation on I and Q channel group delay responses (mean delay removed).

Note that a difference can be observed in the roll-off characteristics between the uncompensated and compensated plots in Figure 6.40. This is due to the fact that the actual low-pass filters have a 4th order Chebyshev magnitude characteristic while the desired channel response was chosen to have a 4th order Butterworth characteristic magnitude response.

IQ Modulator Operation

Envelope measurements made on the system with and without the digital compensation filters in place are shown in Figure 6.42.
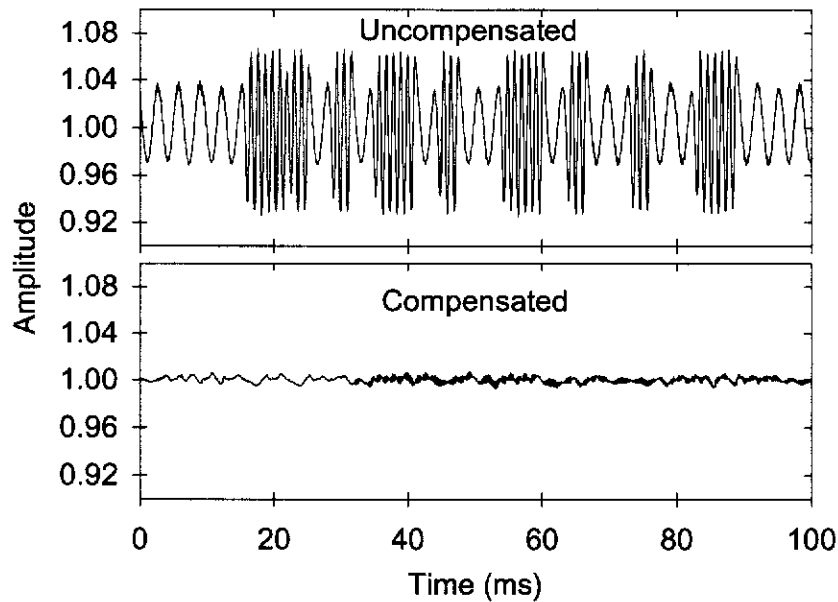
Figure 6.42. Envelope ripple without and with digital compensation.

The RMS values of the signals in Figure 6.42 are provided in Table 6.7.

	RMS value (mV)
Uncompensated system	20.28
With digital compensation	1.49
Reduction factor	14

Table 6.7. RMS values of AM present in the CPFSK signal envelope: Chebyshev reconstruction filters.

Comparing Figure 6.42 and Table 6.7 above with Figure 6.25 and Table 6.3 in Section 6.3.4 it can be seen that there is a marked improvement (approximately two-fold) in envelope ripple reduction. Thus, in this case, using a desired channel response that has a Butterworth magnitude characteristic to compensate for the Chebyshev reconstruction filters produces better results. This improvement is due to the smoother pass-band magnitude characteristic of the Butterworth response.

Figure 6.43 shows the output power spectrum of the RF amplifier for the uncompensated and compensated signals. As in the previous sections, the measurements for this figure were obtained by adjusting the variable attenuator shown in Figure 6.5 so that the RF amplifier was operating approximately at its 1dB compression point.
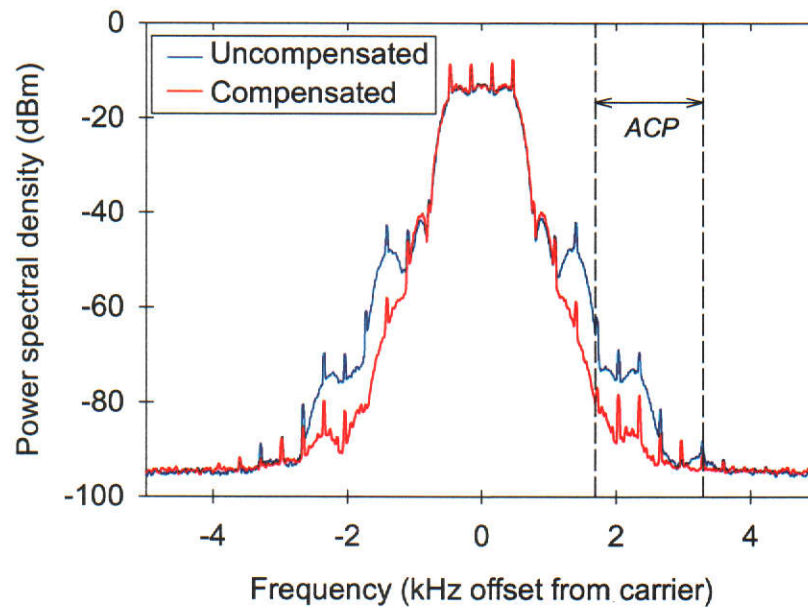
Figure 6.43. RF amplifier output power spectrum.

The ACP values measured for the spectrum plots in Figure 6.43 are given in Table 6.8.

	ACP value (dBc)
Uncompensated system	-60.0
Digitally compensated system	-71.8
Improvement	11.8

Table 6.8. ACP measurements for the uncompensated and compensated modulator systems: Chebyshev response reconstruction filters.

Comparing the ACP improvement values in Table 6.8 and Table 6.4 it can be seen that the improvements noted above in the envelope ripple are also reflected in the ACP measurements.

6.4 Conclusion

In this chapter it has been demonstrated that the proposed automatic digital compensation technique can be successfully implemented in hardware and software on a DSP platform. Due to the availability of A/D converters at the time of implementation the results presented in this chapter are for a scaled version of a full-rate 4-PAM/CPFSK ERMES system. It is noted, however that A/D converters are available that allow a full-rate implementation of the ERMES system.

The experimental results presented here confirm the findings of theoretical work and computer simulation in previous chapters that the digital compensation technique is effective in reducing residual AM in the envelope function of a CPFSK signal. It has been clearly demonstrated that the reductions in envelope ripple afforded by the digital compensation technique lead to substantial improvements in the adjacent channel performance of the modulator system. Experiments have shown, however, that careful attention must be paid to correct signal scaling and implementation of the reconstruction filters so as to minimise dynamic distortion of the I and Q channel signals.

An underlying assumption in the digital compensation technique is that the I and Q channels can be modelled as linear systems. Static and dynamic non-linearities such as slew-rate limiting or device saturation in the I and Q channels are therefore not explicitly dealt with, although the compensation technique may implicitly approximate these effects with a linear model.

Chapter 7. Summary, Conclusions and Suggestions for Further Work

7.1 Summary and Conclusions

In this thesis it has been shown that the two analogue signal reconstruction filters in the DSP-based IQ modulator structure considered here play a fundamental role in determining the nature of the vector modulator output signal envelope function and hence the performance of the modulator system. Specifically, practical realisation of the filter responses and implementation errors result in the pass-band characteristics departing from constant magnitude and linear phase. Furthermore, implementation errors will also cause some imbalance between the I and Q channel filter frequency responses.

It was shown that for typical realisations of practical low-pass filters, pass-band magnitude and phase imbalance between the filters and non-constant group delay in either of the filters has a far more detrimental effect on the signal envelope than departures from a flat magnitude response in either of the filters. This fact was used to develop a least-squares optimisation problem that incorporated a novel *desired* channel response that ensured that the compensation would be effective in reducing ripple in the envelope function.

A characterisation of the solution to the optimisation problem allowed the establishment of a numerical framework for implementing the digital compensation technique on a DSP platform. The characterisation of the solution also provided a method for finding a stable solution in a finite numerical precision environment.

Two methods were developed to allow automation of the digital compensation process: a frequency domain method and a time domain method. From computer simulation evaluations carried out on the two methods, both were shown to work effectively in reducing envelope ripple. However, the time domain approach was selected for implementation since it involved the use of test signal that could be very simply constructed on a DSP system. Furthermore the time domain approach had

certain advantages for systems with a low number of bits and in the presence of noise.

It was shown that the automatic digital compensation technique could be successfully implemented on a DSP platform. Experimental testing of the system using several different analogue reconstruction filter scenarios demonstrated that the technique was extremely effective in reducing ripple in the vector modulator output signal envelope. More importantly it was shown that the digital compensation technique significantly reduced adjacent channel emissions.

The automatic digital compensation algorithm developed is not truly adaptive as the modulator system can not be operated on line while the training signal is being sent. However, since the reconstruction filter characteristics drift relatively slowly with time, re-training the digital compensation filters using the training signals need only be done at infrequent intervals.

7.2 Suggestions for Further Work

7.2.1 Development of Analytical Expressions for Envelope Ripple Functions

In Chapter 3 numerical methods were used to determine the effect of the following frequency domain characteristics of the two analogue reconstruction filters on the CPFSK RF signal envelope:

- Departures from constant pass-band magnitude in each filter.
- Departures from linear pass-band phase in each filter.
- Magnitude imbalance between the two filters.
- Phase imbalance between the two filters.

An obvious extension of this work is an analytical treatment of the problem. This might provide useful additional insights into the relationships between the envelope ripple and the underlying filter parameters. A brief review of the literature on the effects of linear filtering on FM signals given in Chapter 3 indicates that this remains a challenging problem. Nonetheless, the investigations in Chapter 3 point to the

possibility that some simple relationships may exist between, for example, magnitude and phase imbalance and envelope ripple.

7.2.2 Alternative Desired Channel Responses

In Section 4.4 a desired channel response was proposed that had the same magnitude response as that of the nominal reconstruction filter characteristic while the phase was constrained to be linear. This approach was chosen to ensure that the degrees of freedom in the optimisation are used effectively in meeting the objective of reducing envelope ripple. It is assumed in this approach that the nominal reconstruction filter response is sufficiently flat through the pass-band to produce acceptable envelope ripple levels.

It was shown in Chapter 6 that for the digital FM application considered in this thesis, practically realisable reconstruction filter designs could readily be found that are sufficiently flat through the pass-band region to ensure adequate envelope ripple performance. However, in other applications this may not be the case and a different desired channel response must be chosen.

In Section 4.8 it was shown that a "brick-wall" magnitude, linear phase desired response overly constrains the optimisation and results in poorer modulator performance for FIR compensation filter lengths of practical interest. However, in Section 6.3.6 it was shown that a 4th order Butterworth magnitude characteristic desired response provided better compensation for nominal 4th order Chebyshev reconstruction filters than that obtained using the proposed "same magnitude" desired response.

Hence, a useful extension to the work presented here would be an investigation into alternative desired channel responses.

7.2.3 IIR Filters

The digital compensation techniques developed and demonstrated in this thesis use FIR (Finite Impulse Response) digital filters to achieve the objective of reducing in-band frequency-dependent shaping of I and Q channel signals. It has been demonstrated that FIR filters of the order of 50 taps in length are required to provide

adequate digital compensation. While it has been shown that these filters can be accommodated on a practical DSP platform, they are nonetheless computationally demanding to implement.

An extension to the work presented here would be to investigate the use of digital IIR (Infinite Impulse Response) filters to achieve the same objective. The capacity of IIR filters to produce long impulse responses using only a small number of filter coefficients may provide an effective means of reducing the computational load of the digital compensation.

7.2.4 Integer DSP Implementation

Chapter 6 described the implementation of the digital compensation techniques on a floating point DSP platform. The floating point numerical environment is attractive in that it offers high numerical precision without the need for careful scaling of program variables as is the case for an integer (fixed-point) environment.

Many existing communications systems, however, are based on fixed-point DSP platforms. In addition there are generally other factors to be considered in choosing a particular DSP architecture for new implementations, for example computational speed or DSP chip costs, that might necessitate the use of a fixed-point DSP platform.

Parts of the digital compensation algorithms developed here are sensitive to finite numerical precision effects (eigenvalue decomposition of the R matrices for example). Hence, an important extension to the work presented in this thesis would be an investigation into the effects of an integer DSP environment on the digital compensation technique and the development of additional and/or alternative techniques that need to be adopted.

7.2.5 Adaptive Algorithms

The algorithms developed in Chapter 5 allow the optimum digital FIR compensation filter tap-weights to be automatically updated from time-to-time to reflect changes in the I and Q channel characteristics. The updating process is quite short as described in Chapter 6 and does not need to be repeated frequently. However, the special test

signals require the modulator to be taken off-line during the process. An area for further work in this respect is the development of an adaptive algorithm that runs on-line and uses "live" modulator input data to make the required measurements.

7.2.6 Applications in Other Modulation Formats

The work in this thesis has considered (ideally) constant RF envelope signals such as CPFSK. However, the DSP-based quadrature modulator structure considered here is also widely used for the generation of other modulation formats such as QAM or QPSK. Therefore, the digital compensation techniques developed in this thesis may find application in other modulation formats.

Some issues that may arise in considering wider application of the techniques developed here are:

1. In the case of signal formats such as QAM or QPSK a constant RF signal envelope is no longer the criterion for effective compensation as the *ideal* signals have non-constant envelope. Nevertheless the use of the frequency-dependent digital compensation techniques developed here may lead to improvements in other performance aspects of the modulator system such as inter-symbol interference.

2. In situations where digital base-band PA linearisation schemes are used, *memory effects* in the I and Q channels of the quadrature modulator have a significant impact on the effectiveness of the schemes [12]. The compatibility of the digital compensation techniques developed here with other compensation schemes such as digital predistortion therefore need to be investigated.

Appendix A. Results for Chapter 2

This appendix presents results used in Chapter 2. The first section relates to the calculation of samples of the phase function for the digital modulator. The second section provides a derivation of the envelope function for the output signals of the I and Q channel D/A converters in the digital modulator system.

A.1. Incremental Phase Calculation

Let $g_s(t)$ be the step-response of the Symbol filter shown in Figure 2.1. The response of the filter to a square pulse of duration T_d is given by

$$b(t) = g_s(t) - g_s(t - T_d).$$
(A.1)

The following assumptions are made for the subsequent derivations in this section:

1. The symbol filter step response, $g_s(t)$, reaches its final value within one symbol period. (Note that the same approach used in the following derivations can be extended for cases of longer symbol filter step responses.)

2. The sampling period of the digital system in Figure 2.2 be given by

$$T = \frac{T_d}{M}$$
(A.2)

where M is a positive integer.

Substituting $b(t)$ from (A.1) into (2.1) gives

$$m(t) = \sum_{k=0}^{\infty} s_k \left(g_s(t - kT_d) - g_s(t - (k+1)T_d) \right).$$
(A.3)

Let $\phi_m(t)$ denote the phase function $\phi(t)$ between the mth and the $(m+1)^{th}$ input symbols. From (2.3) and (A.3) $\phi_m(t)$ is given by

$$\phi_m(t) = K_0 \sum_{k=0}^{m} s_k \int_0^t \left(g_s(\tau - kT_d) - g_s(\tau - (k+1)T_d) \right) d\tau;$$

$$mT_d \leq t < (m+1)T_d \tag{A.4}$$

From (A.2) and (A.4) and using the two assumptions stated earlier, $\phi_m(t)$ can be rewritten as

$$\phi_m(mT_d + lT) = K_0 T_d \sum_{k=0}^{m-2} s_k + K_0 s_{m-1}(\alpha + lT)$$

$$+ K_0(s_m - s_{m-1}) \int_0^{lT} g_s(\tau) d\tau; \tag{A.5}$$

$$mT_d \leq mT_d + lT < (m+1)T_d.$$

where
$$\alpha = \int_0^{T_d} g_s(\tau) d\tau \tag{A.6}$$

Let $\{S_j\}; j = 0,1,\ldots,M-1$ be a sequence of real numbers such that

$$S_i = \int_{iT}^{(i+1)T} g_s(\tau) d\tau. \tag{A.7}$$

From (A.7) equation (A.5) can be rewritten as

$$\phi_m(mT_d + lT) = K_0 \left[T_d \sum_{k=0}^{m-2} s_k + s_{m-1}(\alpha + lT) + (s_m - s_{m-1}) \sum_{n=0}^{l-1} S_n \right];$$

$$mT_d \leq mT_d + lT < (m+1)T_d. \tag{A.8}$$

Recall from (2.26) that

$$\phi'(nT) = \left. \frac{\phi(t)}{2\pi} \right|_{t=nT} \tag{A.9}$$

and letting

$$K' = \frac{K_0}{2\pi}, \tag{A.10}$$

then from (A.8), the discrete-time phase function between the mth and the $(m+1)^{th}$ input symbols, denoted $\phi_m'(nT)$, is given by

$$\phi_m'(mT_d + lT) = K'\left[T_d \sum_{k=0}^{m-2} s_k + s_{m-1}(\alpha + lT) + (s_m - s_{m-1})\sum_{n=0}^{l-1} S_n \right] \tag{A.11}$$

$$mT_d \le mT_d + lT < (m+1)T_d.$$

From (A.11) the following recursive function can be derived

$$\phi_m'((l+1)T) = \left[\phi_m'(lT) + K'\Delta_{\phi_m'}(lT) \right] \bmod(2);$$
$$l = 0,1,\ldots,M-1; \tag{A.12}$$
$$mT_d \le mT_d + lT < (m+1)T_d,$$

where
$$\Delta_{\phi_m'}(lT) = s_{m-1}T + (s_m - s_{m-1}S_l). \tag{A.13}$$

The $\bmod(2)$ in (A.12) represents the modulo 2 operation and ensures that the phase function, $\phi_m'(nT)$, is bounded. A $\bmod(2)$ operation is required in practical applications to prevent the sum from exceeding the finite range of a practical system and causing numerical overflow. Note from Figure 2.2 that the modulo 2 operation in (A.12) is only permissible when the *phase function synthesis block* is followed by the $A\cos(\pi x)$ and $A\sin(\pi x)$ function blocks since

$$i'(nT) = \cos(\pi\phi'(nT)) = \cos(\pi(\phi'(nT)\pm 2))$$
$$q'(nT) = \sin(\pi\phi'(nT)) = \sin(\pi(\phi'(nT)\pm 2)). \tag{A.14}$$

A.2 I and Q Channel D/A Converter Output Envelope

The output signals of the I and Q channel zero-order hold D/A converters are given by (2.33) and (2.44) and are repeated below for convenience.

$$\breve{i}(t) = \sum_n i'(nT)p_s(t - nT) \tag{A.15}$$

$$\breve{q}(t) = \sum_n q'(nT)p_s(t - nT) \tag{A.16}$$

From (2.8) the envelope function corresponding to the signals $\breve{i}(t)$ and $\breve{q}(t)$ is

$$r_{\breve{y}}(t) = \sqrt{\breve{i}^2(t) + \breve{q}^2(t)} \tag{A.17}$$

It follows from (2.24), (A.15), (A.16) and (A.17) that

$$
\begin{aligned}
r_{\breve{y}}^2(t) = A^2 \Bigg[&\left(\sum_n \cos\left(\pi\phi'(nT)\right) p_s(t-nT) \right)^2 \\
&+ \left(\sum_n \sin\left(\pi\phi'(nT)\right) p_s(t-nT) \right)^2 \Bigg]
\end{aligned}
\tag{A.18}
$$

Equation (A.18) can be rewritten as

$$
\begin{aligned}
r_{\breve{y}}^2(t) = A^2 \Bigg[&\sum_k \sum_l \cos\left(\pi\phi'(kT)\right)\cos\left(\pi\phi'(lT)\right) p_s(t-kT)p_s(t-lT) \\
&+ \sum_k \sum_l \sin\left(\pi\phi'(kT)\right)\sin\left(\pi\phi'(lT)\right) p_s(t-kT)p_s(t-lT) \Bigg] \\
= A^2 &\sum_n \left(\cos^2\left(\pi\phi'(kT)\right) + \sin^2\left(\pi\phi'(kT)\right)\right) p_s^2(t-nT) \\
+ A^2 &\sum_k \sum_{l;l\neq k} \cos\left(\pi\phi'(kT)\right)\cos\left(\pi\phi'(lT)\right) p_s(t-kT)p_s(t-lT) \\
+ A^2 &\sum_k \sum_l \sin\left(\pi\phi'(kT)\right)\sin\left(\pi\phi'(lT)\right) p_s(t-kT)p_s(t-lT).
\end{aligned}
\tag{A.19}
$$

From (2.35)

$$p_s(t-kT)\, p_s(t-lT) = \begin{cases} p_s(t) & k=l \\ 0 & k \neq l \end{cases}, \tag{A.20}$$

and (A.19) can be simplified to

$$
\begin{aligned}
r_{\breve{y}}^2(t) &= A^2 \sum_n p_s(t-nT) \\
&= A^2.
\end{aligned}
\tag{A.21}
$$

Equation (A.21) is the required result.

Appendix B. Equivalent Time-domain Formulation

In this appendix it is shown that the matrix $\boldsymbol{R}$ and the vector $\boldsymbol{p}$ given in terms of frequency domain parameters in (4.12) and (4.13) can be represented equivalently in terms of time domain parameters.

It is assumed that the impulse responses $d(nT)$ and $h'(nT)$ in Figures 4.3 and 4.4 are both real-valued functions. The functions $D(e^{j\omega T})$ and $H'(e^{j\omega T})$ in (4.12) therefore have the property

$$D(e^{j\omega T}) = D^*(e^{-j\omega T})$$
$$H'(e^{j\omega T}) = H'^*(e^{-j\omega T}).$$
(B.1)

i.e., conjugate symmetry about the imaginary axis.

From (4.12) and using the properties in (B.1), the kth element of the vector $\boldsymbol{p}$ can be expressed as

$$[\boldsymbol{p}]_k = \frac{1}{\omega_s} \int_{-\omega_s/2}^{\omega_s/2} A(e^{j\omega T}) e^{-j\omega(k-1)T} d\omega;$$
$$k = 1, 2, \ldots, K.$$
(B.2)

where
$$A(e^{j\omega T}) = D^*(e^{j\omega T}) H'(e^{j\omega T})$$
(B.3)

The function $A(e^{j\omega T})$ in (B.3) is a periodic function in ω with period ω_s and can be expressed as the Fourier series

$$A(e^{j\omega T}) = \sum_{n=-\infty}^{\infty} a_n e^{jn\omega T},$$
(B.4)

where
$$a_n = \frac{1}{\omega_s} \int_{-\omega_s/2}^{\omega_s/2} A(e^{j\omega T}) e^{-jn\omega T}; n = 0, \pm 1, \pm 2, \ldots$$
(B.5)

Note from (B.5) that the RHS of (B.2) is the $(k-1)^{\text{th}}$ coefficient of the Fourier series expansion of the periodic function $A\left(e^{j\omega T}\right)$, i.e.,

$$[p]_k = a_{(k-1)}; k = 1, 2, \ldots, K.$$ (B.6)

The sequence $\{a_n\}; n = 0, \pm 1, \pm 2, \ldots$ in (B.4) and (B.5) is the impulse response sequence of a digital filter having a frequency response $A\left(e^{j\omega T}\right)$. Taking the inverse discrete Fourier transform of $A\left(e^{j\omega T}\right)$ in (B.3) it can be shown that

$$[p]_k = \sum_{n=-\infty}^{\infty} h'(nT) d\left((n - k + 1)T\right);$$

$$k = 1, 2, \ldots, K.$$ (B.7)

From (4.13), the $(k,l)^{\text{th}}$ element of the R matrix can be written as

$$[R]_{k,l} = \frac{1}{\omega_s} \int_{-\omega_s/2}^{\omega_s/2} H_m\left(e^{j\omega T}\right) e^{-j\omega(k-l)T} d\omega.$$ (B.8)

where

$$H_m\left(e^{j\omega T}\right) = \left|H'\left(e^{j\omega T}\right)\right|^2$$ (B.9)

Note from (B.8) and (B.9) it can be easily shown that

$$[R]_{k,l} = [R]_{l,k},$$ (B.10)

i.e., the matrix R is symmetric.

Using the same approach taken above for the p vector it can be shown that

$$[R]_{k,l} = \sum_{m=-\infty}^{\infty} h'(mT) h'\left((m - k + l)T\right);$$

$$k, l = 1, 2, \ldots, K.$$ (B.11)

Appendix C. Choosing Frequency Sample Points for the Frequency Domain Estimation Method

For the discrete frequency optimisation problem proposed in Section 5.2, the matrix $\tilde{R}$ is constructed according to the summation given in (5.3) (repeated below for convenience)

$$\tilde{R} = \sum_{k=1}^{N} \left(s_R \left(e^{j\omega_k T} \right) s_R^T \left(e^{j\omega_k T} \right) + s_I \left(e^{j\omega_k T} \right) s_I^T \left(e^{j\omega_k T} \right) \right) \left| H' \left(e^{j\omega_k T} \right) \right|^2, \qquad \text{(C.1)}$$

where $\tilde{R} \in \mathbb{R}^{K \times K}$ and where, from (4.7), the vectors, $s_R \left(e^{j\omega_k T} \right), s_I \left(e^{j\omega_k T} \right) \in \mathbb{R}^{K \times 1}$, are given by

$$\left[s_R \left(e^{j\omega_k T} \right) \right]_i = \text{Re} \left[\left[s \left(e^{j\omega_k T} \right) \right]_i \right] = \cos \left(\omega_k (i-1) T \right) \triangleq \left[C_k \right]_i,$$

$$\left[s_I \left(e^{j\omega_k T} \right) \right]_i = \text{Im} \left[\left[s \left(e^{j\omega_k T} \right) \right]_i \right] = -\sin \left(\omega_k (i-1) T \right) \triangleq \left[S_k \right]_i, \qquad \text{(C.2)}$$

$$k = 1, 2, \ldots, N,$$

$$i = 1, 2, \ldots, K.$$

To simplify notation in the following derivations, let

$$\alpha_k \triangleq \left| H' \left(e^{j\omega_k T} \right) \right|;$$

$$k = 1, 2, \ldots, N. \qquad \text{(C.3)}$$

With the definitions in (C.2) and (C.3) the expression for the $\tilde{R}$ matrix in (C.1) can be rewritten as

$$\tilde{R} = \sum_{k=1}^{N} \alpha_k \left(C_k C_k^T + S_k S_k^T \right). \qquad \text{(C.4)}$$

In this appendix conditions on the number and distribution of the N frequency points are derived for the matrix, $\tilde{R}$, to be full rank.

C. 1. Arbitrary Distribution of Frequency Sample Points

Consider the case where $N = K$ frequency points $\{\omega_k\}; k = 1, 2, \ldots, N$ are chosen such that

$$\begin{aligned} \omega_m - \omega_n &\neq l\omega_s; \\ l &= 0, \pm 1, \pm 2, \ldots; \\ K &\geq m > n \geq 1. \end{aligned} \tag{C.5}$$

and where

$$H'\left(e^{j\omega_k T}\right) \neq 0 \ \forall \ k = 1, 2, \ldots, K. \tag{C.6}$$

Given the conditions in (C.5) and (C.6) it is shown below that $\tilde{R}$ has full rank.

Consider the Vandermonde matrix [79], $V \in \mathbb{C}^{K \times K}$, constructed from the K frequency points in (C.5) and given by

$$V = \begin{pmatrix} 1 & 1 & \cdots & 1 \\ e^{-j\omega_1 T} & e^{-j\omega_2 T} & \cdots & e^{-j\omega_K T} \\ \vdots & \vdots & \ddots & \vdots \\ e^{-j\omega_1(K-1)T} & e^{-j\omega_2(K-1)T} & \cdots & e^{-j\omega_K(K-1)T} \end{pmatrix}. \tag{C.7}$$

The determinant of V given by [79]

$$\det[V] = \prod_{K \geq m > n \geq 1} \left(e^{-j\omega_m T} - e^{-j\omega_n T}\right), \tag{C.8}$$

is non-zero for the frequency points chosen according to (C.5) since it can be easily shown that

$$\begin{aligned} \left(e^{-j\omega_m T} - e^{-j\omega_n T}\right) &\neq 0 \ \forall \ \{\omega_m, \omega_n\}; \\ K &\geq m > n \geq 1. \end{aligned} \tag{C.9}$$

The matrix, V, is therefore non-singular and has full column rank, i.e., the columns of V form a set of K linearly independent vectors.

The K columns of V denoted by the vectors $v_i \in \mathbb{C}^{K \times 1}, i = 1, 2, \ldots, K$ are given by

$$
v_i = \begin{pmatrix} 1 \\ e^{-j\omega_i T} \\ \vdots \\ e^{-j\omega_i(K-1)T} \end{pmatrix} ; \; i = 1, 2, \ldots, K \tag{C.10}
$$

Since the set of vectors, $\{v_i\}; i = 1, 2, \ldots, K$ are linearly independent then, by definition [114], for a set of scalars $\{c_i\} \in \mathbb{C}; i = 1, 2, \ldots, K$ the following holds

$$
\sum_{i=1}^{K} c_i v_i = 0 \Leftrightarrow \{c_i\} = 0. \tag{C.11}
$$

From (C.3) and (C.10) the set of K vectors $\{v_i\}; i = 1, 2, \ldots, K$ can be represented as

$$
v_i = C_i + jS_i, i = 1, 2, \ldots, K \tag{C.12}
$$

Let $c_i = c_i^R + jc_i^I$, $i = 1, 2, \ldots, K$ where $c_i^R, c_i^I \in \mathbb{R}$ then

$$
\sum_{i=1}^{K}\left(c_i^R C_i - c_i^I S_i\right) + j\sum_{i=1}^{K}\left(c_i^R S_i + c_i^I C_i\right) = 0 \Leftrightarrow \begin{cases} \sum_{i=1}^{K}\left(c_i^R C_i - c_i^I S_i\right) = 0 \\ \sum_{i=1}^{K}\left(c_i^R S_i + c_i^I C_i\right) = 0 \end{cases} \tag{C.13}
$$

But from (C.11) and (C.13)

$$
\begin{cases} \sum_{i=1}^{K}\left(c_i^R C_i - c_i^I S_i\right) = 0 \\ \sum_{i=1}^{K}\left(c_i^R S_i + c_i^I C_i\right) = 0 \end{cases} \Rightarrow \{c_i\} = 0 \tag{C.14}
$$

Consider the matrix $X \in \mathbb{R}^{2K \times 2K}$ formed from the vectors $\{C_i\}$ and $\{S_i\}$ as follows

$$
X = \begin{bmatrix} C_1 & C_2 & \cdots & C_K & -S_1 & -S_2 & \cdots & -S_K \\ S_1 & S_2 & \cdots & S_K & C_1 & C_2 & \cdots & C_K \end{bmatrix}. \tag{C.15}
$$

Let the vector $\chi \in \mathbb{R}^{2K \times 1}$ be

$$\chi = \begin{bmatrix} x_1^R & x_2^R & \cdots & x_K^R & x_1^I & x_2^I & \cdots & x_K^I \end{bmatrix}^T, \tag{C.16}$$

then the product $X\chi$ is given by

$$X\chi = \begin{bmatrix} \sum_{i=1}^{K} \left(x_i^R C_i - x_i^I S_i \right) \\ \sum_{i=1}^{K} \left(x_i^R S_i + x_i^I C_i \right) \end{bmatrix}. \tag{C.17}$$

From (C.14)

$$X\chi = 0 \quad \Rightarrow \chi = 0 \tag{C.18}$$

and hence the matrix X is full rank.

Let the matrix $D \in \mathbb{R}^{2K \times 2K}$ be the diagonal matrix defined by

$$D \triangleq \text{diag} \begin{bmatrix} \alpha_1 & \alpha_2 & \cdots & \alpha_K & \alpha_1 & \alpha_2 & \cdots & \alpha_K \end{bmatrix}, \tag{C.19}$$

where, from (C.3) and (C.6), $\alpha_i > 0;\ i = 1, 2, \ldots, K$.

From (C.15) and (C.19) the matrix $XDX^T \in \mathbb{R}^{2K \times 2K}$ is given by

$$XX^T = \begin{bmatrix} \sum_{i=1}^{K} \alpha_i \left(C_i C_i^T + S_i S_i^T \right) & \sum_{i=1}^{K} \alpha_i \left(C_i S_i^T - S_i C_i^T \right) \\ \sum_{i=1}^{K} \alpha_i \left(S_i C_i^T - C_i S_i^T \right) & \sum_{i=1}^{K} \alpha_i \left(C_i C_i^T + S_i S_i^T \right) \end{bmatrix}. \tag{C.20}$$

Since X and D are full rank it can be shown [74] that XDX^T is positive definite and therefore all the principal submatrices are also positive definite [74]. Hence the principal $K \times K$ submatrix of XDX^T is positive definite, i.e.,

$$\sum_{i=1}^{K} \alpha_i \left(C_i C_i^T + S_i S_i^T \right) = \tilde{R} > 0 \tag{C.21}$$

C.2. Uniformly Distributed Frequency Sample Points

In the following it is shown that a full-rank $\tilde{R}$ matrix in (C.4) can be constructed using $N = K/2 + 1$ frequency sample points when the distribution of points is restricted to a particular uniformly spaced set.

Consider the case where the set of η equally spaced frequency points are chosen such that

$$\eta = \frac{K}{2} - 1 \ (K \text{ even}) \tag{C.22}$$

and

$$\omega_i = \frac{i\omega_s}{2(\eta + 1)}; \ i = 1, 2, \ldots, \eta. \tag{C.23}$$

Define the set of vectors $\{v_i\}; i = 1, 2, \ldots, \eta$ as

$$v_i = s\left(e^{j\omega_i T}\right); i = 1, 2, \ldots, \eta \tag{C.24}$$

where the η frequencies $\{\omega_i\}; i = 1, 2, \ldots, \eta$ are given by (C.23). From (4.7) and (C.23) the vectors $\{v_i\}; i = 1, 2, \ldots, \eta$ can be expressed as

$$v_i = \begin{pmatrix} 1 \\ e^{-j\left(\frac{i\omega_s}{2(\eta+1)}\right)T} \\ e^{-j2\left(\frac{i\omega_s}{2(\eta+1)}\right)T} \\ \vdots \\ e^{-j(K-1)\left(\frac{i\omega_s}{2(\eta+1)}\right)T} \end{pmatrix}; i = 1, 2, \ldots, \eta. \tag{C.25}$$

The inner product between vectors v_m and v_n is given by

$$v_m^* \bullet v_n = \sum_{l=1}^{K} e^{j\left(\frac{(m-n)\omega_s}{2(\eta+1)}\right)(l-1)T} \, . \tag{C.26}$$

Letting

$$r = e^{j\left(\frac{(m-n)\omega_s}{2(\eta+1)}\right)T} \tag{C.27}$$

equation (C.26) can be rewritten as

$$v_m^* \bullet v_n = \sum_{l=1}^{K} r^{(l-1)} = \frac{1-r^K}{1-r} \, . \tag{C.28}$$

Note from (C.23) and (C.27) that $r \neq 1$.

From (C.22) and (C.27)

$$r^K = e^{j(m-n)2\pi}$$
$$= 1 \quad \forall \; m; n = 1, 2, \ldots, \eta. \tag{C.29}$$

and from (C.28) and (C.29)

$$v_m^* \bullet v_n = 0 \quad \forall \; m; n = 1, 2, \ldots, \eta;$$
$$m \neq n. \tag{C.30}$$

i.e., the vectors v_m and v_n are orthogonal.

Using the same approach used above in (C.26) to (C.30) it can be shown that

$$\left.\begin{array}{l} \mathrm{Re}\left[v_m\right] \bullet \mathrm{Im}\left[v_m\right] = C_m \bullet S_m = 0 \\ \mathrm{Re}\left[v_m\right] \bullet \mathrm{Re}\left[v_n\right] = C_m \bullet C_n = 0 \\ \mathrm{Im}\left[v_m\right] \bullet \mathrm{Im}\left[v_n\right] = S_m \bullet S_n = 0 \\ \mathrm{Re}\left[v_m\right] \bullet \mathrm{Im}\left[v_n\right] = C_m \bullet S_n = 0 \end{array}\right\} \begin{array}{c} m; n = 1, 2, \ldots, \eta \\ m \neq n \end{array} \tag{C.31}$$

From (C.31) the 2η vectors $\left\{C_i; S_i\right\}; i = 1, 2, \ldots, \eta$ are orthogonal.

Since $\tilde{R}$ has dimensions $K \times K$ the matrix constructed using the η frequency sampling points given by (C.22) and (C.23) has a rank of $(2K - 2)$ and is therefore rank-deficient by 2. Consider the two additional frequency sampling points

$$\omega_0 = 0; \quad \omega_{\eta+1} = \omega_s/2 . \tag{C.32}$$

The vectors v_0 and $v_{\eta+1}$ corresponding to these points are given by

$$v_0 = \begin{pmatrix} 1 \\ 1 \\ 1 \\ \vdots \\ 1 \end{pmatrix}; \quad v_{\eta+1} = \begin{pmatrix} 1 \\ -1 \\ 1 \\ \vdots \\ -1 \end{pmatrix} \tag{C.33}$$

Clearly, for K-even these two vectors are orthogonal. Using the same approach used in (C.26) to (C.30) it can also be shown that v_0 and $v_{\eta+1}$ are orthogonal to the vectors $\{v_i\}i = 1, 2, \ldots, \eta$.

A full-rank $\tilde{R}$ matrix can therefore be constructed from $(K/2 + 1)$ frequency sampling points distributed as follows

$$\{\omega_i\} = \frac{i\omega_s}{2(\eta+1)} ; i = 0, 1, \ldots, \eta+1 \tag{C.34}$$

where η is given by (C.22).

C.3. Lower Bound on the Number of Frequency Sample Points

A lower bound on N is now derived below which the matrix $\tilde{R}$ constructed according to (C.4) is singular.

From (C.4) the matrix $\tilde{R}$ is the sum of N matrices that have at most rank two, i.e.,

$$\tilde{R} = \sum_{k=1}^{N} \alpha_k A_k , \tag{C.35}$$

where

$$A_k = C_k C_k^T + S_k S_k^T,$$

(C.36)

and

$$\text{rank}\left[A_k\right] \leq \text{rank}\left[C_k C_k^T\right] + \text{rank}\left[S_k S_k^T\right] \leq 2.$$

(C.37)

Assuming $\alpha_k \neq 0; k = 1, 2, \ldots, N$ then from (C.37) the rank of $\tilde{R}$ is given by the inequality

$$\text{rank}\left[\tilde{R}\right] \leq \sum_{k=1}^{N} \text{rank}\left[A_k\right] \leq 2N.$$

(C.38)

However, for the $K \times K$ dimension matrix $\tilde{R}$ to be invertible

$$\text{rank}\left[\tilde{R}\right] = K,$$

(C.39)

and from (C.38) and (C.39) the following is obtained

$$N \geq \frac{K}{2}.$$

(C.40)

Hence, from (C.40) if the number of frequency points N in the summation in (C.1) is less than the half the dimension of the matrix $\tilde{R}$ then $\tilde{R}$ is singular.

Appendix D. Least Squares Fitting of Sinusoidal Functions

In (5.19) the following N minimisation problems were posed

$$\min_{\alpha_k,\beta_k}\left[J\left(\alpha_k,\beta_k\right)\right]; k=1,2,\ldots,N, \tag{D.1}$$

where the cost function, $J\left(\alpha_k,\beta_k\right)$, is given by

$$J\left(\alpha_k,\beta_k\right)=\frac{1}{L-l_0}\sum_{n=l_0}^{L}\left(\hat{y}_k\left(nT\right)-\alpha_k\sin\left(\omega_k nT\right)-\beta_k\cos\left(\omega_k nT\right)\right)^2. \tag{D.2}$$

Expanding the square in (D.2) gives

$$\begin{aligned}
J\left(\alpha_k,\beta_k\right)=&\frac{1}{L-l_0}\sum_{n=l_0}^{L}\hat{y}_k^2\left(nT\right)\\
&-\frac{2\alpha_k}{L-l_0}\sum_{n=l_0}^{L}\hat{y}_k\left(nT\right)\sin\left(\omega_k nT\right)\\
&-\frac{2\beta_k}{L-l_0}\sum_{n=l_0}^{L}\hat{y}_k\left(nT\right)\cos\left(\omega_k nT\right)\\
&+\frac{\alpha_k^2}{L-l_0}\sum_{n=l_0}^{L}\sin^2\left(\omega_k nT\right)\\
&+\frac{\beta_k^2}{L-l_0}\sum_{n=l_0}^{L}\cos^2\left(\omega_k nT\right)\\
&+\frac{2\alpha_k\beta_k}{L-l_0}\sum_{n=l_0}^{L}\sin\left(\omega_k nT\right)\cos\left(\omega_k nT\right).
\end{aligned} \tag{D.3}$$

Since $J\left(\alpha_k,\beta_k\right)$ is a quadratic function of the two variables α_k and β_k, the optimum values $\breve{\alpha}_k$ and $\breve{\beta}_k$ can be found by setting the first partial derivatives of $J\left(\alpha_k,\beta_k\right)$ with respect to α_k and β_k to zero and solving the resulting set of linear equations. The first partial derivatives are given by

$$\left. \frac{\partial J\left(\alpha_k, \beta_k\right)}{\partial \alpha_k} \right|_{\substack{\alpha_k = \breve{\alpha}_k \\ \beta_k = \breve{\beta}_k}} = -\frac{2}{L-l_0} \sum_{n=l_0}^{L} \hat{y}_k\left(nT\right)\sin\left(\omega_k nT\right)$$

$$+\frac{2\breve{\alpha}_k}{L-l_0} \sum_{n=l_0}^{L} \sin^2\left(\omega_k nT\right) \qquad \text{(D.4)}$$

$$+\frac{2\breve{\beta}_k}{L-l_0} \sum_{n=l_0}^{L} \sin\left(\omega_k nT\right)\cos\left(\omega_k nT\right)$$

$$= 0$$

and

$$\left. \frac{\partial J\left(\alpha_k, \beta_k\right)}{\partial \beta_k} \right|_{\substack{\alpha_k = \breve{\alpha}_k \\ \beta_k = \breve{\beta}_k}} = -\frac{2}{L-l_0} \sum_{n=l_0}^{L} \hat{y}_k\left(nT\right)\cos\left(\omega_k nT\right)$$

$$+\frac{2\breve{\beta}_k}{L-l_0} \sum_{n=l_0}^{L} \cos^2\left(\omega_k nT\right) \qquad \text{(D.5)}$$

$$+\frac{2\breve{\alpha}_k}{L-l_0} \sum_{n=l_0}^{L} \sin\left(\omega_k nT\right)\cos\left(\omega_k nT\right)$$

$$= 0$$

Making the assignments

$$S_k = \sum_{n=l_0}^{L} \sin^2\left(\omega_k nT\right)$$

$$C_k = \sum_{n=l_0}^{L} \cos^2\left(\omega_k nT\right)$$

$$B_k = \sum_{n=l_0}^{L} \sin\left(\omega_k nT\right)\cos\left(\omega_k nT\right) \qquad \text{(D.6)}$$

$$\hat{Y}_{k,s} = \sum_{n=l_0}^{L} \hat{y}_k\left(nT\right)\sin\left(\omega_k nT\right)$$

$$\hat{Y}_{k,c} = \sum_{n=l_0}^{L} \hat{y}_k\left(nT\right)\cos\left(\omega_k nT\right)$$

the expressions in (D.4) and (D.5) can be solved for $\breve{\alpha}_k$ and $\breve{\beta}_k$:

$$\breve{\alpha}_k = \frac{C_k \hat{Y}_{k,s} - B_k \hat{Y}_{k,c}}{C_k S_k - B_k^2}. \qquad \text{(D.7)}$$

and

$$\breve{\beta}_k = \frac{S_k \hat{Y}_{k,c} - B_k \hat{Y}_{k,s}}{C_k S_k - B_k^2}.$$

(D.8)

where it is assumed that $C_k S_k - B_k^2 \neq 0 \;\; \forall k = 1, 2, \ldots, N$.

The signal $\hat{y}(nT)$ can be represented as

$$\hat{y}_k(nT) = y_k(nT) + v_k(nT)$$

(D.9)

where $v_k(nT)$ is the noise present in the output signal for the kth input sinusoidal test signal.

Hence, substituting for $\hat{y}_k(nT)$ in the expressions for $\hat{Y}_{k,s}$ and $\hat{Y}_{k,c}$ in (D.6) gives the following equations for $\breve{\alpha}_k$ and $\breve{\beta}_k$

$$\breve{\alpha}_k = \frac{C_k Y_{k,s} - B_k Y_{k,c}}{C_k S_k - B_k^2} + \frac{C_k V_{k,s} - B_k V_{k,c}}{C_k S_k - B_k^2}$$

(D.10)

and

$$\breve{\beta}_k = \frac{S_k Y_{k,c} - B_k Y_{k,s}}{C_k S_k - B_k^2} + \frac{S_k V_{k,c} - B_k V_{k,s}}{C_k S_k - B_k^2}$$

(D.11)

where

$$Y_{k,c} = \sum_{n=l_0}^{L} y_k(nT) \cos(\omega_k nT)$$

(D.12)

$$Y_{k,s} = \sum_{n=l_0}^{L} y_k(nT) \sin(\omega_k nT)$$

(D.13)

$$V_{k,c} = \sum_{n=l_0}^{L} v_k(nT) \cos(\omega_k nT)$$

(D.14)

$$V_{k,s} = \sum_{n=l_0}^{L} v_k(nT) \sin(\omega_k nT).$$

(D.15)

The steady-state noiseless output signal, $y_k(nT)$, of the system in Figure 5.1 is given simply by

$$
\begin{aligned}
y_k(nT) &= A_k \rho \sin(\omega_k nT + \phi_k) \\
&= A_k \rho \cos(\phi_k) \sin(\omega_k nT) + A_k \rho \sin(\phi_k) \cos(\omega_k nT)
\end{aligned}
\tag{D.16}
$$

By substituting the right hand side in (D.16) for $y_k(nT)$ in (D.12) and (D.13), equations (D.10) and (D.11) can be rewritten as

$$
\breve{\alpha}_k = A_k \rho \cos(\phi_k) + \varepsilon_{\alpha,k}
\tag{D.17}
$$

and

$$
\breve{\beta}_k = A_k \rho \cos(\phi_k) + \varepsilon_{\beta,k}
\tag{D.18}
$$

where

$$
\varepsilon_{\alpha,k} = \Gamma_k \left(C_k \sum_{n=l_0}^{L} v_k(nT) \sin(\omega_k nT) - B_k \sum_{n=l_0}^{L} v_k(nT) \cos(\omega_k nT) \right)
\tag{D.19}
$$

and

$$
\varepsilon_{\beta,k} = \Gamma_k \left(S_k \sum_{n=l_0}^{L} v_k(nT) \cos(\omega_k nT) - B_k \sum_{n=l_0}^{L} v_k(nT) \sin(\omega_k nT) \right)
\tag{D.20}
$$

and where

$$
\Gamma_k = \frac{1}{C_k S_k - B_k^2}
\tag{D.21}
$$

Taking the expected values of the parameter estimates $\breve{\alpha}_k$ and $\breve{\beta}_k$ in (D.17) and (D.18) gives

$$
\begin{aligned}
E[\breve{\alpha}_k] &= A_k \rho \cos(\phi_k) \\
&+ \Gamma_k \left(C_k \sum_{n=l_0}^{L} E[v_k(nT)] \sin(\omega_k nT) \right. \\
&\left. - B_k \sum_{n=l_0}^{L} E[v_k(nT)] \cos(\omega_k nT) \right),
\end{aligned}
\tag{D.22}
$$

$$E\left[\breve{\beta}_k\right] = A_k \rho \sin\left(\phi_k\right)$$

and
$$+\Gamma_k\left(S_k \sum_{n=l_0}^{L} E\left[v_k\left(nT\right)\right]\cos\left(\omega_k nT\right)\right.$$
$$\left. - B_k \sum_{n=l_0}^{L} E\left[v_k\left(nT\right)\right]\sin\left(\omega_k nT\right)\right).$$
(D.23)

If $v_k\left(nT\right)$ is a zero-mean stochastic signal then

$$E\left[v_k\left(nT\right)\right] = 0$$
(D.24)

and equations (D.22) and (D.23) reduce to

$$E\left[\breve{\alpha}_k\right] = A_k \rho \cos\left(\phi_k\right),$$
(D.25)

and
$$E\left[\breve{\beta}_k\right] = A_k \rho \sin\left(\phi_k\right),$$
(D.26)

i.e., the estimators $\breve{\alpha}_k$ and $\breve{\beta}_k$ are unbiased.

The variances of the estimators $\breve{\alpha}_k$ and $\breve{\beta}_k$ are defined as

$$\mathrm{var}\left[\breve{\alpha}_k\right] \triangleq E\left[\left(\breve{\alpha}_k - E\left[\breve{\alpha}_k\right]\right)^2\right]$$
(D.27)

and
$$\mathrm{var}\left[\breve{\beta}_k\right] \triangleq E\left[\left(\breve{\beta}_k - E\left[\breve{\beta}_k\right]\right)^2\right]$$
(D.28)

From (D.17), (D.19) and (D.25) equation (D.27) can be expanded as

$$\mathrm{var}\left[\breve{\alpha}_k\right]$$
$$= E\left[\left(\Gamma_k\left(C_k \sum_{n=l_0}^{L} v_k\left(nT\right)\sin\left(\omega_k nT\right) - B_k \sum_{n=l_0}^{L} v_k\left(nT\right)\cos\left(\omega_k nT\right)\right)\right)^2\right]$$
(D.29)

Expanding the square in (D.29) gives

$$\text{var}\left[\breve{\alpha}_k\right] = \Gamma_k^2 C_k^2 \sum_{m=l_0}^{L} \sum_{n=l_0}^{L} E\left[V_k\left(mT\right)V_k\left(nT\right)\right]\sin\left(\omega_k mT\right)\sin\left(\omega_k nT\right)$$

$$-2\Gamma_k^2 C_k B_k \sum_{m=l_0}^{L} \sum_{n=l_0}^{L} E\left[V_k\left(mT\right)V_k\left(nT\right)\right]\sin\left(\omega_k mT\right)\cos\left(\omega_k nT\right) \quad \text{(D.30)}$$

$$+\Gamma_k^2 B_k^2 \sum_{m=l_0}^{L} \sum_{n=l_0}^{L} E\left[V_k\left(mT\right)V_k\left(nT\right)\right]\cos\left(\omega_k mT\right)\cos\left(\omega_k nT\right)$$

If the additive noise, $V_k\left(nT\right)$, is white then

$$E\left[V_k\left(mT\right)V_k\left(nT\right)\right] = \begin{cases} \sigma_v^2 & m = n \\ 0 & m \neq n \end{cases} \quad \text{(D.31)}$$

and (D.30) can be simplified to

$$\text{var}\left[\breve{\alpha}_k\right] = \Gamma_k^2 \sigma_{v_k}^2 \sum_{n=l_0}^{L} \left(C_k \sin\left(\omega_k nT\right) - B_k \cos\left(\omega_k nT\right)\right)^2. \quad \text{(D.32)}$$

Similarly, (D.28) can be expressed as

$$\text{var}\left[\breve{\beta}_k\right] = \Gamma_k^2 \sigma_{v_k}^2 \sum_{n=l_0}^{L} \left(S_k \cos\left(\omega_k nT\right) - B_k \sin\left(\omega_k nT\right)\right)^2. \quad \text{(D.33)}$$

Appendix E. Quantisation Noise in the Cross-Correlation Technique

In this appendix it is shown that given a PRBN test input signal, $x(nT)$, to the channel under test shown in Figure 5.3, the equivalent additive quantisation noise, $v_Q(nT)$, resulting from quantisation in the A/D converter is approximately uncorrelated with the signals $x(nT)$ and $y(nT)$ even for coarse quantisation characteristics.

In the following derivations the system noise, $v_s(nT)$, is assumed to be zero, i.e.,

$$v_s(nT) = 0. \tag{E.1}$$

The output of the channel in Figure 5.3 is therefore given by

$$\hat{y}(nT) = y(nT) + v_Q(nT) \tag{E.2}$$

i.e., the output, $\hat{y}(nT)$, is the sum of the unquantised signal $y(nT)$ and the equivalent quantisation noise, $v_Q(nT)$.

Suppose that the unquantised signal, $y(nT)$, is a sequence of samples of the random variable Y with probability density function (PDF), $f_Y(y)$. The characteristic function, $w_Y(\alpha)$, is defined as [115]

$$w_Y(\alpha) = \int_{-\infty}^{\infty} f_Y(y)e^{jy\alpha}dy, \tag{E.3}$$

i.e., the Fourier transform of the PDF.

In [102] and [103] it is shown that the quantisation noise, $v_Q(nT)$, is uncorrelated with $y(nT)$ if

$$w_Y(\alpha) = 0; \quad |\alpha| \geq 2\pi/\Delta_q, \tag{E.4}$$

where Δ_q is the quantisation step size of the A/D converter.

Assuming the duration of the channel impulse response, $h'(nT)$, is limited to N samples, the output, $y(nT)$ in Figure 5.3 can be written as the convolution sum

$$y(nT) = \sum_{l=0}^{N-1} h'(lT)x((n-l)T).$$

(E.5)

If the input signal to the channel, $x(nT)$, is a zero-mean random process then the signal, $y(nT)$, given by (E.5) is a weighted sum of N random variables.

Taking the expected value of $y(nT)$ in (E.5) gives

$$\begin{aligned}
E\left[y(nT)\right] &= E\left[\sum_{k=0}^{N-1} h'(kT)x((n-k)T)\right] \\
&= \sum_{k=0}^{N-1} h'(kT)E\left[x((n-k)T)\right] \\
&= 0.
\end{aligned}$$

(E.6)

The variance of $y(nT)$ is therefore given by

$$\begin{aligned}
\sigma_y^2 &= E\left[\left(\sum_{k=0}^{N-1} h_d(kT)x((n-k)T) - E\left[y(nT)\right]\right)^2\right] \\
&= \sum_{k=0}^{N-1} h'^2(kT)E\left[x((n-k)T)^2\right] \\
&= \sigma_x^2 \sum_{k=0}^{N-1} h'^2(kT),
\end{aligned}$$

(E.7)

where σ_x^2 is the variance of $x(nT)$.

From the central limit theorem for unequal distributions [115] the sum in (E.5) has a probability distribution function that asymptotically approaches the Gaussian distribution as $N \rightarrow \infty$. In the following example it is shown that the probability distribution function of $y(nT)$ closely approximates a Gaussian distribution for the PRBN input test signals considered in Chapters 5 and 6 and for values of N that are of the order of the duration of the impulse response, $h'(nT)$.

Example 1.

The distribution density function shown in Figure E.1 was obtained by passing a PRBN signal with a period of 16383 through a 50-tap ($N = 50$ in (E.5)) FIR low-pass filter (representative of the I and Q channels of the IQ modulator). Also shown for comparison is a Gaussian distribution function.
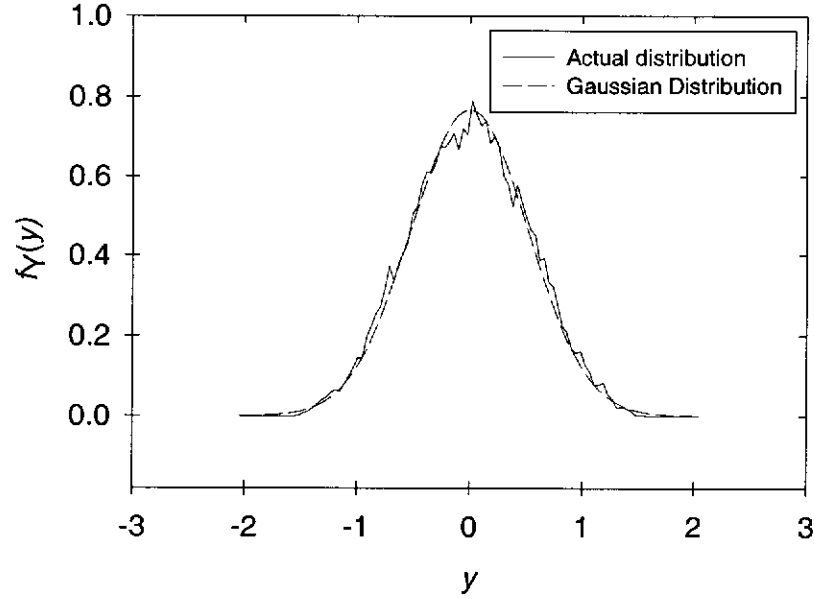
Figure E.1. PDF of the output of a 50-tap FIR filter with a PRBN input signal.

From Figure E.1 it can be seen that the output of the discrete-time channel resulting from a PRBN input signal is approximately Gaussian distributed.

■

For a unit amplitude PRBN test input signal, $\sigma_x^2 = 1$ in (E.7) and the variance, σ_y^2 is given by

$$\sigma_y^2 = \sum_{k=0}^{N-1} h'^2(kT).$$

(E.8)

The signal $y(nT)$ therefore has a variance equal to the sum of the squares of the discrete-time filter coefficients given by (E.8) and has a PDF, $f_Y(y)$, that is approximately Gaussian distributed. From (E.3), the characteristic function, $w_Y(\alpha)$, is therefore also Gaussian and is given by

$$w_Y(\alpha) = \frac{1}{\sqrt{2\pi}\sigma_y} \int_{-\infty}^{\infty} e^{-y^2/2\sigma_y^2} e^{jy\alpha} dy$$

$$= e^{-\alpha^2\sigma_y^2/2}.$$

(E.9)

The function $w_Y(\alpha)$ is shown plotted in Figure E.2.
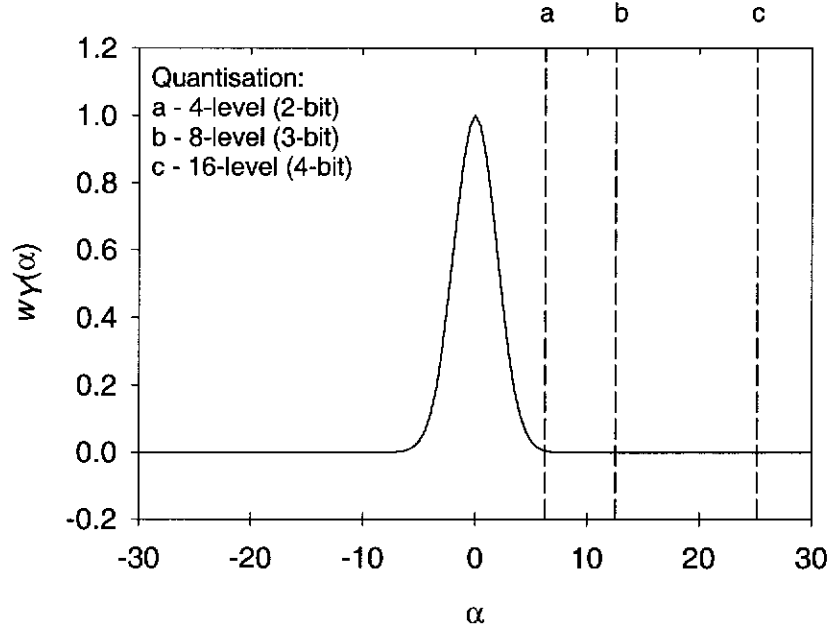
Figure E.2. Characteristic function of quantiser input signal.

The variance value $\sigma_y^2 = 0.27$ was used to generate the Gaussian distribution in Figure E.1 and the characteristic function in Figure E.2. This is a typical value for the sum in (E.8) for practical modulator discrete-time I or Q channel impulse responses.

In Table E.1 the values of $\alpha = 2\pi/\Delta_q$ for three quantisation conditions are indicated. These correspond to quantisation step sizes of $\Delta_q = 1.0$, $\Delta_q = 0.5$ and $\Delta_q = 0.25$. Since the dynamic range of the signal $y(nT)$ is approximately -2 to 2 (see Figure E.1), these step sizes are associated with 4, 8 and 16 level quantisation respectively. The values of $w_Y(\alpha)$ for various quantisation step sizes are given in Table E.1.

Quantisation			Characteristic function, $w_Y(\alpha)$
Bits	Levels	Step size	
2	4	1.0	4.8×10^{-3}
3	8	0.5	5.1×10^{-10}
4	16	0.25	6.8×10^{-38}
8	256	15.625×10^{-3}	2.2×10^{-9516}

Table E.1. Characteristic function of the quantiser input for different quantisation conditions.

From Figure E.2 and Table E.1, it can be seen that the characteristic function, $w_Y(\alpha)$, is approximately zero even at values of α representing quite coarse quantisation environments. The conditions on the characteristic function and the quantisation step size for statistical independence of the quantisation noise from the input signal are thus met (approximately).

References

[1] Z. Kostic and S. Seetharaman, "Digital Signal Processors in Cellular Radio Communications," *IEEE Comm. Mag.*, pp. 22 – 35, Dec. 1997.

[2] H. Meyr and R. Subramanian, "Advanced Digital Receiver Principles and Technologies for PCS," *IEEE Comm. Mag.*, pp. 68 – 78, Jan. 1995.

[3] M. Cummings and S. Haruyama, "FPGA in the Software Radio," *IEEE Comm. Mag.*, pp. 108 – 112, Feb. 1999.

[4] J. E. Gunn, K. S. Barron and W. Ruczczyk, "A Low-Power DSP Core-Based Software Radio Architecture," *IEEE J. Select. Areas Comm.*, vol. 17, no. 4, pp. 574 – 590, Apr. 1999.

[5] T. Hentschel, M. Henker and G. Fettweis, "The Digital Front-End of Software Radio Terminals," *IEEE Personal Comm.*, pp. 40 – 46, Aug. 1999.

[6] K. C. Zangi and R. D. Koilpillai, "Software Radio Issues in Cellular Base Stations," *IEEE J. Selcet. Areas Comm.*, vol. 17, no. 4, pp. 561 – 573, Apr. 1999.

[7] R. H. Walden, "Analogue-to-Digital Converter Survey and Analysis," *IEEE J. Selcet. Areas Comm.*, vol. 17, no. 4, pp. 539 – 550, Apr. 1999.

[8] W. H. W. Tuttlebee, "Software-Defined Radio: Facets of a Developing Technology," *IEEE Personal Comm.*, pp. 38 – 44, Aug. 1999.

[9] A. K. Salkintzis, H. Nie and P. T. Mathiopoulos, "ADC and DSP Challenges in the Development of Software Radio Base Stations," *IEEE Personal Comm.*, pp. 47 – 55, Aug. 1999.

[10] Bustillo, J. Rodriguez-Palanca, M. and Pérez, J., "4-PAM/FM Modulator with DSP: A Solution For ERMES," *IEEE 41st Vehicular Technology Conference*, pp. 584-588, 1991.

[11] European Telecommunications Standards Institute (ETSI) standard ETS 300 133-4, "Paging Systems (PS); European Radio Message System (ERMES)," Part 4: Air Interface Specification, July 1992.

[12] L. Sundström, M. Faulkner and M. Johansson, "Effects of Reconstruction Filters in Digital Predistortion Linearizers for RF Power Amplifiers," *IEEE Trans. Vehic. Tech.*, vol. 44, no. 1, Feb. 1995.

[13] S. Stapleton and F. C. Costescu, "An Adaptive Predistorter for a Power Amplifier Based on Adjacent Channel Emissions," *IEEE Trans. Vehic. Tech.*, vol. 41, no. 1, pp. 49 - 56, Feb. 1992.

[14] S. Leyonhjelm and M. Faulkner, "The Effect of Reconstruction Filters on Direct Upconversion in a Multichannel Environment," *IEEE Trans. Vehic. Tech.*, vol. 44, no. 1, pp. 95 – 102, Feb. 1994.

[15] A. M. Saleh, "Frequency-Independent and Frequency-Dependent Nonlinear Models of TWT Amplifiers," *IEEE Trans. Comms.*, vol. 29, no 11, pp. 1715-1720, November 1981.

[16] S. Pupolin and L. J. Greenstein, "Performance Analysis of Digital Radio Links with Nonlinear Transmit Amplifiers," *IEEE J. Select. Areas Comms.*, vol. 5, no. 3, pp. 534-546, April 1987.

[17] A. Bateman, R. J. Wilkinson and J. D. Marvill, "The Application of Digital Signal Processing to Transmitter Linearisation," *Proc. 8th European Conference on Electrotechnics (EUROCON 88)*, pp. 64 – 67, 1988.

[18] S. W. Cheung and A. H. Aghvami, "Performance of a 16-ARY DEQAM modem employing a baseband or RF predistorter over a regeneartive satellite link," *IEE Proc.*, vol. 135, pt. F, no. 6, pp. 547 – 557, Dec. 1988.

[19] E. Biglieri, S. Barberis and M. Catena, "Analysis and Compensation of Nonlinearities in Digital Transmission Systems," *IEEE J. Select. Areas Comms.*, vol. 6, no. 1, pp. 42 - 51, Jan. 1988.

[20] S. Ariyavisitakul T. –P. Liu, "Characterizing the Effects of Nonlinear Amplifiers on Linear Modulation for Digital Portable Radio Communications," *IEEE Trans. Vehic. Tech.*, vol. 39, no. 4, pp. 383 – 389, Nov. 1990.

[21] J. K. Cavers, "Amplifier Linearization Using a Digital Predistorter with Fast Adaptation and Low Memory Requirements," *IEEE Trans. Vehic. Tech.*, vol. 39, no. 4, pp. 374 - 382, Nov. 1990.

[22] A. S. Wright and W. G. Durtler, "Experimental Performance of an Adaptive Digital Linearized Power Amplifier," *IEEE Trans. Vehic. Tech.*, vol. 41, no. 4, pp. 395-400, Nov. 1992.

[23] S. P. Stapleton, G. S. Kandola and J. K. Cavers, "Simulation and Analysis of an Adaptive Predistorter Utilizing a Complex Spectral Convolution," *IEEE Trans. Vehic. Tech.*, vol. 41, no. 4, pp. 387 - 394, Nov. 1992.

[24] C. N. Smith and N. Dillon, "Cartesian Loop Linearisation of Power Amplifiers at 2 GHz," *Technical Report*, Roke Manor Research Ltd., pp. 1 – 9, 1992.

[25] M. Gharderi, S. Kumar and D. E. Dodds, "Fast adaptive polynomial I and Q predistorter with global optimisation," *IEE Proc. -Commun*, Vol. 143, no. 2, pp. 78 – 86, Apr. 1996.

[26] N. Benvenuto, F. Piazza, A. Uncini and M. Visintin, "Generalised backpropagation algorithm for training a data predistorter with memory in radio systems," *Electron. Letters*, vol. 32. No. 20, pp. 1925 – 1926, Sep. 1996.

[27] J. K. Cavers, "Optimum Indexing in Predistorting Amplifier Linearizers," *Proc. IEEE 47th Vehic. Tech. Conf.*, vol. 2, pp. 676 – 680, 1997.

[28] A. Bernardini and S. De Fina, "Analysis of Different Optimisation Criteria for IF Predistortion in Digital Radio Links With Nonlinear Amplifiears," *IEEE Trans. Comm.*, vol. 45, no. 4, Apr. 1997.

[29] W. G. Jeon, K. H. Chang and Y. S. Cho, "An Adaptive Data Predistorter for Compensation of Nonlinear Distortion in OFDM Systems," *IEEE Trans. Comm.*, vol. 45, no. 10, Oct. 1997.

[30] C. Eun and E. J. Powers, "A New Volterra Predistorter Based on the Indirect Learning Architecture," *IEEE Trans. Sig. Proc.*, vol. 45, no. 1, Jan. 1997.

[31] A. M. Smith and J. K. Cavers, "A Wideband Architecture for Adaptive Feedforward Linearization," *Proc. IEEE 48th Vehic. Tech. Conf. (VTC '98)*, vol. 3, pp. 2488 - 2492, 1998.

[32] J. K. Cavers, "Optimum Table Spacing in Predistorting Amplifier Linearizers," *IEEE Trans. Vehic. Tech.*, vol. 48, no. 5, pp. 1699 - 1705, Sep. 1999.

[33] J. T. Stonick, V. L. Stonick and J. M. F. Moura, "Multi-stage Adaptive Predistortion of HPA Saturation Effects for Digital Television Transmission," *Proc. IEEE Int. Conf. Acoust., Speech Sig. Proc. (ICASSP)*, Phoenix March, 1999.

[34] J. J. Murillo-Fuentes and F. J. Gonzáles-Serrano, "Applying GCMAC to Predistortion in GSM Base Stations," *Proc. IEEE Int. Conf. Acoust., Speech Sig. Proc. (ICASSP)*, Phoenix March, 1999.

[35] Members of the Technical Staff, *Transmission Systems for Communications*, Fourth Edition, Bell Telephone Laboratories, 1970.

[36] J. K. Cavers and M. Liao, "Adaptive Compensation for Imbalance and Offset Losses in Direct Conversion Transceivers," *Proc. IEEE Vehic. Tech. Conference*, St. Loui, MO, pp. 578 – 583, 1991.

[37] N. F. Barber, "Narrow band-pass filter using modulation," *Wireless Engineer*, pp. 132 – 134, Mar 1947.

[38] A. L. Sinsky and P. C. P. Wang, "Error analysis of a quadrature coherent detector processor," *IEEE Trans. Aerosp. Electron. Syst.*, vol. AES-10, pp. 880 – 883, Nov. 1974.

[39] F. E. Churchill, G. W. Ogar and B. J. Thompson, "The Correction of I and Q Errors in a Coherent Processor," *IEEE Trans. Aerosp. Electron. Syst.*, vol. AES-17, no. 1, pp. 131 – 137, Jan. 1981.

[40] M. Faulkner, T. Mattsson and W. Yates, "Automatic Adjustment of Quadrature Modulators," *Electron. Letters*, vol. 27, no. 3, pp. 214 – 216, Jan. 1991.

[41] A. E. Jones and J. G. Gardiner, "Phase Error Correcting Vector Modulator for Personal Communications Network (PCN) Transceivers," *Electron. Letters*, vol. 27, no. 14, pp. 1230 – 1231, July 1991.

[42] D. S. Hilborn, S. P. Stapleton and J. K. Cavers, "An Adaptive Direct Conversion Transmitter," *IEEE Trans. Vehic. Tech.*, vol. 43, no. 2, pp. 223 – 233, May 1994.

[43] K. Gerlach and M. J. Steiner, "An Adaptive Matched Filter that Compensates for I, Q Mismatch Errors," *IEEE Trans. Sig. Proc.*, vol. 45, no. 12, pp. 3104 – 3107, Dec. 1997.

[44] Y.- H. Leung and A. Phillips, "Auto-Compensation of Quadrature Modulators," *Proceedings of the 2nd Australian Workshop on Signal Processing Applications (WOSPA '97)*, Brisbane, Australia, pp. 19-23, December 1997.

[45] J. K. Cavers, "A Fast Method for Adaptation of Quadrature Modulators and Demodulators in Amplifier Linearization Circuits," *Proc. IEEE 46th Vehic. Tech. Conf.*, vol. 2, pp. 1307 – 1311, 1996.

[46] J. K. Cavers, "The Effect of Quadrature Modulator and Demodulator Errors on Adaptive Digital Predistorters," *Proc. IEEE 46th Vehic. Tech. Conf.*, vol. 2, pp. 1205 – 1209, 1996.

[47] J. K. Cavers, "The Effect of Quadrature Modulator and Demodulator Errors on Adaptive Digital Predistorters for Amplifier Linearization," *IEEE Trans. Vehic. Tech.*, vol. 46, no. 2, pp. 456 – 466, May 1997.

[48] J. K. Cavers, "New Methods for Adaptation of Quadrature Modulators and Demodulators in Amplifier Linearization Circuits," *IEEE Trans. Vehic. Tech.*, vol. 46, no. 3, pp. 707 – 716, Aug. 1997.

[49] L. E. Franks, *Signal Theory*, Prentice-Hall, Englewood Cliffs, N.J., 1969.

[50] W. R. Bennett and J. Salz, "Binary Data Transmission by FM over a Real Channel," *Bell Syst. Tech. J.*, Vol. 42, pp. 2387-2426, September 1963.

[51] R. R. Anderson and J. Salz, "Spectra of Digital FM," *Bell Syst. Tech. J.*, Vol. 44, pp. 1165-1189, September 1965.

[52] S. O. Rice, "Envelopes of Narrow-Band Signals," *Proc. IEEE*, Vol. 70, No. 7, pp. 692 – 699, July 1982.

[53] J. Dugundji, "Envelopes and Pre-Envelopes of Real Waveforms," *IRE Trans. Info. Theory*, pp. 53 – 57, March, 1958.

[54] T. G. Kincaid, "The Complex Representation of Signals," *Technical Information Series*, General Electric Company: Heavy Military Electronics Department, no. R67EMH5, October 1966 (revised October 1968).

[55] H. Rodder, "Effects of Tuned Circuits upon a Frequency Modulated Signal," *Proc. IRE*, Vol. 25, pp. 1617-1647, December 1937.

[56] J. R. Carson and T. C. Fry, "Variable Frequency Electric Circuit Theory with Application to the Theory of Frequency Modulation," *Bell Syst. Tech. J.*, vol. 16, pp. 513 – 540, October 1937.

[57] D. Middleton, *An Introduction to Statistical Communication Theory*, McGraw-Hill, New York, 1960.

[58] E. J. Baghdady, (Editor), *Lectures on Communication System Theory*, McGraw-Hill, New York, 1961.

[59] J. J. Downing, *Modulation Systems and Noise*, Prentice-Hall, Englewood Cliffs, N. J., 1964.

[60] H. E. Rowe, *Signals and Noise in Communication Systems*, D. Van Nostrand Co., Princeton, N.J. 1964.

[61] P. F. Panter, *Modulation, Noise, and Spectral Analysis – Applied to Information Transmission*, McGraw-Hill, New York, 1965.

[62] I. Gumowski, "Transient Response in FM," *Proc. IRE*, pp. 820-822, May 1954.

[63] D. A. Linden, Correspondence: "Transient Response in FM," *Proc. IRE*, pp. 1017-1018, July 1957.

[64] H. Salinger, "Transients in Frequency Modulation," *Proc. IRE*, pp. 378-383, August 1942.

[65] R. E. McCoy, "FM Transient Response of Band-Pass Circuits," *Proc. IRE*, pp. 574-579, March 1954.

[66] F. L. H. M. Stumpers, "Distortion of Frequency-Modulated Signals in Electrical Networks," *Communication News*, Vol. IX, No. 3, pp. 82-92, April 1948.

[67] M. L. Liou, "Noise in an FM System Due to an Imperfect Linear Transducer," *Bell Syst. Tech. J.*, pp. 1537-1561, November 1966.

[68] S. Haykin, *Communication Systems*, Second Edition, John Wiley & Sons, New York, 1983.

[69] A. Antoniou, *Digital Filters: Analysis, Design and Applications*, Second Edition, McGraw-Hill, New York, 1993.

[70] L. R. Rabiner, B. Gold, and C. A. McGonegal, "An Approach to the Approximation Problem for Nonrecursive Digital Filters," *IEEE Trans. Audio Electroacoustics*, Vol. 18, pp.83-106, June 1970.

[71] T. G. Cross, "Intermodulation Noise in FM Systems Due to Transmission Deviations and AM/PM Conversion," *Bell Syst. Tech. J.*, pp. 1749-1773, December 1966.

[72] B. C. Kuo, *Digital Control Systems*, Holt, Rinehart and Winston, Inc., New York, 1980.

[73] D. G. Luenberger, *Optimisation by Vector Space Methods*, John-Wiley & Sons, New York, 1969.

[74] G. Golub and C. Van Loan, *Matrix Computations*, Second Edition, Johns Hopkins University Press, Baltimore, 1989.

[75] E. Kreyszig, *Advanced Engineering Mathematics*, Sixth Edition, John Wiley & Sons, New York, 1988.

[76] U. Grenander and G. Szego, *Toeplitz Forms and their Applications*, University of California Press, Berkeley, 1958.

[77] E. J. Hannan, *Time Series Analysis*, Methuen and Co. Ltd., London, 1960.

[78] J. R. Westlake, *A Handbook of Numerical Matrix Inversion and Solution of Linear Equations*, John Wiley & Sons, Inc., New York, 1968.

[79] R. A. Horn and C. R. Johnson, *Matrix Analysis*, Cambridge University Press, Cambridge, 1985.

[80] W. Press, S. Teukolsky, W. Vetterling and Flannery, B., *Numerical Recipes in C*, Second Edition, Cambridge University Press, Cambridge, 1992.

[81] A. Ralston and P. Rabinowwitz, *A First Course in Numerical Analysis*, Second Edition, McGraw-Hill, New York, 1978.

[82] M.E. Van Valkenburg, *Analogue Filter Design*, Holt, Rienhart & Winston, New York, 1982.

[83] P. Eykhoff, *System Identification: Parameter and State Estimation*, John Wiley & Sons, London, 1974.

[84] L. Ljung, *System Identification: Theory for the User*, Prentice-Hall, Englewood Cliffs, New Jersey, 1987.

[85] T. Söderström and P. Stoica, *System Identification*, Prentice-Hall, Englewood Cliffs, New Jersey, 1989.

[86] R. Johansson, *System Modelling and Identification*, Prentice-Hall, Englewood Cliffs, New Jersey, 1993.

[87] D. W. Clarke and P. A. N. Briggs, "Errors in Weighting Sequence Estimation," *International Journal on Control*, Vol. 11, No. 1, pp. 49-65, 1970.

[88] G. C. Goodwin and R. L. Payne, *Dynamic System Identification: Experiment Design and Data Analysis*, Academic Press, New York, 1977.

[89] K. R. Godfrey, "Correlation Methods," *Automatica*, Vol. 16, pp. 527-534, 1980.

[90] D. V. Sarwate and M. B. Pursley, "Crosscorrelation Properties of Pseudorandom and Related Sequences," *Proc. IEEE*, Vol. 68, No. 5, pp. 593-619, May 1980.

[91] M. G. Bellanger, *Adaptive Digital Filters and Signal Analysis*, Marcel Dekker, Inc., New York, 1987.

[92] J. S. Bendat and A. G. Piersol, *Measurement and Analysis of Random Data*, John Wiley & Sons, New York 1966.

[93] D. Everett, "Periodic Digital Sequences with Pseudonoise Properties," *G.E.C. Journal*, Vol. 33, No. 3, pp. 115-126, 1966.

[94] H. R. Simpson, "Statistical Properties of a Class of Pseudorandom Sequencs," *Proc. IEE*, Vol. 113, No. 12, pp. 2075-2080, December 1966.

[95] C. B. Speedy, R. F. Brown and G. C. Goodwin, *Control Theory: Identification and Optimal Control*, Oliver and Boyd, Edinburgh, 1970.

[96] G. Hoffmann de Visme, *Binary Sequences*, The English Universities Press Ltd, London 1971.

[97] W. W. Peterson and E. J. Weldon, *Error-Correcting Codes*, Second Edition, The MIT Press, Massachusetts, 1972.

[98] J-S. No, S. W. Golomb, G. Gong, H-W. Lee and P. Gaal, "Binary Sequences of Period $2^n - 1$ with Ideal Autocorrelation," *IEEE Trans. Info. Theory*, Vol. 44, No. 2, pp. 814-817, March 1998.

[99] J-S. No, H. Chung and M-S. Yun, "Binary Pseudorandom Sequences of Period $2^m - 1$ with Ideal Autocorrelation Generated by the Polynomial $z^d + (z+1)^d$," *IEEE Trans. Info. Theory*, Vol. 44, No. 3, pp. 1278-1282, May 1998.

[100] R. M. Gray, "Quantization Noise Spectra," *IEEE Trans. Inform. Thoery*, Vol. 36, No. 6, pp. 1220-1244, November 1990.

[101] W. R. Bennett, "Spectra of Quantized Signals," *Bell Syst. Tech. J.*, Vol. 27, pp. 446-472, July 1948.

[102] B. Widrow, "A Study of Rough Amplitude Quantization by Means of Nyquist Sampling Theory," *IRE Trans. Circuit Theory*, CT-3, p. 226, 1956.

[103] D. G. Watts, "A General Theory of Amplitude Quantization with Applications to Correlation Determination," *IEE Monograph*, No. 481M, pp. 209-218, November 1961.

[104] B. A. Spirad and D. L. Snyder, "A Necessary and Sufficient Condition for Quantization Errors to be Uniform and White," *IEEE Trans. Acoust., Speech and Sig. Proc.*, Vol. 25, No. 5, pp. 442-448, October 1977.

[105] T. A. C. M. Claasen and A. Jongepier, "Model for the Power Spectral Density of Quantization Noise," *IEEE Trans. Acoust. Speech and Signal Proc.*, Vol. 29, No. 4, pp. 914-917, August 1981.

[106] J. H. Blythe "The Spectrum of a Quantized Sinusoid," *GEC Journal of Research*, Vol. 3, No. 4, pp. 229-242, 1985.

[107] M. F. Wagdy and W.-M. Ng, "Validity of Uniform Quantization Error Model for Sinusoid Signals Without and With Dither," *IEEE Trans. Instrum. Meas.*, Vol. 38, No. 3, pp. 718-722, June 1989.

[108] J. D. Echard and M. L. Watt, "The Quantization Noise Spectrum of a Sinusoid in Colored Noise," *IEEE Trans. Signal Proc.*, Vol. 39, No. 8, pp. 1780-1787, August 1991.

[109] L. Schuchman, "Dither Signals and Their Effect on Quantization Noise," *IEEE Trans. Commun. Theory*, pp. 162-165, December 1964.

[110] N. S. Jayant and L. R. Rabiner, "The Application of Dither to the Quantization of Speech Signals," *Bell Syst. Tech. J.*, Vol. 51, No. 6, pp. 1292-1304, July-August 1972.

[111] B. Brannon, "Overcoming Converter Nonlinearities with Dither," *Application Note AN-410*, Analog Devices, Norwood, MA, USA.

[112] Texas Instruments, "TMS320C3x Users Guide," *Texas Instruments Digital Signal Processing Products*, USA, 1995.

[113] Maxim Integrated Products, *MAXIM 4th- and 8th-Order Continuous-Time Active Filters*, Maxim data sheet 19-4191, Rev. 1, July 1992.

[114] D. T. Finkbeiner II, *Elements of Linear Algebra*, W. H. Freeman and Co., San Francisco, 1972.

[115] Peebles, P. Z., *Probability, Random Variables, and Random Signal Principles*, McGraw-Hill, New York, 1980.